Spin Correlation in $t\bar{t}$ Production from $p\bar{p}$ Collisions at $\sqrt{s} = 1.8$ TeV

Suyong Choi

Under the supervision of
Professor SunKee Kim

A dissertation submitted to the Graduate
Faculty of Seoul National University
in partial fulfillment of the requirement
for the Degree of Doctor of Philosophy

Department of Physics
The Graduate School of Natural Sciences
Seoul National University
Seoul, KOREA

August, 1999

Abstract

The Standard Model predicts that the lifetime of the top quark is shorter than the typical time scale at which hadronization process occurs, and the spin information at its production is preserved. Spin correlation of the $t\bar{t}$ system from $p\bar{p}$ collisions at the Tevatron is analyzed using 6 events in the dilepton channels collected using the DØ detector. Spin correlation factor of $\kappa > -0.25$ at 68% CL is obtained from the data.

Key Words : Standard Model, top quark, spin correlation, Tevatron, DØ detector, correlation factor κ

Preface

MAJORANA: There are scientists who "happen" only once in every 500 years, like Archimedes or Newton. And there are scientists who happen only once or twice in a century, like Einstein or Bohr.

FERMI: But where do I come in, Majorana?

MAJORANA: Be reasonable, Enrico! I am not talking about you or me. I am talking about Einstein and Bohr.

Who am I? Indeed, no other question can be both trite and profound as this. At some point in the history when mankind had acquired sufficient intelligence and had become self-conscious, they probably asked such question. Qualities such as curiosity, ability to use language and intelligence, have enabled humans to build roads through the wilderness, make civilization possible, and it may have motivated us to seek answers to why we or anything exist at all. Could we say that we have come any closer to answering this

question?

One cannot help but think of the incidental nature of human existence, given the fact that numerous conditions must have been met, some physical and some historical, before we could ever put feet on the face of this Earth. History of Earth tells us that there were five mass extinctions and at each extinction 90% of all the living species perished, and those that survived the extinctions were the simplest of living organisms. Besides these historical considerations, there are physical constraints on life as we know it, and by no means is it trivial that living organisms will thrive in any of the places that satisfy such conditions. Are we the inevitable end product or just an accident?

I am quite fortunate enough to be curious about where we are and to have learned the means to pursue the still unanswered questions about the place of which we are a part and to which we will return in oblivion. In my mind, physics offers a unique vantage point into these matters, as it investigates the fundamentals behind the epi-phenomena.

In physics, we rephrase the question into "What are the physical requirements for life?" The relevance of such question to our existence depends on how strongly we owe our being to the physical world. Life on Earth is the only life we know. And this life is not possible without elements such as

carbon, hydrogen and oxygen. It is certainly not a sufficient condition, but a necessary one at least. Were these elements present ever since the Universe came to be? We think not. Only hydrogen and a small amount of helium were present in the prime-ordeal universe. The heavier elements, we think, were synthesized in stars through a chain of events that takes several tens to hundreds of millions of years. And those heavier elements would have been accessible only if the star died a fiery death in the form of supernova, a light that signifies an end but also a beginning. Is it not truly amazing that we were once a brightly shining star?

The fundamental constituents of matter and interactions among them, which are the object of interest in particle physics, are prevalent in everything animate and inanimate, and is eventually responsible for physically realizing life as we know it. The belief we hold is that most of the physical phenomena could be understood by means of reducing a complex phenomenon into simple elements. By simplifying, isolating and studying different elements of a complex phenomena, we can hope to achieve the understanding of the whole. An assumption implicit in this approach is that the property of the whole is derivable from properties of its sub-parts.

A naïve assumption though it may be, this reductionist approach has made science what it is. We do not yet know why it works, we cannot

prove nor disprove its correctness. Assumptions both explicit and implicit make the analysis of validity of scientific methods a very complicated field. However, no one can doubt that it works. An important part of the scientific method is the corrective mechanism which culls out erroneous models that are disproved by experiments.

Our current understanding of the fundamental processes is summarized by the Standard Model (SM) which has some 19 arbitrary parameters. The values of these parameters can not be determined *a priori* from first principles, but must be determined from experimental measurements, and it means that the current model leaves a lot to be desired in order for it to acquire the status of completeness. Even with such deficiencies, the SM allows us to postdict (as opposed to predict) the history of universe, the stellar evolutions and correctly calculate the abundances of various elements. The most interesting part of this whole scenario is that if the values of the SM parameters were off by a small amount, stars would not have formed and there would not have been any heavy nuclei from which we could take form. Very fine tuning of the parameters are required for the universe to look the way it does. In addition, the initial conditions in the universe has to be just right, homogeneous but not too homogeneous.

The manner in which a particle or high-energy physicist approaches a

question of why we are here, is by hypothesizing and measuring the properties of fundamental particles and interactions among them. Of course in our everyday life, we do not think of such deeply philosophical questions, but we all realize that our research in some sense will aid in understanding our world and our place in it. Quarks are quirky entities. While over more than 20 years of experiments have, beyond doubt, proven their existence, we have not yet been able to observe it in isolation. They reside in the nuclei which forms atoms, but they are fractionally charged in units of e, and has never been observed by itself. What does it mean to say something exists, when we can observe it only in association with something else?

Spin is an intrinsic property of particles that constitute matter. The spin of the quark has so far been inferred indirectly by measuring the angular distribution of entities called "jets." Top quark is expected to decay before the spin information at its production is diluted and offers us a unique view of an almost "free quark."

An analysis of spin-correlation in $t\bar{t}$ system from $p\bar{p}$ collisions at the Tevatron in Fermilab is presented in this thesis. This analysis allowed me to work on developing new analysis, employing new techniques. Most of all observing that the top quark might be indeed decaying as a free quark excited me. It would be a telltale signature of a free quark.

The thesis is organized as follows: Introduction to top quark and spin correlation of $t\bar{t}$ system is given in Chapter 1. The Tevatron accelerator complex and DØ detector system is described in Chapter 2. The manner in which the information from the detector is used to reconstruct and identify particles is detailed in Chapter 3. Chapter 4 discusses the selection of $t\bar{t}$ events and backgrounds to the signal. The analysis of spin-correlation in $t\bar{t}$ system is described in Chapter 5. Finally, results are summarized in the Conclusion.

Contents

List of Figures

List of Tables

Chapter 1

Introduction

Particle physics is often called a fundamental science. It is fundamental in the sense that the processes of interest in physics occurs universally. While a human being can be described in terms of functions of its organs, the organs in terms of cells, cells in terms of chemical factories inside it and so forth, but at the deepest level, there are interactions among quarks and leptons. However, by no means is particle physics alone in its claim of fundamentality, the laws of thermodynamics are fundamental in this sense also.

Our current understanding of "fundamental" particles and its interactions is summarized in the Standard Model (SM). The power and beauty of gauge symmetry is exemplified in the unification of electromagnetic and weak interactions [1]. The SM is an effective law, that has stood up to prob-

ings at energies of the order of TeV. For the top quark, SM predicts that its lifetime is short compared to the typical time scale of hadronization and spin information at the production will be preserved in the decay products. At the Tevatron, spins of t and $\bar{t}$ produced in pairs are expected to be correlated. The reality of quarks can more strongly be argued by observing the spin correlation of top quarks.

1.1   The Standard Model

Our understanding of Nature has changed profoundly during the 20th century. The role of experimentation in discovery of new principles that govern our world cannot be over-emphasized. Theoretical dilemma concerning the explanation of black body radiation has brought about the discovery of quantum mechanics. Our everyday language of the macroscopic world breaks down in the microscopic world and a new language of wave mechanics is needed in microscopic world. Quantum mechanics is still a deterministic theory and only when a "measurement" is performed on a non-commuting variable does the wave function "collapse". While the collapsing of wave function is not well understood, still, quantum mechanics provides everyday physicist with good working principles, with which he or she can do

meaningful experimentations. Michelson-Morley interferometry experiment proved that there is no preferred frame of reference in this world, and gave inspiration to the theory of special relativity, the generalization of which is the theory of general relativity. The discovery of these theories has shown that classical theories are only approximations valid when applied to things that are not too small, too fast or too massive. Numerous scientists throughout the 20th century have probed deeper into smaller regions and farther out into the universe, always testing the limits of our knowledge and instruments.

While we know that the methodology of acquiring scientific knowledge cannot be systematized, we do know that aesthetics has provided us with a very powerful tool in our quest for a more unified understanding of phenomena around us, as is evident from the formulations of quantum mechanics, theories of special and general relativity. An idea which is not at all trivial is the belief that there is unique law from which everything can be derived. Perhaps a monotheistic belief prevalent in the western civilization could have helped its people drive to seek this idea, but it is nonetheless important when one looks back on the development of science.

The marriage of quantum mechanics and special relativity is then perhaps a natural next step. Any law of fundamental nature must be consistent with both quantum mechanics and special relativity (i.e. fundamental law

must be written in a Lorentz covariant form). The Dirac equation was the first successful attempt at combining the two. The Dirac equation describes particles of spin $\frac{1}{2}$, but also predicts that there should be anti-particles. Dirac equation still had the serious difficulty of interpretation of negative energy states, when it was first formulated. Dirac interpreted that the reason particles are stable is because the negative energy states are filled, and thus elevating the status of Dirac equation to a many-particle equation. Thus was born the quantum field theory.

Quantum field theory is more of a tool than an insight in guiding us to the fundamental laws. It is only by virtue of the fact that particles interact that we may observe them. Therefore, it is important to enquire how one may describe particle interactions in field theory. In the 1950s and 1960s, there was a degree of arbitrariness in the choice of interaction. For example, the pion-nucleon interaction could be interpreted as $\bar{\psi}_{\mathrm{N}} \gamma_5 \psi_{\mathrm{N}} \phi_\pi$ or as $\bar{\psi}_{\mathrm{N}} \gamma^\mu \gamma_5 \psi_{\mathrm{N}} \partial_\mu$. Present day theories, however, do not allow such freedom. They state that interactions between fundamental fields are dictated by a gauge principle, requirement that quantities which are conserved are conserved locally and not merely globally. By "conservation of charge" we usually mean that the disappearance of charge at one point be accompanied by a current, which makes possible its appearance at another point. Philosophically, the local

gauge principle arises because locally, one has a choice in defining "positive" or "negative" charge arbitrarily but that physics must be invariant of how one defines it.

These matters are the concern of Noether's theorem, which connects symmetries and conservation laws, using a Lagrangian formulation of field theory. At the same time it emerges that, in order to have a local symmetry, we need a spin 1 massless gauge field, whose interaction with the 'matter' fields is dictated uniquely. This gives us the electromagnetic, weak and strong interactions, the respective gauge fields being the photon, the weak bosons and the gluons.

The interactions between quarks and leptons are unified in the Standard Model through the use of $SU(3) \times SU(2)_L \times U(1)_Y$ local gauge symmetries. The $SU(3)$ local symmetry of the Lagrangian density necessitates color octet gluons and color triplet fermions, which are quarks. The parity violating weak interaction is described by the $SU(2)_L$ gauge symmetry acting only on the left-handed fermions. The electromagnetic interaction is well-described by the $U(1)$ symmetry. Before spontaneous symmetry breaking through the Higgs mechanism, all the gauge bosons are massless. When the symmetry is spontaneously broken the gauge particles (W and Z) involved in charged and neutral current exchange become massive.

1.1.1   Quantum Electrodynamics

$U(1)$ local gauge invariance demands that there be a *gauge field* A_μ which interacts with fermions in a prescribed way. The Lagrangian density for the electromagnetic field A_μ interacting with a spin-$\frac{1}{2}$ field ψ of bare mass m is

$$\mathcal{L} = -\frac{1}{4}F_{\mu\nu}F^{\mu\nu} + \bar{\psi}(i\gamma^\mu D_\mu - m)\psi. \tag{1.1}$$

Here, $F_{\mu\nu}$ is the electromagnetic field tensor

$$F_{\mu\nu} = \partial_\mu A_\nu - \partial_\nu A_\mu \tag{1.2}$$

and D_μ is the covariant derivative

$$D_\mu = \partial_\mu - ieA_\mu Q, \tag{1.3}$$

where e is the unit of electric charge and Q is the charge operator. This Lagrangian is invariant under local gauge transformations,

$$\psi(x) \quad \rightarrow \quad U(x)\psi(x) \tag{1.4}$$

$$A_\mu(x) \quad \rightarrow \quad A_\mu(x) + \partial_\mu \alpha(x) \tag{1.5}$$

with

$$U(x) = \exp(-ieQ\alpha(x)) \tag{1.6}$$

for arbitrary $\alpha(x)$. The mass term $\frac{1}{2}m^2 A_\mu A^\mu$ is prohibited by gauge invariance.

When the Lagrangian above is expanded, term that describes the interaction between fermion and the gauge field becomes evident.

$$\mathcal{L}_{\text{QED}} = -\frac{1}{4}F_{\mu\nu}F^{\mu\nu} + \bar{\psi}(i\gamma^\mu\partial_\mu - m)\psi - e\bar{\psi}\gamma^\mu A_\mu\psi \tag{1.7}$$

The last term describes the QED interaction and commonly written as

$$\mathcal{L}_{int} = -eJ^\mu_{em}A_\mu, \text{ where } J^\mu_{em} = \bar{\psi}\gamma^\mu Q\psi, \tag{1.8}$$

and J^μ_{em} is the electromagnetic current.

1.1.2 Non-Abelian Gauge Symmetry

In analogy with QED, invariance under the infinitesimal local gauge transformation on spin-$\frac{1}{2}$ fields

$$\psi \to [1 - ig\vec{\alpha}(x) \cdot \vec{T}]\psi(x), \tag{1.9}$$

where $\vec{\alpha}(x)$ is an arbitrary infinitesimal vector in isospin space and $\vec{T} = (T_1, T_2, T_3)$ is the isospin operator whose components T_i are the generators of SU(2) symmetry transformations. The T_i do not commute

$$[T_i, T_j] = i\epsilon_{ijk}T_k, \tag{1.10}$$

and the gauge group is said to be *non-Abelian*. Operating on isospin doublets, the matrix representation is $T_i = \frac{1}{2}\tau_i$ where τ_i are the Pauli matrices.

The ψ-field part of the Lagrangian can be made gauge invariant by introducing an appropriate covariant derivative D_μ and Yang-Mills gauge fields $\mathbf{W}_{i\mu}$ ($i = 1, 2, 3$).

$$D_\mu = \partial_\mu + ig\vec{W}_\mu\vec{T} \tag{1.11}$$

$$\vec{W}_\mu(x) \rightarrow \vec{W}_\mu(x) + \partial_\mu\vec{\alpha}(x) + g\vec{\alpha}(x) \times \vec{W}_\mu(x). \tag{1.12}$$

The $\mathbf{W}$-field part of the Lagrangian is

$$\mathcal{L}_W = -\frac{1}{4}\mathbf{W}_{\mu\nu} \cdot \mathbf{W}^{\mu\nu}, \tag{1.13}$$

where

$$\mathbf{W}_{\mu\nu} = \partial_\mu W_\nu - \partial_\nu W_\mu - gW_\mu \times W_\nu. \tag{1.14}$$

In addition to the usual kinetic energy terms, this introduces cubic and quartic self-couplings of $\mathbf{W}_\mu$ fields. Self-coupling is required by gauge invariance and an essential property of non-Abelian gauge fields.

This method can be extended to arbitrary non-Abelian gauge group. Assuming that T_i's are the generators of some unspecified group, satisfying the commutation relations

$$[T_i, T_j] = if_{ijk}T_k. \tag{1.15}$$

The coefficients f_{ijk} are the *structure constants* of the group. In any given representation, the T_i are traceless and normalized by $\text{Tr}(T_iT_j) = c\delta_{ij}$, where c is a constant depending on the representation. There is a gauge field $W_{i\mu}$ for each independent generator T_i and the Lagrangian is defined by

$$\mathcal{L} = -\frac{1}{4}W_{i\mu\nu}W_i^{\mu\nu} + \bar{\psi}(i\gamma^\mu D_\mu - m)\psi, \tag{1.16}$$

where,

$$W_{i\mu\nu} = \partial_\mu W_{i\nu} - \partial_\nu W_{i\mu} - gf_{ijk}W_{j\mu}W_{k\nu}, \tag{1.17}$$

$$D_\mu \;\; = \;\; \partial_\mu + igW_{i\mu}T_i. \tag{1.18}$$

The Lagrangian is invariant under the transformations

$$\psi(x) \;\; \rightarrow \;\; [1 - ig\alpha_i(x)T_i]\psi(x), \tag{1.19}$$

$$W_{i\mu}(x) \;\; \rightarrow \;\; W_{i\mu} + \partial_\mu\alpha_i(x) + gf_{ijk}\alpha_j(x)W_{k\mu}(x) \tag{1.20}$$

Again, mass terms for the gauge fields are not allowed due to gauge invariance. The conserved current of the gauge group is

$$J_i^\mu = \bar{\psi}\gamma^\mu T_i\psi + f_{ijk}W_j^{\mu\nu}W_{k\nu}. \tag{1.21}$$

1.1.3   Unbroken $SU(2)_L \times U(1)_Y$

To generate the left-handed structure of charged-current weak interactions, an SU(2) gauge symmetry is applied to left-handed fermion fields ψ_L only, where left and right-handed fields are defined as

$$\psi_L \;\; = \;\; \frac{1}{2}(1 - \gamma_5)\psi, \tag{1.22}$$

$$\psi_R \;\; = \;\; \frac{1}{2}(1 + \gamma_5)\psi. \tag{1.23}$$

	T	T_3	$\frac{Y}{2}$	Q
ν_{eL}	$\frac{1}{2}$	$\frac{1}{2}$	$-\frac{1}{2}$	0
e_L	$\frac{1}{2}$	$-\frac{1}{2}$	$-\frac{1}{2}$	-1
u_L	$\frac{1}{2}$	$\frac{1}{2}$	$\frac{1}{6}$	$\frac{2}{3}$
u_L	$\frac{1}{2}$	$-\frac{1}{2}$	$\frac{1}{6}$	$-\frac{1}{3}$
e_R	0	0	-1	-1
u_R	0	0	$\frac{2}{3}$	$\frac{2}{3}$
d_R	0	0	$-\frac{1}{3}$	$-\frac{1}{3}$

Table 1.1: Weak quantum numbers for the first generation of quarks and leptons.

The fermion mass term is not invariant under $SU(2)_L$ since $\bar{\psi}\psi = \bar{\psi}_L \psi_R + \bar{\psi}_R \psi_L$. The conserved quantum number is weak isospin **T**.

In addition to $SU(2)_L$, an independent $U(1)_Y$ gauge symmetry is introduced whose conserved quantum number Y is called *weak hypercharge*. The $U(1)_Y$ symmetry is essential in order to incorporate the electric charge Q and unify the weak and electromagnetic interactions. The weak hypercharges are specified according to the formula

$$Q = T_3 + \frac{Y}{2}. \tag{1.24}$$

Right handed fermions transform under $U(1)_Y$ while left handed fermions transform under both $SU(2)_L$ and $U(1)_Y$. The weak quantum numbers for the first generation of quarks and leptons are given in Table 1.1.

The Lagrangian is

$$\mathcal{L} = -\frac{1}{4}\mathbf{W}^{\mu\nu} \cdot \mathbf{W}_{\mu\nu} - \frac{1}{4}B^{\mu\nu}B_{\mu\nu} + \bar{\psi}i\gamma^{\mu}D_{\mu}\psi, \tag{1.25}$$

where $\mathbf{W}_{\mu}$ is the massless gauge field for $SU(2)_L$ and B_{μ} for $U(1)_Y$. There is a separate fermion term for each field ψ_L and ψ_R. The covariant derivative is

$$D_{\mu} = \partial_{\mu} + ig\mathbf{W}_{\mu} \cdot \mathbf{T} + ig'\frac{Y}{2}B_{\mu}. \tag{1.26}$$

For the electromagnetic interaction to be unified with the weak interaction in this model, the electromagnetic term $ieQA$ must be contained in the neutral current term $i(gW_{3\mu}T_3 + g'\frac{Y}{2}B_{\mu})$ of the covariant derivative. Therefore, the W_3 and B fields are linear combinations of A and another neutral field Z.

$$\begin{pmatrix} W_3 \\ B \end{pmatrix} = \begin{pmatrix} \cos\theta_W & \sin\theta_W \\ -\sin\theta_W & \cos\theta_W \end{pmatrix} \begin{pmatrix} Z \\ A \end{pmatrix}, \tag{1.27}$$

where θ_W is the electroweak mixing angle. Hence,

$$\begin{aligned} igW_3T_3 + ig'\frac{Y}{2}B &= iA[g\sin\theta_W T_3 + g'\cos\theta_W \frac{Y}{2}] \\ &+ iZ[g\cos\theta_W T_3 - g'\sin\theta_W \frac{Y}{2}]. \end{aligned} \tag{1.28}$$

For the coefficient of A to equal $ieQ = ie(T_3 + \frac{Y}{2})$, we need $g = e/\sin\theta_W$ and

$g' = e/\cos\theta_W$. The Z term of the covariant derivative can then be written

as

$$D^Z_\mu = ig_Z Z_\mu (T_3 - x_W Q), \tag{1.29}$$

where $g_Z = e/(\sin\theta_W \cos\theta_W)$ and $x_W = \sin^2\theta_W$.

The interaction term of the Lagrangian is

$$-\mathcal{L}_{int} = eJ^\mu_{em}A_\mu + \frac{g}{\sqrt{2}}\left(J^{+\mu}_L W^+_\mu + J^{-\mu}_L W^-_\mu\right) + g_Z J^\mu_Z Z_\mu, \tag{1.30}$$

where

$$
\begin{aligned}
J^{\pm\mu}_L &= \sqrt{2}\bar{\psi}\gamma^\mu T^\pm_L \psi, &\tag{1.31}\\
J^\mu_Z &= \bar{\psi}\gamma^\mu [T_{3L} - x_W Q]\psi, &\tag{1.32}\\
J^\mu_{em} &= \bar{\psi}\gamma^\mu Q\psi, &\tag{1.33}\\
T^\pm &= \frac{1}{\sqrt{2}}(T_1 \pm iT_2), &\tag{1.34}\\
W^\pm_\mu &= \frac{1}{\sqrt{2}}(W_{1\mu} \mp iW_{2\mu}). &\tag{1.35}
\end{aligned}
$$

The T_L operations vanish on ψ_R and have the representation $T^i_L = \frac{1}{2}\sigma^i$, where

σ^i are the Pauli matrices.

	T	T_3	$\frac{1}{2}Y$	Q
ϕ^+	$\frac{1}{2}$	$\frac{1}{2}$	$\frac{1}{2}$	1
ϕ^0	$\frac{1}{2}$	$-\frac{1}{2}$	$\frac{1}{2}$	0

Table 1.2: Quantum numbers assigned to the Higgs doublet.

1.1.4   The Higgs Mechanism

In the Standard Model, introduction of a doublet of scalar fields Φ provides a mechanism for giving mass to the otherwise massless gauge particles and fermions. The addition to the Lagrangian is

$$\mathcal{L}_\Phi = |D_\mu\Phi|^2 - V(|\Phi|^2), \tag{1.36}$$

where $|\Phi|^2 = \Phi^\dagger\Phi$. The most general renormalizable form for the scalar potential V is

$$V = \mu^2|\Phi|^2 + \lambda|\Phi|^4. \tag{1.37}$$

The Higgs doublet

$$\Phi = \begin{pmatrix} \phi^+ \\ \phi^0 \end{pmatrix}, \tag{1.38}$$

where ϕ^+ and ϕ^0 are each complex fields with the quantum numbers shown in Table 1.2.

The Higgs field assumes the ground state with non-vanishing vacuum expectation value (VEV) at $|\Phi|^2 = -\frac{1}{2}\mu^2/\lambda$, if $\mu^2 < 0$. The spontaneous symmetry breaking selects a preferred direction in weak isospin plus hypercharge space. In the unitary gauge, the Higgs field has only a neutral component

$$\Phi(x) = \begin{pmatrix} 0 \\ v + H(x) \end{pmatrix}. \tag{1.39}$$

where, $v/\sqrt{2} = (-\mu^2/2\lambda)^{\frac{1}{2}}$. And the covariant derivative applied to the Higgs field is

$$D_\mu \Phi = \frac{1}{\sqrt{2}} \begin{pmatrix} \frac{1}{\sqrt{2}} i g W_\mu^+ (v + H) \\ \partial_\mu H - \frac{i}{2} g_Z Z_\mu (v + H) \end{pmatrix}. \tag{1.40}$$

The Lagrangian then becomes

$$\mathcal{L}_\Phi = \frac{1}{2}(\partial H)^2 + \frac{1}{4} g^2 W^+ W^- (v + H)^2 \tag{1.41}$$
$$+ \frac{1}{8} g_Z^2 ZZ(v + H)^2 - V\left[\frac{1}{2}(v + H)^2\right].$$

Expanding the Lagrangian above, there are terms like $(v^2 g^2/4)W^+ W^-$ and $(v^2 g_Z^2/8)ZZ$ which provide W and Z boson masses, $M_W = gv/2$ and $M_Z = g_Z v/2 = M_W/\cos\theta_W$. And there are terms which couple the Higgs field H to W and Z bosons.

Masses of Leptons and Quarks

The Higgs mechanism not only allows initially massless gauge fields to become massive, but also allows fermions to have mass terms that are renormalizable and invariant under $SU(2)_L \times U(1)_Y$ transformations through Yukawa coupling. For example, for electron,

$$\mathcal{L}_e = -G_e \left[\bar{e}_R (\Phi^\dagger \ell_L) + (\bar{\ell}_L \Phi) e_R \right], \tag{1.42}$$

where, G_e is a coupling constant and

$$\ell_L = \begin{pmatrix} \nu_e \\ e \end{pmatrix}_L. \tag{1.43}$$

Then, the $\mathcal{L}_e$ becomes

$$\mathcal{L}_e = -(G_e v/\sqrt{2}) \bar{e} e - (G_e/\sqrt{2}) H \bar{e} e. \tag{1.44}$$

Thus the electron acquires a mass $m_e = G_e v/\sqrt{2}$ and also a coupling to the Higgs boson that is proportional to the mass. However, this mechanism does not explain the origin of the lepton masses, and coupling constants of Higgs to leptons (G_e, G_μ and G_τ) are arbitrary parameters.

In a similar manner, quark mass terms can be added. If we assume that the weak eigenstates of the unbroken gauge theory are

$$D_{iL} = \begin{pmatrix} u_i \\ d_i \end{pmatrix}, \ u_{iR}, \ d_{iR}, \ (i = 1, 2, 3), \tag{1.45}$$

where D_{jL} is an $SU(2)$ doublet with hypercharge assignment of $Y = \frac{1}{3}$ and u_{iR}, d_{iR} are singlets with $Y = \frac{4}{3}$, $-\frac{2}{3}$, respectively and i denotes generation. The most general Yukawa interaction that gives quark mass terms is

$$\mathcal{L}_q = -\sum_{i=1}^{3} \sum_{j=1}^{3} \left[\tilde{G}_{ij} \bar{u}_{iR} (\tilde{\Phi}^\dagger D_{jL}) + G_{ij} \bar{d}_{iR} (\Phi^\dagger D_{jL}) \right] + \text{h.c} \tag{1.46}$$

where $\tilde{\Phi} = i\tau_2 \Phi^*$ is the conjugate multiplet which transforms as a doublet with $Y = -1$. The G_{ij} and $\tilde{G}_{ij}$ are complex couplings. In general, G_{ij} and $\tilde{G}_{ij}$ need not be diagonal, i.e. the weak eigenstates may not be mass eigenstates. A suitable unitary matrix U and D can be found such that the

mass matrix $M_{ij}^u = \frac{v}{\sqrt{2}}\tilde{G}_{ij}$ and $M_{ij}^d = \frac{v}{\sqrt{2}}G_{ij}$ can be diagonalized.

$$
U_R^{-1}\mathcal{M}^u U_L = \begin{pmatrix} m_u & 0 & 0 \\ 0 & m_c & 0 \\ 0 & 0 & m_t \end{pmatrix}, \quad D_R^{-1}\mathcal{M}^u D_L = \begin{pmatrix} m_d & 0 & 0 \\ 0 & m_s & 0 \\ 0 & 0 & m_b \end{pmatrix},
$$
$$(1.47)$$

and

$$
\begin{pmatrix} u_1 \\ u_2 \\ u_3 \end{pmatrix}_{L,R} = U_{L,R} \begin{pmatrix} u \\ c \\ t \end{pmatrix}_{L,R}, \quad \begin{pmatrix} d_1 \\ d_2 \\ d_3 \end{pmatrix}_{L,R} = D_{L,R} \begin{pmatrix} d \\ s \\ b \end{pmatrix}_{L,R}, \qquad (1.48)
$$

These transformations have important consequences for the weak interaction terms of the Lagrangian. In the neutral current terms, mixing between generations do not occur, while in the charged-current exchange terms, it does. The charged-current term becomes

$$
\overline{(u_1, u_2, u_3)_L}\gamma_\mu \begin{pmatrix} d_1 \\ d_2 \\ d_3 \end{pmatrix}_L = \overline{(u, c, t)_L}\gamma_\mu U_L^\dagger D_L \begin{pmatrix} d \\ s \\ b \end{pmatrix}_L. \qquad (1.49)
$$

The generation mixing of mass eigenstates is described by the matrix

$$V \equiv U_L^\dagger D_L. \tag{1.50}$$

By convention, the mixing is ascribed completely to the $T_3 = -\frac{1}{2}$ states by defining

$$\begin{pmatrix} d' \\ s' \\ b' \end{pmatrix}_L = V \begin{pmatrix} d \\ s \\ b \end{pmatrix}_L \tag{1.51}$$

This matrix V is called the *Cabbibo-Kobayashi-Maskawa matrix*. The matrix elements are labelled by the quarks that they link,

$$V = \begin{pmatrix} V_{ud} & V_{us} & V_{ub} \\ V_{cd} & V_{cs} & V_{cb} \\ V_{td} & V_{ts} & V_{tb} \end{pmatrix}. \tag{1.52}$$

The 90% confidence limits on the magnitude of the elements of the matrix

are (assuming 3 generations) [2]:

$$
\begin{pmatrix}
0.9745 \sim 0.9760 & 0.217 \sim 0.224 & 0.0018 \sim 0.0045 \\
0.217 \sim 0.224 & 0.9737 \sim 0.9753 & 0.036 \sim 0.042 \\
0.004 \sim 0.013 & 0.035 \sim 0.042 & 0.9991 \sim 0.9994
\end{pmatrix} . \qquad (1.53)
$$

Of these matrix elements, only 4 are independent, due to the unitarity requirement of the CKM matrix. In the Wolfenstein parameterization, a complex phase is ascribed to V_{ub}. $\rho = \mathrm{Re}(V_{ub})/|V_{us}V_{cb}|$, $\eta = \mathrm{Im}(V_{ub})/|V_{us}V_{cb}|$, $|V_{us}|$ and $|V_{cb}|$ are independent parameters.

The Standard Model has 19 free parameters, 3 lepton masses[1], 6 quark masses, 3 gauge couplings, 1 vacuum expectation value, 4 CKM matrix parameters, the Higgs boson mass and CP violating QCD phase. The current measured values of the SM parameters are shown in Table 1.3.

The precision electroweak measurements have shown the enormous success of the Standard Model and the discovery of the Higgs boson will mark the closure of this low energy phenomena. The fundamental building blocks of this world are hypothesized to be spin 1/2 fermions, the 6 quarks and 6 leptons. The leptons engage in electroweak interactions by mediating W, Z

---

[1]Note that neutrinos do not get mass terms in SM.

Quark masses	up(u)	$1.5 \sim 5\,\mathrm{MeV/c^2}$
	down(d)	$3 \sim 9\,\mathrm{MeV/c^2}$
	charm(c)	$60 \sim 170\,\mathrm{MeV/c^2}$
	strange(s)	$1.1 \sim 1.4\,\mathrm{MeV/c^2}$
	top(t)	$173.8 \pm 5.2\,\mathrm{GeV/c^2}$
	bottom(b)	$4.1 \sim 4.4\,\mathrm{GeV/c^2}$
Lepton masses	electron(e)	$0.51099907 \pm 0.00000015\,\mathrm{MeV/c^2}$
	muon(μ)	$105.658389 \pm 0.000034\,\mathrm{MeV/c^2}$
	tau(τ)	$1777.05^{+0.29}_{-0.26}\,\mathrm{MeV/c^2}$
Strong coupling constant	$\alpha_s(M_Z)$	0.119 ± 0.002
Electro-weak coupling	α_{em}	$1/137.0359895$
	$\sin^2\theta(M_Z)$	0.23124 ± 0.00024
	M_Z	$91.187 \pm 0.007\,\mathrm{GeV/c^2}$
CKM matrix	ρ	0.156 ± 0.090
	η	0.328 ± 0.054
	$|V_{us}|$	0.2196 ± 0.0023
	$|V_{cb}|$	0.0395 ± 0.0017
Higgs boson mass		$76^{+85}_{-47}\,\mathrm{GeV/c^2}$ (indirect)
		$> 90\,\mathrm{GeV/c^2}$ (direct searches)
CP violating QCD phase	θ_{QCD}	$< 1.9 \times 10^{-10}$

Table 1.3: 19 parameters of the Standard Model and their values [2, 3, 4, 5].

bosons and photons (γ). The charged current interaction through the exchange of intermediate W boson explains phenomena such as weak decay. QED is responsible for processes such as bremsstrahlung and annihilation.

The quarks engage not only in electroweak interactions but also in color interactions by exchanging gluons with other quarks. Quarks, while being fundamental particles, has never been observed on its own. Quantum chromodynamics (QCD) describes the strong interactions and it is well known that strongly interacting particles will be confined.

1.2   Quarks and Gluons

The correct theory that describes the strong force is hypothesized to be the quantum chromodynamics (QCD), where quarks interact through the exchange of non-Abelian gauge fields. There are several compelling reasons to believe there is this next layer to the structure of matter beyond the nucleons.

First, the large cross sections observed in deeply inelastic lepton-hadron and hadron-hadron scattering indicate important structure at distance scales of less than 10^{-16} centimeters, where as the overall proton electromagnetic radius is of order 10^{-15} centimeters. The angular dependences observed in

these experiments suggest that the underlying charged constituents carry half-integer spin.

A second impetus for a theory of quarks lies in low energy hadron spectroscopy. It was the successes of the eightfold way of Gell Mann and Ne'eman which originally motivated the quark model.

Third, we have further evidence for compositeness in the excitations of the low-lying hadrons. Particles differing in angular momentum fall neatly into place on the famous 'Regge trajectories'. In this way, families of states group together as orbital excitations of some underlying system. The sustained rising of these trajectories with increasing angular momentum points toward strong long-range forces. This originally motivated the string-like models of hadrons.

Finally, the idea of quarks became incontrovertible with the discovery of the 'hydrogen atoms' of elementary particle physics. The intricate spectroscopy of the charmonium and upsilon states is explained well with potential models for non-relativistic bound states of heavy quarks.

Despite these successes, an isolated quark has never been detected. The difficulty in producing quarks has led to the speculation of an exact confinement. This is where gauge theories can possibly possess a simple mechanism for giving constituents infinite energy when in isolation.

1.2.1   QCD Lagrangian

A quark of specific flavor comes in 3 colors and gluons come in 8 colors. Hadrons are color-singlet combinations of quarks, anti-quarks and gluons. The Lagrangian that describes the interactions of quarks and gluons is

$$
\begin{aligned}
\mathcal{L}_{\text{QCD}} &= -\frac{1}{4} F^{(a)}_{\mu\nu} F^{\mu\nu(a)} + i \sum_q \bar{\psi}^i_q \gamma^\mu (D_\mu)_{ij} \psi^j_q \qquad (1.54)\\
&\quad - \sum_q m_q \bar{\psi}^i_q \psi_{qi}, \\
F^{(a)}_{\mu\nu} &= \partial_\mu A^a_\nu - \partial_\nu A^a_\mu + g_s f_{abc} A^b_\mu A^c_\nu, \qquad (1.55)\\
(D_\mu)_{ij} &= \delta_{ij} \partial_\mu - i g_s \sum_a \frac{\lambda^a_{i,j}}{2} A^a_\mu, \qquad (1.56)
\end{aligned}
$$

where g_s is the QCD coupling constant, and the f_{abc} are the structure constants of the SU(3) algebra. λ^a's are the generators of the group and $A^a_\mu(x)$ are the 8 Yang-Mills gluon fields.

The principle of "asymptotic freedom" determines that the renormalized QCD coupling is small only at high energies, and in this region, high-precision tests can be performed using perturbative theory.

1.2.2 Running Coupling Constant and Asymptotic Freedom

The renormalization scale dependence of the effective QCD coupling $\alpha_s = g_s^2/4\pi$ is controlled by the β-function:

$$\mu\frac{\partial\alpha_s}{\partial\mu} = -\frac{\beta_0}{2\pi}\alpha_s^2 - \frac{\beta_1}{4\pi^2}\alpha_s^3 - \frac{\beta_2}{64\pi^3}\alpha_s^4 - \cdots, \tag{1.57}$$

$$\beta_0 = 11 - \frac{2}{3}n_f, \tag{1.58}$$

$$\beta_1 = 51 - \frac{19}{3}n_f, \tag{1.59}$$

$$\beta_2 = 2857 - \frac{5033}{9}n_f + \frac{325}{27}n_f^2, \tag{1.60}$$

where n_f is the number of quarks with mass less than the energy scale μ. The first two terms are independent of the renormalization scheme used, while the next terms may depend on the schemes, this is due to the fact that the series is truncated. In solving this differential equation for α_s, a constant of integration is introduced. This constant of QCD must be determined from experiment. A usual convention is to introduce a dimensionful parameter Λ_{QCD} such that:

$$\alpha_s(\mu) = \frac{4\pi}{\beta_0\ln(\mu^2/\Lambda^2)}\left[1 - \frac{2\beta_1}{\beta_0^2}\frac{\ln[\ln(\mu^2/\Lambda^2)]}{\ln(\mu^2/\Lambda^2)} + \cdots\right]. \tag{1.61}$$
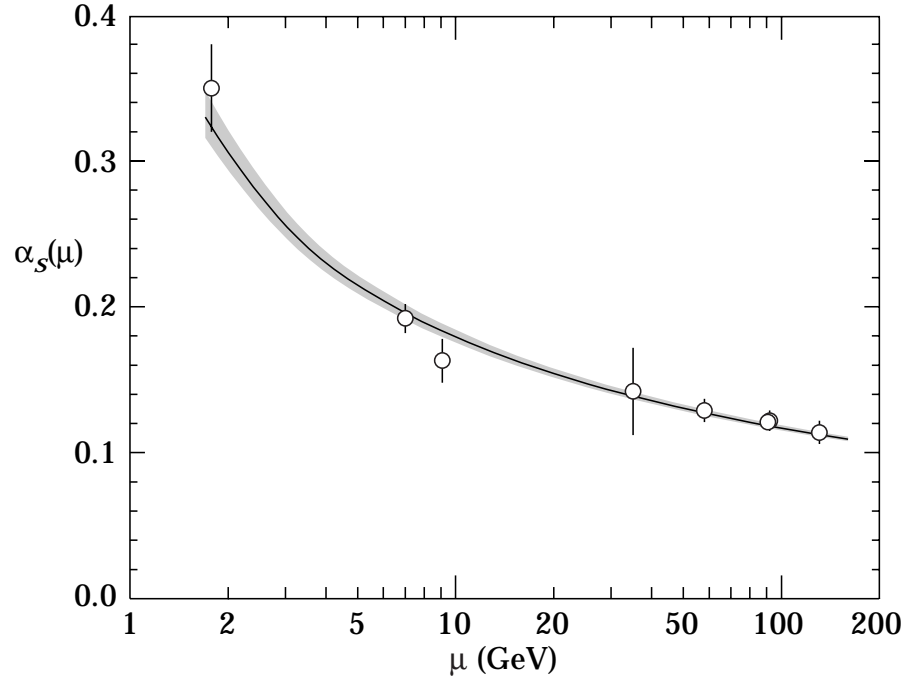
Figure 1.1: Running of α_s from experimental measurements.

α_s is extracted from numerous experiments and the running is well confirmed (Figures 1.1 and 1.2). The running of α_s has a simple interpretation. As one probes to partons, one sees less color charge of the same color as the original parton, meaning there is more screening when partons are probed at smaller distances, and therefore coupling constant becomes smaller.
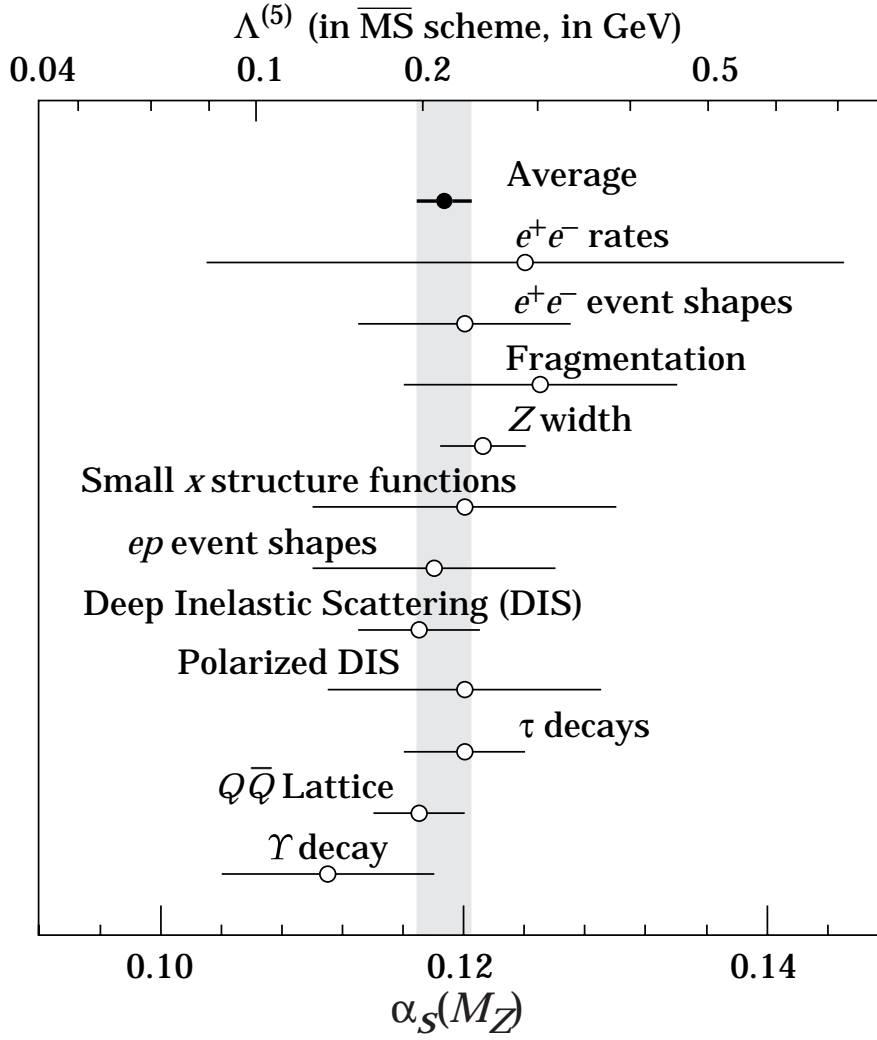
Figure 1.2: Summary of the values $\alpha_s(M_Z)$ and $\Lambda^{(5)}$ from various processes.

1.2.3   Quark Masses

Unlike the leptons, quarks are confined inside hadrons and are not observed as physical particles. Quark masses, save for top quark, cannot be determined directly. They are determined indirectly through their influence on the properties of hadrons. The values of the quark masses, therefore, depend on precisely how they are defined.

The simplest way to define the mass of a quark would be by making a fit to the hadron mass spectrum to a non-relativistic quark model. The extracted quark masses would make sense only in the context of a particular quark model. They also depend on the phenomenological potential used, and on how the relativistic effects are taken into account. And quark masses thus defined cannot be connected with the quark masses in the QCD Lagrangian.

The QCD Lagrangian gives finite scattering amplitudes after renormalization, a procedure that invokes a subtraction scheme to render the amplitudes finite and requires the introduction of dimensionful scale parameter μ. The mass parameters in the QCD Lagrangian depend on the renormalization scheme used to define the theory and also on the scale parameter μ. The most commonly used renormalization scheme used for QCD perturbation theory is the *minimal subtraction* ($\overline{MS}$) scheme.

Experimentally measured top quark mass is a quantity that produces a pole in the quark propagator of top quark. The relation between the pole mass and the mass in $\overline{MS}$ scheme is [6, 7]:

$$\frac{m_t^{\text{pole}}}{m_t^{\overline{MS}}(m_t^{\text{pole}})} = 1 + \frac{4}{3}\left(\frac{\alpha_s(m_t^{\text{pole}})}{\pi}\right) + 10.91\left(\frac{\alpha_s(m_t^{\text{pole}})}{\pi}\right)^2 + \mathcal{O}(\alpha_s^3). \quad (1.62)$$

This ratio is 1.06 for $m_t^{\text{pole}} = 170$ GeV/c^2.

1.2.4   Quark Model

The fact that the strong coupling constant becomes large at low energies, means that quarks and gluons cannot exist in an unbound state. Quarks were originally hypothesized in order to explain the multiplicity and mass spectrum of mesons and baryons, which are combinations of quarks and anti-quarks into colorless states. Nearly all known mesons are bound states of a quark (q) and an anti quark ($\bar{q}'$). If the orbital angular momentum of the $q\bar{q}'$ state is L, the parity is $P = (-1)^{L+1}$. A state $q\bar{q}$ of a quark and its own anti-quark is also an eigenstate of charge conjugation, with $C = (-1)^{L+S}$, where S is the spin (0 or 1), since charge conjugation is the same as exchange of spatial wave-function and spins, therefore, the sign change under such an exchange is $-(-1)^{S+1}(-1)^L$. The $L = 0$ states are the pseudo-scalars
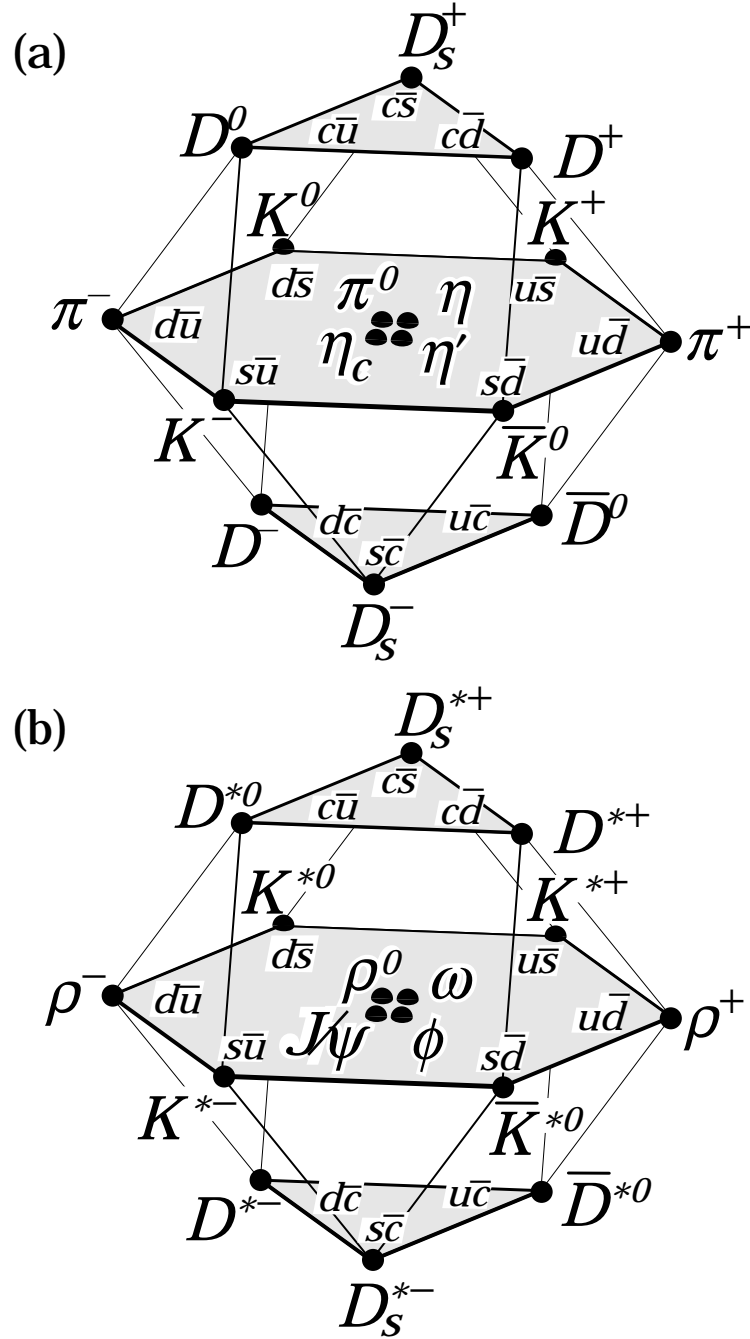
Figure 1.3: 16-plets for the (a) pseudo-scalar and (b) vector mesons made of u, d, s and c quarks.

$(J^P = 0^-)$ and the vectors $(J^P = 1^-)$. This fact is borne out well with experimental measurements [2].

Quantitative properties of these bound states, however, are not calculable within the framework of the perturbative QCD. One non-perturbative approach which is accepted to be the most exact is the lattice QCD. The lattice formulation of the QCD tries to solve the QCD equations numerically in an approximate way by drastically reducing the number of field degrees of freedom. Continuous space-time is replaced by discrete points. Lattice gauge theory correctly predicts the ratio of hadron masses (Table 1.4) [8]. One thing we have learned from the lattice QCD results is that the dynamical gluon degrees of freedom, which can be treated exactly, are much more important than the quark dynamical degrees of freedom, which were approximated crudely. Although various technical and theoretical problems remain to be solved with the lattice formulation of QCD, lattice calculations show that QCD is the theory that successfully describes confinement and that it is the correct theory that describes the strong interaction.

Figure 1.4: 20-plets for the (a) octet and (b) decuplet mesons made of u, d, s and c quarks.
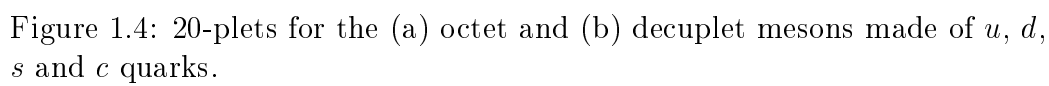
Mass ratios	Lattice QCD	Observed
m_K^*/m_ρ	1.166 ± 0.016	1.164
m_Φ/m_ρ	1.333 ± 0.032	1.327
m_N/m_ρ	1.216 ± 0.104	1.222
m_Δ/m_ρ	1.565 ± 0.122	1.604
m_{Ξ^*}/m_ρ	2.055 ± 0.065	1.996
m_Ω/m_ρ	$2,296 \pm 0.089$	2.177

Table 1.4: Mass ratios of hadrons calculated from lattice QCD.

1.2.5   High-Energy Hadron Collisions

High-energy hadron-hadron colliders provide a good way to test perturbative QCD and search for new phenomena. While the total cross-section for e^+e^- collisions scale as $\sim 1/E^2$, hadron-hadron interaction cross-section scales roughly as E (Figure 1.5). In hadron-hadron collision, one probes partons inside the hadrons and also the hard scattering calculable by perturbative QCD. The rise in cross-section is related to the fact that the parton distribution functions exhibit scaling violations. Inclusive cross section for producing some particle c from collision of hadron A and B

$$A + B \to c + X \tag{1.63}$$

is obtained by multiplying the parton subprocess cross section $\hat{\sigma}$ for

$$a + b \to c + X \tag{1.64}$$

by $dx_a f_{a/A}(x_a)$ and $dx_b f_{b/B}(x_b)$, summing over parton and anti-parton types a, b and integrating over the parton momentum fraction x_a and x_b. Color averaging over the colors of partons a and b must also be done. The resulting relation is

$$\sigma(AB \to cX) = \sum_{a,b} C_{ab} \int dx_a dx_b [f_{a/A} f_{b/B} + (A \leftrightarrow B \text{ if } a \neq b)] \hat{\sigma}(ab \to cX),$$
$$\tag{1.65}$$

where C_{ab}'s are the color averaging factors ($C_{qq} = C_{q\bar{q}} = 1/9$, $C_{qg} = 1/24$ and $C_{gg} = 1/64$).

Parton Distributions

The structure of hadrons represented by parton distributions is an essential part of our knowledge of the elementary particle physics world. The interpretation of existing experimental data in terms of the Standard Model (SM), the precision measurements of SM parameters, as well as the direct seach for signals for physics beyond the SM, all rely heavily on calculations
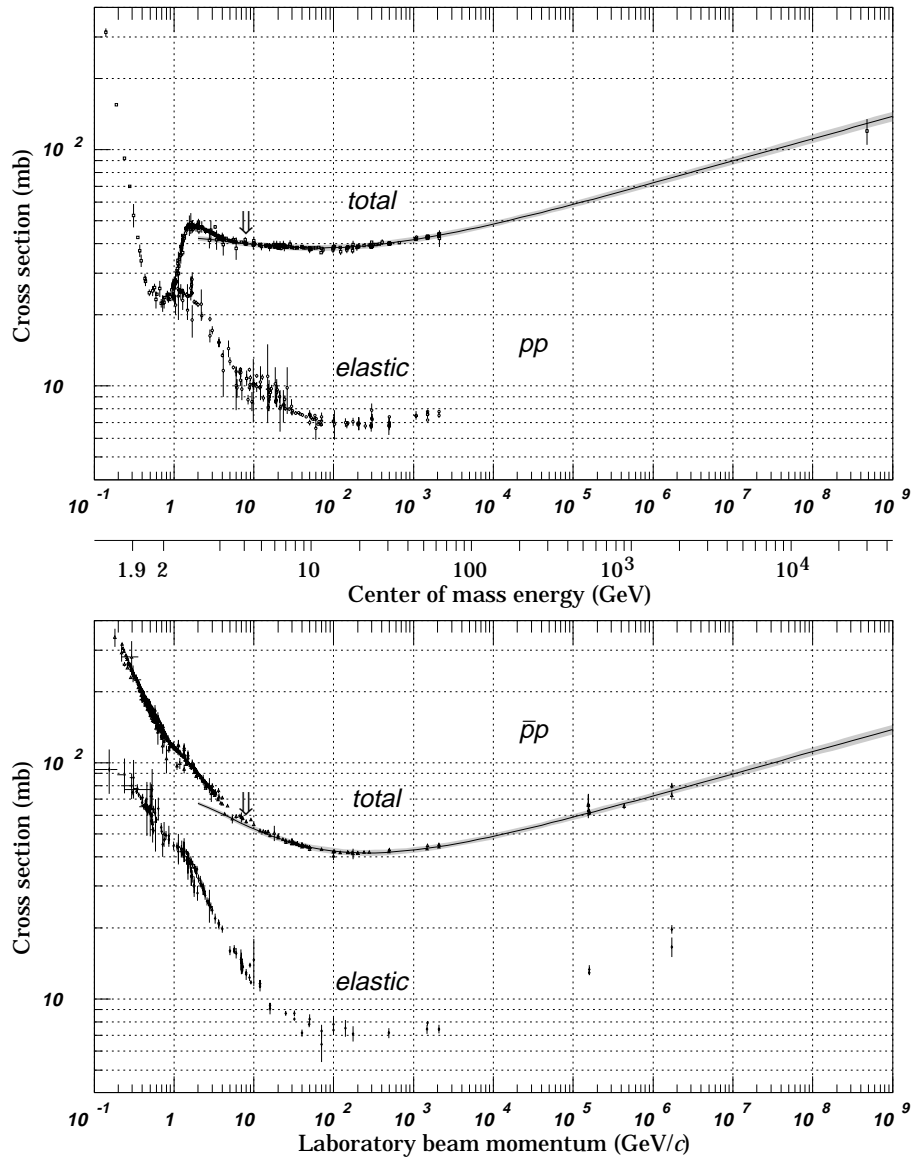
Figure 1.5: pp and $p\bar{p}$ total cross-section.
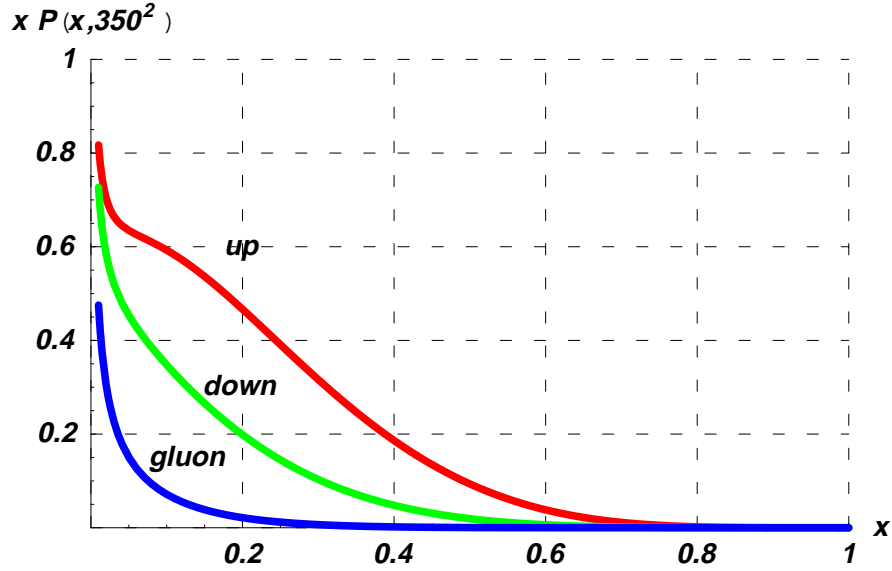
Figure 1.6: Parton distributions of u, d and g inside proton at top pair production threshold $(Q^2 = 350^2 \text{ GeV}^2)$.

based on Quantum Chromodynamics (QCD) and the QCD-parton picture, with the parton distribution functions as essential input. The parton distribution functions at some given momentum scale are currently determined phenomenologically by a global analysis of a wide range of available hard scattering processes involving initial-state hadrons, using the perturbative QCD-parton framework [9].

1.3 Top Quark

In the Standard Model, the top quark is necessary to cancel the triangle anomaly, otherwise the theory would be unrenormalizable [10, 11]. Indirect experimental evidence of the top quark comes from the observed mixings of $K^0 - \bar{K}^0$ and $B^0 - \bar{B}^0$, where the GIM mechanism plays an important role [12, 13, 14].

The top quark was jointly discovered by two collider experiments at Fermilab, DØ and CDF collaborations in 1995 [15, 16]. The mass of the top quark has been measured in various channels by both experiments yielding the Tevatron averaged top mass of $174.3 \pm 5.1 \, \mathrm{GeV/c^2}$ and is the best measured of all the quark masses, with fractional error of only 3% (Figure 1.7). The production cross sections measured by both experiments (5.9 ± 1.7 pb for DØ and $7.6^{+1.8}_{-1.5}$ pb for CDF) agree with theoretical calculations (Figure 1.8) [17].

Measurement of the properties of the top quark provides a unique way to test the Standard Model. The production of the top quark is a QCD process with a well defined scale. The decay of the top quark is a weak process, allowing us to probe the $t \to bW$ vertex, where the right-handed W is suppressed. And together with mass of the W, mass of the top quark
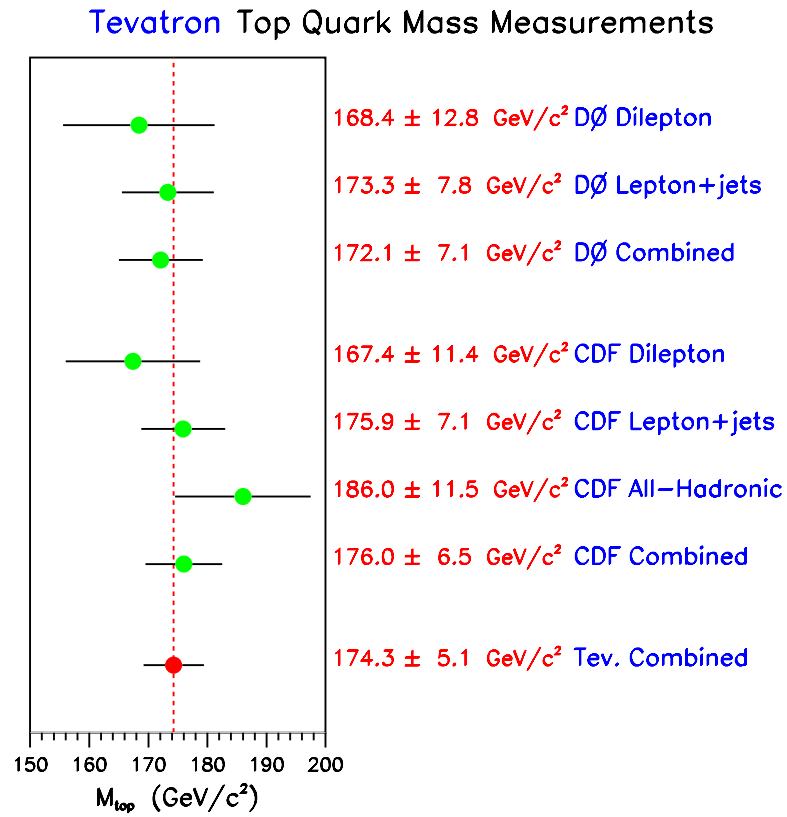
Figure 1.7: Summary of measurements of mass of the top quark at the Tevatron.
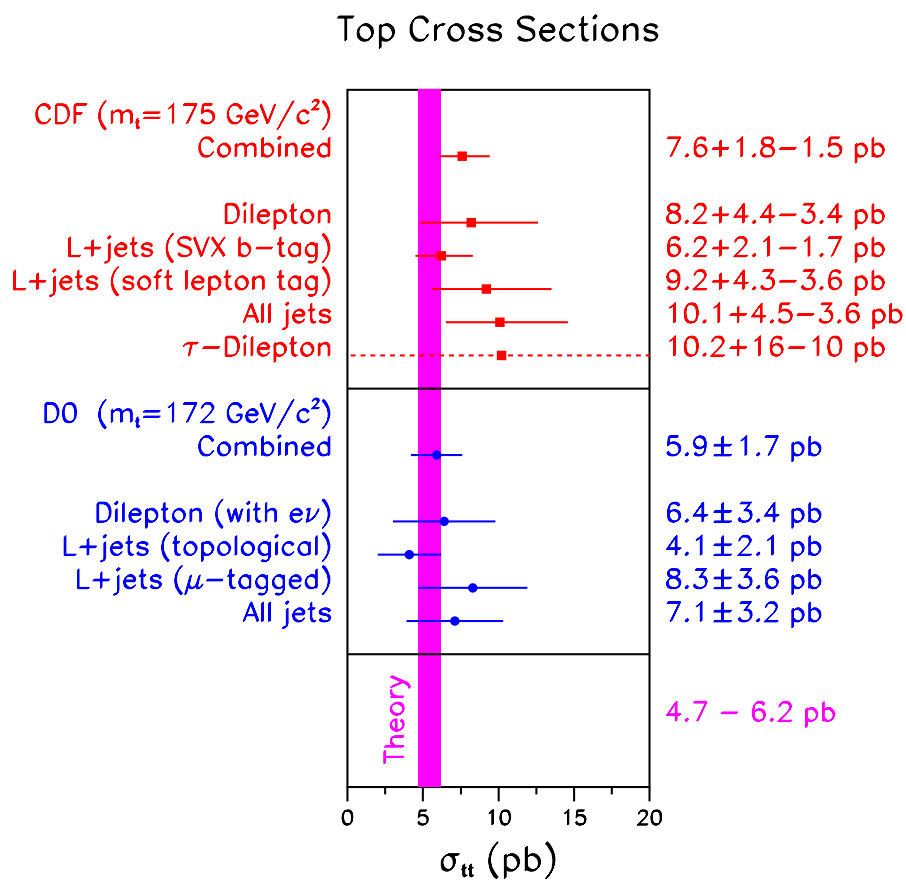
Figure 1.8: Summary of measurements of the top quark production cross section at the Tevatron.

allows us to pin down the elusive Higgs boson, since, in electroweak radiative corrections to the W propagator, both top quark and Higgs boson contribute (Figures 1.9 and 1.10).

One of the consequences of the Standard Model is that the $t\bar{t}$ produced at colliders (hadron as well as e^+e^- colliders) will exhibit spin correlation which will be observable indirectly from the angular correlations between the decay products. Any non-SM interactions, either at production or at decay will change the amount of correlation observed.

In the following sections, the production of top quarks at the Tevatron, their decay modes and some of the properties of the top quark from the Standard Model will be discussed.

1.3.1   Production of the Top Quark at the Tevatron

At the Tevatron, protons and anti-protons collide to create top quark pairs. They are produced through two distinct modes, one is through the annihilation of $q\bar{q}$ initial states, producing $t\bar{t}$ through an intermediate spin-1 gluon and the other is through gluon-gluon fusion (Figure 1.11). At the Tevatron energy ($\sqrt{s} = 1.8$ TeV), 90% of top quark pairs are expected to be produced through annihilation processes.
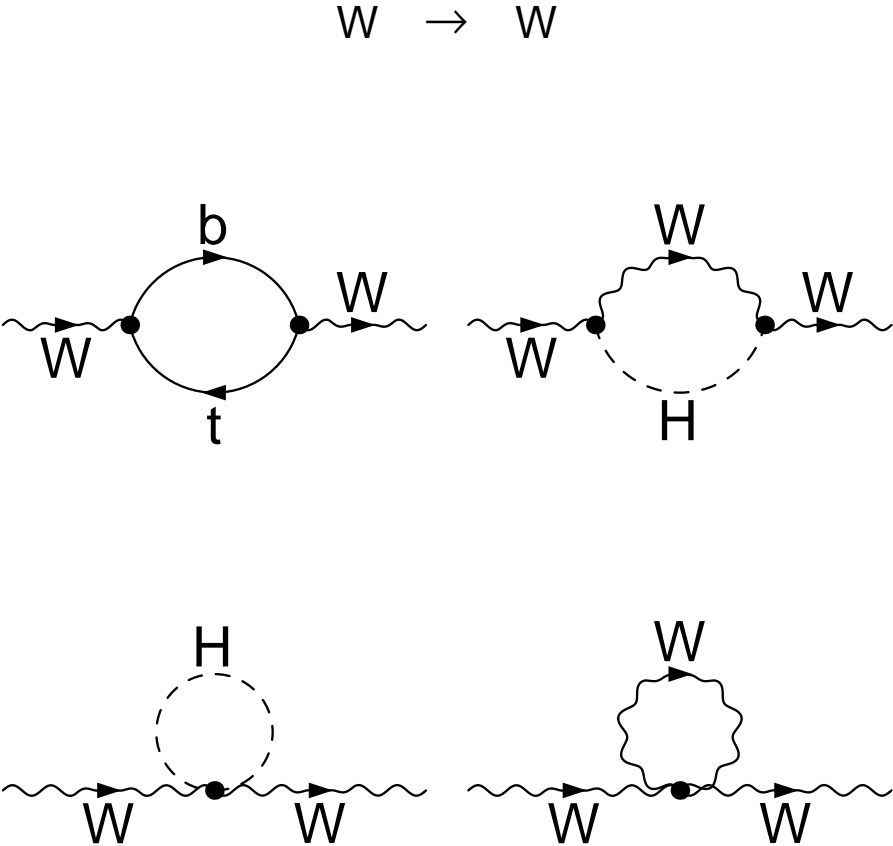
Figure 1.9: Electroweak radiative corrections to the W boson propagator: these corrections are proportional to m_t^2 and $\ln m_H$.
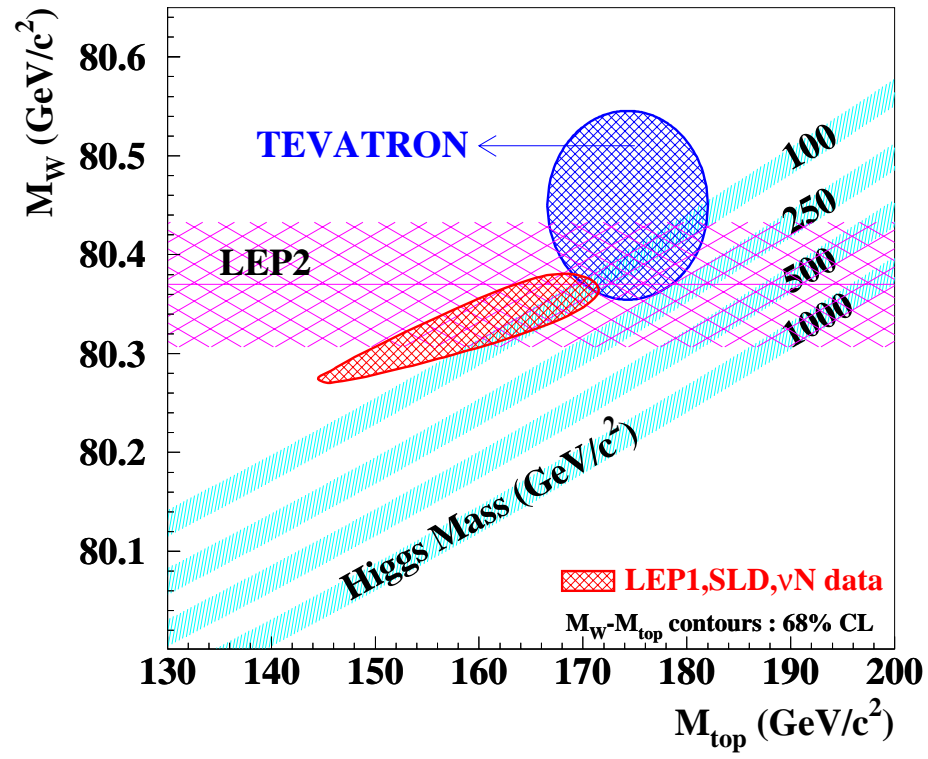
Figure 1.10: M_W versus m_t plot with 68% confidence level contours of world's measurements together with M_H bands.
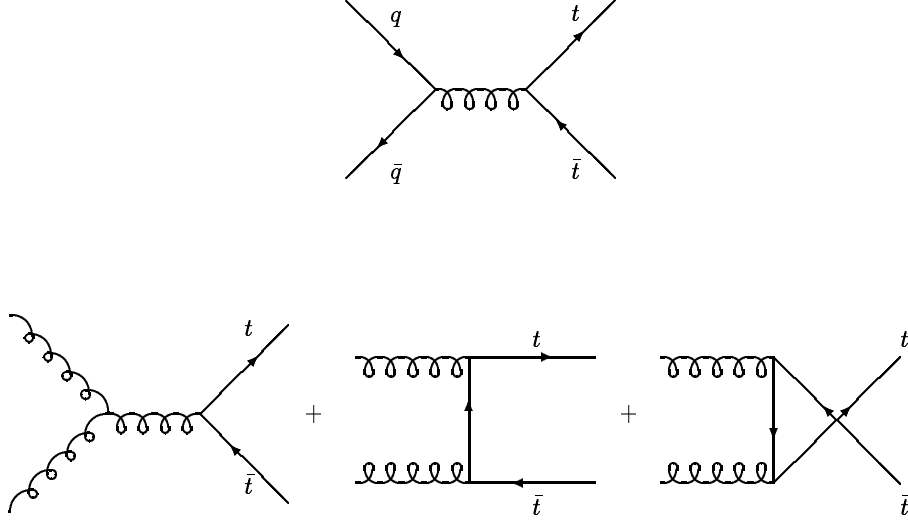
Figure 1.11: Feynman diagrams of pair production of top quark at the hadron colliders.

The matrix elements of tree-level diagrams are:

$$\sigma(q\bar{q} \to t\bar{t}) = \frac{2}{9}\frac{4\pi\alpha_s^2}{3Q^2}(1 + \frac{1}{2}\gamma)(1 - \gamma)^{\frac{1}{2}}, \tag{1.66}$$

$$\sigma(gg \to t\bar{t}) = \frac{\pi\alpha_s^2}{3Q^2}\left[(1 + \gamma + \frac{1}{16}\gamma^2)\ln\frac{1 + (1 - \gamma)^{1/2}}{1 - (1 - \gamma)^{1/2}}\right.$$
$$\left. - \left(\frac{7}{4} + \frac{31}{16}\gamma\right)(1 - \gamma^2)^{1/2}\right], \tag{1.67}$$

where $\gamma = 4m_t^2/Q^2$ and Q^2 is the center-of-mass energy of incoming partons [18]. The tree-level ($\mathcal{O}(\alpha_s^2)$) [18] and next-to-leading ($\mathcal{O}(\alpha_s^3)$) [19, 20] cross-section has been available for quite some time. The fact that these NLO

$$W \quad g \quad \rightarrow \quad t \quad b$$
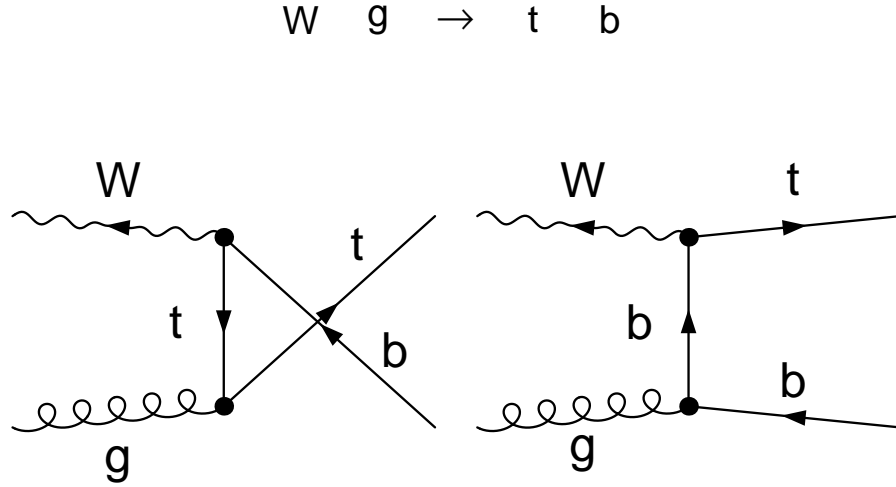
Figure 1.12: Wg fusion Feynman diagram for single top production.

terms are particularly large prompted the investigation of the effects of gluon resummations. These processes have been calculated to $O(\alpha_s^4)$ including resummation of soft gluons in the region close to the production threshold (Figure 1.8) [21, 22, 23].

There is another mode of production called single-top production, where a W boson and a gluon fuses to create a top quark accompanied by a hard jet (Figure 1.12). This mode is very difficult to identify experimentally, and due to its small cross section (~ 2 pb), this mode of production has not been observed yet.

1.3.2 Spin Correlation in $t\bar{t}$ System

As was described earlier, 90% of $t\bar{t}$ pairs come from $q\bar{q}$ annihilation. The total spin of the $t\bar{t}$ system should reflect this fact and therefore, their spin will be correlated. Indeed, it is found that in an optimized spin-quantization basis, unlike spin combination is suppressed for top quarks produced through annihilation of $q\bar{q}$ [25].

Top quark pairs produced from gg initial state will also have its spins correlated but the optimized basis is different from that of above. Since we cannot distinguish between different initial states, events from this initial state will dilute the correlation to be measured.

Assuming that the particle momenta are represented by its symbol, it is possible to decompose the momentum of the top(antitop) into a sum of two massless momenta, $t = t_1 + t_2$ $(\bar{t} = \bar{t}_1 + \bar{t}_2)$, such that in the rest frame of the top quark(anti-top quark), the spatial momentum of $t_1(\bar{t}_1)$ defines the spin axis for the top (anti-top) quark [25]. For $q\bar{q} \to t\bar{t}$,

$$
\begin{aligned}
\sum_{\uparrow\downarrow,\downarrow\uparrow} |\mathcal{M}(q\bar{q} \to t\bar{t})|^2 &= \frac{16g_s^4}{(2q \cdot \bar{q})^2}[(2q \cdot t_1)(2\bar{q} \cdot \bar{t}_2) + (2q \cdot \bar{t}_1)(2\bar{q} \cdot t_2) \\
&\quad + \frac{1}{m_t^2}\mathrm{Tr}(qt_1t_2\bar{q}\bar{t}_2\bar{t}_1)] + (q \leftrightarrow \bar{q}) \qquad (1.68) \\
\sum_{\uparrow\uparrow,\downarrow\downarrow} |\mathcal{M}(q\bar{q} \to t\bar{t})|^2 &= \frac{16g_s^4}{(2q \cdot \bar{q})^2}[(2q \cdot t_1)(2\bar{q} \cdot \bar{t}_1) + (2q \cdot \bar{t}_2)(2\bar{q} \cdot t_2)]
\end{aligned}
$$

$$+\frac{1}{m_t^2}\text{Tr}(qt_1t_2\bar{q}\bar{t}_1\bar{t}_2)] + (q \leftrightarrow \bar{q}) \qquad (1.69)$$

The arrows indicate the spins of the two top quarks. Each term has explicit dependence on the choice of spin axis $t_1(\bar{t}_1)$, therefore, the relative ratio of like-spin to unlike-spin production rate is dependent on the specific choice of spin axis.

The spin correlations are also present in case of other quark-antiquark pair productions. However, in the lighter quarks, the hadronization time is far shorter than its decay time that the spin correlation information at its production is lost.

With its high mass of about 175 GeV, the top quark decays before it hadronizes. Because of its large mass, at the Tevatron the $t\bar{t}$ system is essentially non-relativistic and can be regarded as being in an effectively "coulombic" potential $V = -4\alpha_s/3r$. In the ground state of hypothetical $t\bar{t}$ bound state, the quark velocity is $v_{rms} = 4\alpha_s/3$, and has an atomic radius $r_0 = 3/(2\alpha_s m_t)$[24]. Therefore, a characteristic orbit has a period of $t = 2\pi r_0/v_{rms} = 9\pi/(4\alpha_s^2 m_t)$. Using $\alpha_s(r_0) = 0.12$ for the coupling, we obtain $t = 1.9 \times 10^{-24}s$. In contrast, lifetime of the top quark is expected to be $4.0 \times 10^{-25}s$. These comparisons imply that a heavy top quark has an appreciable probability of decaying before completion of even a single hypo-

thetical bound state orbit. Thus, the decay products of top quarks produced in a definite spin states should display angular correlations that characterize the production process.

Even if the top quark is longer-lived than the hadronization time-scale, the spin-flip time is considered to be much longer than $1/\Lambda_{\text{QCD}}$. The time scale for spin flip in interactions between the spin and electro-magnetic field is given by the inverse of precession frequency $m_e c/eB$. In analogy with QED, the coupling of spin with the color field will be related to its chromo-magnetic moment g_s/m_Q, implying weaker coupling and longer time scale the more massive the m_Q. Typical time scale will be on the order of $m_Q/(\Lambda_{\text{QCD}})^2$ [27]. Therefore, the time it takes to flip the spins is about ~ 1000 times longer than the typical hadronization scale.

There are three motivations for carrying out this study. First, observation of the expected spin correlation would confirm that the top quark has spin $1/2$, and that it decays before strong interaction has much effect on spins, thereby setting an upper bound on lifetime of the top quark. And this, in turn, would place a lower bound on the width of the top quark. A precise measurement of the shape of the invariant mass of the top quark would also provide an upper bound on the width. The width of the top quark is proportional to the sum of the Kobayashi-Maskawa (KM) matrix elements

$|V_{td}|^2 + |V_{ts}|^2 + |V_{tb}|^2$, and if neutral currents can be ignored this quantity must equal unity, assuming three quark generations. However, this sum can be far smaller if there are more than 3 generations. Assuming more than three generations, observation of the spin correlation would imply $|V_{td}|^2 + |V_{ts}|^2 + |V_{tb}|^2 > (0.03)^2$ [26]. If we assume $|V_{tb}|$ is much larger than $|V_{td}|$ or $|V_{ts}|$, this would imply in turn that $|V_{tb}| > 0.03$. If $|V_{tb}|$ proves to be less than this bound, it would mean that the recently-discovered "top" quark is not the $SU(2)$ partner of the bottom quark, and that the real top quark is yet to be found.

Second, the study of spin correlations can be used to probe the presence of non-standard interactions. Presence of techni-eta in two scale technicolor [28] will enhance the unlike spin combination in helicity basis, whereas a vector particle associated with top-color [29] could affect the spin correlations at production by changing the relative mixture of $q\bar{q}$ to gg intiated production of top quarks, and by distorting the zero momentum frame speed (β^*) for the $q\bar{q}$ component. On the decay side, charged Higgs decay of the top could affect the correlation coefficient α of the decay products and modify the observed angular correlations [30].

It is known that the spin correlation of the $t\bar{t}$ systems produced in the proposed future generations of e^+e^- colliders may be sensitive to new physics

[31], most notably, theories on the large extra dimensions. Large extra dimensions are not expected to play a role in top quark production in hadron colliders where the intermediating bosons are the gluons, but in e^+e^- since γ and Z bosons are mediating the interaction, the spin configurations are significantly modified by the presence of extra large dimensions. In order to claim that the large extra dimensions are responsible for the modified spin configuration, it is important to measure the spin correlation from hadron colliders and verify that anomalous effects are not present.

It can also be claimed that by observing spin correlations, one studies "bare" quarks, free from the long-distance effects of QCD, such as hadronization and confinement. This has never been done before. Quarks produced through annihilation, whether the source is incident proton-antiproton or electron-positron channels will, to leading order, always have correlated spins. However, for lighter quarks, all such evidence will be greatly diluted because hadronization time is far shorter than the lifetime. Probing top quarks prior to hadronization is tantamount to confirming that partons are indeed true physical objects.

New spin-analysis techniques have been developed and optimized for the Tevatron regime, thereby improving sensitivity for observing spin correlation in our existing data [25]. We will follow these new directions.
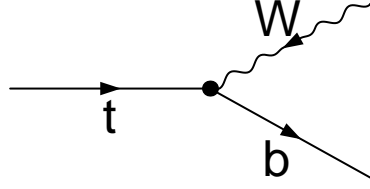
Figure 1.13: Feynman diagram for $t \to bW$ from which the decay width of the top quark (Γ_t) can be calculated to leading order.

1.3.3 Weak Decay of Top

Decay Width of the Top Quark

The total decay width of the top quark can be calculated by considering the Feynman diagram in Figure 1.13. Neglecting the non-zero mass of b quark and the width of the W boson, the total decay rate can be written as follows [32]:

$$\Gamma(t \to bW) = \frac{G_F m_t^3}{16\pi\sqrt{2}}[\mathcal{F}_0(y) - a_s \mathcal{F}_1(y)], \tag{1.70}$$

where

$$a_s = \frac{2\alpha_s}{3\pi} \tag{1.71}$$

$$y = (M_W/m_t)^2 \tag{1.72}$$

$$\mathcal{F}_0(y) = 2(1-y)^2(1+2y) \tag{1.73}$$

$$\mathcal{F}_1(y) = \mathcal{F}_0(y)\left[\frac{2}{3}\pi^2 + 4\text{Li}_2(y) + 2\ln y \ln(1-y)\right]$$

$m_t(\text{GeV/c}^2)$	$\Gamma_t(\text{GeV/c}^2)$
150.0	0.809
160.0	1.033
170.0	1.287
180.0	1.572
190.0	1.890
200.0	2.242

Table 1.5: Top quark width as the function of m_t.

$$-(1-y)(5+9y-6y^2)+4y(1-y-2y^2)\ln y$$

$$+2(1-y)^2(5+4y)\ln(1-y). \tag{1.74}$$

The values of QCD corrected Γ_t including the effects of non-zero b mass W boson widths are shown in Table 1.5. The QCD corrections to the tree-level decay width are about -8.5%, while corrections from electro-weak and non-zero W boson width are 1.7% and -1.5% respectively.

Classification of $t\bar{t}$ Events

Most of the top quarks are expected to decay into real W and b quarks. This can be inferred from the CKM matrix $|V_{tb}|$. While none of the CKM matrix elements involving the top quark has been measured to a sufficient accuracy, the fact that the matrix must be unitary together with the direct measurements of the CKM matrix elements involving lighter quarks imply

Final State	Branching Fraction
$e\nu_e$	1/9
$\mu\nu_\mu$	1/9
$\tau\nu_\tau$	1/9
ud	1/3
cs	1/3

Table 1.6: Decay mode of real W and its branching fractions.

that $|V_{tb}| \approx 0.999$ [2]. The W boson then can decay into a doublet in the weak isospin space (Table 1.6). Since there are 2 W's in a $t\bar{t}$ event, the event types are named according to how the two W's decay. The break down of event types and its branching fractions are shown in Figure 1.14.

All jets channel, where both W's decay into jets, has the highest branching fraction (44%), but suffers from enormous QCD multi-jet background. The lepton (e,μ) plus jets channels have reasonable branching fractions combined with more manageable background than all jets channel, and these channels have yielded most information about the mass and the cross section. The dilepton channels, where both W's decay leptonically, is by far the cleanest but suffers from low branching fractions.
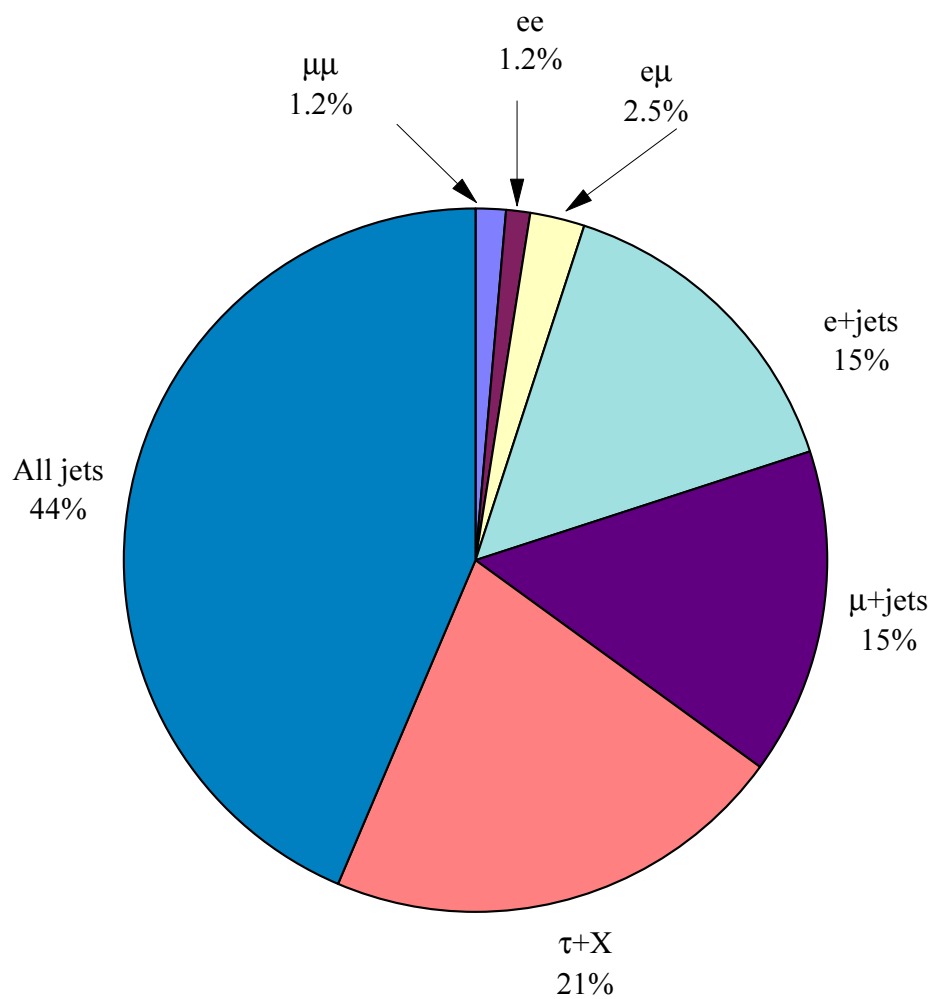
Figure 1.14: Breakdown of $t\bar{t}$ events into various final states and their branching fractions.
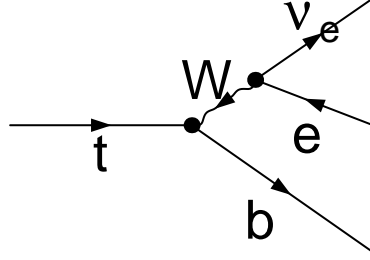
Figure 1.15: Feynman diagram for the process $t \to b e \nu_e$.

Decay of Polarized Top Quark

First, we consider the decay of unpolarized top quark. Evaluating the feynman diagram in Figure 1.15,

$$\overline{|\mathcal{M}(t \to b\bar{e}\nu_e)|^2} = \frac{4g_w^4(\nu \cdot b)(\bar{e} \cdot t)}{(2\nu \cdot \bar{e} - M_W^2)^2 + M_W^2 \Gamma_W^2}. \tag{1.75}$$

For hadronic decay of the top quark $(t \to b\bar{d}u)$, one should replace $\bar{e}$ with $\bar{d}$ and ν with u in the above expression. It is interesting to note that while both ν_e and $\bar{e}$ come from decay of a real-W, the matrix element is not symmetric with respect to the exchange of $e \leftrightarrow \nu_e$.

In case of the polarized top quark toward the spin axis t_1, the matrix

element becomes

$$|\mathcal{M}(t_\uparrow \rightarrow b\bar{e}\nu_e)|^2 = \frac{4g_w^4 (\nu \cdot b)(\bar{e} \cdot t_2)}{(2\nu \cdot \bar{e} - M_W^2)^2 + M_W^2 \Gamma_W^2}, \qquad (1.76)$$

where t_1 and t_2 is defined in Section 1.3.2. Figure 1.16 shows the helicity configurations possible if the W and b decay back-to-back, parallel to the polarization of the top quark. The b quark can be considered massless and therefore an eigenstate of helicity with helicity of -1/2. This means that W cannot have positive polarization. The angular distribution of W with respect to the polarization direction of a polarized top quark is given by the d-function.

- Longitudinally polarized W_0:

$$\frac{d\Gamma}{d\cos\theta} = |d_{\frac{1}{2},\frac{1}{2}}^{\frac{1}{2}}|^2 = \frac{1 + \cos\theta}{2} \qquad (1.77)$$

- -1 helicity W_-:

$$\frac{d\Gamma}{d\cos\theta} = |d_{\frac{1}{2},-\frac{1}{2}}^{\frac{1}{2}}|^2 = \frac{1 - \cos\theta}{2} \qquad (1.78)$$

The contributions to the decay rate of 0 and -1 helicity W are in the ratio 1 : $2y$, where $y = (M_W/m_t)^2$. This ratio is approximately 7 : 3 with the currently
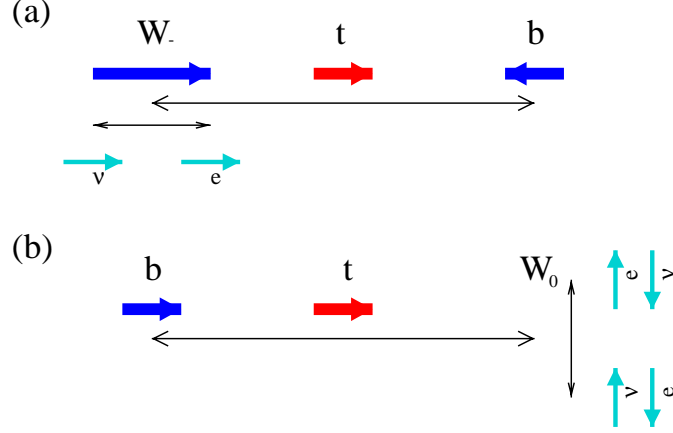
Figure 1.16: Helicity configurations of decay particles: (a) Negative helicity for W if b-quark decays towards the polarization direction of the top. (b) Longitudinal polarization for W if b-quark decays away from the top polarization. The ν_e and e helicities in the rest frame of W are shown.

known masses, and the resulting angular distribution of W is $(1+0.4\cos\theta)/2$.

To leading order in the electroweak coupling, the relative decay rate for particles observed in the rest frame of the top quark, is given by:

$$\frac{1}{\Gamma}\frac{d\Gamma}{d(\cos\theta_i)} = \frac{1+\alpha_i\cos\theta_i}{2}, \tag{1.79}$$

where θ_i is the angle between some direction of quantization and the direction of motion of the ith decay product, where i can be either $b, \bar{e}$ or ν (alternatively, b, u or $\bar{d}$) for decays involving only the first generation of fermions [25]. The coefficients α_i can be computed from the decay matrix element, and for

Particle	Correlation coefficient α	α at $M_t = 175 GeV$
$\bar{e}$ or d	1	1
ν or u	$\frac{(\xi-1)(\xi^2-11\xi-2)+12\xi\ln\xi}{(\xi+2)(\xi-1)^2}$	-0.31
W^+	$\frac{\xi-2}{\xi+2}$	0.41
b	$-\frac{\xi-2}{\xi+2}$	-0.41

Table 1.7: Correlation coefficients α for both semi-leptonic and hadronic decays of W bosons in the decay of a spin-up top quark, as a function of $\xi \equiv m_t^2/m_W^2$, for $m_b = 0$. The numerical values are for $m_t = 175$ GeV.

a polarized top quark are determined essentially by the ratio of the two mass scales in the system $(m_t/m_W)^2$. All other remnants in the $t \to bW$ decay are assumed massless. The coefficients for a spin-up anti-top are opposite in sign to those for spin-up top (Table 1.7). This can be confirmed by performing a CP operation on a spin-up top quark.

For the case of the lighter quarks, which decay via a virtual W boson, the coefficient α is -1/3 for neutrinos and 1/3 for quark jets from semi-leptonic decay, while the charged lepton retains a coefficient of $\alpha = +1$.

With $\alpha = 1$, the charged leptons or down-quark jets are most sensitive to the spin direction of the top quark. Thus, the angular information on these particles can be used most effectively to determine the spin of the top quark in a statistical manner.

Unfortunately, there is no information about the top spin direction in
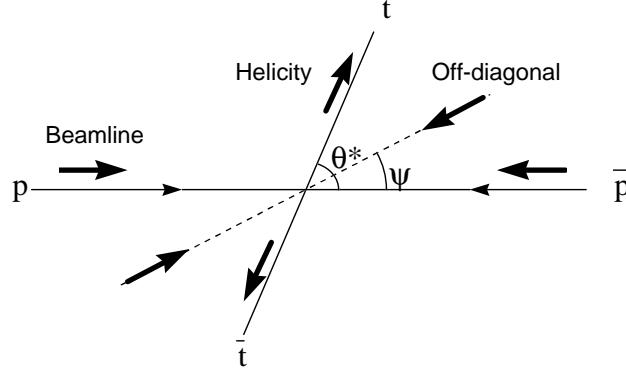
Figure 1.17: Helicity, beamline and off-diagonal bases in the rest frame of incoming-parton collision frame.

the $t\bar{t}$ events, and α therefore cannot be measured. However, because of $t\bar{t}$ spin-correlation at production, these parameters can be studied through the correlated decays of t and $\bar{t}$.

1.3.4   Correlations in $t\bar{t}$ production and decays

At Tevatron energies ($\sqrt{s} \sim 2$ TeV), about 90% of top production comes from the $q\bar{q} \rightarrow t\bar{t}$ annihilation process. The sensitivity to the number of produced like-spin and opposite-spin top quark pairs depends on the chosen spin-quantization axes. For the case of production of ultra-relativistic $t\bar{t}$ pairs, the usual helicity basis, where the spin-quantization axis is the flight direction of top or anti-top, is recognized as the best choice [33]. For the

intermediate gluon state, helicity conservation guarantees that the top and anti-top will have oppositely-directed spins. However, at the Tevatron, where top quarks are produced with mean velocities of $\beta = 0.55$, the helicity basis is not the best choice. There is a particular choice called the "off-diagonal" basis, in which effects from the like-spin contributions vanish to leading order in QCD. In this basis, the quantization axis is defined by an angle ψ with respect to the beam direction in the constituent rest frame i.e., the frame in which the interacting partons have opposite but equal momentum,

$$\tan\psi = \frac{\beta^{*2}\sin\theta^*\cos\theta^*}{1 - \beta^{*2}\sin^2\theta^*}, \tag{1.80}$$

where θ^* is the angle between the direction of top and the incident quark, and β^* is the velocity of top in the constituent quark rest frame. In the limit of $\beta^* = 1$, $\tan\psi$ equals $\tan\theta^*$, and the off-diagonal basis tends to the helicity basis, as is expected from the above arguments. While in the limit of $\beta = 0$, i.e., top quarks produced at rest, $\tan\psi$ becomes zero, which coincides with the beam-axis and what we call the "beamline" basis. The relation between various spin quantization axes is sketched in Figure 1.17.

Chapter 2

The Apparatus

The data for this analysis were produced using the Tevatron proton-antiproton collider at Fermilab and collected using the DØ detector. The protons and anti-protons are accelerated in a series of accelerators and are injected into the Tevatron ring where they are accelerated to an energy of 900 GeV. Inside the 1 km radius ring, protons and anti-protons counter-rotate and collide at two points inside the ring, and at one of these points sits the DØ detector. The following sections describe the main components of the Tevatron accelerator and the DØ detector

2.1   The Tevatron Accelerator

The Tevatron accelerator consists of many small accelerators effective in its own regime. The whole process of accelerating protons start in the ion source. The H^- ions are accelerated in the Cockroft-Walton generator and the electrons are stripped using a thin foil. The protons make their way into the Linac, booster ring, main ring and finally the super-conducting Tevatron ring. The anti-protons are generated by steering some of the protons in the booster ring onto a target. The anti-protons are then accumulated in the accumulator ring and when sufficient number of anti-protons are collected, they are injected into the main ring (Figure 2.1).

2.1.1   The Ion Source

The production of proton beam starts with the injection of hydrogen gas into the H^- ion source (Figure 2.2). The source consists of an ovoid cathode, a surrounding anode, and an external magnetic field. Pulses of hydrogen gas enter the 1 mm gap between the cathode and anode with a typical pressure of ~ 100 mTorr. Many H_2 molecules become adsorbed to the cathode, while free electrons and positive ions travel in a helical path in the gap. The crossed electric and magnetic fields ensure high-density for this spiraling plasma.
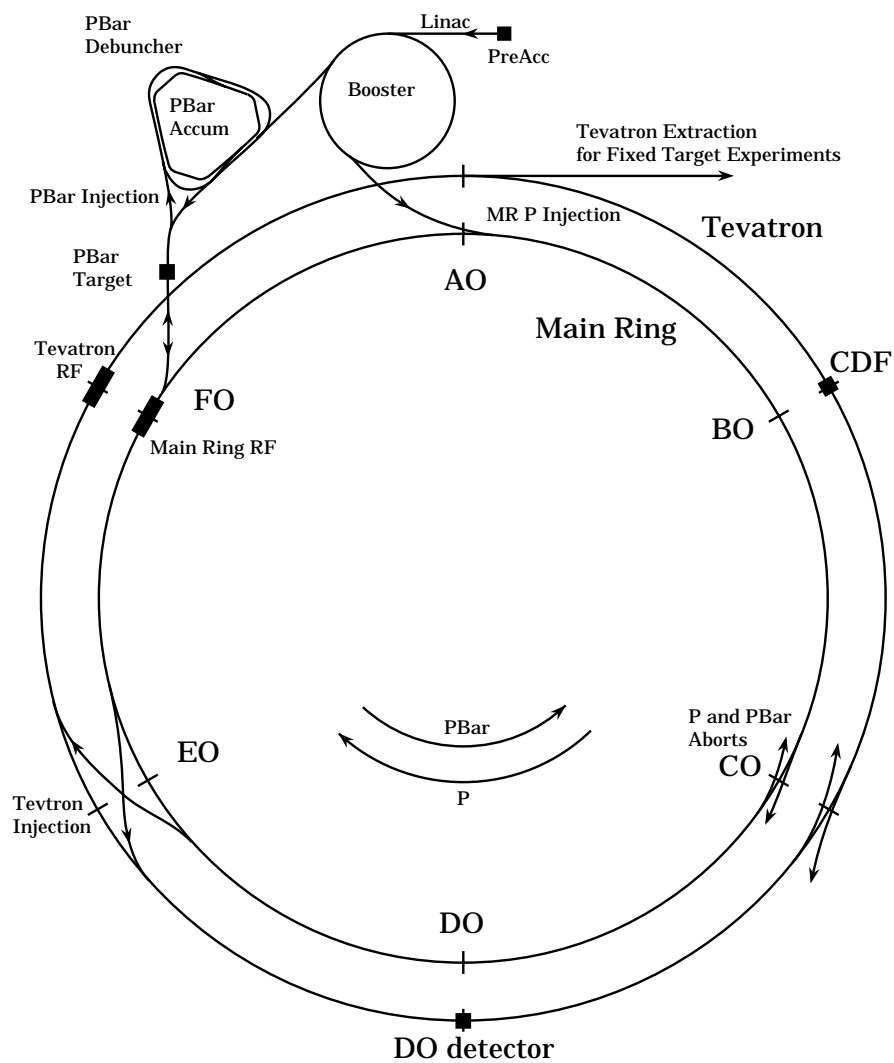
Figure 2.1: Schematic view of the Tevatron.

When positive ions and energetic particles collide with the adsorbed hydro-
gen, they eject hydrogen atoms and a small number of H^- ions. A charged
plate extracts the produced H^- ions through an anode aperture with a typ-
ical energy of 18 keV. A small admixture of cesium vapor boosts operating
efficiency by lowering the work function of the cathode. The likelihood of a
sputtered hydrogen atom to associate with an extra electron increases from
0.2% to 10%.

Similar devices can create H^+ and eliminate the need to strip electrons
from the ions later, but positive ion sources require higher current and longer
pulse times. The fast-pulsing negative ion source improves beam quality for
the downstream accelerators because there is a small spread in creation time.

2.1.2   The Cockroft-Walton Pre-accelerator

The H^- ions generated from the ion source are injected into the Cockroft-
Walton accelerator and are accelerated electro-statically (Figure 2.3). The
high voltage is generated by applying low voltage (75 kV) to a configuration
of capacitors, charging them in parallel and then discharging them in series. 5
stages are used to achieve a voltage multiplication of 10 with little fluctuation.
The H^- ions are accelerated to a kinetic energy of 750 keV.
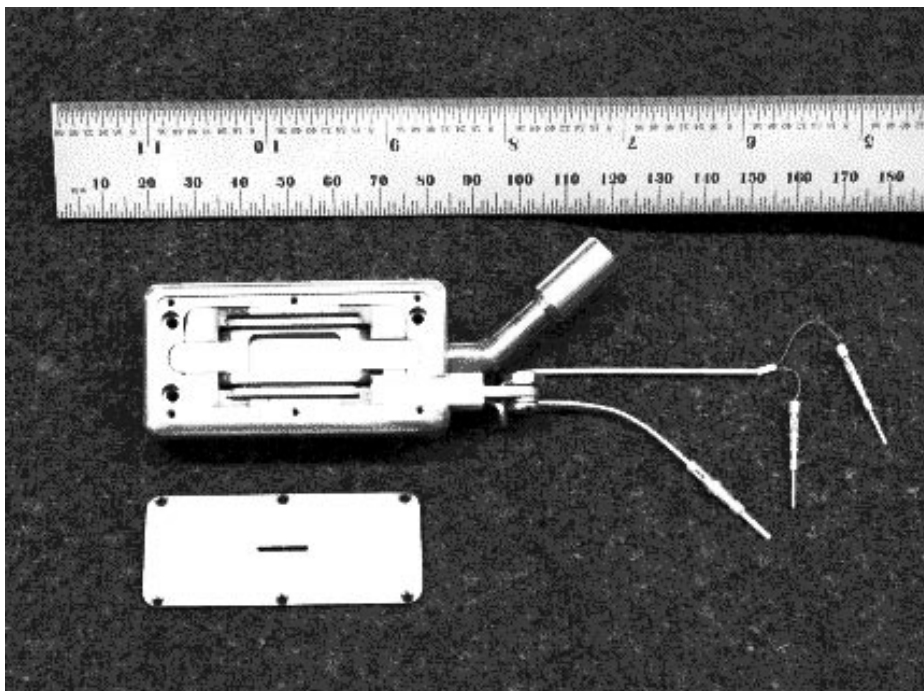
Figure 2.2: H$^-$ ion source.
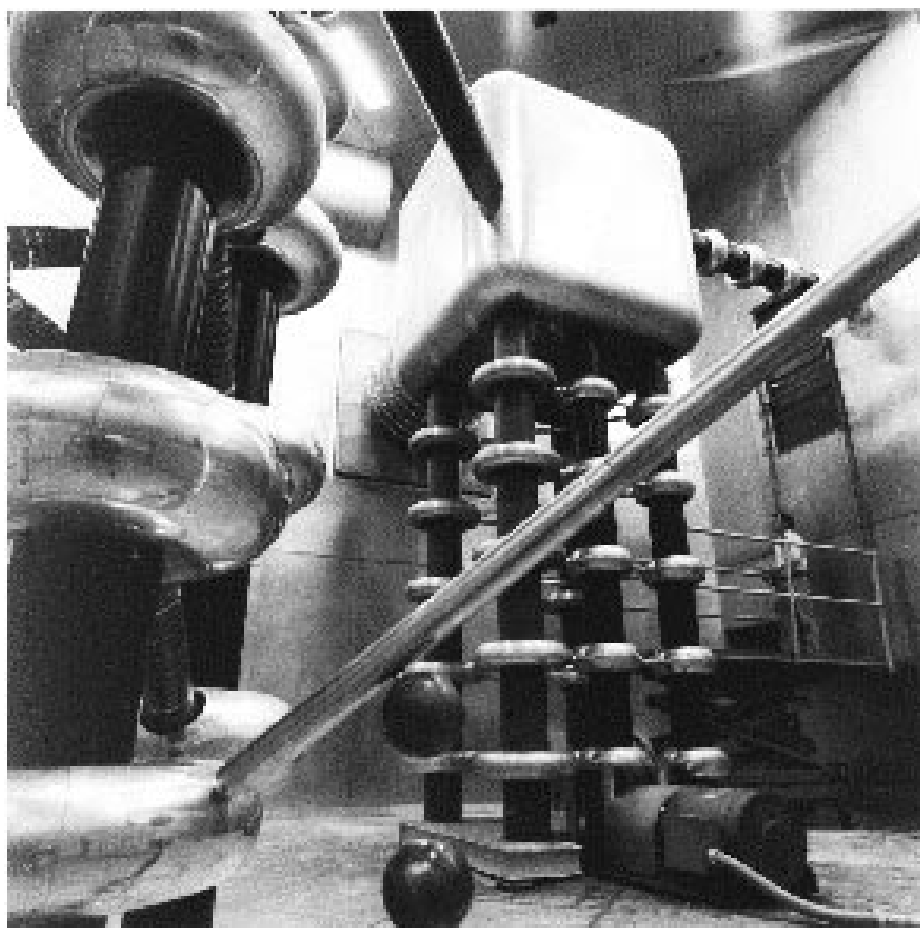
Figure 2.3: Cockroft-Walton pre-accelerator.

The beams from the Cockroft-Walton accelerator are pulsed, because a switching process is involved. There is a time to charge the capacitors followed by a time to apply the multiplied voltage to particle acceleration [34, 35].

2.1.3   The Linac

After leaving the Cockroft-Walton, negative hydrogen ions enter a linear accelerator called the Linac, which is approximately 146 m long. The Linac consists of drift tubes spaced further and further apart. An alternating electric field, with a frequency of 201.24 MHz, is applied to the tubes. The particles travel through the drift tubes, hiding in them when the electric field is in a direction that would slow them down and emerging into the gaps between the drift tubes when the field is in the direction to speed them up. The second stage of Linacs operate at a much higher frequency of 805 MHz, with particles every fourth cycle. The H^- ions emerge with an energy of 400 MeV and drift an additional 46 m before injection into the booster.

2.1.4   The Booster

At this stage, the H$^-$ ions are sent through a carbon foil which strips off electrons. The protons are then steered into the Booster synchrotron ring (500 m in circumference). A synchrotron is a cyclic machine in which particles are confined to a closed orbit by a series of bending magnets. The particle's energy is increased by accelerating it in a synchronized RF cavity. As the momentum increases, the magnetic field in the bending magnet must be increased if the particles are to stay in the ring. Thus for a given ring, the maximum particle energy is limited by the maximum strength of the magnets. The protons have an energy of 8 GeV on exiting the booster. The protons are then injected in to the main ring.

2.1.5   The Main Ring and the Tevatron Ring

Both the main ring and the Tevatron ring are housed in a single tunnel. The main ring has 1000 m radius and consists of 774 dipole magnets to bend the beam and 240 quadrupole magnets to refocus it. The main ring is used to accelerate the protons to 120 GeV. The protons in the main ring then could either be injected into the Tevatron ring or be directed to a target hall in order to create anti-protons.
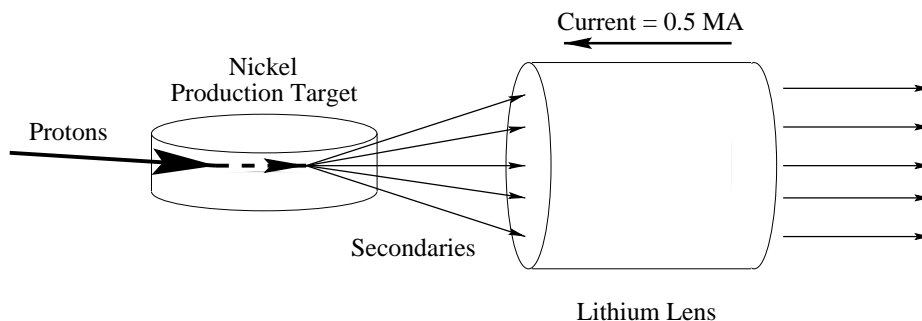
Figure 2.4: Creation process of antiprotons.

Creating Anti-protons

The proton bunches hit a cylindrical Nickel/Copper target, creating about 20 million anti-protons per bunch (for every million protons which strike the target only about 20 anti-protons make it to the next step) (Figure 2.4. The incident proton energy of 120 GeV is optimized for the number of anti-protons produced with 8 GeV energy, matching the booster injection energy. The anti-protons of different energies and directions are initially focused using a lithium lens, a cylinder of liquid lithium that transforms a current pulse of 500,000 amperes into a focusing magnetic field. The lithium is ideal due to its low density and high conductivity, thus minimizing the energy loss and multiple scattering of anti-protons while still accommodating a high magnetic field.

A pulsed dipole magnet selects 8 GeV anti-protons, directing them into

the first ring of two anti-proton storage rings, known as the debuncher. So-phisticated radio-frequency techniques are used to "squeeze" the incoher-ent anti-proton beam into as compact a phase space as possible. Initially, the anti-protons have a large spread in momentum and many are oscillat-ing transverse to the beam direction. the process whereby the momentum spread and emittance are reduced is known as "cooling". The debuncher uses two cooling processes. The first method, called debunching, was in-vented at Fermilab. As a bunch of anti-protons circulates around the ring complex, computer controlled radio-frequency techniques act to smooth the anti-protons into a uniform continuous ring, where all the particles have ap-proximately the same momentum. The second process, which reduces the transverse oscillations of the anti-protons, is known as stochastic cooling. Particles whose orbits are not ideal are identified by sensors which send cor-rection signals to kicker electrodes that on the average adjust the path of the wayward particle. When the process is completed, the anti-protons are in a single continuous ring at about the same momentum and with very little transverse momentum.

The above process runs continuously and sends about 20 billion anti-protons into the second anti-proton storage ring, the anti-proton accumu-lator. The debuncher and accumulator reside in the same tunnel of 520 m

circumference. Several different systems within the accumulator provide further cooling and increase the density of anti-protons by a factor of about one million. After four to six hours, the population in the accumulator reaches about 200 billion which is enough for a "shot" into the main ring.

The Tevatron Ring

In the next step, anti-protons are transferred to the main ring, accelerated to 150 GeV and, together with the protons, then injected into the Tevatron. The Tevatron is in the same tunnel as the main ring but uses super-conducting magnets that are able to reach higher magnetic fields (operating at a temperature of 4.7 K, they produced a field of ~ 4 Tesla) and can therefore achieve a much higher energy.

In the final step, the 6 bunches of protons (typically 2×10^{11} protons/bunch) and six bunches of anti-protons (typically 7×10^{10} anti-protons/bunch) are simultaneously raised to full energy of 0.9 TeV during run periods 1A and 1B. Once at full energy, the beams are squeezed at two beam crossing points BØ (CDF) and DØ. The beam radius at these points is about 50 μm. The longitudinal beam size is quite broad, resulting in the distribution of collisions along the beam direction to be roughly gaussian with $\sigma \approx 30$ cm. The protons and anti-proton bunches collide at the two interaction regions every

3.5 μs. Before the data taking process begins, significant amount of clean up needs to be done to remove halos and other debris from the beam. This is accomplished by a process known as "scraping" whereby metal plates collimate the beam. A typical beam lifetime lasts from 7 to 30 hours in collision mode, depending on the luminosity requirements of both experiments. In Run 1B, typical luminosity was around $2 \times 10^{31} \text{cm}^{-2}\text{s}^{-1}$.

2.2   The DØ Detector

As detailed in the previous chapter, the final state from $t\bar{t}$ may contain electrons, muons, jets and neutrinos. The DØ Detector is designed to identify and measure the energy of these objects. The DØ detector consists of a moderate tracking system in a non-magnetic environment, an excellent liquid argon/uranium sampling calorimeter and a muon detector which provides good muon identification with low background [36]. The tracking system further consists of Vertex Chamber(VTX), Transition Radiation Detector(TRD) and Central Drift Chamber(CDC) and Forward Drift Chamber(FDC) and its main purposes are to identify the vertex, detect charged particle tracks and together with the calorimeter, aid in identifying electrons. The calorimeter is used to measure the energy of electromagnetic objects, such as photons and

electrons, and hadronic jets. Muon momentum is measured by drift chambers by measuring the amount of deflection it undergoes in the presence of magnetic field in the toroid magnets.

In discussing the positions of objects within the detector, a right-handed coordinate system is used, with the origin at the center of the detector, positive z-axis along the proton direction and y-axis upward. The azimuthal angle ϕ defined by the angle with respect to x-axis and polar angle θ (defined by the angle with respect to z-axis) are also used. The pseudorapidity ($\eta = -\ln \tan(\theta/2)$) is often used in hadron colliders as the pseudorapidity intervals are invariant under Lorentz boost.

Particle identification will be described after the relevant detector components have been defined.

2.2.1 The Tracking System

The central tracking systems measure the trajectories of charge particles, and also aid in identification of electrons. The tracking system of the DØ detector occupies the inner-most region of the detector. The sub-detectors are largely based on wire drift chamber technology. The full set of tracking detectors fits within the inner cylindrical aperture of the calorimeters in a
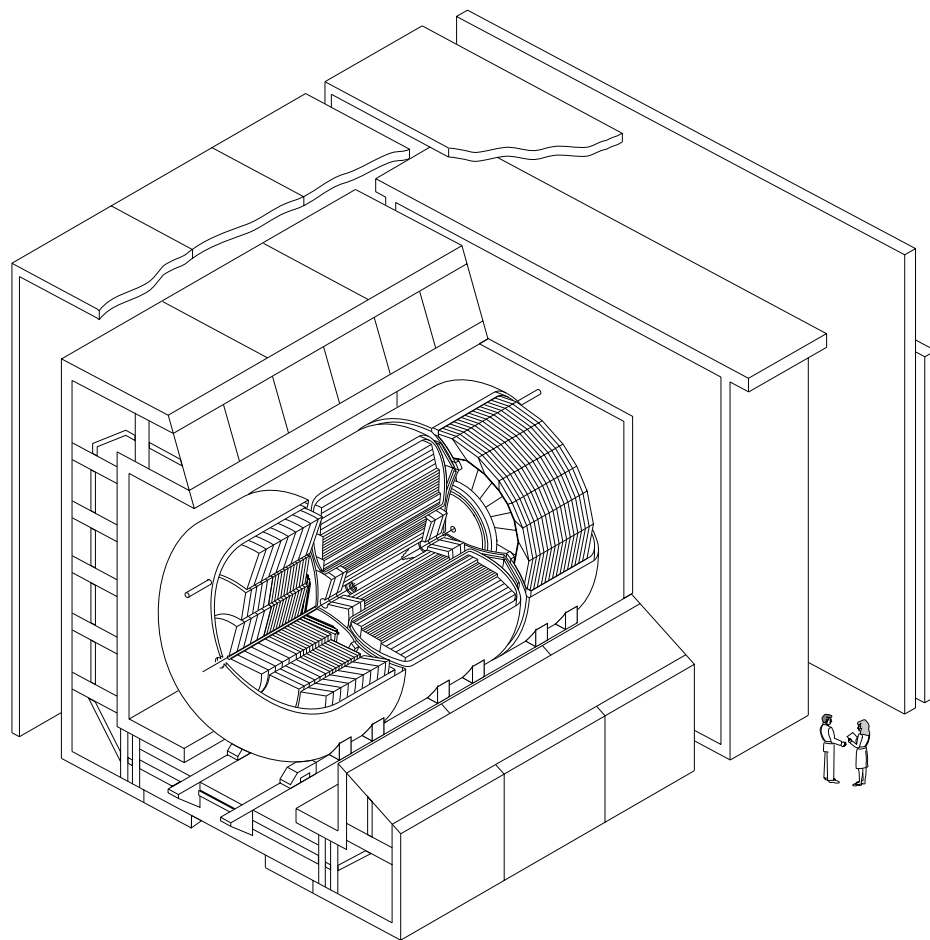
DØ Detector

Figure 2.5: An isometric view of the DØ detector.

volume bounded by $r = 78$cm and $z = \pm 135$ cm.

The tracking detectors were designed to match the collider bunch-time interval of $3.5\,\mu$s. This time allows relatively long drift cells. Good two-track resolving power is obtained by employing a flash analog-to-digital conversion (FADC) system for digitization in which the charge is sampled at $\approx$ 10ns intervals. This gives an effective detector granularity of 100–350 μm. In order to obtain robust measurement of the z coordinate, several different methods are used. They include charge division (VTX), helical cathode pads (TRD), and delay lines (CDC).

The Vertex Chamber (VTX)

The Vertex Chamber is the innermost tracking detector in DØ. It has an inner radius of 3.7 cm, just outside the beryllium beam pipe, and an outer radius of 16.2 cm. There are 4 concentric layers of cells, each supported by thin G-10 bulkheads mounted on carbon fiber support tubes. In each cell, eight sense wires, which are 25 μm NiCoTin at 80 g tension, provide measurement of the $r - \phi$ coordinate. The field is set up so that the ions drift toward the sense wires in azimuthal direction. The time of the hit allows one to determine how far the primary ionization is from the sense wire, but carries no information about which side of the wire the particle
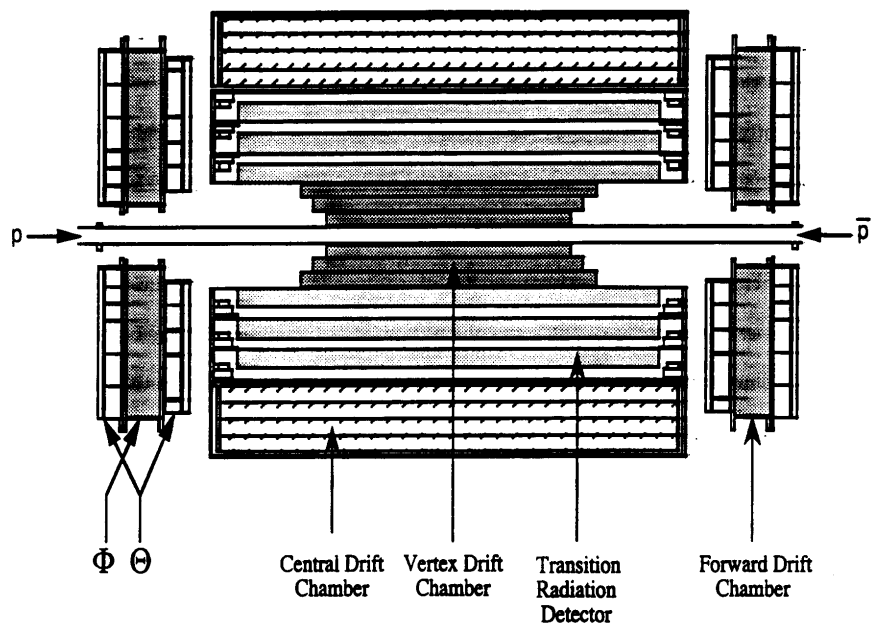
Figure 2.6: DØ tracking system.

traversed. Adjacent sense wires are staggered by 100 μm to resolve such left-right ambiguities. The sense wires have resistivity of 1.8 kΩ/m and provide measurement of the z coordinate by having signals read out at both ends and comparing the signal sizes.

Two grounded grid wires near each sense wire combine with the cathodes to shape the drift field in the cell (Figure 2.7). The cathode consists of aluminum traces on the inner surface of the support cylinder (coarse field-shaping) and a cage of 152 μm diameter gold-plated aluminum wires around the edges of the cell (fine field-shaping).

The gas chosen for operation of the VTX is CO_2(95%)-ethane(5%) at 1 atm with small admixture of H_2O. The gas is operated in a voltage regime such that the electron drift velocity is proportional to the drift field. The drift velocity was 7.3 μm/ns.

Axial position resolutions of around 50 μm and 1 cm z-resolution from charge division is achieved.

Transition Radiation Detector (TRD)

The TRD occupies the space between the VTX and the CDC, and provides independent electron identification in addition to that given by the calorimeters. Transition radiation X-rays are produced when highly relativistic par-
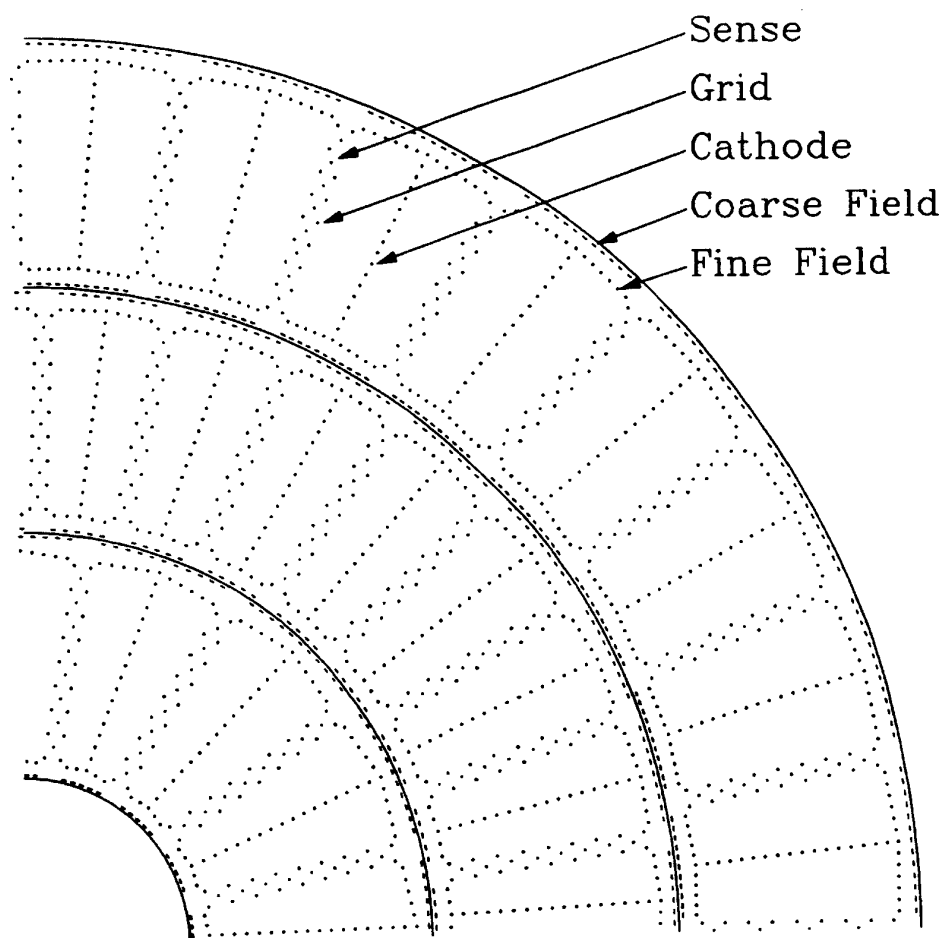
Figure 2.7: Cross section of the VTX chamber.

CROSS−SECTION OF TRD LAYER 1

OUTER CHAMBER SHELL ⌐

70μm GRID WIRE ⌐

ALUMINIZED MYLAR ⌐

8mm

65mm

2mm   15mm

$2\pi/256$ 2mm   4mm

RADIATOR STACK   CONVERSION
                        STAGE
N_2

30μm ANODE WIRE ⌐

23μm MYLAR WINDOWS ⌐

100μm POTENTIAL WIRE ⌐

HELICAL CATHODE STRIPS ⌐
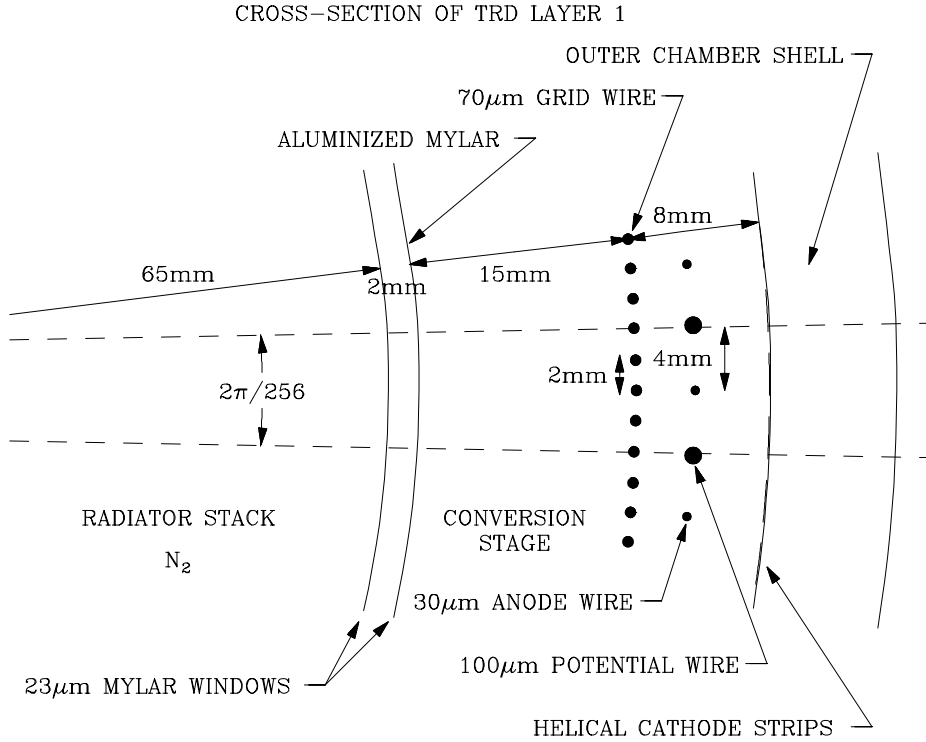
Figure 2.8: Cross section of the TRD chamber.

ticles ($\gamma > 10^3$) traverse boundaries between media with different dielectric constants. As electrons and positrons are the only charged particles produced at the Tevatron which have such large γ factors, measuring the transition radiation allows one to discriminate between electrons and charged hadrons. The TRD consists of three separate units, each containing a radiator and an X-ray detection chamber (Figure 2.8).

The radiator section of each TRD unit consists of 393 foils of 18 μm

thick polypropylene in a volume filled with nitrogen gas. The mean gap between foils is 150 μm. The transition radiation spectrum from this arrangement peaks at 8 keV. The detection of X-rays is accomplished in a two-stage time-expansion radial-drift PWC mounted just after the radiator. The X-rays will convert mainly in the first stage of the chamber, and the resulting charge drifts radially outward to the sense cells, where avalanche occurs. Each drift cell in this reagion is approximately square, with dimension of $8mm \times 8mm$. The drift field is radial, and the sense and field wires are parallel to the z axis. The gas used in the PWC section is a mixture of $\text{Xe}(91\%)/\text{CH}_4(7\%)/\text{C}_2\text{H}_6(2\%)$. The thickness of the full TRD at $\theta = 90°$ is 8.1% of a radiation length and 3.6% of an interaction length.

While all charged particles will deposit energy in the PWC, electrons can be distinguished by both the magnitude and timing of the deposited charge. The magnitude will be greater both due to the energy deposition from transition radiation and the fact that the more relativistic electrons will have somewhat larger energy loss (dE/dx) than charged hadrons. The difference in timing mainly reflects that the transition X-rays generally convert in the first few mm of the inner section of the PWC, so the energy from them tends to be deposited at longer drift times, while for a charged particles traversing the chamber, the energy deposition will be uniform for all drift time.

Central Drift Chamber (CDC)

The central drift chamber provides coverage for tracks at large angles, after the TRD and just prior to their entrance into the calorimeter. The CDC is a cylindrical shell of length 184 cm and radii between 49.5 and 74.5 cm. It consists of 4 concentric rings of 32 azimuthal cells per ring. Each cell contains seven 30 μm gold plated tungsten sense wires running parallel to the beam direction, read out at one end, and two delay lines located just before the first sense wire and the other after the last sense wires, each read out at both ends. The maximum drift distance is about 7 cm and the drift field is about 620 V/cm leading to an electron drift velocity of about 34 μm/ns. The gas used is a mixture of argon (92.5%), methane (4%), carbon dioxide (3%) and water (0.5%).

The sense wires provide the $r - \phi$ measurement and adjacent wires are staggered 200 μm to resolve left-right ambiguity in the track position. The measurement of the z coordinate is performed by inductive delay lines. These lines are composed of a wire wrapped on a carbon-fiber/epoxy core. Signals propagate at 2.4μm/ns along the wires, so that reading out the delay lines at both ends and noting the time difference between the signals allows a measurement of z with a resolution of 4 mm.
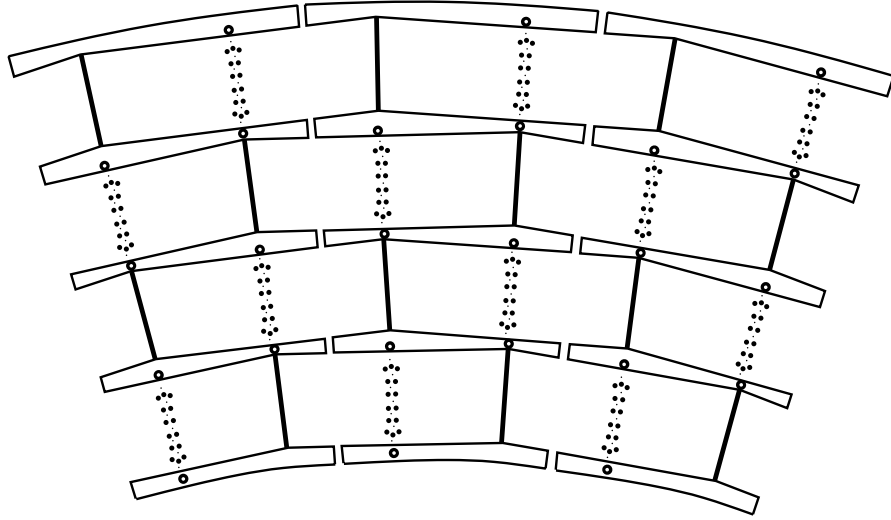
Figure 2.9: Cross section of the CDC.

Forward Drift Chambers (FDC)

The forward drift chamber covers charged particle tracking down to $\theta \approx 5°$ with respect to both emerging beams. These chambers are located at either end of the barrels of VTX, TRD and CDC and just before the end calorimeters.

Each FDC consists of the Φ module whose sense wires are radial and measure the azimuthal coordinate, sandwiched between a pair of Θ modules whose sense wires measure the θ coordinate.
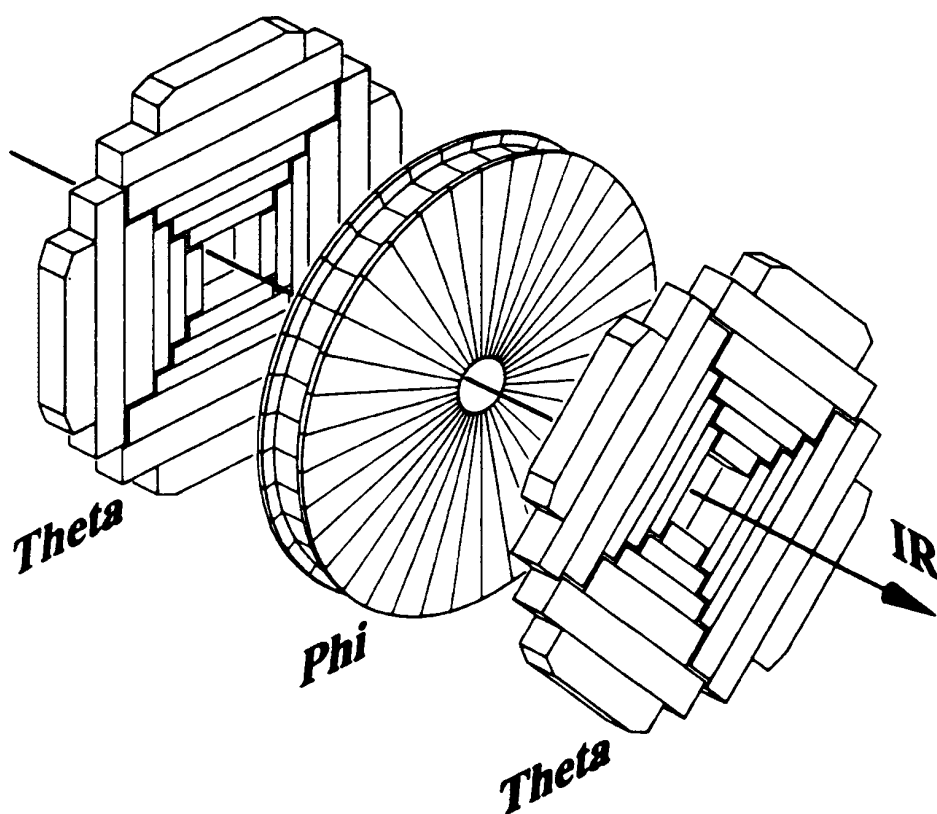
Figure 2.10: Cross section of the FDC.

Central Detector Electronics

The VTX, TRD, CDC, and FDC have preamplifiers mounted on the detector surfaces. Besides handling the output signals during data taking, the preamplifiers are also able to inject test charges onto the sense wires for calibration purposes.

The signals from preamplifiers are carried by coaxial cables to shaping circuits on the platform beneath the detector. The signals are shaped and sent to digitizing electronics about 45 m away from the detector.

The digitization is done by flash analog-to-digital converters (FADCs), which have an 8-bit dynamic range and have a clock speed of 106 MHz. Digitization at high rate is necessary in order to separate multiple hits down to small distances. A wider dynamic range is desirable to obtain a precise measurement of the dE/dx. The signals enters analog buffers before the FADCs. The small signals are amplified a factor of 8.5 than large signals, which in effect increases the dynamic range of the digitization to 9.5 bits.

The total number of signals from the central detectors is 6080, and attempting to read out every channel for every event would require a bandwidth of 325 Mbytes/s, which is beyond the capabilities of the readout system. A zero-suppression circuitry compares the size of the signal for each digitization

cycle and the difference in signal between adjacent cycles to programmable thresholds in order to define the leading and trailing edges of a signal. Only the digitization cycles between these edges are kept for further processing.

2.2.2 The Calorimeter

A calorimeter is used to measure the energies of particles. Its design parameters are determined by the particle species and the energy range to be measured. The DØ calorimeter consists of liquid argon as its active sampling medium and uranium as its absorver. The calorimeter is designed with a particular emphasis on the measurement of photons/electrons and jets with good resolution and linearity.

Energies of electrons and photons are measured in the front part of the calorimeter, also known as the electromagnetic portion of the calorimeter, as they have a relatively short interaction length, described by the radiation length X_0,

$$X_0 = \frac{716.4 \, \text{g/cm}^2 \text{A}}{Z(Z+1)\ln(287/\sqrt{Z})} \tag{2.1}$$

where Z is the atomic number of the material and A is the atomic mass, and for uranium $X_0 = 0.32cm$ [2]. At energies above some critical energy (≈ 9

MeV for uranium),

$$E_c = \frac{800}{Z + 1.2} \text{MeV},\qquad\qquad(2.2)$$

an electron looses its energy mainly by bremsstrahlung at a rate nearly proportional to its energy. And these photons will in turn create $e^+ e^-$ pairs in the medium and will result in a cascade of showers of electrons and positrons. The transverse dimensions of the shower development is described by Molière radius $R_M = X_0 E_s / E_c$, where $E_s = 21$ MeV, and is only a function of the material. The longitudinal electromagnetic shower development has a logarithmic dependence on the incident electron or photon, and the depth at which the shower reaches maximum multiplicity is given by $(\ln(E/E_c) - 0.5)X_0$, which means that the total amount of material needed scales only as the log of the incident particle. However, the mean total track length of ionizing secondaries in the shower is proportional to the incident energy E, and measuring the total amount of ionization present in the detector allows one to estimate E.

The resolution of the electromagnetic calorimeter is, in some sense, determined by how accurately one can measure the total length of the ionizing particles, and since the shower development is itself a statistical process, resolution scales as $\sqrt{E}$. In sampling calorimeters, ionizations are sampled

only in the active medium, worsening the resolution because of additional sampling fluctuations.

The hadronic particles upon entering calorimeters do not produce electromagnetic showers as the critical energy E_c scales as square of the mass of the incident particle, but they mainly scatter inelastically with the nuclei of the calorimeter medium, producing more hadrons and thus initiating hadron showers. Eventually, these showers will be detected by the calorimeter by the ionization they produce. The scale for the nuclear process is the nuclear interaction length $\lambda = A/(\sigma_{in} N_o \rho)$, where σ_{in} is the inelastic nuclear cross-section, N_o is the Avogadro number, and ρ is the density of the absorber. The shower maximum again scales as the log of the energy of the incident particle, $\approx (0.2 \ln(E\ in\ GeV) + 0.7)\lambda$, and 95% of the shower is contained in a depth a little more than 2.5λ beyond this. The transverse spread is approximately 1λ.

The resolution of hadronic energy measurement is typically limited by the fluctuations in the composition of hadronic showers. In particular, the fluctuations in the number of π_0's can severely affect the energy resolution, since π_0's decay promptly to 2 photons and most of this energy will be measured, while charged hadrons have typically lower response, known as e/h ratio. A non-unity e/h will yield worse resolutions and non-linearities. And

DØ LIQUID ARGON CALORIMETER

END CALORIMETER

Outer Hadronic
(Coarse)

Middle Hadronic
(Fine & Coarse)

**CENTRAL
CALORIMETER**

Electromagnetic

Fine Hadronic

Coarse Hadronic

Inner Hadronic
(Fine & Coarse)

Electromagnetic

1ᵐ
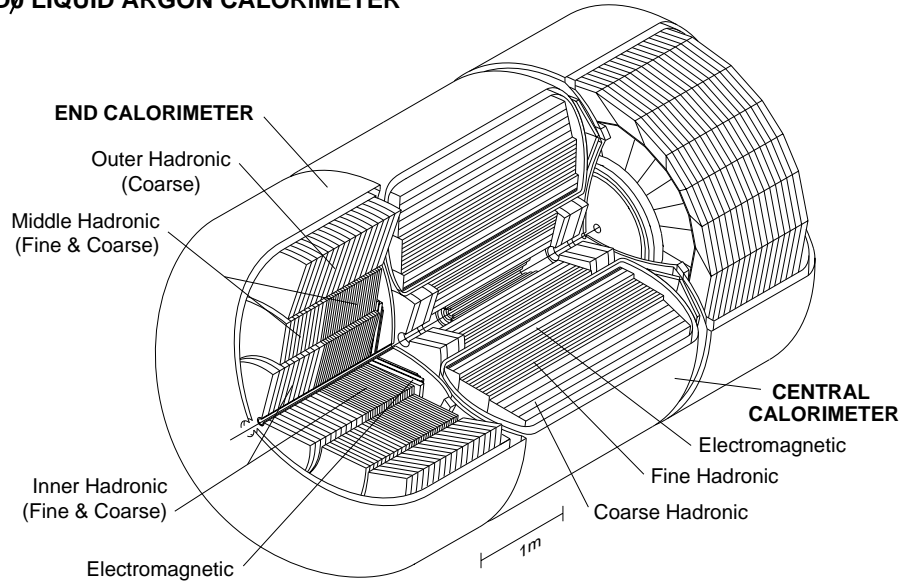
Figure 2.11: The DØ calorimeter.

hadronic showers can produce neutrinos and muons, and will escape the detector. Nuclear excitations and breakups can occur in hadronic interactions in the calorimeters, the energy of which may not be detected. Using uranium as the absorber can recover some of this loss as fission of uranium nuclei will be induced in the process, and some of the energy can be detected.

The calorimeter performance is crucial for DØ since there is no central magnetic field and the tracking detectors cannot provide information about particle momenta. The calorimetry must provide the energy measurement for electrons, photons and jets. In addition, the calorimeters play impor-

tant roles in the identification of electrons, photons, jets and muons, and in establishing the transverse energy in an event. Liquid argon was chosen as an active medium to sample the ionization produced in electromagnetic or hadronic showers. This choice was in part inspired by the unit gain of liquid argon, the relative simplicity of calibration, the flexibility offered in segmenting the calorimeter into transverse and longitudinal cells, the good radiation hardness, and the relatively low unit cost for readout electronics. Factors weighing against the choice of liquid argon included the complication of cryogenic systems the need for relatively massive containment vessels (cryostats) which give regions of uninstrumented material, and the inaccessibility of the calorimeter modules during operation.

There are 3 cryostats that house the calorimeters, one for the central calorimeter (CC), and two for pair of end calorimeters (EC) (Figure 2.11). Both CC and EC further consist of 3 modules, the electromagnetic module (EM) which has thin uranium absorber plates, fine hadronic section (FH) that has thicker uranium plates and course hadronic section (CH) which has thick copper and iron plates. At $\eta = 0$, the CC has a total of 7.2 nuclear absorption lengths (λ_A); at the smallest angle of the EC, the total is 10.3 λ_A.

A typical calorimeter unit cell is shown in Figure 2.12. The electric field is established by grounding the metal absorber plate and connecting the
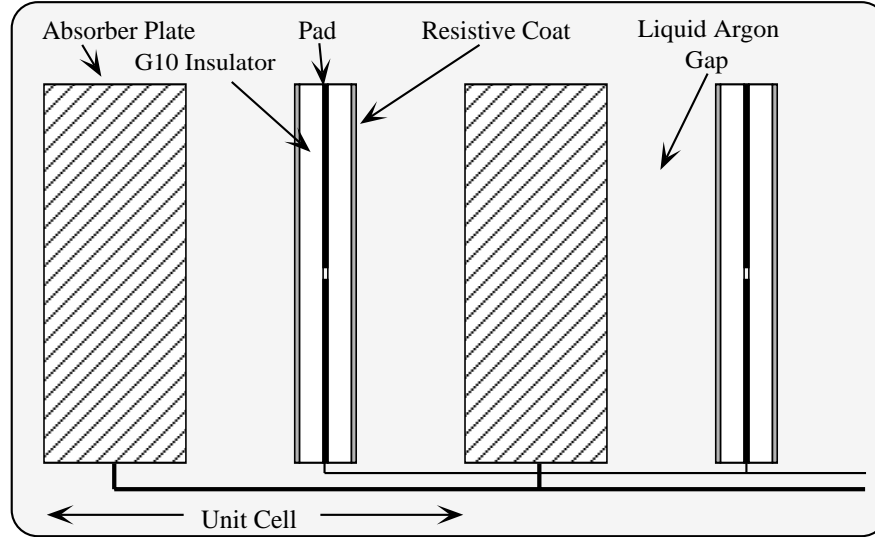
Figure 2.12: Schematic view of the liquid argon gap and signal board unit cell.

resistive surfaces of the signal boards to positive high voltage (2.0-2.5 kV). The electron drift time across the 2.3 mm gap is ≈ 450 ns.

Different absorber plate materials were used in different locations. The EM modules for both CC and EC used nearly pure depleted uranium; the thicknesses were 3 and 4 mm respectively. The fine hadronic modules have 6 mm thick uranium-niobium (2%) alloy. The coarse hadronic module sections contain relatively thick (46.5 mm) plates of either copper (CC) or stainless steel (EC).

Signal boards for all but the EM and small-angle hadronic modules in the

EC were constructed by laminating two separate 0.5 mm thick G-10 boards. Each signal board had one surface coated with high resistivity $(40\mathrm{M}\Omega/\square)$ carbon-loaded epoxy. One of the inner surfaces was left with bare G-10 on the uncoated side; the other sheet, originally copper clad, was milled into the pattern desired for the segmented readout. Several such pads at approximately the same η and ϕ are gang-ed together in depth to form a readout cell.

The pattern and sizes of readout cells were determined from several considerations. The transverse sizes of the cells were chosen to be comparable to the transverse size of showers: $\sim$1-2 cm for EM showers and $\sim$10 cm for hadronic showers. Longitudinal subdivision within the EM, fine hadronic and coarse hadronic sections is useful since the longitudinal shower profiles help distinguish electrons and hadrons.

The calorimeter cells are arranged in pseudo-projective tower form. The term pseudo-projective refers to the fact that the centers of cells of increasing shower depth lie on rays projecting from the center of the interaction region, but the cell boundaries are aligned perpendicular to the absorber plates. The EM modules in CC and EC have four separate depth layers each. The first two layers are typically 2 radiation lengths (X_0) thick and are included to help measure the longitudinal shower development near the beginning of showers
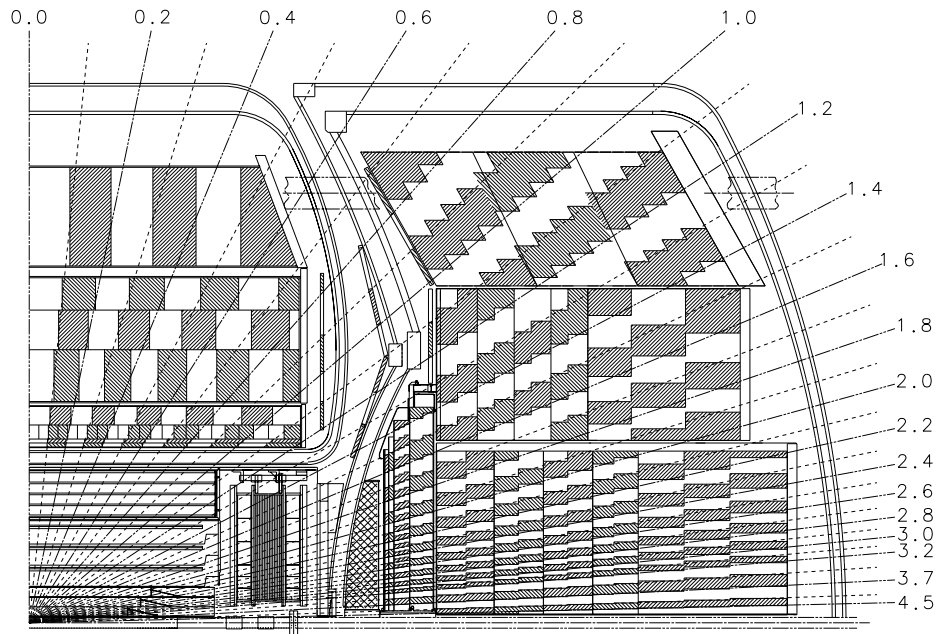
Figure 2.13: One quarter section view of the DØ calorimeters showing the segmentation pattern.

where photons and π^0's differ statistically. The third layer spans the region of maximum EM shower energy deposits and the fourth layer completes the EM coverage of approximately $20 X_0$. The fine hadronic modules are typically segmented into three or four layers; coarse hadronic modules are ganged into one or three layers. Typical transverse size of the EM and hadronic modules are $\Delta\eta = 0.1$ and $\Delta\phi = 2\pi/64 \approx 0.1$. The third layer of EM modules is twice as finely segmented in both η and ϕ to allow a more precise determination of the shower centroid.

Central Calorimeters

The central calorimeter (CC) provides coverage for $|\eta| < 1.0$ and consists of 3 concentric cylindrical shells. There are 32 EM identical modules in the inner ring, 16 fine hadronic in the surrounding ring, and 16 coarse hadronic modules in the outer ring. EM, FH and CH module boundaries are rotated so that no projective ray encounters more than one intermodule gap.

The CC-EM modules have 4 longitudinal ganging of signals of approximately 2.0, 2.0, 6.8 and 9.8 X_0. The total number of signals for the 32 modules is about 10400, spanning 24 $\Delta\eta = 0.1$ towers along the 2.6 m length. A full module comprises 20.5 X_0 and 0.76 λ_A and weighs 0.6 metric tons.

The CC-FH modules have 3 longitudinal ganging of approximately 1.3,

1.0 and 0.9 λ_A. The CC-CH modules contain just one depth segment of 3.2 λ_A. The CC-CH (CC-FH) modules weigh 8.3 (7.2) metric tons and provide about 3500 (770) signals.

End Calorimeters

The end calorimeters provide coverage for $1.0 < |\eta| < 4.2$ and each contains four module types as shown in Figure 2.13. The module closest to the central tracker is the EM section. The hadronic sections are arranged in a concentric manner, with the module closest to the beam-pipe being called the inner hadronic (IH) modules, surrounding them are the middle hadronic (MH) modules and at the outer most are the outer hadronic (OH) modules. There are one EM module, one IH module and 16 concentric rings of MH and OH modules in each end calorimeter.

The EC-EM module contains four readout sections (0.3, 2.6, 7.9, and $9.3X_0$) with radii varying between 84 and 104 cm and inner radius of 5.7 cm (Figure 2.14). The material of the cryostat brings the total absorber for the first section up to $2X_0$. EC-EM module weighs 5 metric tons and provides 7488 signals.

The EC-IH modules are cylindrical. In the front, closer to the central detectors, the fine hadronic portion consists of 4 readout sections, each con-
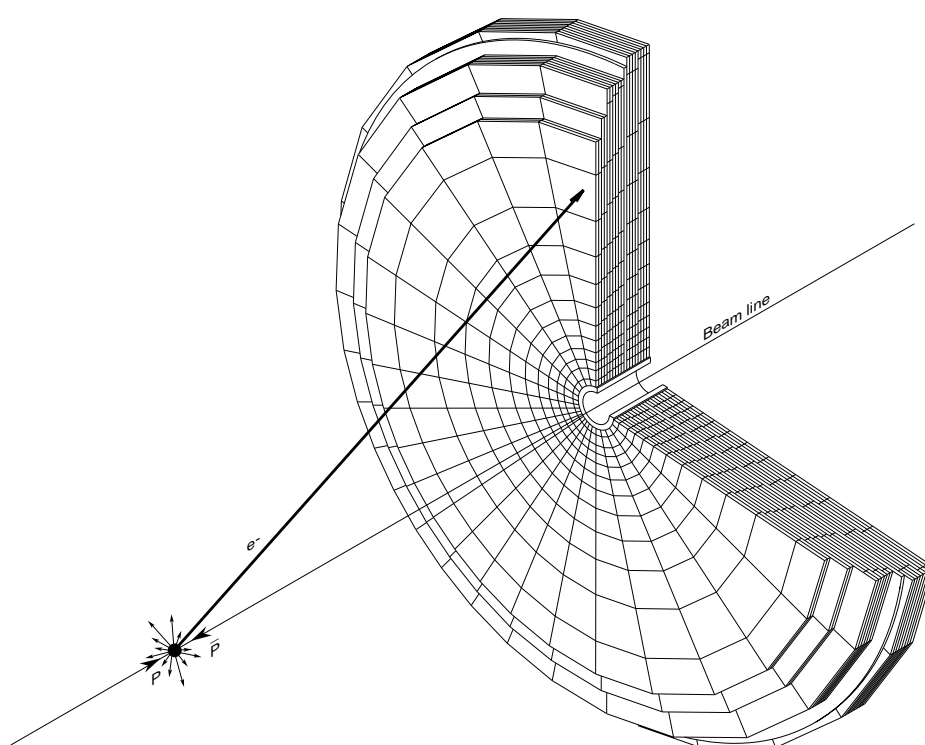
DØ END CALORIMETER ELECTROMAGNETIC MODULE

Figure 2.14: View of the end EM calorimeter.

taining sixteen 6 mm semicircular uranium plates (1.1 λ_A each). Alternate plates have their boundary rotated by 90° to avoid through-going cracks. The coarse hadronic section has a single readout section containing 46.5 mm stainless steel plates ($4.1\lambda_A$). The EC-IH provides 5216 signals.

Each of EC-MH modules has four fine-hadronic (uranium) sections of about 0.9 λ_A each and a single course-hadronic (stainless steel) section of 4.4 λ_A, and provide 1856 signals.

The EC OH modules employ stainless steel plates inclined at an angle of about 60° with respect to the beam axis, and each module provides 960 signals.

ICD and Massless Gap Detectors

In the transition region ($0.8 \leq |\eta| \leq 1.4$) between CC and EC, there are a lot of uninstrumented material (cryostat walls, module end-plates, etc.). The material profile along a particle path varies rapidly with rapidity in this region. To correct for energy deposited in the uninstrumented walls, two detectors called inter-cryostat detectors (ICD) are mounted on the front surface of the EC's. Each ICD consists of 384 scintillator tiles of size $\Delta\eta = \Delta\phi = 0.1$, matching the calorimeter cells. In addition, separate single-cell structures called massless gaps are installed in both CC and EC calorimeters.

Calorimeter Electronics

The total number of readout channels is about 47000. The signals from calorimeter preamplifiers are sent to the base-line subtractor (BLS) circuits on the detector platform, which sample the integrated charge just before a beam crossing and 2.2 μs later, and the signal is defined as the difference between the two. The signal from the BLS is then amplified 1 or 8, depending on the size of the signal, increasing the effective dynamic range of the 12-bit ADC's in the movable counting house (MCH) to 15 bits. Zero-suppression is applied to remove the cells without significant energy.

Performance of the Calorimeter

As mentioned above, the final signal is the number of electrons which are registered in the readout pads. Two important measures of performance are resolution and the linearity. The resolution of the calorimeter for measuring of an incident particle is determined by the fluctuations in the number of these electrons. These fluctuations have several sources:

- Sampling fluctuations - fluctuations in the energy deposited in the active layers due to shower development

- Noise in the active layers due to natural radioactivity of the depleted uranium plates

- Electronic noise

- Gain variations - high voltage, spacing, electronics, LAr temperature, O_2 contamination in LAr.

For DØ, the resolution is parameterized as

$$\left(\frac{\sigma(E)}{E}\right)^2 = C^2 + \frac{S^2}{E} + \frac{N^2}{E^2}, \tag{2.3}$$

where C is the constant term which represents calibration errors, S is the sampling fluctuation term, and N is the noise term which includes electronics and Uranium noise and is giving a constant variance in σ_E independent of the energy. From the test beam data, it is found that for electrons, $C = 0.003 \pm 0.002$, $S = 0.157 \pm 0.005 \, (GeV)^{\frac{1}{2}}$, and $N \approx 0.140 \, GeV$. And for pions, $C = 0.032 \pm 0.004$, $S = 0.41 \pm 0.04 \, (GeV)^{\frac{1}{2}}$, and $N \approx 1.28 \, GeV$.

2.2.3   Muon System

Muons are primarily identified by their penetrating nature. Muons do not interact strongly, and because of its large mass, for energies below ~ 500
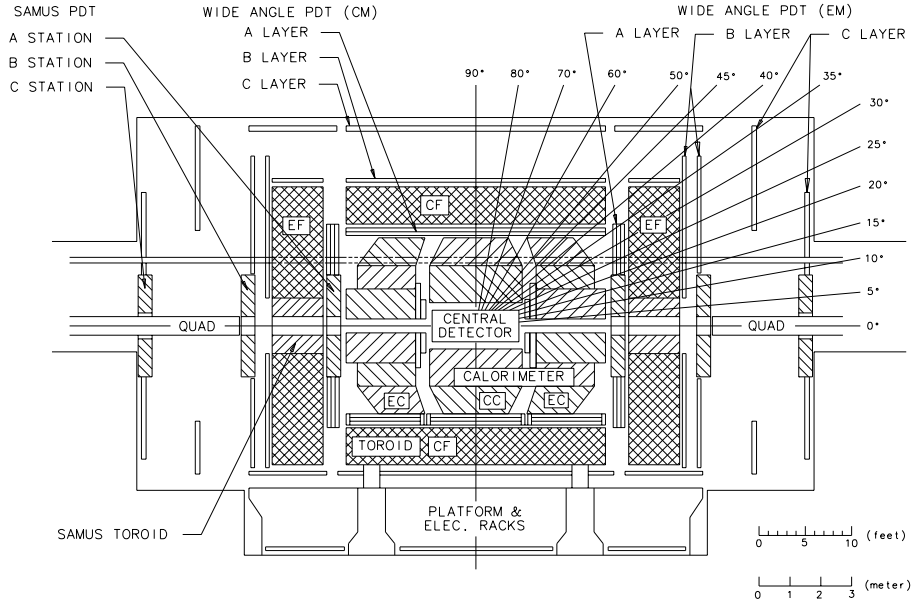
Figure 2.15: Elevation view of the DØ detector showing the five muon toroids and the PDT's.

GeV, do not produce electromagnetic showers.

The DØ muon detection system consists of five separate solid-iron toroidal magnets, together with sets of proportional drift tube chambers (PDT's) to measure track coordinates down to approximately 3 degrees. The purpose of this system is the identification of muons produced in $p\bar{p}$ collisions and determination of their trajectories and momenta.

The central toroid (CF) covers the region $|\eta| \leq 1$ and two end toroids (EF's) cover $1 < |\eta| \leq 2.5$. The small-angle muon system (SAMUS) toroids fit in the central hole of the EF toroids and cover $2.5 < |\eta| \leq 3.6$ (Figure

2.15). Associated with these magnets are several layers of proportional drift tube chambers: one just inside the iron (A layer), one just outside the iron(B layer), and one after an air gap of 1-3 m (C layer). Each of these layers is divided into sublayers of drift tubes: four for the A layer and three for each of the B and C layers (Figure 2.16). Due to various practical considerations (i.e. calorimeter and toroid supports), not all regions of $\eta - \phi$ space have full 3 layer (A, B, and C) coverage. The large number of interaction lengths in the calorimeter and muon toroids provide a very clean environment with negligible punch-through for the identification and momentum measurement of high P_T muons over most of the η region (Figure 2.17). This allows muons to be identified in the middle of jets with an efficiency much greater than that for electrons. The minimum momentum required for a muon to pass through the calorimeter and iron varies from ~ 3.5 GeV/c at $\eta = 0$ to ~ 5 GeV/c at higher η [36].

The muon system has only one wire per drift cell (50 μm gold plated tungsten). The maximum drift distance is 5 cm. The field shaping yields a linear space-time relationship to a good approximation. Hits in the bend view (perpendicular to the wires) are determined by measuring the drift time, similar to the technique used in the central tracking chambers. Hits in the other view (parallel to the wires) are obtained by crudely measuring
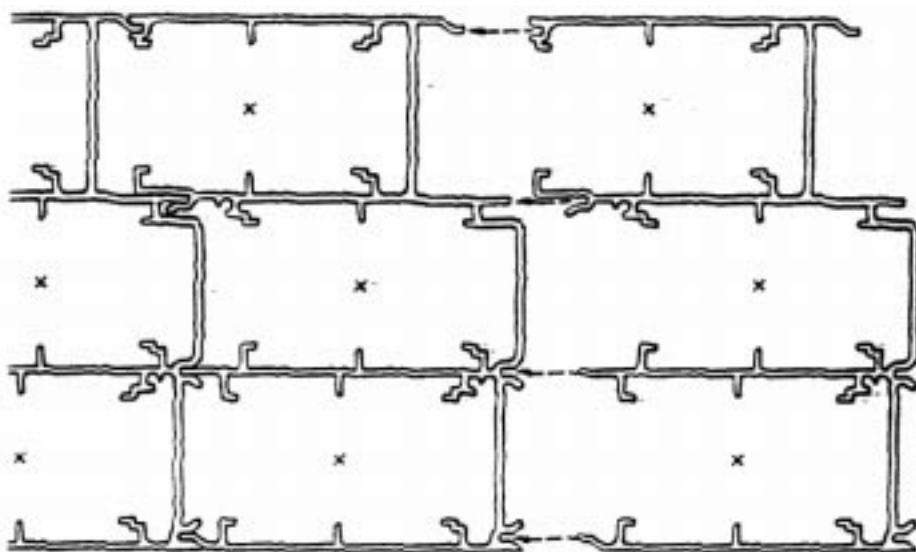
Figure 2.16: Extruded aluminum section from which the B and C layer PDT chambers are constructed. The A layer chamber extrusions are similar, but have four cells instead of three. The 'x' marks the position of the wire.
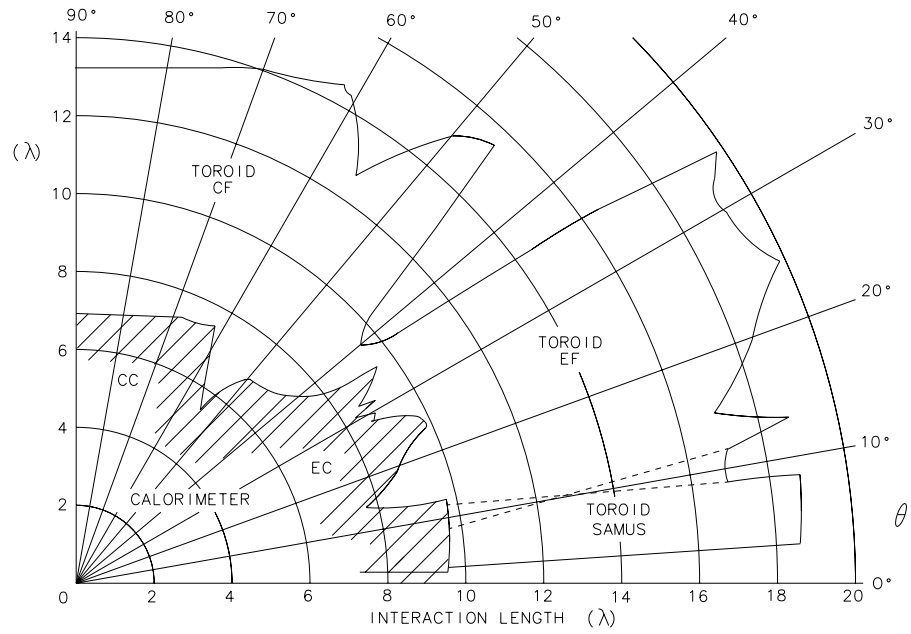
Figure 2.17: The thickness of the DØ detector and its subcomponents as a function of angle.

the signal arrival time difference between the two ends of the wire and more precisely with a system of vernier cathode pads inserted into the the top and bottom of each cell. The upper and lower cathode planes are made from two independent electrodes forming the inner and outer portions of a repeating diamond pattern whose repeat distances s 61 cm. The two inner pads of a given cell are added and read independently of the sum of the outer pads. Calculation of the ratio of the sum and difference of inner and outer signals gives a measure of the coordinate along the wire. The position resolution of 3 mm is achieved using this method.

The muon toroid (Figure 2.18) is a square annulus 109 cm thick and weighs about 2000 metric tons. The CF is completed by 2 C-shaped shells which can be moved perpendicular to the beams to allow access to interior detectors. Twenty coils of 10 turns each carry currents of 2500 A and create internal fields of 1.9 T, perpendicular to the beam axis. Therefore, muon trajectories are bent in the r–z plane. In order to measure the bend, and thus measure the momentum, the muon trajectory is measured both before and after the iron. The lever arm after the iron is the distance between the B and C layers. Tracks in the A layer are matched to tracks in the central detector and, for isolated muons, often to minimum ionizing traces in the calorimeter. The incident trajectory is then formed from a combination of
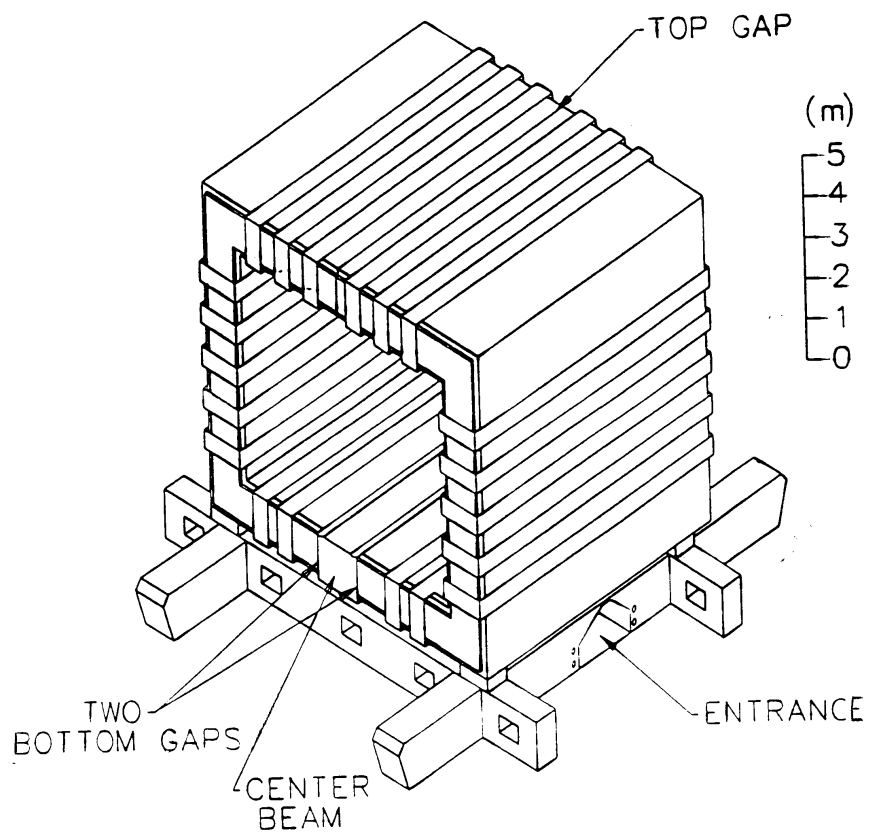
Figure 2.18: Perspective view of the CF toroid and the support beams in the detector platform.

the primary interaction point, the CD match, and the muon A layer track. The momentum resolution is parameterized by [37]:

$$\sigma\left(\frac{1}{p}\right) = 0.18(p-2)/p^2 \oplus 0.003, \qquad (2.4)$$

where the unit of p measured is in GeV/c. Multiple coulomb scattering in the iron limits the relative momentum resolution to $\geq 18\%$, up to the limit imposed by the bend coordinate resolution of the proportional drift tubes.

2.2.4 Trigger System and Data Acquisition

In order to make the most of the limited data acquisition bandwidth, complex trigger systems were designed to select and record interesting physics and calibration events. The trigger has three levels of increasingly sophisticated event characterization. The Level 0 scintillator based trigger indicates the occurrence of an inelastic collision. At a luminosity of $\mathcal{L} = 5 \times 10^{30}$ cm^{2}s^{-1}, the Level 0 trigger rate is about 150 kHz. Level 1 is a collection of hardware trigger elements arranged in a flexible software-driven architecture which allows easy modification. Many Level 1 triggers operate within the 3.5 μs time interval between beam crossings and thus contribute no dead time. Others, however require several bunch crossings to complete and are referred

to as the Level 1.5 triggers. The rate of successful Level 1 triggers is about 200 Hz; after the action of the Level 1.5 triggers, the rate is reduced to under 100 Hz. Candidates from Level 1 and Level 1.5 are passed on the standard DØ data acquisition (DAQ) pathways to a farm of microprocessors which serve as builders as well as the Level 2 trigger systems. Sophisticated algorithms reside in the Level2 processors which reduce the rate to about 2 Hz before passing them on to the host computer for event monitoring and recording on permanent storage media. The data acquisition system is shown in Figure 2.19.

Level Ø Trigger

The Level Ø trigger registers the presence of inelastic collision. Level Ø counters is a series of scintillator hodoscopes located close to the beam-pipe in the forward regions. These hodoscopes are strips of "criss-crossed" scintillators mounted on the surfaces of the end calorimeters. These detectors have partial coverage in the range $1.9 < |\eta| < 4.3$ and almost full coverage in the $2.3 < |\eta| < 3.9$ [36]. It has greater than 99% efficiency for detecting inelastic collisions. The scintillators are read out through photo-multiplier tubes. Level Ø is triggered by the presence of simultaneous activity in the forward and backward regions. They are activity from the spectator partons.
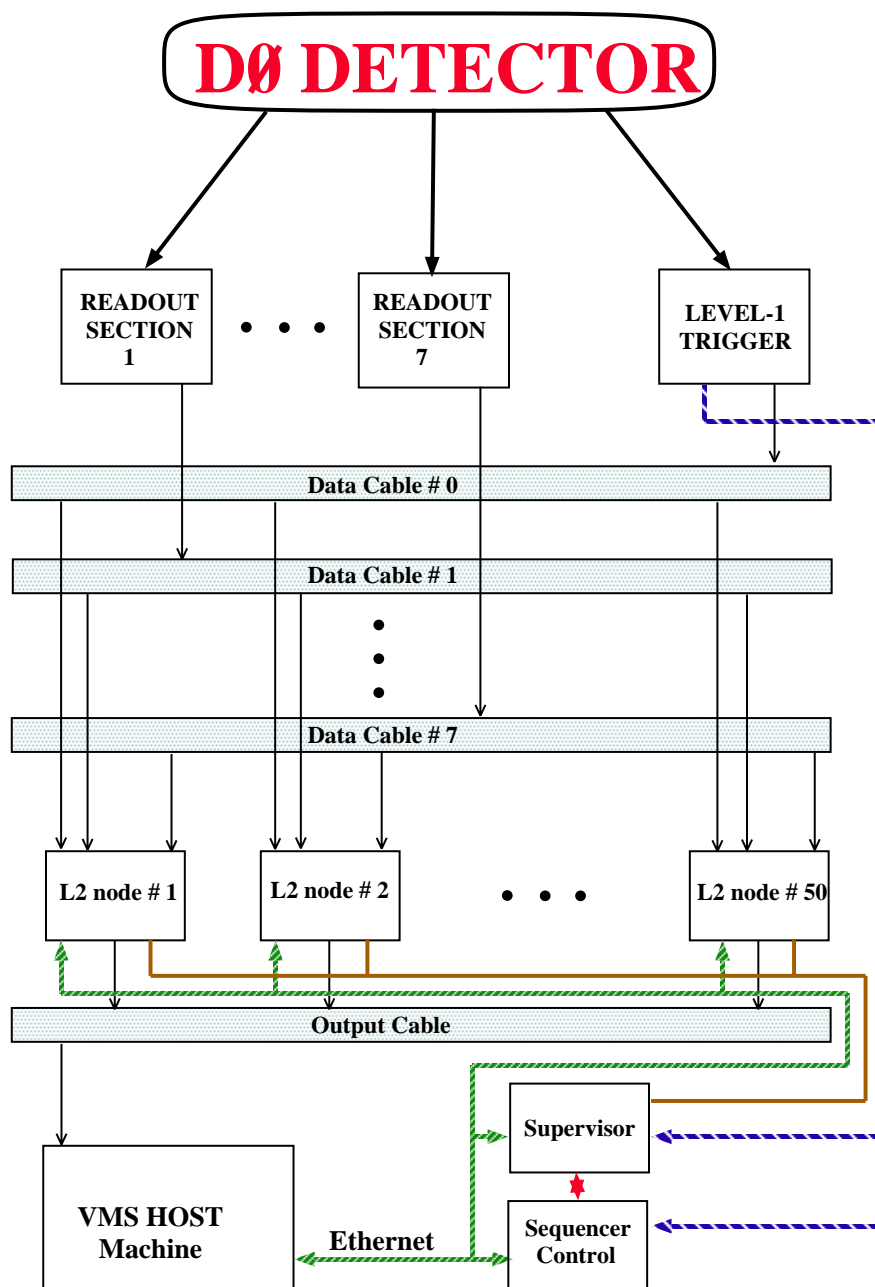
Figure 2.19: Schematic view of the DØ DAQ/Trigger systems.

A measurement of the arrival times at the two ends allows the LØ detector to determine the z position of interaction point. There are fast and slow estimations of this position. The former is based on the analog sum of signals from a subset of Level Ø counters and using a fast TDC, and is used to reject events with $|z_{\text{vtx}}| < 100$ cm, which are usually beam-gas or beam-halo events. This fast estimate is available to the Level 1 trigger for use in the calculation of the transverse energies. A more accurate measurement of the z position takes into account the time and total charge from each counter, applying full calibration and charge slewing corrections to the data, and using the mean time for each hodoscope. The RMS deviation of the time difference is also computed and used to flag events with multiple interactions. For single interactions (one hard scattering per bunch crossing), the resolution on this measurement is ± 3.5 cm. For multiple interactions, the resolution is ± 6 cm.

The Tevatron luminosity is obtained by measuring the rate for non-diffractive inelastic collisions. Events of this type are selected by requiring a Level Ø coincidence with $|z_{\text{vtx}}| < 100~cm$. Scalars count various quantities: live crossings, coincidences satisfying the vertex cut, and single hits in groups of similar counters with and without valid coincidences. These scalars allow the luminosity to be measured independently for each beam bunch and provide feedback to accelerator operations. Instantaneous luminosity is given

approximately by measuring the rate $R_{L\emptyset}$ of Level Ø triggers:

$$\dot{\mathcal{L}}_{meas} = \frac{R_{\mathrm{L}\emptyset}}{\sigma_{\mathrm{L}\emptyset}}, \qquad (2.5)$$

where $\sigma_{L\emptyset}$ is the world average $p\bar{p}$ inelastic collision cross section, corrected for the LØ acceptances and efficiencies measured from Monte Carlo and data. Its value was 46.7 ± 2.5 mb in the 1992-1993 run [39], and 44.4 ± 2.3 mb in the 1994-1996 run [40]. The 5.2% uncertainty on this number is dominated by systematic differences between experimental measurements of the $p\bar{p}$ cross section.

As instantaneous luminosity increases and multiple interactions become more common, the previous equation becomes a poor approximation and must be corrected using Poisson statistics:

$$\dot{\mathcal{L}} = \frac{-\ln(1 - \dot{\mathcal{L}}_{meas}\tau\sigma_{\mathrm{L}\emptyset})}{\tau\sigma_{\mathrm{L}\emptyset}}, \qquad (2.6)$$

where τ is the time between beam crossings. The integrated luminosity is then given by numerical integration of the instantaneous luminosity measurements:

$$\mathcal{L} = \sum_{i=1}^{n} \dot{\mathcal{L}}_i f_{\mathrm{live}}\Delta t_i, \qquad (2.7)$$

where the live fraction f_{live} is measured using a trigger bit dedicated to this purpose.

Level 1 Trigger

The next level of triggers is a hardware network which reduces the event rate to about 200 Hz. Operation of the Tevatron collider with six bunches of protons and anti-protons gives 3.5 μs between crossings. Any rejection of events which can be accomplished in this time incurs no dead-time penalty. The Level 1 "Trigger Framework" processes digital signals from Level Ø, the calorimeter, the muon system, and timing signals from the accelerator and the host computer. In the time between beam crossings, the Trigger Framework must decide whether to keep or reject an event. This decision is true if the event passes one or more of the 32 available trigger bits. Each of these bits is a logical combination of 256 programmable AND-OR input terms. Typical input terms include: Level Ø vertex position, calorimeter energy, and number of muon candidates [38]. Communication with the framework is handled by the trigger control computer (TCC). Through the TCC, users can download the threshold for firing of each the triggers. In addition, *prescale factors* can be defined for triggers whose firing rate would otherwise overwhelm the available bandwidth.
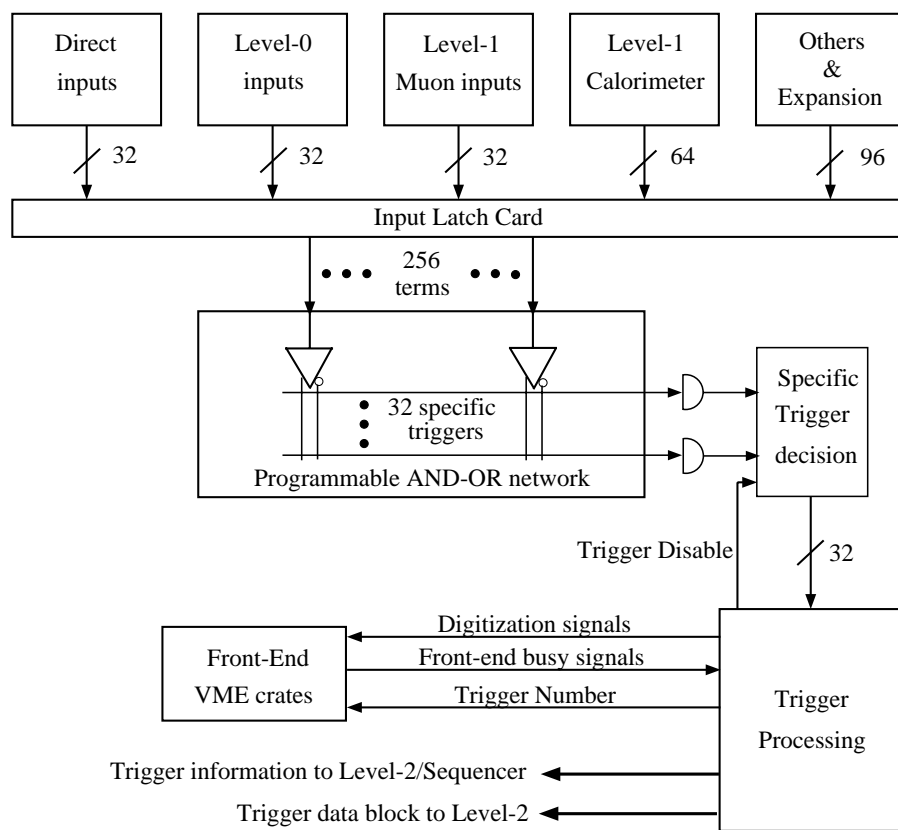
Figure 2.20: Schematic view of the DØ Level 1 processing stages.

The calorimeter trigger takes its input from analog pickoffs from the first stage of the calorimeter electronics (BLS circuits [36]). These analog signals are read out in terms of "trigger towers". A trigger tower is formed by summing the output from all the cells in a region which is $\Delta\eta \times \Delta\phi = 0.2 \times 0.2$ separately for the electromagnetic and fine hadronic sections of the calorimeter. The analog input signals are digitized by 8-bit FADC, and weighted by the sine of the trigger tower polar angle, thus giving an approximate transverse energy (exact if the event vertex is at $z = 0$). These 8 bits, plus three bits from the Level Ø system providing vertex z position information, are used as the address for a look up memory which returns the transverse energy (E_T). Once the trigger tower E_T's are known, the AND-OR terms are defined by comparing such quantities as the total E_T in the event, the transverse energy imbalance, and the electromagnetic and hadronic E_T's in each trigger tower to thresholds downloaded through the TCC.

For most calorimetric information, the above processing is sufficient. However, the fact that some electromagnetic showers share their energy between two trigger towers implies that electron and photon triggers can benefit from a crude clustering algorithm, which is applied at Level 1.5 [41]. The clustering sums the electromagnetic energies from two adjacent towers, and also calculates the total energy in the 3×3 grid of towers centered on the

electromagnetic trigger tower in order to allow calculation of the isolation of the electromagnetic object.

Together with the level 1 calorimeter trigger, the muon level 1 trigger provides digital information to the trigger framework. The muon trigger takes its input from the latch bits from some 16,700 drift cells of the muon system. This gives the bend coordinate of hit drift cells with a granularity of 10 cm. By combining information from multiple layers, a centroid is defined as the center of the half-cell which was most probably hit. The OR of three chambers adjacent in the bend direction being hit is sent to a coarse centroid trigger (CCT) card, which ORs the information by another factor of 4 to create a 60 cm-wide trigger road. If the hit pattern in the A, B, and C layers is consistent with the passage of a muon, a Level 1 bit is asserted and the Level 1.5 trigger is invoked.

The Level 1.5 trigger passes information on all centroids to octant trigger cards (OTC). The OTC then compares all possible combinations of the hit centroids in the three layers to that expected from tracks above some programmable transverse momentum (p_T) thresholds. This Level 1.5 processing reduces the muon trigger rate by a factor of 10-20, at the cost of about 1 % dead-time. Overall, the muon and calorimeter level 1.5 triggers reduces the trigger rate from about 800 Hz passing Level 1 to about 200 Hz for input

into Level 2.

Level 2 - Software Triggers

Once an event passes Level 1, it is shipped to the Level 2 system. Unlike the first two triggers (LØ and L1), Level 2 is a software trigger. Level 2 uses the digitized information from the event to perform a fast reconstruction, allowing the application of more sophisticated criteria to the event decision. The system is based on a farm of 32 VAX Model 4000/60 and 16 VAX Model 4000/90 processors running in parallel. It collects and processes much of the raw data including information from the LØ and L1, performs a fast preliminary reconstruction, and decides whether or not the event should be kept. For this decision to be true, event must satisfy one of the 128 software filters. These filters are built out of a series of algorithms. Typical algorithms are those which look for electromagnetic jets, hadronic jets, muons, missing E_T, etc. After the Level 2 requirements, the event rate reduces to about 4 Hz. The events that pass the various triggers are then saved to tape. Each event record is about 0.5 Mbytes, therefore the detector produces about 2 Mbytes/s of raw data.

During collider operations, all 48 processors are usually running the same code, and it is the job of a separate processor, the Supervisor, to direct

each incoming event to an idle Level 2 node. The event filtering software is built around a collection of "tools", each of which has a specific task related to particle identification, or global event characteristics (such as total E_T). Which tools are invoked, and their order, are controlled by scripts, one of which is associated with each Level 1 bit. It is possible for a single Level 1 bit to cause firing of multiple Level 2 filters.

Main Ring Effects

As described above, the Main Ring passes through the coarse hadronic calorimeter and is usually active as part of the anti-proton generation system while data is being taken. Beam loss from the Main Ring can cause spurious signals in the coarse hadronic calorimeter and muon system. The trigger system is responsible for flagging events that are contaminated by such Main Ring activity [42].

Protons are injected into the Main Ring every 2.4 seconds. At the injection energy, the magnetic field is of poor quality, and beam losses are large. Another large loss occurs 0.3 seconds later as the beam passes through transition. Hence a gate known as MRBS_LOSS is raised at the time of proton injections, and remains on for 0.4 seconds, until the beam has passed through transition and the muon high voltage system recovers.

During the remainder of the Main Ring acceleration cycle, losses are significant only when the passage of the proton beam through the accelerator coincides with a $p\bar{p}$ crossing in the Tevatron. Therefore, a second bit (known as MICRO_BLANK) is raised if a Main Ring beam transit occurs within ± 800 ns of a $p\bar{p}$ crossing. Level Ø counters measure the fraction of crossing which occur during the MRBS_LOSS or MICRO_BLANK windows, allowing analyses which veto these conditions to calculate their correct luminosity. For typical operation, this fraction was roughly 25%.

Data Acquisition

The data acquisition system is intertwined with the trigger systems. Once a Level 1 trigger is fired (and its 1.5 Level confirmation if necessary), the Supervisor's notified, and it in turn notifies another processor, the Sequencer, to begin digitizing the event. The Sequencer signals the front-end crates to begin digitization, which takes about 1 ms to complete. Data is then read out on eight unidirectional cables corresponding to different detector systems.

The data cables, each of which can transfer 40 Mbytes/s, are connected to multi-port memory (MPM) boards on each of the Level 2 node, and the node selected by the Supervisor to process the event receives the data. The MPM's are VAX memory boards with additional ports for the input cables. This

direct interface between the cables and the memory enables the transmission of data to proceed at the necessary speed.

If the event passes any Level 2 filter, it is transferred to the host computer, which writes the event to a buffer disk. Once roughly 500 events have been written to a file, the file is closed and the data copied to 8 mm tape.

Chapter 3

Event Reconstruction

The trigger requirements that are imposed on the events are necessarily general due to the fact that there are time and resource constraints when events are undergoing fast reconstruction by the online farm processors. More detailed and accurate reconstruction is left as a task for another set of processor farms. The information that is necessary to fully reconstruct an event gets saved to the tape when all the trigger requirements are met. The information consists of ADC counts from all of the hit channels in the calorimeter and central tracking chambers, as well as analog and digital signals from the muon system.

It is the task of the reconstruction software DØRECO to process this information into a suitable form for physics analysis, by converting raw sig-

nals into information about various final-state objects in the event. In this chapter, the DØRECO program is described, as well as the techniques used for identifying electrons, muons, jets, and missing E_T.

3.1   The DØRECO Reconstruction Program

DØRECO performs three major tasks. First, the signals from each sense wire of the tracking chambers are converted into spatial location of hits, and the signals from each cell in the calorimeter are converted into energy deposits. Secondly, the tracking chamber hits are joined to form tracks, while the calorimeter cells are grouped into clusters of energy. Finally, the tracking and calorimetric information is combined to reconstruct jets, and to identify electron and muon candidates. The criteria that is used by the reconstruction program to identify physics objects are quite loose, and substantial rejection of spurious electrons and muons is gained by further off-line processing.

After the reconstruction is done, two types of output files are produced:

- STA files - contain the raw data plus the output from the full reconstruction. These files are typically 600 kbytes per event and therefore used primarily for event displaying and for redoing reconstruction of events [36].

- DST (Data Summary Tape) files - contains a compressed version of the full reconstruction. A DST contains summaries of central detectors and muon tracks, calorimeter clusters, all parameters for electron, photon, muon, tau, and jet candidates, and all parameters relevant to missing E_T.

3.1.1   Central Tracking Chamber Reconstruction

The first step in reconstructing the information from the central tracking chambers is identifying sense wire and delay line hits. The algorithm that is employed depends on the difference in signal size between adjacent time bins from the FADCs. The leading edge of a pulse is found when three consecutive bins have differences above a threshold, or when two bins have differences above the threshold, the sum of which exceeds yet another threshold. Similarly, the trailing edge is identified by three consecutive bins whose differences fall below a threshold. The use of differences rather than absolute magnitude of the signals in defining a pulse reduces the sensitivity to fluctuations in the pedestals, and the fact that several bins are used also imposes constraints on the shape of the pulse, eliminating single-bin spikes which may arise due to bad FADC bits, and slowly rising signals due to discharge.

Once the leading and trailing edges of a pulse are found, the pulse size is calculated by summing the signals in the intermediate bins, and the width is taken as the difference between the leading and trailing edges. Time-dependent variations in the electronics gains and pedestals must be corrected for in this measurement. To do so, the response of the drift chamber channels to a calibration pulse is measured in the time between accelerator stores. The gains and pedestals are written to a database, which the reconstruction program accesses in order to determine the values appropriate for a given set of data.

The time of the pulse is given by

$$T = \frac{\sum_{i=1}^{N} i w^{i-1} D(i)}{\sum_{i=1}^{N} w^{i-1} D(i)}, \tag{3.1}$$

where the sum is over all bins after the leading edge up to the trailing edge, w is a weight (0.5 for the VTX, 1.2 for the CDC, 0.6 or 1.0 for FDC signal lines depending on the pulse height), and $D(i)$ is the difference between the ith bin and its predecessor. This gives the time in bins which is converted in units of second since the speed of the digitizer is well-known. The weights are used to increase sensitivity to the signal from electrons arriving in the peak of the pulse. Note that this timing measurement can only give the distance

of the hit from the wire, not which side the hit came from. Therefore, two copies of the hit are stored, one at its actual position and the mirror image on the opposite side of the wire.

This algorithm is used for finding both sense wire and delay line hits. For the delay line, there is the additional requirement that the sum of the times for the signals read out on each end of the line be equal to the delay along the entire line, within a tolerance that allows for the resolution of the time measurements.

Once the individual hits are found, *segments* are defined which connect all of the hits within a given layer of the chamber. All of the hits are sorted in ϕ, and each possible pair of innermost and outermost wire hit combinations are considered. For each combination, a road is defined connecting the two hits, and the set of hits in the intermediate wires within this road which gives the best fit to a straight line is added to the segment. At this point the left-right ambiguity is broken by the staggering of the sense wires, which means that the true hits should have a better fit than their mirror-image hits. Once assigned to a segment, the hits are removed from the list to avoid having the same hit assigned to two segments. Up to two sense wires are allowed to be missing hits when a segment is defined.

The last step is to connect the segments in each layer to form tracks. This

process begins in the outer layer of the chamber. Each segment in the outer layer is compared to the segments in the third layer which lie within a given ϕ distance, and the third-layer segment which matches most closely is added to the track. This process continues until the track extends through all the four layers (one layer is allowed to have a missing segment). After this $r - \phi$ fitting is done, the delay line information is added to fit the z coordinates of the track. Typical resolutions for the track direction are 2.5 mrad in ϕ and 28 mrad in θ [43]. Track finding efficiencies are measured using $Z \rightarrow ee$ events, and found to be $79.4 \pm 0.8\%$ in the CDC and $73.4 \pm 1.1\%$ in the FDC [42]. For more details on the central tracking reconstruction, see [44, 45].

3.1.2   Event Vertex Determination

As mentioned above, the z position of a collision varies widely on an event-by-event basis, with a roughly Gaussian distribution of width of 30 cm. Since it is essential to accurately measure the θ direction of final state objects (in order to assign vector components based on the total calorimeter cluster energy), the z vertex of each event must be reconstructed with the highest possible accuracy.

In order to do this, one considers, the set of CDC tracks, which have an

impact parameter with respect to the beam in the perpendicular direction of less than 2.5 cm. All such tracks are projected to $x = y = 0$, and the distributions of the resulting z positions are made. The peak of the distribution is used to determine the event vertex, with a resolution of 1.2 cm. Additional vertices (from multiple $p\bar{p}$ collisions) can be identified from secondary peaks in the histogram if they lie more than ≈ 7 cm away from the primary vertex [45, 46].

The transverse $(x - y)$ position of the interaction is tightly constrained by the small transverse size of the colliding beams (about 50μm). For any given store, the $x - y$ position at which the beams cross is also quite stable, so the measurement of the $x - y$ vertex position is done on a store-by-store, rather than event-by-event, basis. For this measurement, a collection of 500 events taken from the first run of a store is processed. The CDC tracks from these events are matched to the VTX tracks, which improves the accuracy of the $x - y$ track position. All matched tracks are then extrapolated to either $x = 0$ or $y = 0$, depending on the azimuthal angle of the track, and the position of the orthogonal coordinate is histogrammed. The peak of each histogram gives the mean x and y interaction point for the store, which is recorded on a database for use by DØRECO.

3.1.3   Calorimeter Reconstruction

The reconstruction of calorimeter data begins with conversion of the ADC counts recorded in each calorimeter cell into a value for the energy deposited. To a first approximation, the conversion constant between ADC counts to GeV can be taken from test beam runs performed before the calorimeter was installed for data taking. In these tests, portions of the calorimeter were exposed to electron and pion beams of known energies.

However, the test beam setup was not a perfect reproduction of the conditions that existed at the time of data-taking (some differences were in the amount of upstream material and the length of cables), and thus it is necessary to perform an in situ calibration, which is described later in this chapter.

As in central tracking hit reconstruction, the calorimeter signals must be corrected for time-dependent changes in the gains and pedestals of the readout channels. Calibration runs taken between stores were recorded in the same database as the central tracking gains and pedestals, and accessed by the reconstruction program.

Once the energy deposited in each cell is determined, signals from all of the cells with the same η and ϕ indices are summed into towers. In taking this sum, it is assumed that each cell represents a massless particle. As energy

and momentum are equivalent under this assumption, each cell is assigned an energy four-vector $(E, E \sin\theta \sin\phi, E \sin\theta \cos\theta, E \cos\theta)$, where E is the signal in the cell and the θ and ϕ the directions defined by the cell centroid and the primary reconstructed z vertex. The lower energy four-vector is then given by the sum of each cell's four-vector.

Once this four-vector is assigned, the direction variables of the tower are calculated from it:

$$\phi = \tan^{-1}\frac{E_x}{E_y} \tag{3.2}$$

$$\theta = \tan^{-1}\frac{\sqrt{E_x^2 + E_y^2}}{E_z} \tag{3.3}$$

$$\eta = -\ln(\tan\frac{\theta}{2}) \tag{3.4}$$

These towers are used as the starting point for jet reconstruction, while similar towers which include only the energies in the electro-magnetic layers and innermost hadronic layer are used for electron and photon reconstruction.

3.2   Particle Identification

3.2.1   Electrons

The first step in the reconstruction of electrons and photons is to group electromagnetic towers into clusters of energy. Beginning with the highest-E_T tower, all neighboring towers with E_T above 50 MeV are added to the cluster, and the process repeats until no towers neighboring the cluster satisfy the energy requirement. A new cluster is then begun from the highest-E_T tower not previously assigned to a cluster.

Any cluster in the calorimeter with more than 90% of its energy in the electromagnetic layers of the calorimeter (and more than 40 % in a single tower) is identified by the reconstruction program as an electron or photon candidate. As the typical hadronic jet is broad and deposits only about 10% of its energy in these layers, this cut alone removes most hadronic clusters while still retaining more than 99% of true electrons and photons. Electron candidates are distinguished from the photon candidates by the presence of CDC or FDC track within a road size of $\Delta\eta \times \Delta\phi = 0.1 \times 0.1$ pointing from the primary vertex to the cluster.

There are two primary background processes that can mimic an electron: one is π^0 decay to two photons, producing an electromagnetic cluster, with a

track provided by the random overlap of a low-energy charged hadron. The other is photon conversion to e^+e^- pairs early in the tracking system. With no magnetic field in the tracking region, the electron and positron continue on nearly the same trajectory and may be identified as a single track. In order to suppress these backgrounds while retaining high efficiency for identifying true electrons, information from the calorimeter and the tracking system is combined [43].

There are several quantities that aid us in identifying electrons:

- **Cluster EM fraction:**

$$f_{EM} = \frac{\text{Energy in the EM section}}{\text{Total Energy}} \qquad (3.5)$$

This value is required to be greater than or equal to 0.90 for electron and photon candidates.

- **Cluster isolation:**

$$f_{iso} = \frac{E(0.4) - EM(0.2)}{EM(0.2)} \qquad (3.6)$$

This is defined by comparing the electromagnetic energy within a cone of radius $\Delta R = \sqrt{\delta\eta^2 + \delta\phi^2} = 0.2$ centered on the cluster $(EM(0.2))$ to
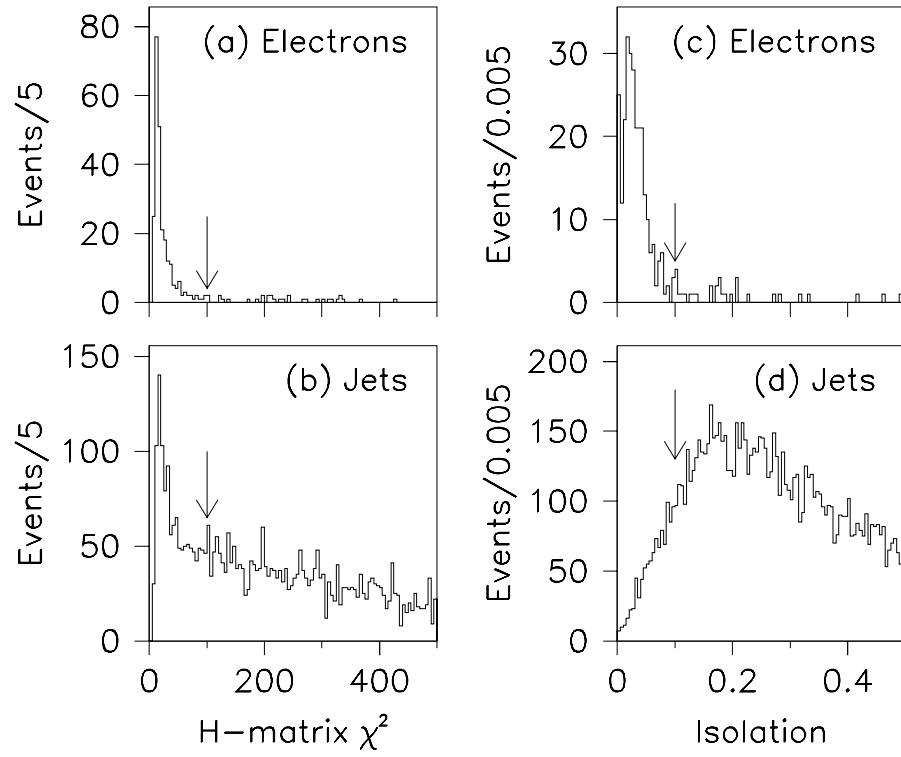
Figure 3.1: Distribution of χ_{em} and f_{iso} for electrons and jets.

the total energy contained within a concentric cone of radius $\Delta R = 0.4$ ($E(0.4)$). Any cluster with $f_{iso} > 0.1$ is rejected (Figure 3.1). This cut retains 98% of electrons while significantly reducing backgrounds from random track overlaps and also from the semileptonic decay of b or c quarks.

- **Cluster Shape:**

  The development of electromagnetic and hadronic showers are sufficiently different that shower shape information can be used to differentiate between electrons (or photons) and hadrons. To exploit these differences to the greatest degree, DØ uses both longitudinal and transverse shower shapes, and also takes into account correlations between energy deposits in the calorimeter cells [47, 48]. A covariance matrix technique is used to compare the shape of a given shower with the shower shape expected from electrons determined from both the testbeam data and Monte Carlo. The covariance matrix, for a sample of N electrons or photons is defined:

  $$M_{ij} = \frac{1}{N} \sum_{n=1}^{N} (x_i^n - \langle x_i \rangle)(x_j^m - \langle x_j \rangle), \qquad (3.7)$$

  where x_i^n is the value of observable i for electron (or photon) n and

$\langle x_i \rangle$ is the mean value of the observable i for the sample. A total of 41 variables are used.

- – The fraction of the total energy contained in the layers 1, 2, and 4 of the electromagnetic (EM) calorimeter and layer 1 of the fine hadronic (FH) calorimeter

- – The fraction of the total energy contained in each cell of a 6×6 array around the shower center in the third layer (which is the region where electromagnetic shower development reaches maximum)

- – The logarithm of the total energy

- – The z position of the primary vertex

The matrix M is calculated individually for towers at different η, and symmetry in ϕ is assumed. Furthermore, reflection symmetry is assumed for the positive and negative η regions of the detector, so there are 37 distinct matrices.

Once M has been calculated, the degree of agreement between an individual shower and that expected from an electron is defined by:

$$\chi^2 = \sum_{i,j=1}^{41} (x_i - \langle x_i \rangle) H_{ij} (x_j - \langle x_j \rangle), \qquad (3.8)$$

where H is the inverse matrix of M. Despite the notation, the fact that the variables are non-Gaussian means that this variable is not distributed as a χ^2 distribution (Figure 3.1). In order to reduce sensitivity to possible differences between data and Monte Carlo electrons, the H matrix is diagonalized and an upper limit is placed on the elements of the diagonalized matrix.

- **Track Matching Significance:**

  To further reject random track overlaps, the consistency between the direction of the central track and the centroid of the shower is calculated. The shower centroid is defined as:

  $$\vec{x}_{cog} = \frac{\sum_i \vec{x}_i w_i}{\sum_i w_i}, \tag{3.9}$$

  where the sums are over all cells in the shower cluster, $\vec{x}_i$ is a vector from the vertex to the cell centroid, and

  $$w_i = \max(0, w_o + \ln(E_i/E)) \tag{3.10}$$

  The logarithmic weighting reflects the logarithmic development of a shower, and the w_o is chosen empirically to optimize the position res-
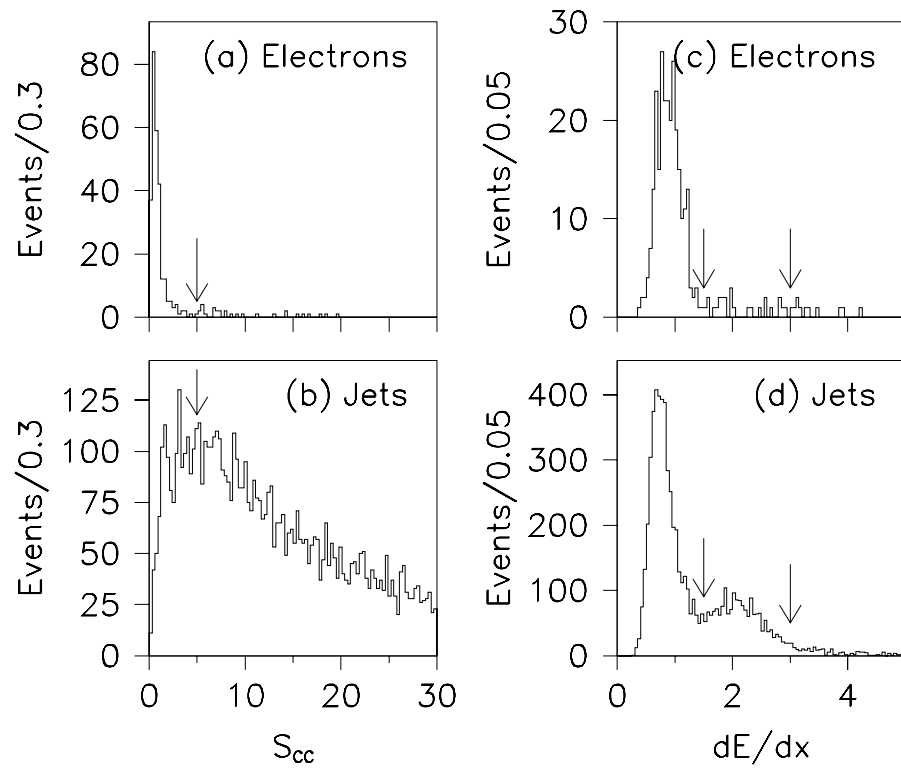
Figure 3.2: Distribution of track match significance and dE/dx for electrons and jets.

olution. The azimuthal resolution of the center of gravity is measured to be about 2.5 mm [43].

The track match significance for clusters in the CC (EC) is given by:

$$\sigma_{\text{TRK}}(CC(EC)) = \sqrt{\left(\frac{\Delta\phi}{\sigma_{\Delta\phi}}\right)^2 + \left(\frac{\Delta z(r)}{\sigma_{\Delta z(r)}}\right)^2}, \qquad (3.11)$$

where Δx is the mismatch in variable x between the shower centroid and the track direction, and $\sigma_{\Delta x}$ is the resolution of the measurement of this mismatch (Figure 3.2).

- **Discrimination of Photons and Electrons:**

  To discriminate between prompt electrons and photon conversions, the track ionization dE/dx is measured. The distribution of energies deposited by a single ionizing particle has a long "Landau" tail on the high end, which reflects the energy transferred to scattered electrons (or *delta rays*). To reduce the sensitivity to these fluctuations, and thereby improve the overall resolution, the third of the CDC wires with the largest signals are removed from the measurement. The mean of the remaining signals is taken as the measurement of dE/dx (Figure 3.2).

- **TRD information:**

The final variable which contributes to electron identification comes from the TRD. The TRD response is characterized by the variable ϵ:

$$\epsilon(E) = \frac{\int_E^\infty \frac{\partial N}{\partial E'}(E')dE\prime}{\int_0^\infty \frac{\partial N}{\partial E'}(E')dE\prime}, \qquad (3.12)$$

where E is the total energy recorded in the TRD minus that recorded in the layer with the largest signal (again, this is done to reduce sensitivity to delta rays) and $\frac{\partial N}{\partial E'}$ is the energy spectrum from a sample of $W \to e\nu$ events [49]. Since ϵ decreases as E increases, hadrons will tend to have values near unity while the distribution from electrons is roughly uniform over the allowed range of 0 to 1.

In order to extract the maximum possible background rejection and efficiency from the H-matrix χ^2, track-match significance, dE/dx, TRD ϵ, and electromagnetic fraction of the cluster, these variables are combined in a vector $\vec{x}$ to calculate an overall consistency of the cluster with an electron. In so doing, it is assumed that these variables are uncorrelated so that the probability of the cluster arising from hypothesis H is:

$$p(\vec{x}|H) = p(\epsilon|H)p(dE/dx|H)p(\chi^2|H)p(\sigma_{\text{TRK}}|H)p(f_{\text{EM}}|H), \qquad (3.13)$$

where the possible hypothesis are electron ($H = e$), hadron overlap ($H = h$), or photon conversion ($H = ee$). Next, the variable $\mathcal{R}$ is defined by:

$$\mathcal{R} = \frac{p(\vec{x}|b)}{p(\vec{x}|e)} = \frac{f_h p(\vec{x}|h) + (1 - f_h) p(\vec{x}|ee)}{p(\vec{x}|e)}, \qquad (3.14)$$

where f_h is the fraction of hadronic overlaps in the background. A cut is imposed $\mathcal{R}(f_h) < 0.5$, and clusters with values below the cut are taken to be electrons.

The probability densities and f_h are determined from the data as described in [49, 50]. f_h is found to be 0.53 in the CC and 0.62 in the EC.

3.2.2 Electromagnetic Energy Calibration

The calibration of electro-magnetic calorimeter begins by correcting for the known differences between the test beam and collider data. Such differences exist in the readout electronics, liquid argon purity, and voltage applied across the gap, and they account for about a 5% offset between the test-beam and collider energy scales [51]. In addition, module-to-module variations are measured using large data samples with electromagnetic clusters. A minimum E_T is imposed, and the number of surviving clusters is plotted for each module. As the underlying physics is symmetric in ϕ, any

nonuniformity must be due to differences in response which artificially move clusters across the threshold, and these variations are corrected. The RMS deviation is 1.3%, with the maximum excursion between any two ϕ modules being 5% [51].

Once this is done, it remains to fix the overall calibration. The high degree of linearity observed in the test-beam studies allows one to infer a linear relationship between measured and true electromagnetic energies:

$$E_{\text{True}} = \alpha E_{\text{Meas}} + \delta, \tag{3.15}$$

where α is the scaling factor and δ is the offset. Reconstructing the invariant mass spectrum of any particle which decays into electrons (or photons) is sufficient to constrain the calibration. In practice, three such calibration points are used: the Z boson, J/ψ, and π^0. The allowed ranges for α and δ are shown in Figure 3.3 and are

$$\alpha = 0.9537 \pm 0.00086$$

$$\delta = -0.16^{+0.03}_{-0.21} \; GeV.$$

This precise calibration of the electromagnetic calorimeter serves as the
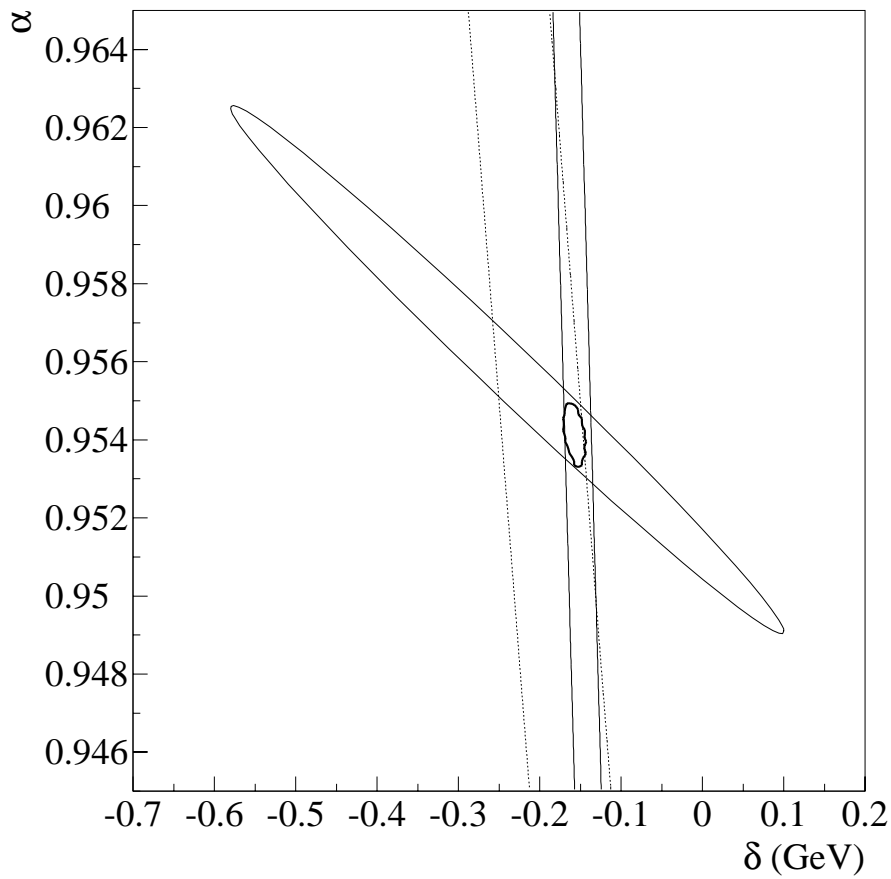
Figure 3.3: 68% confidence level intervals for the electromagnetic response parameters α and δ. The wide band is the constraint from J/ψ decays, the narrow band from π^0 decays, and the ellipse from Z boson decays. The small ellipse is the combined constraint.

starting point for calibration of hadronic energy scale.

3.2.3   Muons

In principle, the reconstruction of muon tracks is similar to the reconstruction of tracks in the central detector. However, differences in the geometry and electronics of the muon system, as well as the need to measure the bend angle (and thus the momentum) of the tracks, require that somewhat different algorithms be used. The information recorded by the detector is a digital pad latch indicating the presence of a hit in a given drift cell, along with analog signals which record the drift time, the difference in time between the signals readout at each end of the sense wire, and the charges on the inner and outer segments of the cathode pads.

As in the CDC, the reconstruction process begins with identifying the spatial location of hits. All hits in pad-latched channels which are associated with a drift time less than the maximum possible for the cell are located (again, two space points are associated with each hit due to left-right ambiguity). The hits are then joined into two straight segments, one including the hits from the A-layer cells and the other from the hits in the B and C layers (hence, this will be labeled BC segment). These segments are reconstructed

using a linear least squares fit considering $r-z$ and $r-\phi$ information separately. Assuming that the set of true hits will fit more closely to a straight line than the set of mirror-image fits allows one to use the fit χ^2 to break the left-right ambiguity, and also any remaining ambiguity in the z position of hits. BC segments are required to have four of a possible 6 hits, while A layer segments must have two of four, and all segments are required to point to within 5 m of the center of the detector. This cut removes randomly-oriented tracks from cosmic ray muons.

Once the segments are formed separately in the $r-z$ and $r-\phi$ views, only those segments which consist of the same hits in each view are retained. The next step is to join the segments into muon tracks. The process begins with the BC segments which are extended to the mid-plane of the toroid. The A layer segment which points most closely to the point of intersection of the BC segment with the toroid mid-plane is then added to the track. If no A segment matches sufficiently well, the pre-toroid direction is defined as the line between the primary interaction vertex and the mid-toroid point. (Muon candidates are also formed for A segments with no matching BC segment, although, since there is no momentum information available for such muons, they are discarded from this analysis).

To first order, the muon momentum is determined by the angle between

the A and BC segments of the track, corrected for the energy lost by the muon in traversing the calorimeter. However, the measurement becomes more accurate if one performs a global fit making use of all possible information, including the presence of a track in the CDC. This fit makes use of a total of 16 input parameters.

- The vertex position in the x and y plane

- The slope and intercept of the CDC track in the r–z and r–ϕ views

- Two angles representing the mismatch of the CDC track and calorimeter track directions

- The slope and intercept for the A and BC segments in the r–z and r–ϕ views

The fit returns seven parameters: four for the CDC track, two representing the multiple scattering in the calorimeter, and the momentum of the track.

The primary backgrounds to muon candidates are from cosmic rays, and tracks formed from random noise hits in the muon chambers, with the contribution from hadrons punching through the calorimeter and toroid being negligible except in the gap region between the central and end toroids.

To reduce these backgrounds, several variables are used to identify good muons. These are:

- A word (IFW4) representing the quality of the track-fit. Tracks with perfect hits have an IFW4 of 0, those with one failure have IFW4 of 1, and all others have IFW4 of 2.

- As the muon traverses the calorimeter, it deposits energy through ionization, and these energy traces are used in the track fit. The fraction of all possible hadronic calorimeter layers which had energy deposits large enough to be included in the fit is recorded (MTC_{frac}), along with the fraction of energy deposited in the outermost possible layer (f_{outer}) [52]. Both of these quantities are useful in rejecting muon tracks formed from random noise in the muon system.

- $\int \vec{\mathbf{B}} \cdot \vec{\mathbf{dl}}$: This quantity is used to reject tracks which pass through the inter-toroid crack. Not only is there a significant punch-through background for such tracks, but their momenta are also poorly measured.

- **Track impact parameter:** Tracks which do not pass near the vertex position are likely to be cosmic rays. The three dimensional impact parameter is calculated, along with the impact parameters in the $r-z$ and $r-\phi$ views.

- **Time offset** (Δt_o)**:** The time of the hits in the track is allowed to float in the fit, and the difference between the best-fit time and the beam-crossing time is calculated. This helps to reject cosmic-ray muons, whose timing is independent of the beam activity.

The variables used, and the values vary not only for the different $t\bar{t}$ decay channels, but also to reflect changes in the operating conditions of the muon chambers and in the reconstruction code. One can divide the data sample into three subsets according to the quality of muon information available:

- Era I (Runs 50000–65000): The reconstruction code did not perform muon tracking in the calorimeter. For these runs, the MTC_{frac} and f_{outer} variables are not available, so a simpler quantity, the amount of energy in a calorimeter road around the muon track is used in muon identification.

- Era II (Runs 65000–89000): Some muon chambers, particularly those in the EF and Main Ring regions, were inefficient due to build up of polymers in the anode wires.

- Era III (Runs 89000–end): Chambers were cleaned to remove polymers and efficiency was restored.

Variable	Cut	Channels
Fiducial region	CF toroid	ℓ+jets, $\ell\ell$
IFW4	≤ 1	ℓ+jets, $\ell\ell$
Cal. MIP	Yes	ℓ+jets, $\ell\ell$
$\int \vec{B} \cdot d\vec{l}$	≥ 0.6 GeV	ℓ+jets
Impact Parameter	< 22 cm (3D)	ℓ+jets
	< 20 cm (rz)	
	< 20 cm ($r\phi$)	
Δt_o	< 100 ns	ℓ+jets

Table 3.1: Criteria for identification of muons in Era I. As dilepton channels have lower backgrounds and require greater efficiency, not all cuts are applied to these channels.

Given this variety of conditions, the muon identification is complicated, and

the requirements are summarized in Tables 3.1 and 3.2.

3.2.4   Missing E_T

An imbalance in the transverse energy of an event as a whole, indicates the

presence of a neutrino, as it does not interact with the detector. Such imbal-

ance is known as "missing E_T", denoted by $\not{E}_T$. This quantity is determined

by summing the transverse energy components of every calorimeter and ICD

cell:

$$\not{E}_x^{cal} = - \sum_{i=1}^{N_{cells}} E_i \sin(\theta_i) \cos(\phi_i) - \sum_j \Delta E_x^j,$$

Variable	Cut	Channels
Fiducial region	CF toroid (Era II)	ℓ+jets, $\ell\ell$
	CF and EF toroids (Era III)	
IFW4	≤ 1 (CF)	ℓ+jets, $\ell\ell$
	$= 0$ (EF)	
Cal. muon track	($MTC_{frac} = 1.0$) OR	ℓ+jets, $\ell\ell$
	($MTC_{frac} > 0.75$ AND $f_{outer} > 0.0$)	
$\int \vec{B} \cdot d\vec{l}$	≥ 0.6 GeV	ℓ+jets
Impact parameter	< 20 cm (3D)	ℓ+jets

Table 3.2: Criteria for identification of muons in Eras II and III.

$$\not{E}_y^{cal} = - \sum_{i=1}^{N_{cells}} E_i \sin(\theta_i) \sin(\phi_i) - \sum_j \Delta E_y^j.$$

The second sum is over the corrections in E_T applied to all electrons and jets in the event. In order to obtain the best energy resolution, ΔE_T^i is obtained by reconstructing the event with $R = 0.7$ cone jets. The magnitude of $\not{E}_T^{cal}$ is obtained by summing the x and y components in quadrature. The equations above are used to estimate the $\not{E}_T$ for events without muons. In the presence of muons, the transverse momentum of the muon is subtracted from $\not{E}_T^{cal}$ in order to estimate the total missing E_T.

$$\not{E}_x = \not{E}_x^{cal} - \sum_i p_x^{\mu_i}$$

$$\not{E}_y = \not{E}_y^{cal} - \sum_i p_y^{\mu_i}$$

This represents the total transverse energy carried away by particles which do not interact in the calorimeter. The resolution of this measurement is greatly enhanced by near-hermeticity of the DØ detector. Based on the distribution of $\not{E}_T$ in a sample of events which were required only to pass the LØ trigger, the resolution can be parameterized as (Figure 3.4) [43]:

$$\sigma(\not{E}_T) = 1.08\text{GeV} + 0.019 \times \sum_{\text{Cells}} E_T \qquad (3.16)$$

3.2.5   Jets

Unlike electrons, muons, and $\not{E}_T$, there is no unambiguous way of defining a jet. In the simplest case, the dijet production, where two partons are produced in the $p\bar{p}$ collision, one would expect each parton to fragment and produce a number of hadrons, which travel in approximately the same direction as the original partons. Then one will observe in the calorimeter two distinct clusters of energy back-to-back in ϕ. Suppose now that one of the original partons radiates a gluon prior to the fragmentation process. This gluon will then fragment to produce another spray of hadrons. If the gluon was emitted at a small angle to the original parton direction, these particles will tend to fall in the same calorimeter cells as the hadrons from the ini-
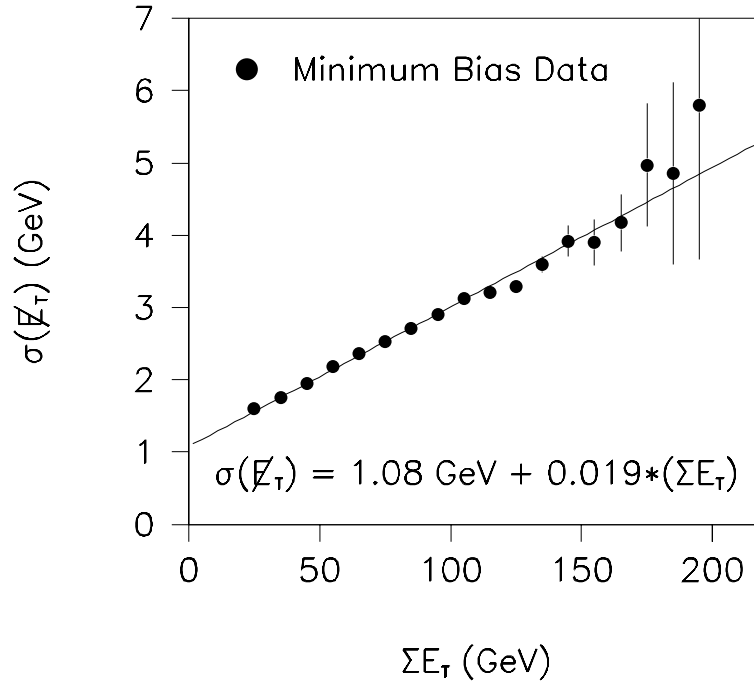
Figure 3.4: Uncorrected $\not{E}_x^{cal}$ distribution for minimum bias data. The line represents a fit to the data points.

tial parton, and one still has two clusters in the event. One might find this cluster if a calorimeter had finer granularity. Even then, one still has to face the possibility that if the gluon is emitted at an even smaller angle, they will look like a single jet.

Jet Cone Algorithm

In order to proceed, one must formulate an algorithm which associates deposits in the calorimeter with jets. The jets used in this analysis are defined using a cone algorithm [43, 53].

Jet finding at DØ uses the E_T of the calorimeter towers which is determined from the energy vector of towers:

$$\vec{E}^{tower} = \sum_{i=cells} \hat{n}_i E_i, \tag{3.17}$$

$$E_T^{tower} = \sqrt{(E_x^{tower})^2 + (E_y^{tower})^2}, \tag{3.18}$$

where $\hat{n}_i$ is the unit vector pointing from the interaction point to the center of calorimeter cell i, and E_i is the magnitude of the energy deposited in cell i. The iterative jet cone algorithm is implemented as follows:

- First, an E_T ordered list of the calorimeter towers is made. For every tower ($\Delta\eta \times \Delta\phi = 0.1 \times 0.1$) with $E_T > 1$ GeV, a precluster is formed

by starting from the highest E_T tower as a seed and including all its
nearest neighbors which have $E_T > 1$ GeV. E_T of a precluster is then
defined as the scalar sum of E_T's of all the cells in the precluster. The
towers included in the precluster are then removed from the seed list.
This procedure is repeated until all the seed list is exhausted and a
precluster list is formed.

• The next step in the reconstruction of jets is the jet clustering. Starting
from the highest E_T precluster, all towers within $\sqrt{(\Delta\eta)^2 + (\Delta\phi)^2} < R$
from the precluster center are assigned to a jet. R was chosen to be 0.5
for this analysis. The $E_T{}^1$ and the direction of the jet is defined as:

$$E_T^{jet} = \sum_i E_{Ti}, \tag{3.19}$$

$$\eta^{jet} = \frac{\sum_i E_{Ti} \times \eta_i}{\sum_i \eta_i}, \tag{3.20}$$

$$\phi^{jet} = \frac{\sum_i E_{Ti} \times \phi_i}{\sum_i \eta_i}, \tag{3.21}$$

where i is the index for all the towers in the jet. This $\eta - \phi$ position of
the jet is taken as a new seed for the jet and the jet clustering is repeated
until the centroid of the jet converges within a radius of $R = 0.001$ of

---

[1] The definition of E_T of the jet used for this analysis is different from the one used in
the reconstruction, and it is $\sqrt{(\sum_{towers} E_x)^2 + (\sum_{towers} E_y)^2}$.

the previous centroid of the jet. The resulting jet is stored if it passes
the minimum E_T of jet to be reconstructed ($E_T > 8$ GeV).

- The jet is then compared to the list of previously reconstructed jets to
  determine if it shares towers with any others. If there are any overlaps,
  the E_T's from all the shared towers are added, and compared to the
  E_T of the softer jet. If the shared E_T is greater than half of the E_T
  of the softer jet, the jets are merged into one object. Otherwise, they
  are split into two jets, with each tower being assigned to the jet with
  nearest center. In either case, the jet axis is recalculated one last time,
  including all the appropriate towers without any further iterations.

3.2.6   Jet Energy Calibration

The ambiguities in the definition of jets complicate the calibration of these
objects. For top quark analysis, one would like to identify the energy of
a jet with the energy of the original parton which gave rise to the jet. In
DØ, the calibration to the parton level is carried out in two steps. In the
first step, effects of the calorimeter are corrected for, so that the jet energy
is, on average, that of the final-state particles contained within the jet cone.
This procedure is applied after the reconstruction package (DØRECO) called

CAFIX [54]. The average correction due to the fact that gluons can radiate from the original parton at large angles, causing some energy to fall outside the jet cone, is done after the application of CAFIX.

CAFIX

The CAFIX package corrects the jet energy reconstructed by the reconstruction program (DØRECO) (E_{jet}^{RECO}) for the following effects:

- **Overall hadronic response R_h:**

  Among the factors which may cause R_h to differ from unity are:

  – The extended nature of hadronic showers, which causes some energy to be lost in intermodule cracks or other poorly instrumented regions.

  – Nonlinearity in calorimeter response to sub-10 GeV particles which may be present in the jet.

  – Any difference between the response measured in the test beam and that obtained during data-taking.

- **Underlying Event:**

  Such particles arise, for example, from the fragmentation of spectator

quarks in the collision, and their production is known as the *underlying event.*

- Noise from both electronics and the fission of uranium nuclei in the calorimeter.

- Due to fluctuations in the spatial extent of a hadronic shower, some of the energy of particles within the cone may be deposited in calorimeter cells outside the cone and vice versa.

Once these correction factors have been determined, the corrected jet energy is given by:

$$E_{jet}^{corr} = \frac{E_{jet}^{\text{RECO}} - O}{(1 - S)R_h}, \tag{3.22}$$

where O is the energy independent offset due to noise and underlying event and S is the correction factor for out-of-cone showering. The magnitude of O is taken from a sample of minimum bias events. The energy $\eta - \phi$ area of these events was plotted as a function of η to get the total offset.

In order to separate the contribution from underlying event, which presumably depends on the number of collisions in a beam crossing, from that due to noise, the minimum bias sample was divided into two subsets. The first of these were events for which the Level Ø and tracking information

combined to yield a high probability for the event to contain only one inter-action, while the second had a high probability for multiple interactions. The relatively low instantaneous luminosity at which the sample was recorded ensures that the multiple interaction subsample consists predominantly of events with exactly two interactions.

The average difference in energy per $\eta - \phi$ area for the two subsamples was identified as the contribution to the underlying event from the second interaction in the multiple-interaction sample, and parameterize as:

$$U/\text{event} = (0.310 + 0.034|\eta_d|) \pm 0.2 \text{ GeV/rad}/\eta, \qquad (3.23)$$

where η_d is the pseudo-rapidity of the calorimeter tower containing the jet axis. In applying the correction, one needs to multiply by the expected number of interactions at the instantaneous luminosity for each event, given by:

$$\langle N \rangle = 0.715 \times \dot{\mathcal{L}}(pb^{-1}s^{-1}) \qquad (3.24)$$

The remaining energy in the minimum bias sample after subtraction of the underlying event is identified as the noise contribution and parameterized

as:

$$N = 0.196 + 1.44 \sin \theta_d \; (\text{GeV/rad}/\eta). \tag{3.25}$$

The hadronic response (R_h) is derived from the electromagnetic response using inclusive photon events. Unlike the case for electromagnetic response, there is no reliable source of resonance states. The $W \rightarrow jj$ events are completely overwhelmed by the inclusive dijet events and are practically unobservable.

The inclusive photon events contain a photon recoiling against one or more jets. Such a sample was defined by imposing the trigger requirement that the event contain a photon passing some energy threshold (ranging from 6 to 40 GeV). Additional cuts on the electromagnetic fraction and isolation of the cluster, and which veto the presence of a track (or significant hits in the CDC) in the road leading to the cluster improve the purity of this sample.

Events which contain real neutrinos are a negligible fraction of this sample. Therefore, we have:

$$R_\gamma \vec{E}_T^\gamma + R_h \vec{E}_T^h = -\vec{\not{E}_T}, \tag{3.26}$$

where $\vec{E}_T^h$ is the net unclustered hadronic vector E_T. Using the fact that momentum balance implies $\vec{E}_T^\gamma = \vec{E}_T^h$, and the fact that the electromagnetic calorimeter has been calibrated so that $R_\gamma = 1$, this reduces to:

$$R_h = 1 + \frac{\vec{\slashed{E}}_T \cdot \hat{n}_T^\gamma}{E_T^\gamma}. \tag{3.27}$$

Since the right-hand side depends only on the well-measured photon variables and $\slashed{E}_T$, this allows a direct measure of R_h.

In principle, R_h can be measured as a function of any variable in the event. While it would be convenient to use the measured jet energy as the variable in which to parameterize R_h, the use of a variable with such poor resolution introduces the possibility of bias in the measurement. Hence, the variable chosen is E', which is defined as:

$$E' \equiv E_T^\gamma \cosh(\eta_{jet}), \tag{3.28}$$

which depends only on well-measured quantities.

In addition, it is found that R_h varies strongly as a function of the width of the energy distribution within the jet, with narrower jets having a higher response. Therefore, the response correction is also determined as a function

of the jet width. Adding this variable does not change the average energy scale but should improve the resolution on a jet-by-jet basis.

As most hadronic events do not contain a photon, E' is in most cases undefined. Thus, it is necessary to determine the response as a function of the measured jet energy. In order to do this without introducing bias, the measured jet energy as a function of E' is measured in the inclusive photon sample. Since R_h is known as a function of E', R_h can be found as a function of the measured jet energy.

After applying the corrections for the variation in the response as a function of jet width, the energy dependence is parameterized as:

$$R_h = a + b \ln(E_{jet}^{MEAS}), \qquad (3.29)$$

where $E_{jet}^{MEAS} \equiv E_{jet}^{RECO} - O$, $a = 0.71(0.74)$ and $b = 0.025(0.031)$ for actual (Monte Carlo simulated) events.

The remaining correction factor to be determined, the out-of-cone showering S, depends explicitly on the jet definition used. To measure the magnitude of this effect, a sample of simulated jet events is created. The locations at which the pions and photons in the jets strike the calorimeter are noted, and showers from test-beam pions and electrons of similar energies are placed

at this location. A companion sample is created using the same simulated jets but placing all of their energy in the first struck cell, thus eliminating the out-of-cone showering for this sample. Comparison of the reconstructed jet energies in the two samples allows one to determine the out-of-cone correction. For 0.5 cone jets, it is found that there is 3% loss for low-energy (15 GeV) jets, which decreases to nearly 0% for 50 GeV jets.

The overall jet correction factor $E_{jet}^{corr}/E_{jet}^{RECO}$ varies as a function of jet energy and η. In the central region, it is 95% for low-energy jets, reaches a maximum of 1.18 for jets with E_T about 90 GeV, and falls to an asymptote of 1.13 for extremely high-energy jets, as shown in Figure 3.5.

All of the corrections listed above, save for that due to out-of-cone showering, represent differences between the energies of the particles produced in a $p\bar{p}$ collision and those energies recorded in the calorimeter. This energy must be recovered not only to obtain accurate jet energies, but also accurate $\not{E}_T$. In order to achieve this, the corrections applied to all 0.7 cone size jets in the event are recorded, and the $\not{E}_T$ is changed to reflect the change in the jet energy.
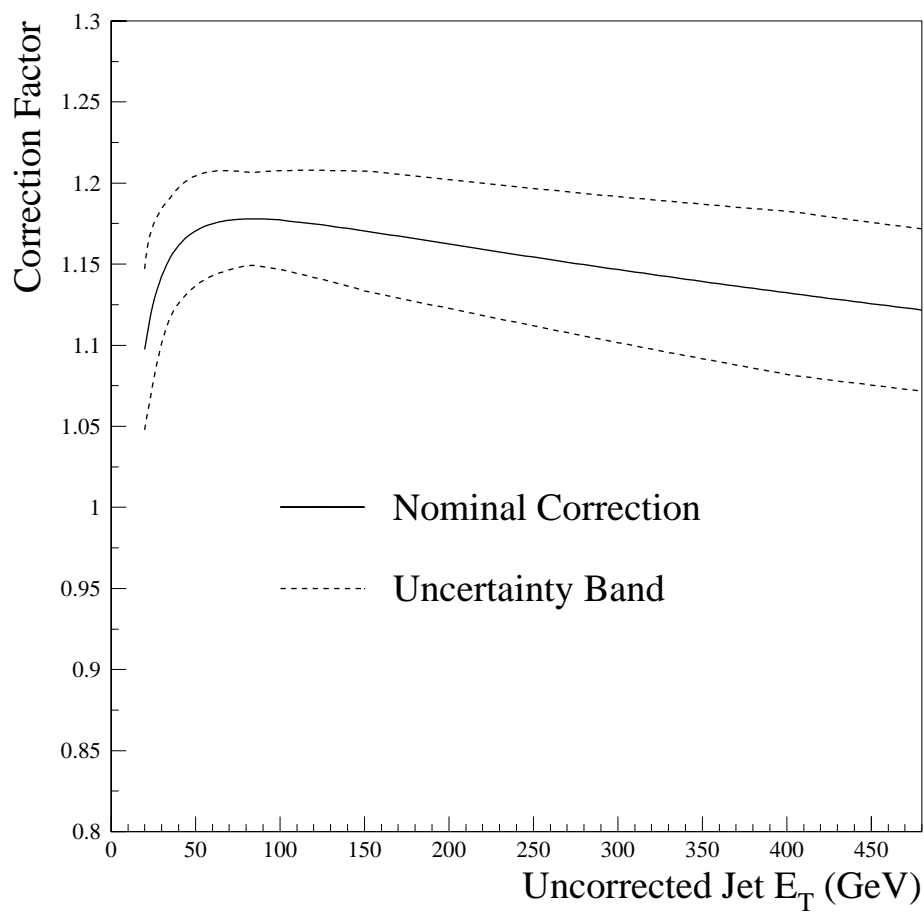
Figure 3.5: Jet correction factor as a function of measured jet transverse energy.

Post-CAFIX Corrections

It is of crucial importance to the top quark analysis that the hadronic energy scale of the DØ detector be reliably modeled by the Monte Carlo. In order to test that the CAFIX corrections meet this criterion, a sample of direct photon events was generated using HERWIG Monte Carlo. The subsample with the photon recoiling against a single reconstructed jet was selected, and the imbalance between jet and photon E_T along the photon direction was recorded. While one should not expect the two objects to exactly balance (it is the entire hadronic recoil, not just that part reconstructed as a jet, which balances the photon), the degree of imbalance should be the same in the Monte Carlo sample and a data sample with identical selection criteria.

It is found that the degree of imbalance is not the same [55]. For jets in the central calorimeter, the discrepancy is small (about 3%), but rises to about 10% for jets in the inter-cryostat and forward regions (Figure 3.6). This is caused by cryostat factor errors and inadequate particle showering correction in the current version of CAFIX. In order to allow the timely completion of the top quark analysis, and also to account as much as possible for our best understanding of the jet energy scale, the decision was made to apply post-CAFIX corrections to account for the discrepancy between data and Monte
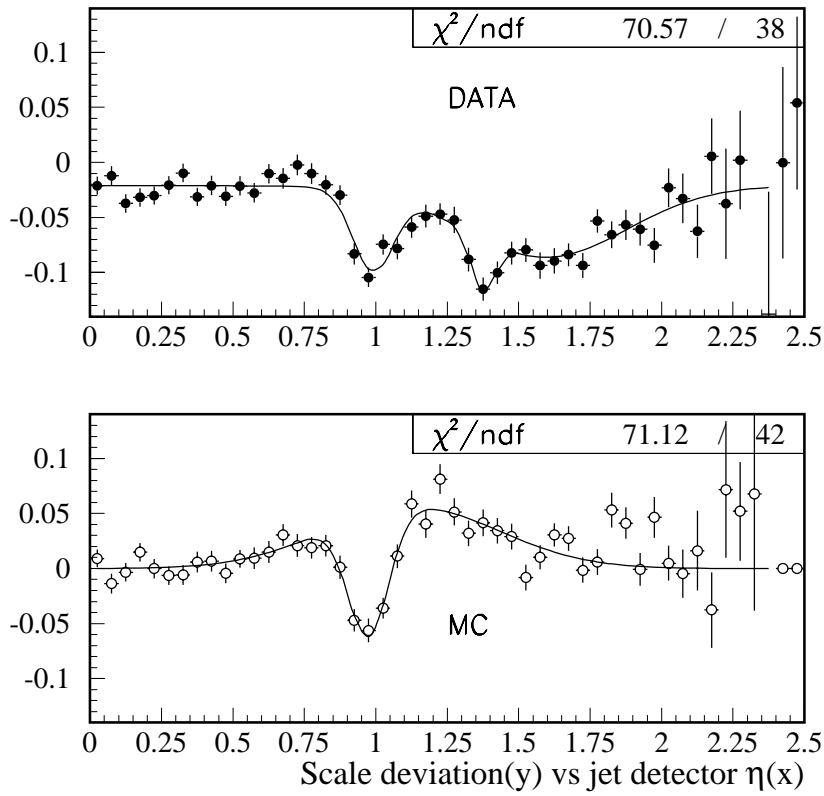
Figure 3.6: Percentage imbalance between photon and jet E_T's for data and Monte Carlo samples. The parameterizations shown area a triple-Gaussian for data and a double-Gaussian for Monte Carlo.

Carlo.

In the dilepton channel analysis, the corrections were applied to the data only, such that the post-correction data would have the same degree of imbalance as the Monte Carlo. The jets in the data are corrected such that

$$
\begin{aligned}
\frac{E'}{E} &= \left(1 - 0.02 - 0.07\exp\left[\frac{\eta_d - 0.99}{0.10}\right]^2 - 0.05\exp\left[\frac{\eta_d - 1.38}{0.06}\right]^2 \right. \\
&\left. \quad -0.06\exp\left[\frac{\eta_d - 1.59}{0.40}\right]^2\right)^{-1}.
\end{aligned}
\tag{3.30}
$$

The degree to which the Monte Carlo and data energies agree after this correction is shown in Figure 3.7.
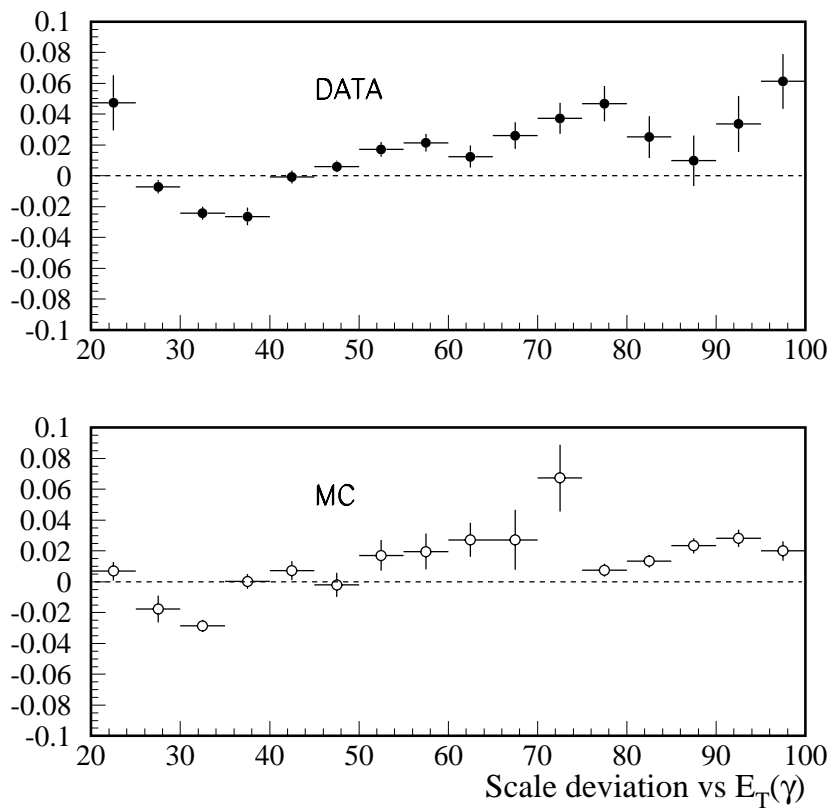
Figure 3.7: E_T balance in data and Monte Carlo direct photon events, after application of the post-CAFIX corrections.

Chapter 4

Top Quark Event Selection

Once the events have been recorded and reconstructed, the task of selecting those that are consistent with $t\bar{t}$ production begins. As most $p\bar{p}$ QCD interactions do not produce high P_T leptons, top events whose decay result in electrons and muons in the final state are easiest to distinguish.

Leptonic decays of $t\bar{t}$ are divided into two categories: the lepton plus jets and dilepton channels. The former has the advantage of a large branching fraction and accounts for about 30% of all $t\bar{t}$ decays, with the disadvantage that electroweak processes (such as $W+jets$ events) or detector misidentification of final state particles can mimic the $t\bar{t}$ signal relatively frequently. The dilepton channels have far lower background, but suffer from small branching fraction, accounting for only 5% of all decays.

4.1 Data Sample

The data used in this analysis were collected between years 1992 and 1996. The total effective luminosity is not identical for all top decay channels for the following reasons.

1. The muon triggers were not fully efficient at the beginning of the run, leaving the channels which require only muons with slightly less luminosity.

2. The analyses of different channels place different cuts on the type of background caused by Main Ring activity allowed.

3. The last period of running in early 1996 is not included by some analyses. Nonetheless, all channels have an integrated luminosity greater than $100\ pb^{-1}$ (Table 4.1).

4.2 Event Cleanup

In order to ensure that the $t\bar{t}$ sample is not contaminated by events arising from detector pathologies, several steps are taken to remove these events. A list of runs with known problems is kept, and no events from these runs are admitted to the sample.

Channel	Luminosity (pb^{-1})
ee	125.3
$e\mu$	108.3
$\mu\mu$	104.5
e + jets (topol.)	115.0
e + jets (μ-tag)	103.7
μ + jets (topol.)	108.3
μ + jets (μ-tag)	104.0

Table 4.1: Integrated luminosity for each of the $t\bar{t}$ decay channels in Run I. There is a 5.3% uncertainty in the luminosity measurement.

Events which were recorded when the beam was present in the Main Ring (MRBS or MICRO_BLANK windows) are processed further to remove Main Ring energy depositions and were included in the cross section analysis for some of the decay channels. However, due to the degradation in jet and $\not{E}_T$ resolution introduced by this procedure, such events are not used in this analysis.

As a general cleanup procedure during reconstruction, isolated cells with large hadronic deposits are removed, since such deposits are likely to arise from a hardware problem (a "hot cell"). The algorithm defines isolation by comparing the energy in a given cell with that in its longitudinal, but not transverse, neighbors. This can lead to the improper removal of energy from a jet, and give rise to a false $\not{E}_T$ signature. Events in which a cell within a jet was removed are retained only if they would have passed the

$\not{E}_T$ cut regardless of the hot cell. In addition, the events are passed through the reconstruction program with the hot cell removal disabled in order to calculate the proper jet energy for top quark mass analysis, with which this analysis closely follows.

Finally, there are two events which have, in addition to the final state objects expected from $t\bar{t}$ decay, a good photon candidate. Such events are retained in the cross section analyses, but rejected in the mass analyses and this analysis as there is no kinematic hypothesis for the presence of a photon.

4.3   Dilepton Channels

While the branching fraction to dileptons is small, there are also relatively few background processes which produce two leptons in association with significant jet and $\not{E}_T$, thus allowing for identification of these events with a reasonable signal-to-background ratio. The backgrounds come from a variety of processes, none of which has a large cross section. The importance of any given background source depends on the channel being considered.

The kinematic selection criteria of dilepton events which is designed to isolate events with the expected final-state signature is described below,

- *ee* **channel:**

- 2 electrons with $E_T > 20$ GeV and $|\eta| < 2.5$

- ≥ 2 jets with $E_T > 20$ GeV and $|\eta| < 2.5$

- $\not{E}_T > 25$ GeV

- $H_T^e > 120$ GeV

- $e\mu$ **channel:**

    - 1 isolated electron with $E_T > 15$ GeV

    - 1 isolated muon with $p_T > 15$ GeV/c

    - ≥ 2 jets with $E_T > 20$ GeV and $|\eta| < 2.5$

    - $\not{E}_T > 10$ GeV and $\not{E}_T^{cal} > 20$ GeV ($\not{E}_T$ refers to the missing E_T including the muon momentum with calorimeter missing E_T.)

    - $H_T^e > 120$ GeV

- $\mu\mu$ **channel:**

    - 2 isolated muons with $p_T > 15$ GeV/c

    - ≥ 2 jets with $E_T > 20$ GeV and $|\eta| < 2.5$

    - $H_T > 100$ GeV

In order to identify muons, an isolation cut is applied in addition to the idenfication criteria described in Chapter 3. A muon is defined as isolated if

Background Processes	ee	$e\mu$	$\mu\mu$
$Z \to \ell\ell$	0.058 ± 0.013	N/A	0.56 ± 0.22
$Z \to \tau\tau \to \ell\ell$	0.078 ± 0.025	0.099 ± 0.076	0.03 ± 0.02
W pair production	0.083 ± 0.026	0.074 ± 0.019	0.007 ± 0.004
Drell-Yan	0.054 ± 0.033	0.002 ± 0.003	0.07 ± 0.03
Instrumental backgrounds	0.197 ± 0.052	0.04 ± 0.13	0.07 ± 0.03

Table 4.2: Number of background events expected in each dilepton channel from various sources.

there is no jet reconstructed within $\Delta R = 0.5$ of the muon in η–ϕ.

H_T and H_T^e are defined as:

$$H_T \quad = \sum_{E_{T\,jets}>15GeV} E_T, \tag{4.1}$$

$$H_T^e \quad = \quad H_T + E_T(\text{leading electron}). \tag{4.2}$$

Especially, H_T^e is found to be a good rejection of background processes. The muon p_T is not included in the sum due to its poor resolution ($\delta p/p > 18\%$). Therefore 100 GeV cut on the H_T for dimuon channel is more restrictive than the 120 GeV cut placed on H_T^e for electron channels.

The number of background events expected from the dominant sources in each dilepton channel after the selection cuts are applied, is given in Table 4.2 [59, 60].

4.3.1 ee Channel

Primary source of background comes from Z boson plus multijet productions, where Z decays into dielectrons. The underlying physics will not produce any missing momentum and E_T imbalance in this case is caused by the fluctuations of measured energies due to finite resolution. Therefore, $\not{E}_T$ cut is effective at reducing the background from this source. To even further reject Z boson events without appreciably reducing $t\bar{t}$ acceptance, the event is required to have $\not{E}_T > 40$ GeV if the reconstructed dielectron invariant mass is within $12\,\mathrm{GeV/c^2}$ of the known Z mass of $91.2\,\mathrm{GeV/c^2}$.

$Z \to ee$ background is estimated from the data. From a sample of multijet events, one selects those most compatible with the kinematic cuts imposed in the $t\bar{t}$ selection, and calculates the fraction passing the $\not{E}_T$ cut. This measures the fraction of the time that detector resolution will produce a false $\not{E}_T$ signal. Then, one considers the total dielectron data sample which passes all selection criteria except for the $\not{E}_T$ cut. Multiplying this number by the probability for an event to give a false $\not{E}_T$ signal yields the total number of $Z \to ee$ events one expects to see in the signal region, which is 0.058 ± 0.013 events.

Another way Z can mimic the signal is through $Z \to \tau\tau \to ee$. As

this mode is difficult to identify in the data, one relies on a Monte Carlo simulation to estimate the rejection power of the kinematic cuts against this background. Multiplying this efficiency by the known Z production cross section times $Z \rightarrow \tau\tau \rightarrow ee$ branching ratio gives the number of events expected from this background (0.078 ± 0.025 events).

The Drell-Yan production is another background, the absolute number of expected background events from this channel is estimated using the DØ measured cross section value in the range of $30 < m_{ee} < 60\,\mathrm{GeV/c^2}$, divided by the fraction of Monte Carlo events that fall into this range (0.054 ± 0.033 events).

The last source is the diboson WW production, where a theoretical calculation of the cross section is used. Monte Carlo event kinematics are used to investigate the rejection power of selection criteria (0.083 ± 0.026 events).

There are instrumental backgrounds to this channel besides the physics backgrounds. $W +$ jets events can look like the signal if one of the jets mimic an electron in our detector and W decays into an electron and a neutrino. Another case would be in the multijets final state production where two jets are misidentified as electrons. To study this effect, from a parent sample containing two electromagnetic jets, events where one of the electromagnetic objects is identified as electron are selected. Then, the second electromag-

netic jet is treated as an electron and all of the kinematic cuts are applied. The number of events in this sample is multiplied by the probability that a jet will pass the electron ID criteria, given that the jet has large electromagnetic content to give the absolute number of 0.197 ± 0.052 events.

The total background is 0.41 ± 0.08 events after correcting for the effective luminosity which is lost by beam related background rejection.

One particular event (Run 95653, event 10822) has two electromagnetic objects, two jets and significant $\not{E}_T$. One of the elctromagnetic objects is identified as an electron, while the other is identified as a photon as there was no reconstructed track pointing to it. A line projecting from the event vertex to te center of the electromagnetic cluster identified as photon, reveals that the line traverses only the two inner layers of the CDC. The hits in the CDC layer points to the electromagnetic cluster and TRD information is consistent with that of an electron. However, the even reconstruction program does not form one or two layer CDC hits into tracks, and thus this particular object looked as if it had no tracks associated with the electromagnetic cluster and therefore was identified as a photon. If the "photon" is reinterpreted as an electron, the event passes all the selection criteria. In addition, a soft muon is associated with a jet, thus strengthening the case that this is a $t\bar{t}$ event. The background due to extension of selection cuts is 0.06 events.

There are 3 *ee* events that pass the selection criteria with an expected background of 0.47 ± 0.09

4.3.2 *eμ* Channel

eμ channel has twice the branching fraction of the *ee* and *μμ* channels. And it is also free of much background from Z decay. The largest background is $Z \rightarrow \tau\tau \rightarrow e\mu + X$, which is suppressed by both branching fraction and kinematics (0.099 ± 0.076 events). Additional physics backgrounds arise from W pair production and other rarer sources. The level of background from these sources are calculated beginning with a measured cross section and scaled down by the efficiency for Monte Carlo events of that source to pass the selection criteria and by the particle identification and trigger efficiencies. In case of W pair production, cross section from a theoretical prediction is used. The number of expected background events from diboson production is 0.074 ± 0.019.

Instrumental backgrounds arise from W bosons that decay to $\mu\nu$ which are produced in association with jets, one of which is mistaken for an electron. The background is estimated by multiplying the number of W plus three or more jet events (where one of the jets has $f_{EM} > 0.9$) by the probability that

such jets would pass the electron identification criteria, resulting in 0.04 ± 0.13 events. Three events remain with the background of 0.21 ± 0.16 events.

4.3.3 $\mu\mu$ Channel

The relatively poorer muon momentum resolution compared to the energy resolution of electron means that the separation of $t\bar{t}$ signal from background from Z decay is more difficult than that of dielectron channel. In order to reduce this background, a kinematic fit to the $Z \to \mu\mu$ hypothesis is applied, and the event is required to have χ^2 probability less than 1% for this fit [58].

The estimation of background is determined from the application of the fit to the Monte Carlo $Z \to \mu\mu$ samples. During the Monte Carlo event generation, some cuts are applied at the generation stage, such as minimum p_T of the Z or requiring 2 final state partons in the calculation. Rather than relying completely on the cross section from calculation, similar cuts are applied to $Z \to ee$ event sample, and scaling the well-measured inclusive Z production cross section by the fraction of events which pass the cut. The $Z \to \mu\mu$ background is the most significant of all the background channels contributing 0.56 ± 0.19 events. An identical procedure is used to estimate the contribution from $Z \to \tau\tau \to \mu\mu$ events, yielding 0.03 ± 0.02 events.

Channel	Events observed	Expected background
ee	2	0.47 ± 0.09
$e\mu$	3	0.21 ± 0.16
$\mu\mu$	1	0.73 ± 0.25

Table 4.3: Number of events observed and expected backgrounds in the dilepton channels from Run I.

The level of the remaining physics backgrounds ($WW \rightarrow \mu\mu + X$, Drell-Yan), are determined solely from Monte Carlo acceptance multiplied by the theoretical cross section (0.07 ± 0.03).

Instrumental backgrounds arise from heavy quark jets with a high-p_T muon that is misidentified as an isolated muon. The number of events with a muon and 3 jets that pass the cut are counted and then the probability of each jet to appear as an isolated muon is used to arrive at the final number of 0.07 ± 0.03 events.

One event is seen in this channel, with the expected background of 0.73 ± 0.25 events.

Total number of events and the backgrounds in each channel are summarized in Table 4.3

Chapter 5

Analysis

5.1 Framing the problem

The degree of spin correlation between t and $\bar{t}$ is contained mainly in the angular correlation between the two leptons in dilepton events (both Ws decaying leptonically, $W^+ \rightarrow \bar{l}\nu$) or the lepton and a down-quark jet in $l + jets$ events (one W decaying leptonically). However, in light of the difficulty of identifying down-jets, we will restrict our discussion to events in the dilepton channels. It is best to identify the decay products and associate them either with the top or an anti-top in any event. But, as will be shown, the distinction between a top or an anti-top is not important. The quantity we are interested in is the angle between the direction of flight of
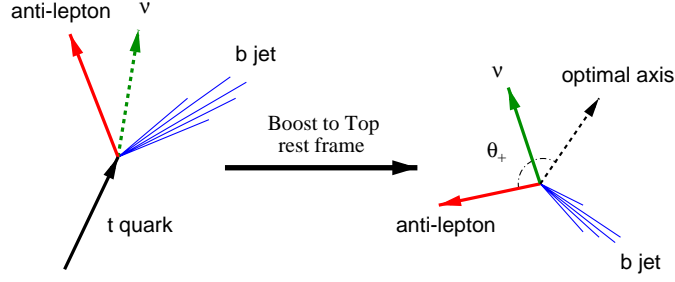
Figure 5.1: The angle θ_+ is defined by the direction of the lepton relative to the quantization axis, with all the vectors transformed into the rest frame of the top quark.

the lepton and the quantization axis of choice in the rest frame of the top quark. Let us call the angles θ_+ and θ_- for top and anti-top, respectively (Figure 5.1). By examining $\cos\theta_+$ vs $\cos\theta_-$, one can infer the existence of any spin correlations. Shown in Figure 5.2 are 2-dimensional density plots of $\cos\theta_+$ vs $\cos\theta_-$ expected for uncorrelated and for correlated $t\bar{t}$ systems. A special-purpose event generator using the fully correlated decay matrix, $\mathcal{M}(p\bar{p} \to t\bar{t} \to b\bar{b}W^+W^- \to b\bar{b}l\bar{l}\nu\bar{\nu})$, was written to generate the correlated distributions, but the decay products were analyzed at the generator level, which assumes complete information about all the final-state particles.

The differential decay rate of the top quark can be parametrized as [25]

$$\frac{1}{\Gamma}\frac{d^2\Gamma}{d(\cos\theta_+)d(\cos\theta_-)} = \frac{1 + \kappa\cos\theta_+\cos\theta_-}{4}. \tag{5.1}$$

The spin-correlation coefficient is denoted κ, and represents the degree to which spin correlation is present in a particular spin quantization axis. κ represents fractional difference between the number of "like" spin events and the number of "unlike" spin events.

$$\kappa = \frac{N_{like} - N_{unlike}}{N_{like} + N_{unlike}} \qquad (5.2)$$

κ is bounded between -1.0 and 1.0, with $\kappa = 0$ for uncorrelated events and $\kappa = 0.51$, 0.80 and 1 for correlated systems in the helicity, beamline and off-diagonal basis, respectively, when only $q\bar{q}$ contributions are included. When the gg contributions are added κ becomes 0.40, 0.68 and 0.88. Since the differential cross section is symmetric about $\theta_+ = \theta_-$, it is not crucial to distinguish between top and anti-top. This is fortunate because DØ does not have a central magnetic field to identify charge of the electron.

From the differential cross section, one can see that extracting κ is effectively a one-dimensional problem, with $\xi = \cos\theta_+ \cos\theta_-$ as a single variable. The spin correlation shows up as an asymmetry in the distribution $d\sigma/d(\cos\theta_+ \cos\theta_-)$ about $\cos\theta_+ \cdot \cos\theta_- = 0$ (Figure 5.3). The asymmetry
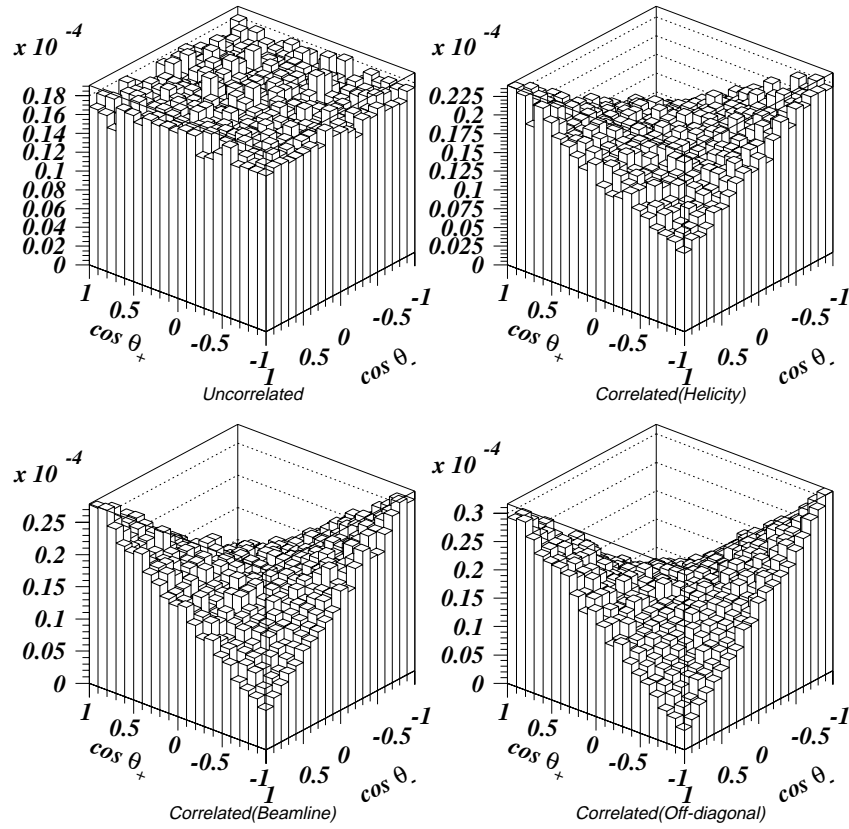
Figure 5.2: Probability density for $\cos\theta_+$ vs $\cos\theta_-$ for uncorrelated $t\bar{t}$ events (top left) and for correlated $t\bar{t}$ events, as observed in the helicity basis (top right), beamline basis (bottom left) and off-diagonal basis (bottom right). Results are shown prior to application of any data-selection criteria.

can be defined as

$$
\begin{aligned}
\mathcal{A} &= \frac{1}{N} \int_0^1 \frac{dN}{d(\cos\theta_+ \cos\theta_-)} d(\cos\theta_+ \cos\theta_-) \\
&\quad - \frac{1}{N} \int_{-1}^0 \frac{dN}{d(\cos\theta_+ \cos\theta_-)} d(\cos\theta_+ \cos\theta_-) \\
&= \frac{\kappa}{4},
\end{aligned} \tag{5.3}
$$

where N is the total number of events.

Being directly proportional to κ, the asymmetry parameter contains all the information about the correlation coefficient κ at least for perfect resolution.

The above relation between κ and $\mathcal{A}$ is correct as long as the detector has full acceptance, full efficiency for all particles, and the dilepton events are fully reconstructed unambiguously. For the case of DØ, it is therefore necessary to investigate the effects of finite acceptance and any selection criteria that are applied to the events, and also the effects from the fitting technique employed in the reconstruction of dilepton events.

The effect of energy smearing due to finite resolution, and imposition of experimental selection criteria, at the generator level, is shown in Figure 5.4. The extracted values of $\mathcal{A}$ are shown in Table 5.1. Resolution smearing and the imposition of selection criteria dilute the correlations a little, and the
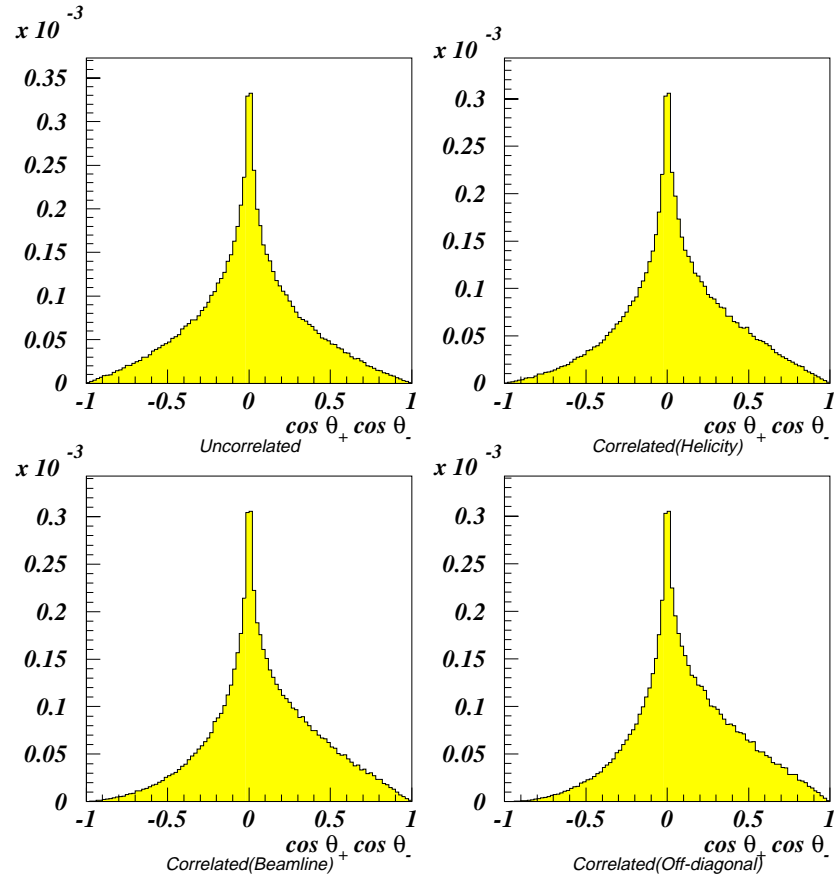
Figure 5.3: Plots of distribution in the product $\cos\theta_+ \cdot \cos\theta_-$ prior to imposition of selection criteria and resolution smearing.

	$\mathcal{A}$ before cuts and smearing	$\mathcal{A}$ after cuts and smearing
Uncorrelated	0.0	0.0
Correlated (Helicity)	0.10	0.10
Correlated (Beamline)	0.17	0.14
Correlated (Off-diagonal)	0.22	0.19

Table 5.1: Effects of selection criteria and energy resolutions on asymmetry $\mathcal{A}$. These include gg contributions.

simple linear relation between κ and $\mathcal{A}$ no longer holds.

5.2 Reconstruction of Dilepton Events

Because using $l + jets$ events requires the identification of the down quark, which is very difficult, only top events in dilepton channels are used in this analysis. The charged leptons are most sensitive to $t\bar{t}$ spin information, and are easy to identify. There are also fewer possible combinations associated with identifying a b-jet than in $l + jets$ channels, since there are only 2 jets per event to leading order. Also, there is far less background in the dilepton channels than in $l + jets$ channels, thereby simplifying background subtraction. The disadvantage of using these channels is that the statistics are poor (3 eμ, 2 ee and 1 $\mu\mu$ events). Also, there are 2 neutrinos in an event that must be reconstructed in order to establish the 4-vector of the top
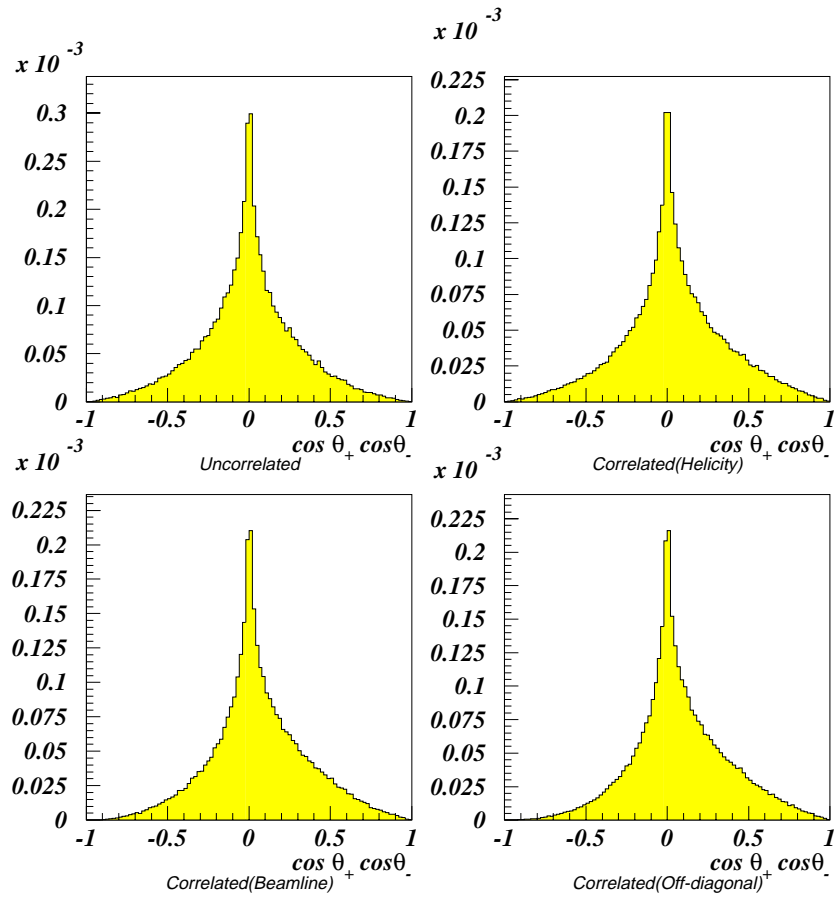
Figure 5.4: Distributions in the product of $\cos\theta_+ \cdot \cos\theta_-$ after resolution smearing and application of acceptance criteria to $t\bar{t}$ Monte Carlo events at the generator level.

quark, which is needed to boost the daughter particles to the top rest frames for calculating the angles of interest, θ_+ and θ_-.

The ν-weighted event fitter developed by Strovink and Varnes[59] is applied to the 6 dilepton events with the constraint of $m_t = 175\,\text{GeV}$. The system then becomes soluble with zero constraints. Rather than using the measured value of missing E_T, the event fitter scans the rapidities of the 2 neutrinos, and returns the likelihood of each solution by comparing the resulting missing transverse momentum with the measured value. The unknowns in this system are 2 neutrino 3-momenta, which makes it 6 unknowns. The constraints are

$$(l_1 + \nu_1)^2 = M_W^2 \tag{5.4}$$

$$(l_2 + \nu_2)^2 = M_W^2 \tag{5.5}$$

$$(l_1 + \nu_1 + b_1)^2 = M_{top}^2 \tag{5.6}$$

$$(l_2 + \nu_2 + b_2)^2 = M_{top}^2 \tag{5.7}$$

$$\eta_{\nu 1} = \eta_1 \tag{5.8}$$

$$\eta_{\nu 2} = \eta_2 \tag{5.9}$$

where the l_i, ν_i and b_i refer to four-momenta of the charged leptons, neutrinos

and b jets respectively, and the η_i are the values of pseudo-rapidities of the neutrinos sampled in the calculation of the solutions.

The logical flow of the neutrino weighting method is as follows:

1. Assume $\eta_{\nu 1} = \eta_1 \ \eta_{\nu 2} = \eta_2$, where η_1 and η_2 are sequentially scanned at discrete points in rapidity. The sampling points are determined by the shape of the neutrino rapidity distribution, which is reasonably parameterized by gaussian (Figure 5.5) whose width is given as

$$\sigma_\eta(m_t) = 5.56 \times 10^{-6} m_t^2 - 2.16 \times 10^{-3} m_t + 1.314. \qquad (5.10)$$

2. System of equations is solved and either 0 or 4 solutions are returned. The weight of each solution is given by:

$$\mathcal{L} = \prod_{k=x,y} \exp\left[-\left(\frac{\not{E}_k - p_k(\nu\nu)}{2\sigma^2(\not{E}_k)} \right) \right]. \qquad (5.11)$$

3. With the neutrino momentum explicitly reconstructed, the information can be used to boost the decay products to the rest frame of the top quark and calculate θ_+ and θ_-. The θ_+ and θ_- are used to fill histograms with weights returned by the equation above.
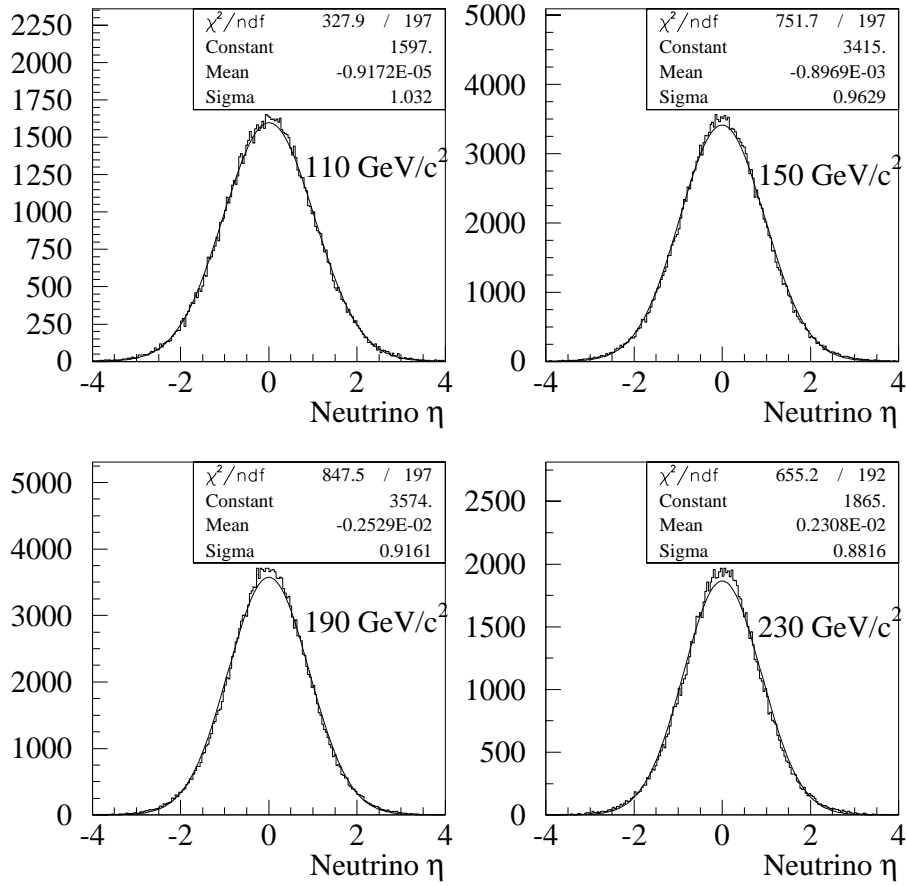
Figure 5.5: Neutrino rapidity distribution for various assumed top masses.
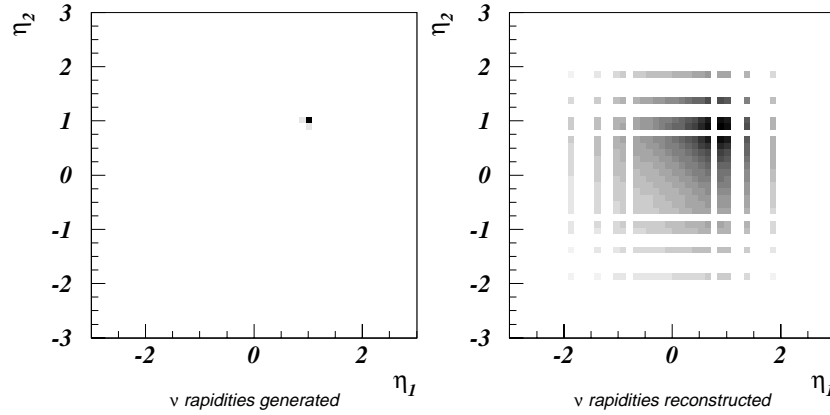
Figure 5.6: Left: Rapidity of neutrinos at the generator level; Right: Rapidities of neutrinos returned from the event fitter.

4. Permute the leptons assigned to the jets and repeat the steps 2 and 3

5. Scan η_1 and η_2 and repeat steps 2-4

6. The measured energies of jets and leptons are smeared and steps 1-5 are repeated.

Figure 5.6 shows the reconstructed rapidities of neutrino for events generated with neutrino rapidities $\eta_1 = \eta_2 = 1$. The histogram is filled with weights returned from the event fitter.

We could choose to smear the events from Monte Carlo simulation and compare it with the data, or alternatively "unsmear" the data and then

Event	Event	Bases			
	type	Helicity	Beamline	Diagonal	Diagonal $(M_t = 170 \text{ GeV})$
10822	ee	-0.06	-0.03	0.34	0.26
12814	$e\mu$	0.80	-0.15	-0.16	-0.20
15530	$\mu\mu$	-0.11	-0.14	0.50	0.53
26920	$e\mu$	-0.02	0.90	0.85	0.85
30317	ee	0.11	0.74	0.52	0.58
417	$e\mu$	0.84	0.24	-0.19	-0.23
$\mathcal{A}$		0.26	0.26	0.31	0.30

Table 5.2: The asymmetry $\mathcal{A}$ for the 6 dilepton events smeared 2000 times. The numbers in the last column are asymmetry values when the events are analyzed assuming $M_t = 170 \text{GeV}$.

compared this with results of Monte Carlo. By using the ν-weighting scheme, we have essentially opted for the latter method. The only information we use in our analysis corresponds to the measured angles, energies and resolutions. By forcing the kinematics of the events to be consistent with those of top-like events and fixing the top mass, we are selecting at the most likely event parameters.

Figure 5.7 shows the likelihood as a function of the top mass for our six dilepton events [59]. Assuming $m_t = 175 \text{ GeV/c}^2$, each dilepton event is smeared 2000 times, and the likelihood for all solutions are used as the weight in the distribution for $\cos\theta_+ \cdot \cos\theta_-$ shown in Figures 5.8, 5.9 and 5.10, in three spin bases respectively. Table 5.2 summarizes the results.
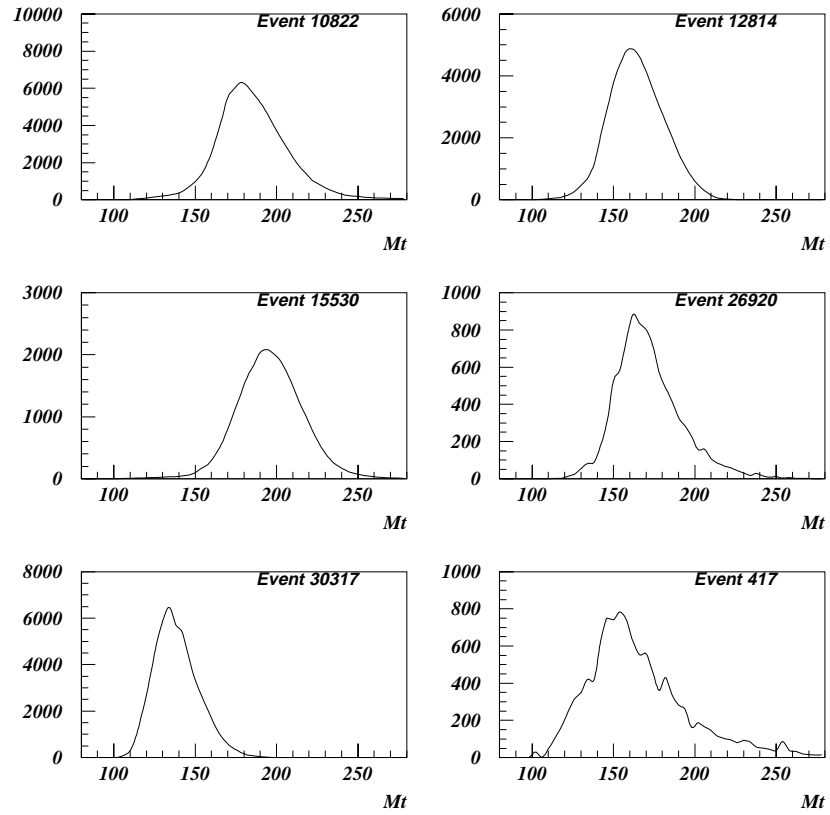
Figure 5.7: Likelihood returned from the event fitter, as a function of the top mass, for the 6 events in the dilepton channels.
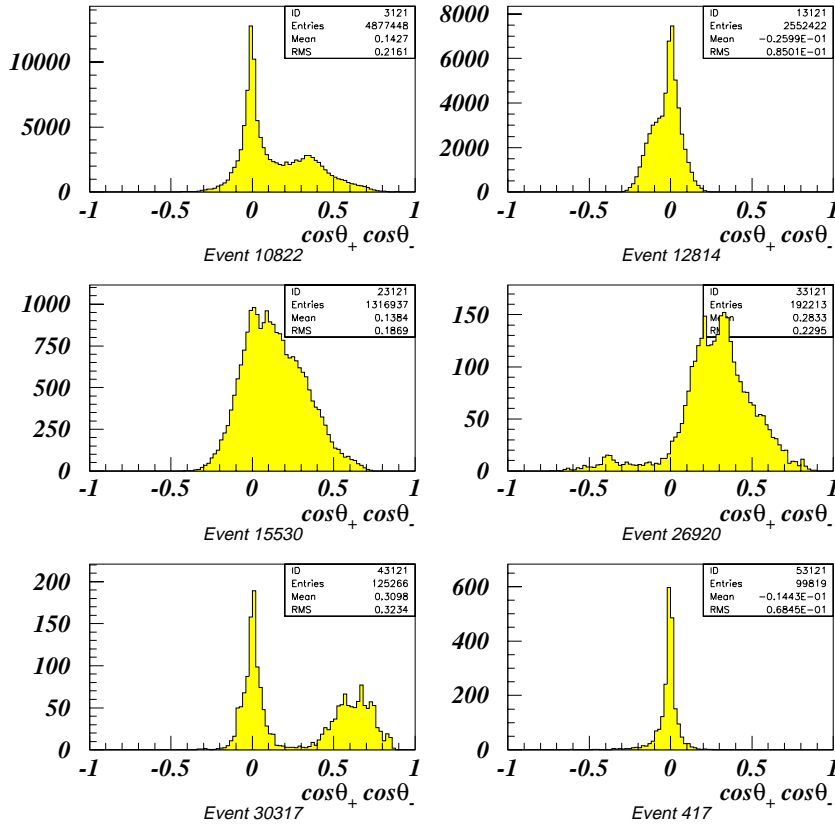
Figure 5.8: Likelihood as a function of the product of $\cos\theta_+ \cdot \cos\theta_-$ in the off-diagonal basis for event number 10822(0.34), 12814(-0.16) 15530(0.53), 26920(0.85), 30317(0.58), and 417(-0.23). Where the numbers in parentheses are the Asymmetries.
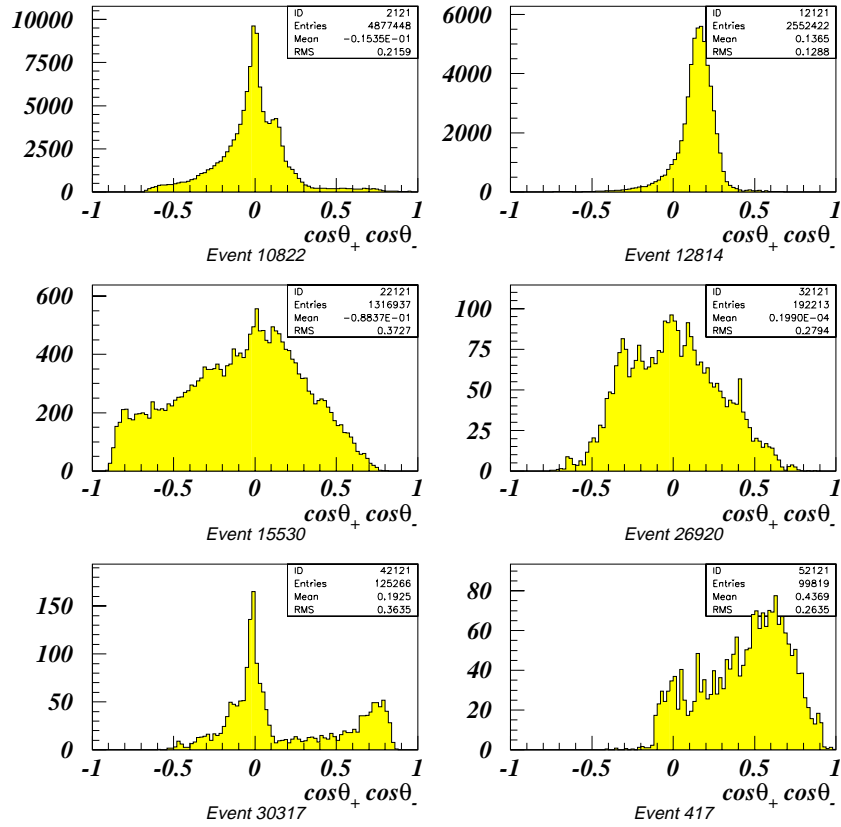
Figure 5.9: Likelihood as a function of the product $\cos\theta_+ \cdot \cos\theta_-$ in the helicity basis for event number 10822(-0.06), 12814(0.80) 15530(-0.11), 26920(-0.02), 30317(0.11), and 417(0.84). Where the numbers in parentheses are Asymmetries.
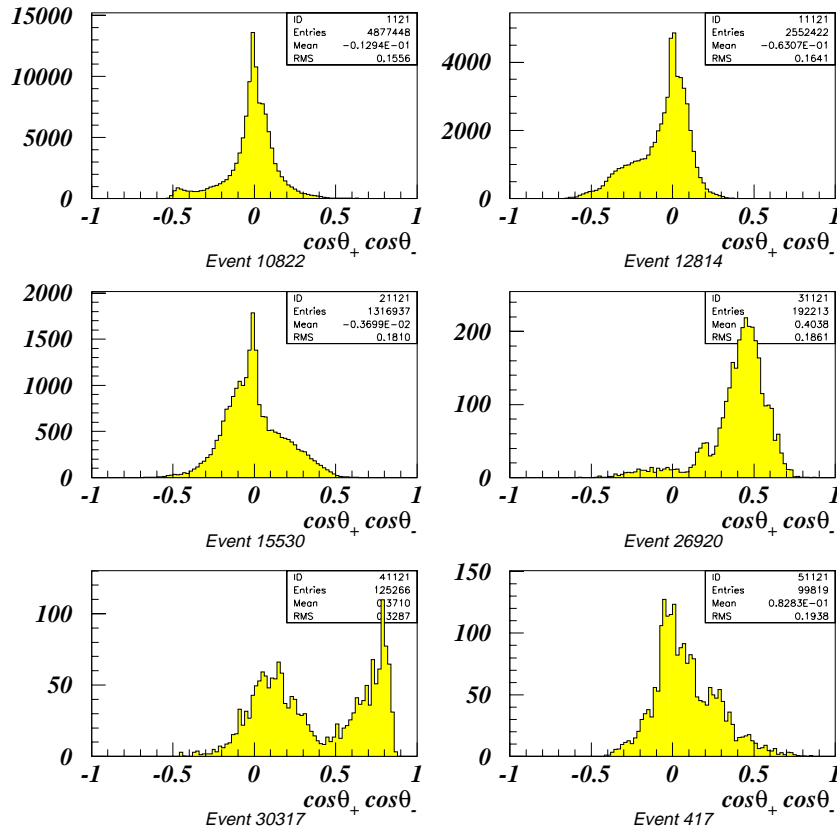
Figure 5.10: Plots of $\cos\theta_+ \cdot \cos\theta_-$ in the beamline basis for event number 10822(-0.03), 12814(-0.15) 15530(-0.14), 26920(0.90), 30317(0.74), and 417(0.24). Where the numbers in parentheses are Asymmetries.

5.3   Description of Spin Correlated

Monte Carlo

The event generators frequently used to generate $t\bar{t}$ events like HERWIG [61] and PYTHIA [62] do not use spin-correlated matrix elements. For this study, I have developed an event generator that uses Kleiss and Sterling's fully correlated matrix element including decays [63]. For the phase space generator, I have used was RAMBO [64]. Incorporated into the generator are also the structure function and sampling of parton momenta(x1, x2) from DYRAD Monte Carlo program [65].

The presence of spin correlations does not affect individual spectra of transverse energy or angular distribution of any single particle. Therefore, spin correlation does not affect the measurement of the top quark mass [66]. Figure 5.11 shows charged lepton E_T distributions from spin-correlated Monte Carlo and PYTHIA and their ratios. Plots from the original calculations [25, 67] are reproduced in Figure 5.12.
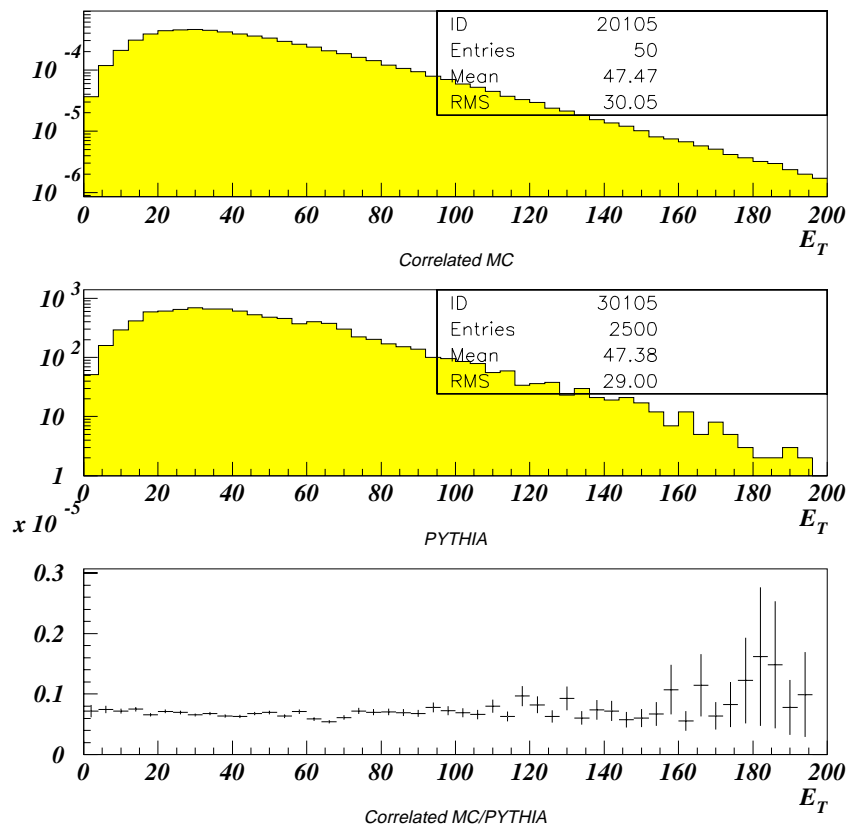
Figure 5.11: Charged lepton E_T distributions from spin-correlated Monte Carlo (top), PYTHIA (middle) and their ratios (bottom).
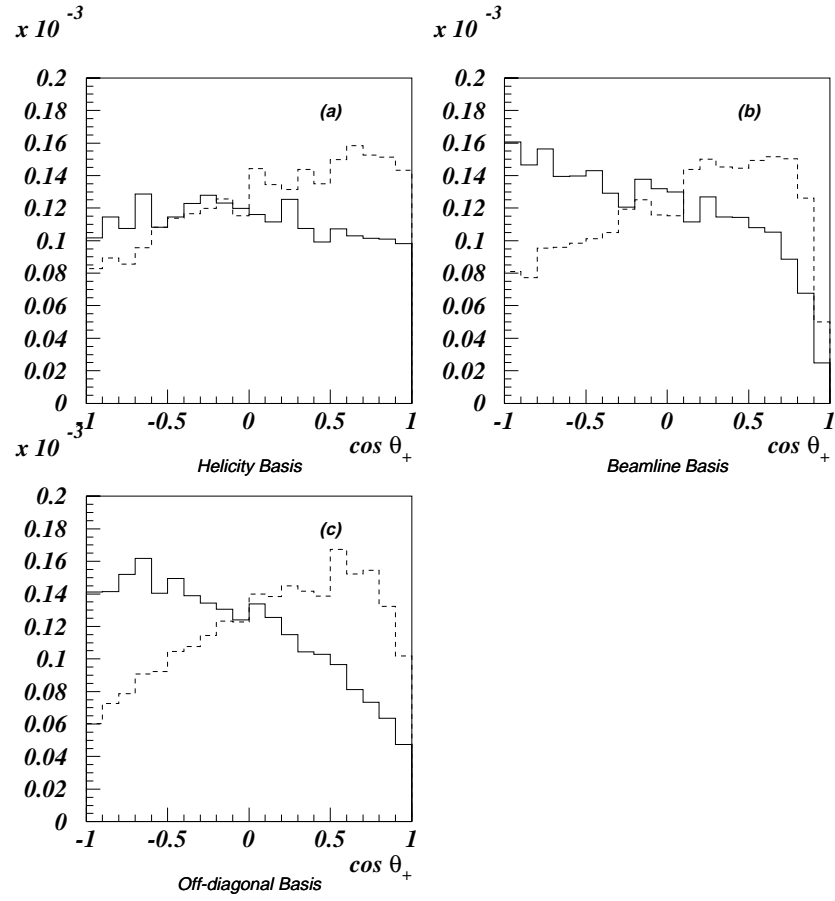
Figure 5.12: Distribution of $\cos\theta_+$ for $\cos\theta_- > 0$ (solid) and $\cos\theta_- < -$ (dashed) in (a) helicity basis, (b) beamline basis and (c) off-diagonal basis.

5.4 Expectations from Monte Carlo

5.4.1 Strategy of Analysis

Because there is no clear way to choose the "correct solution" for any event, it is best to use the distributions in Figures 5.8, 5.9 and 5.10 to characterize the data and to calculate $\mathcal{A}$ from Equation 5.3, after normalizing the distribution for each event to unity. This is a viable way of proceeding because, on the basis of Monte Carlo studies, we have found that the distribution of such reconstructed $\cos\theta_+\cos\theta_-$ values is strongly correlated with the generated $\cos\theta_+\cos\theta_-$.

Figure 5.13 shows the clear correlation between $\cos\theta_+ \cdot \cos\theta_-$ at the generator level versus the mean of the reconstructed values in the off-diagonal basis. In an ideal world, where we have perfect information, $\mathcal{A}$ would be either 1 or -1 for an event since $\cos\theta_+\cos\theta_-|_{gen.}$ can only be either greater or less than zero on an event by event basis. Only when there is sufficient statistics, does $\mathcal{A}$ approach $\kappa/4$. Under current circumstances, where information is diluted, Figure 5.14 shows that the calculated value of $\mathcal{A}$ is still sensitive to the presence of spin correlation.

Table 5.1 suggests that, from naive considerations, the value of asymmetry ($\mathcal{A}$) is expected to be 0.10, 0.14, and 0.19 for the asymmetry($\mathcal{A}$) value
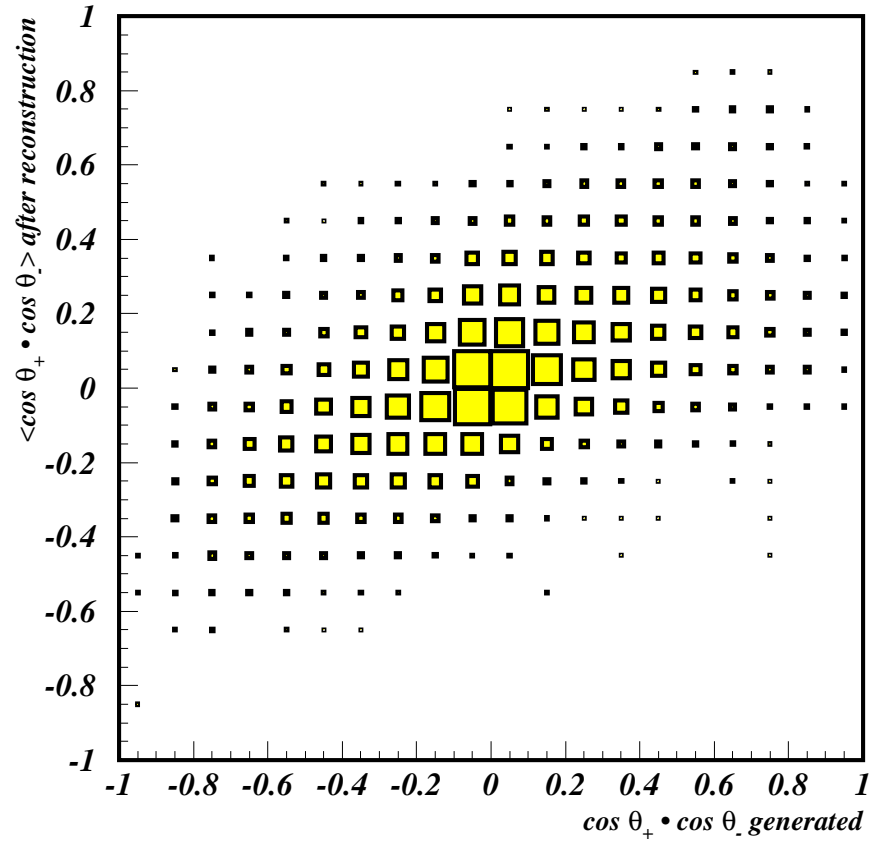
Figure 5.13: Value of average $\cos\theta_+\cos\theta_-$ after fitter reconstruction versus $\cos\theta_+\cos\theta_-$ at the generator level after imposition of acceptance criteria versus the average of the distribution after fitter reconstruction for dilepton events. One can see a definite correlation in the scatter plot.
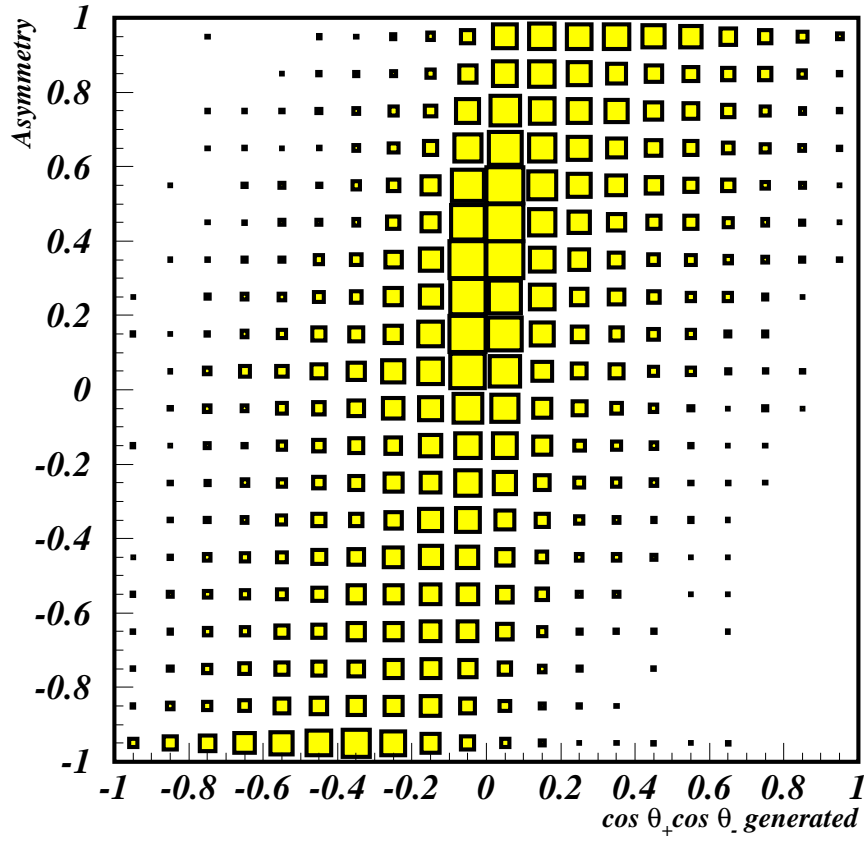
Figure 5.14: Value of $\cos\theta_+ \cos\theta_-$ at the generator level versus $\mathcal{A}$ calculated from the distribution of $\cos\theta_+ \cos\theta_-$ after fitter reconstruction. Ignoring acceptance and resolution, for any given event, we would get only $\mathcal{A} = -1$ for $\cos\theta_+ \cos\theta_- < 0$ and $\mathcal{A} = 1$ for $\cos\theta_+ \cos\theta_- > 0$.

in the helicity, beamline, and off-diagonal bases respectively. Correct estimate can be obtained by generating ensembles of 6 events and passing these through the event fitter. This was done using 40,000 events generated for each channel. Figures 5.15, 5.16 and 5.17 show distributions in $\mathcal{A}$ per event for the three channels, for different choices of quantization axes. It is clear that the off-diagonal basis provides the most sensitive choice.

To generate the ensembles of 6 dilepton events (2 ee, 3 eμ and 1 $\mu\mu$), events were selected randomly in proper proportion from the above asymmetry distributions. The background was admitted with the probability 1.4/6. The background samples used were those that were used in estimating the number of background events. The resulting averaged asymmetry distribution of 1,500 ensembles is shown in Figure 5.18. The Monte Carlo 6-event ensembles with spin correlation yield mean asymmetry values of 0.20 ± 0.17 (helicity basis), 0.15 ± 0.20 (beamline basis) and 0.20 ± 0.22 (off-diagonal basis).

Monte Carlo 6-event ensembles without spin correlation for each channel were generated for comparison, and the results are shown in Figures 5.19, 5.20 and 5.21. The expected mean and uncertainty in $\mathcal{A}$ without spin correlation is shown in Figure 5.22, yielding 0.17 ± 0.18, 0.10 ± 0.20 and 0.12 ± 0.22, for the helicity, beamline and off-diagonal bases, respectively. This seemingly

Figure 5.15: Asymmetry distribution for 40,000 ee events generated using a correlated spin matrix element, and processed through the dilepton event fitter for $m_t = 175 GeV$. The distributions are for the helicity, beamline and off-diagonal bases in (a), (b) and (c), respectively.
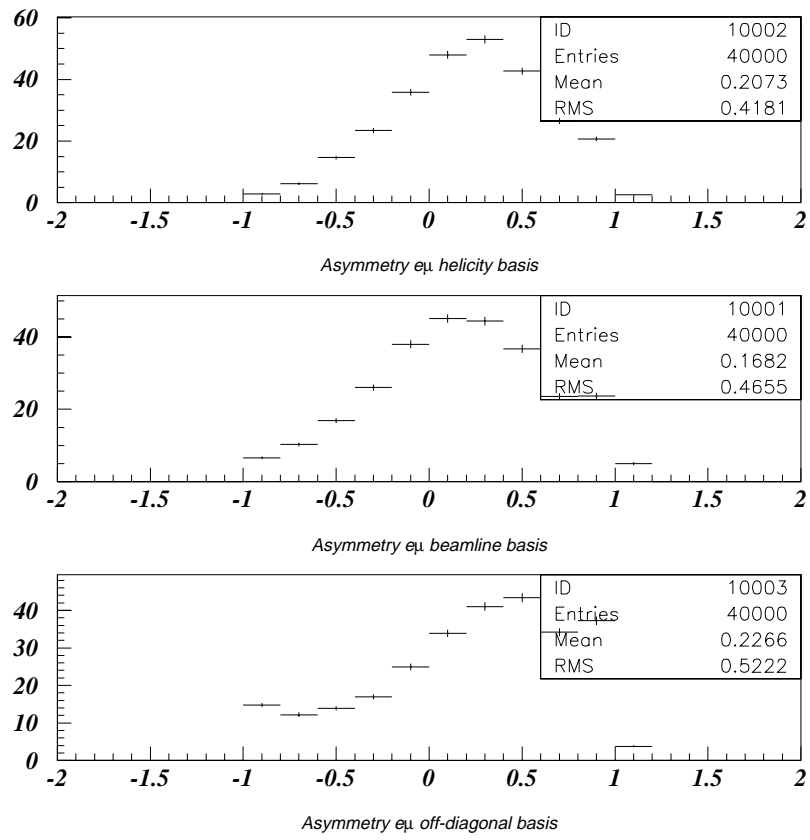
Figure 5.16: Asymmetry distributions for correlated eμ events as in Figure 5.15
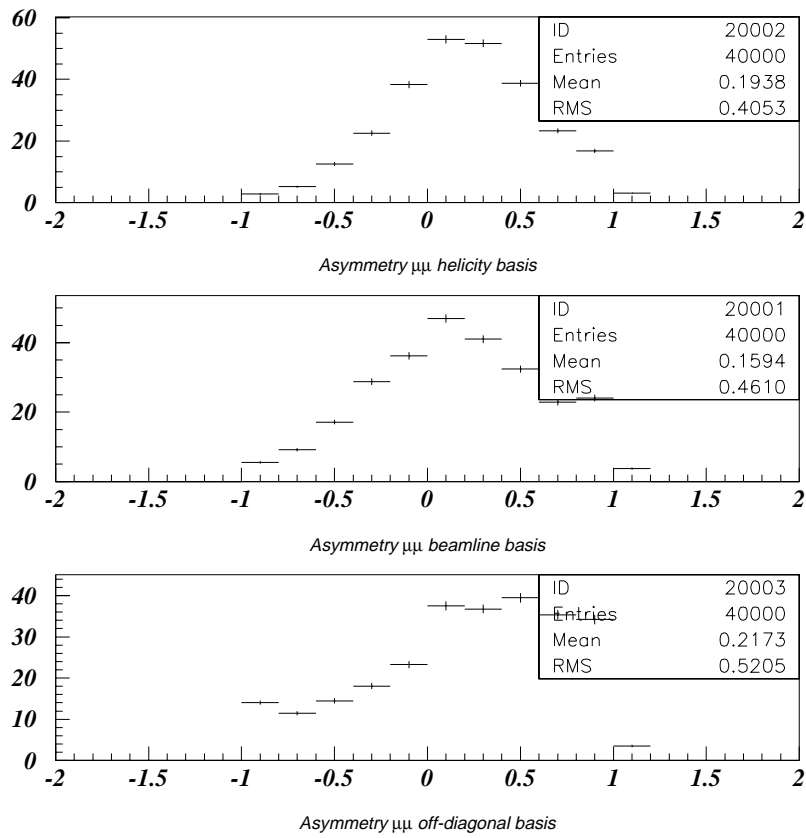
Figure 5.17: Asymmetry distributions for correlated $\mu\mu$ events as in Figure 5.15

Figure 5.18: Asymmetry distributions for 1,500 ensembles of 6 events picked randomly from the distributions given in Figures 5.15-5.17 plus backgrounds.

positive correlation, even for the uncorrelated case, is caused by mispairing of leptons with jets as will be discussed in a later section.

To check the effect of spin correlations, events generated by PYTHIA were weighted through appropriate event sampling in the $\cos\theta_+$, $\cos\theta_-$ space. In this manner, we were able to generate events in the off-diagonal basis that were equivalent to those obtained using our spin-correlated Monte Carlo samples. This alternative method was to implement since it relied on an already well-tested event generator. This method also made it possible to change the amount of correlations through a simple change in κ, while in the spin-correlated Monte Carlo, an explicit change in the matrix element was required for such needs. Both methods yield identical results in terms of asymmetry.

Figure 5.23 shows the dependence of $\mathcal{A}$ on κ, for PYTHIA events without the presence of additional gluon radiation, but with events passed through event fitter, and $\mathcal{A}$ determined as described above. The solid line drawn through the points is a linear fit, and the other line corresponds to $\mathcal{A} = \kappa/4$, which is what would be expected if there were no bias in the method. One can see that the extracted value of $\mathcal{A}$ is, in fact, biased, and the slope is about three times smaller than what is expected. But the sensitivity is not necessarily reduced by that factor, since one has to take into account the
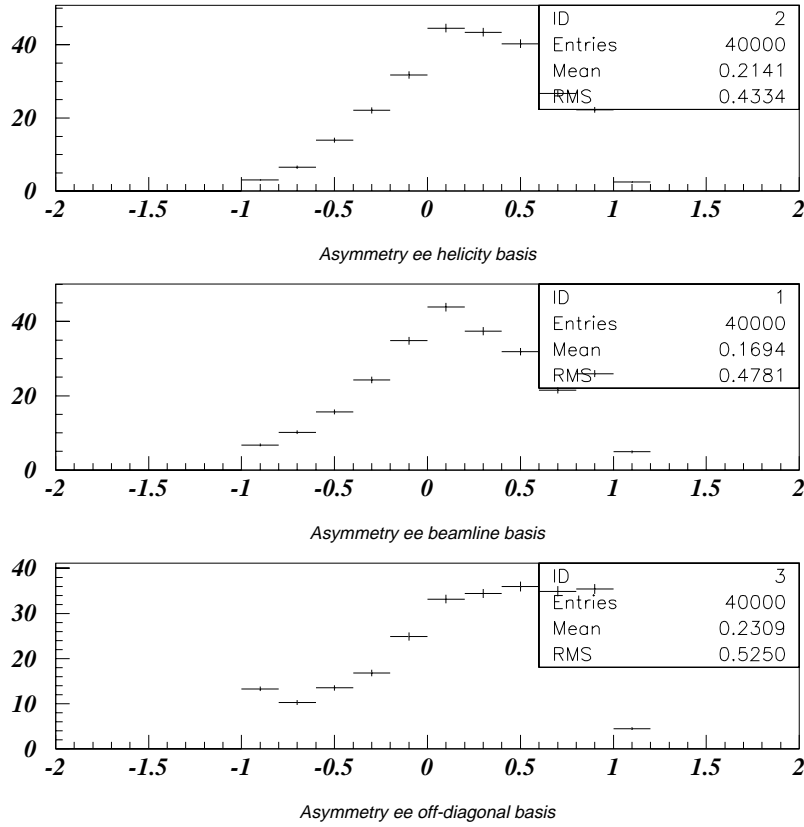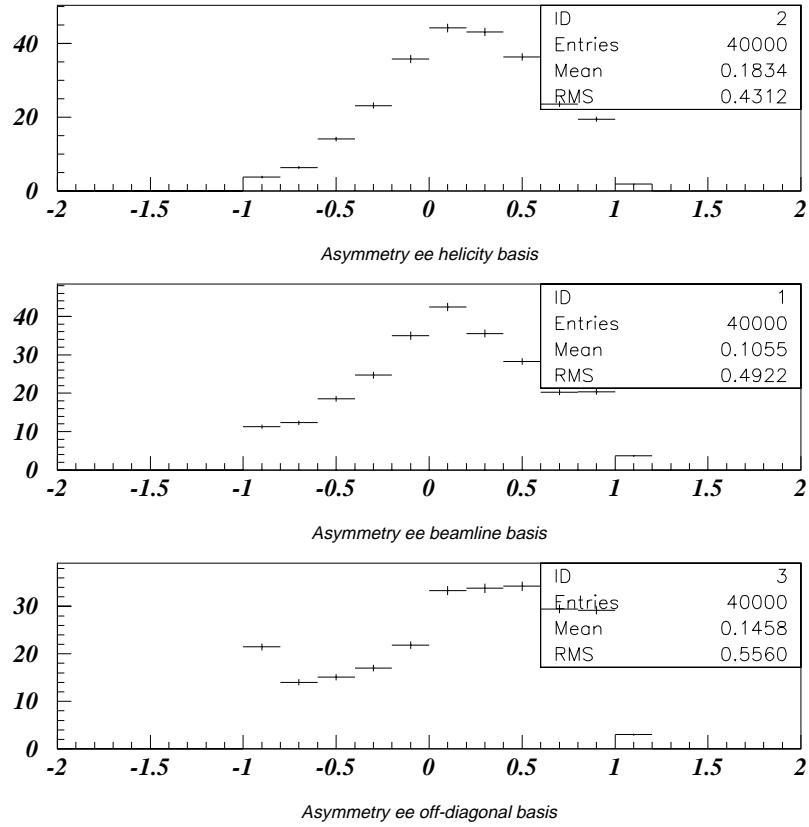
Figure 5.19: Asymmetry distribution for 40,000 ee events generated using a uncorrelated spin matrix element, and processed through the dilepton event fitter for $m_t = 175 GeV$. The distributions are for the helicity, beamline and off-diagonal bases in (a), (b) and (c) respectively.

ID	10002
Entries	40000
Mean	0.1796
RMS	0.4226

Asymmetry eμ helicity basis

ID	10001
Entries	40000
Mean	0.1074
RMS	0.4781

Asymmetry eμ beamline basis

ID	10003
Entries	40000
Mean	0.1344
RMS	0.5406

Asymmetry eμ off-diagonal basis
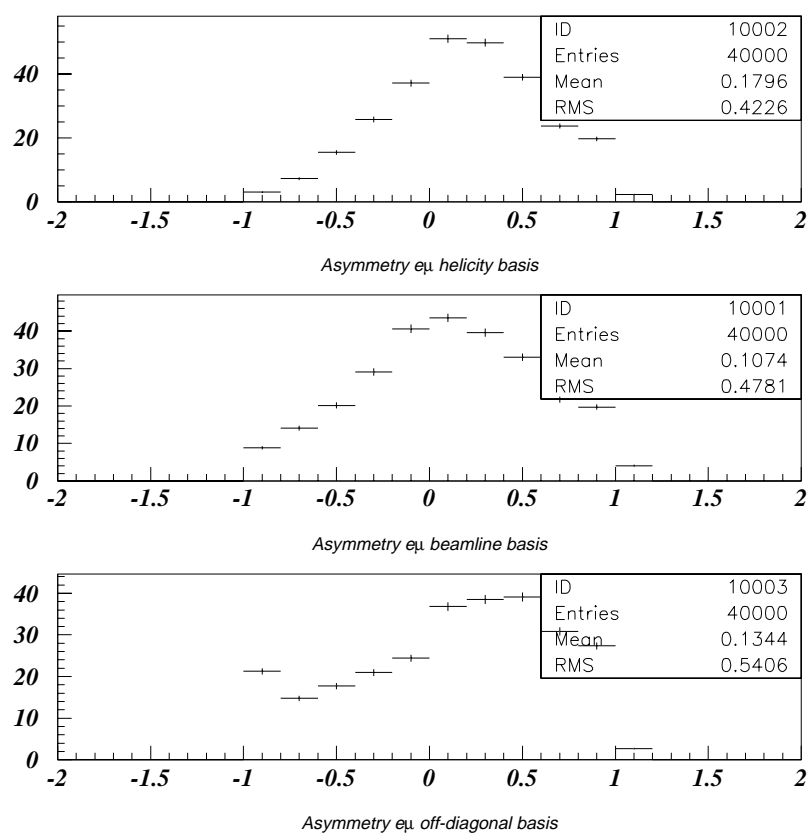
Figure 5.20: Asymmetry distribution for 40,000 eμ events as in Figure 5.19

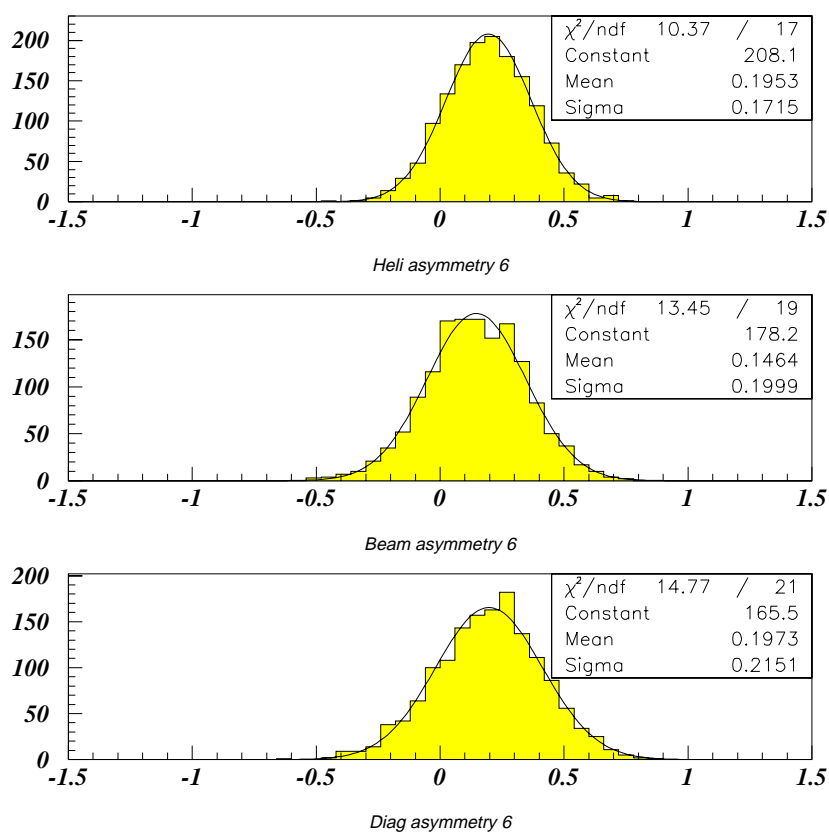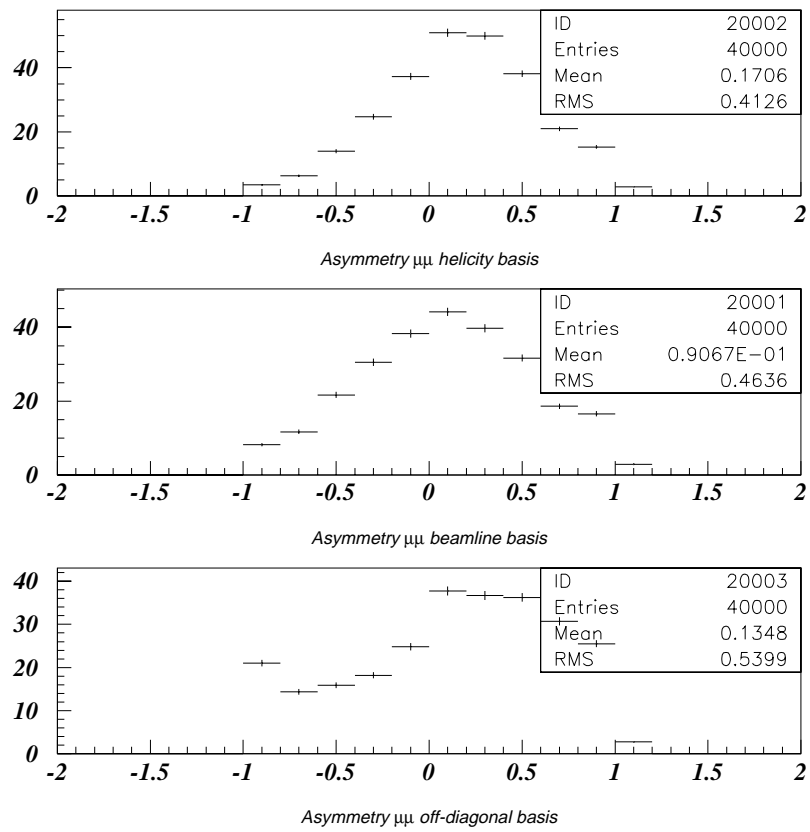Figure 5.21: Asymmetry distribution for $\mu\mu$ events as in Figure 5.19
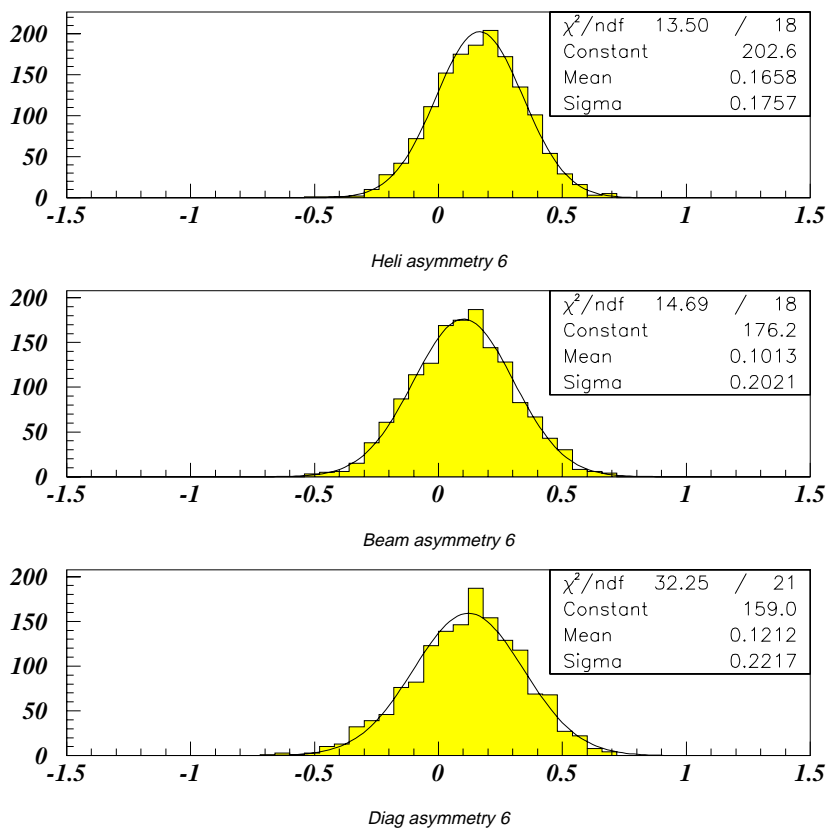
Figure 5.22: Asymmetry distribution for 10,000 ensembles of 6 spin-uncorrelated events as in Figure 5.18

dispersion of asymmetry.

5.5 Backgrounds

The background contribution to the dilepton channels is estimated to be quite low, 1.4 events as described in Section 4.3. The single largest background source of 0.56 events comes from $Z + jets$ production with $Z \to \mu\mu$. Figure 5.24 shows that the distribution in asymmetry from this particular channel when it is analyzed as $t\bar{t}$ production. The asymmetry is small. This is due to the fact that the correlation between lepton and the jets is not correct, and the kinematics are not quite right. Table 5.5 lists various background sources and their contributions to the asymmetry.

5.6 Sensitivity of the method and Source of Bias

As described in Section 5.4.1, there is some bias in the method. In this section, we will identify the cause of bias and discuss the issue of sensitivity of our method.

The main source of the bias stems from wrong combinations of lepton and
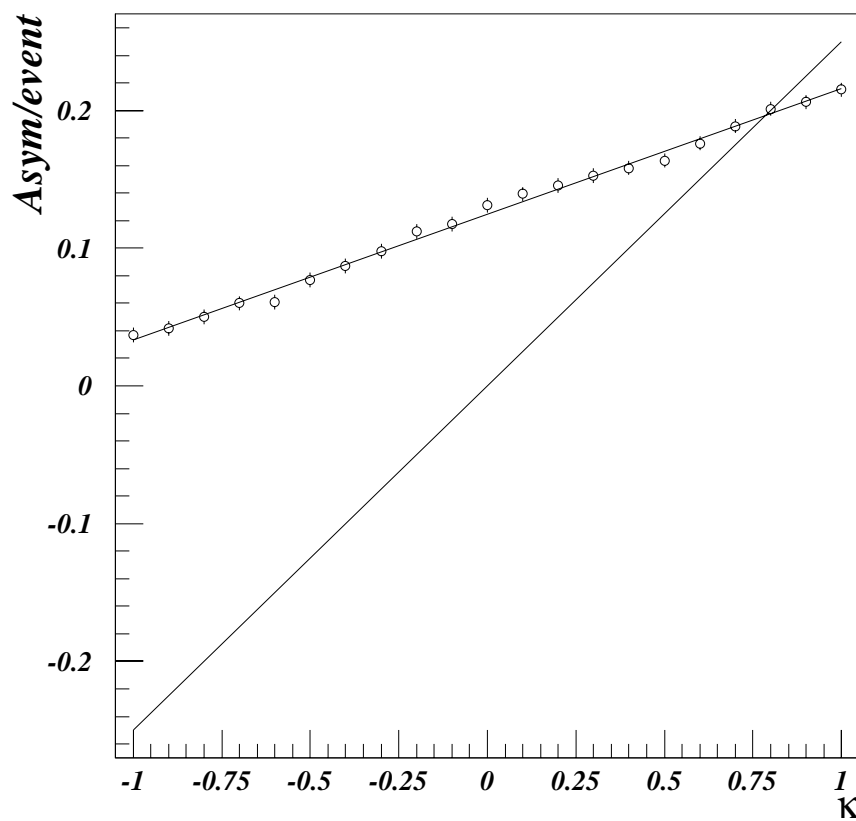
Figure 5.23: $\mathcal{A}$ vs κ for PYTHIA events smeared and passed through the event fitter. The diagonal line below the points corresponds to $\mathcal{A} = \kappa/4$.
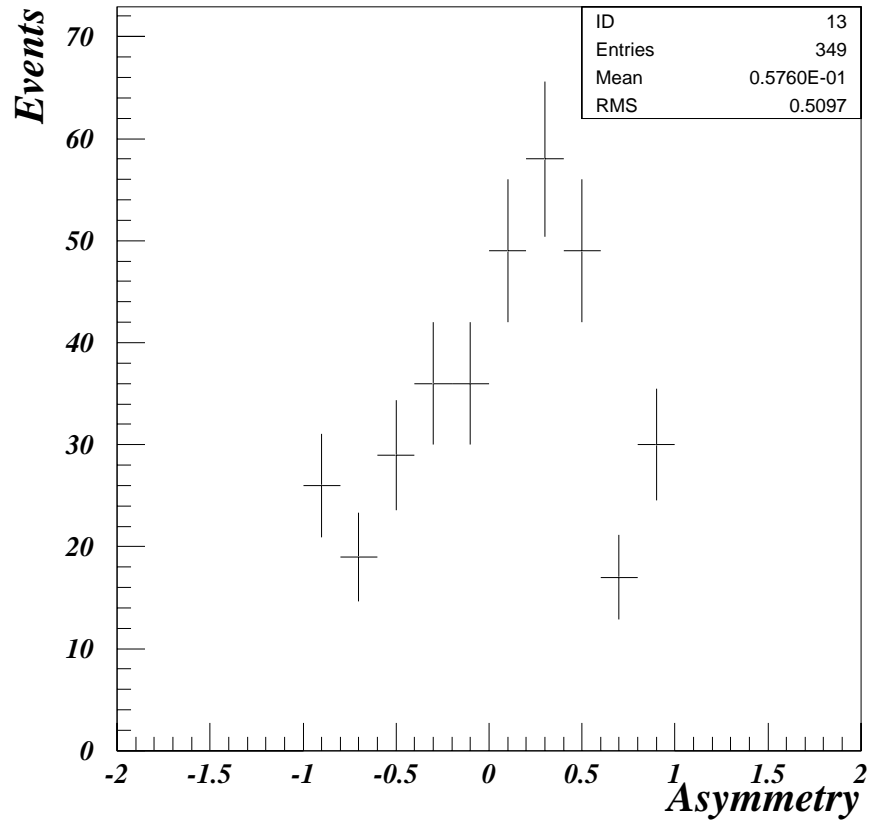
Figure 5.24: Distribution of $\mathcal{A}$ per event for $Z \to \mu\mu$ backgrounds within the $t\bar{t}$ acceptance.

Channel	Sources	Number of events	Asymmetry
ee	$Z \to \tau\tau$	0.078 ± 0.016	0.0
	$Z \to ee$	0.058 ± 0.013	0.0034 ± 0.0008
	W pair production	0.083 ± 0.014	0.0033 ± 0.0006
	Drell-Yan	0.054 ± 0.030	-
	Instrumental	0.197 ± 0.052	-
$e\mu$	$Z \to \tau\tau$	0.087 ± 0.072	0.030 ± 0.024
	W pair production	0.061 ± 0.014	0.012 ± 0.003
	Drell-Yan	0.002 ± 0.003	-
	Instrumental	0.04 ± 0.10	0.0028 ± 0.0007
$\mu\mu$	$Z \to \mu\mu$	0.56 ± 0.19	0.033 ± 0.011
	$Z \to \tau\tau$	0.03 ± 0.02	-0.0003 ± 0.0002
	W pair production	0.007 ± 0.003	0.0006 ± 0.0002
	Drell-Yan	0.07 ± 0.03	-
	Instrumental	0.07 ± 0.03	-
$Total$		1.39 ± 0.24	0.085 ± 0.027

Table 5.3: Contribution to Asymmetry from various background sources The relative uncertainties quoted on $\mathcal{A}$ correspond to those on the expected number of background events.
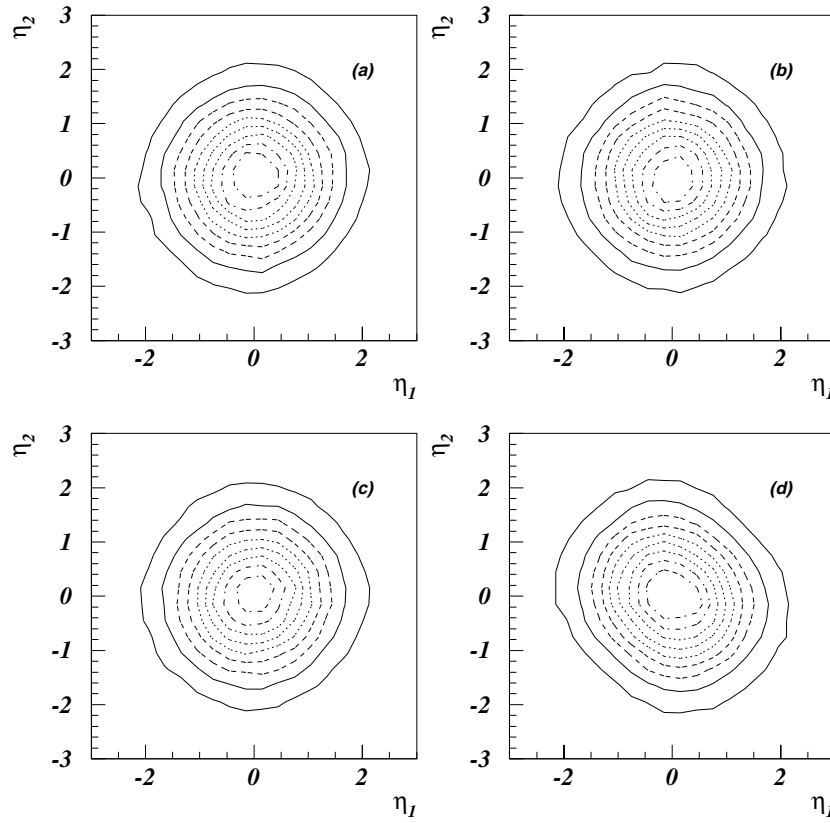
Figure 5.25: Two dimensional rapidity distributions for:(a) two neutrinos with no spin-correlation, (b) two neutrinos with spin-correlation, (c) two charged leptons without spin-correlation and (d) two charged leptons with spin correlation.

jet. Using Monte Carlo events, in which we know the correct combination of jets and leptons, and the rapidity of neutrinos, we can switch on or off different assumptions in the event fitter.

One source of this bias might expected to be how the neutrino rapidity is sampled. However, considering the fact that the neutrino is the particle least sensitive to the polarization, this effect might be small. Figure 5.25 shows that the neutrino rapidity distributions with and without correlations look almost identical and hence cannot be the cause of the bias.

The event fitter, as was explained earlier, tries both lepton and jet combination in a two jet event. And since the fitter has no neutrino information except the missing E_T vector, neutrino rapidity space is sampled according to what would be expected from a top decay. And the fact that the objects in an event are smeared by the fitter might also be contributing to the bias is also another possibility. Using only either the correct combination or the wrong combination of leptons and jets could be used to answer the question of bias arising from combinatorics. Similarly, fixing the neutrino rapidity to the generated rapidity would demonstrate the degree of bias neutrino rapidity scanning induces. Turning on or off the smearing would be used to check the bias arising from the smearing.

Table 5.4 shows the asymmetry at $\kappa = -1$, $\kappa = 0$ and $\kappa = 1$ when
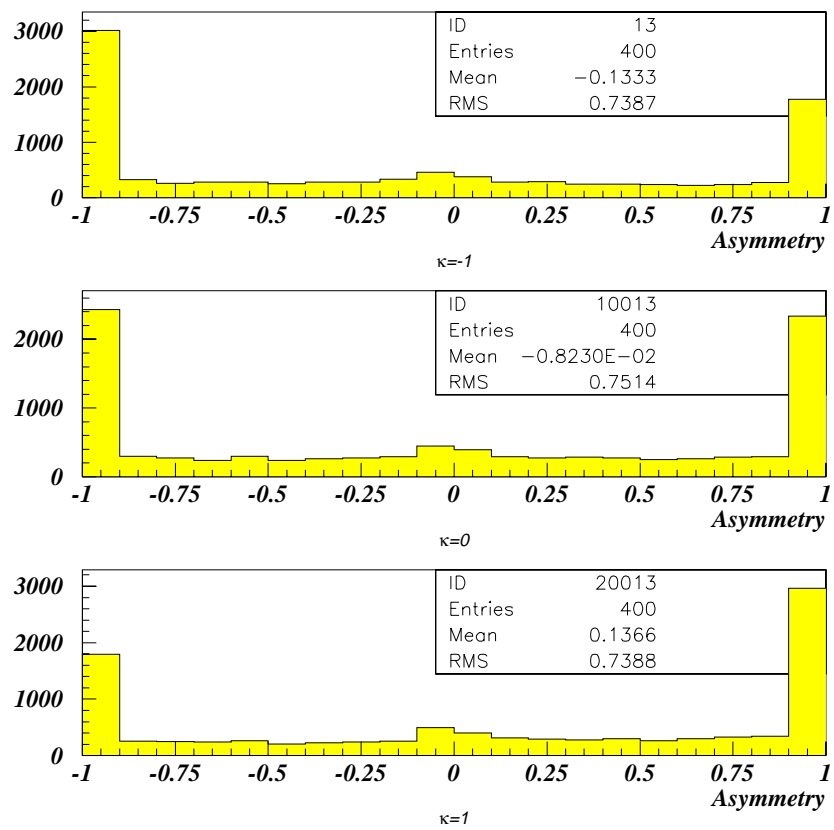
Figure 5.26: Asymmetry distributions when jets are assigned to the correct leptons.
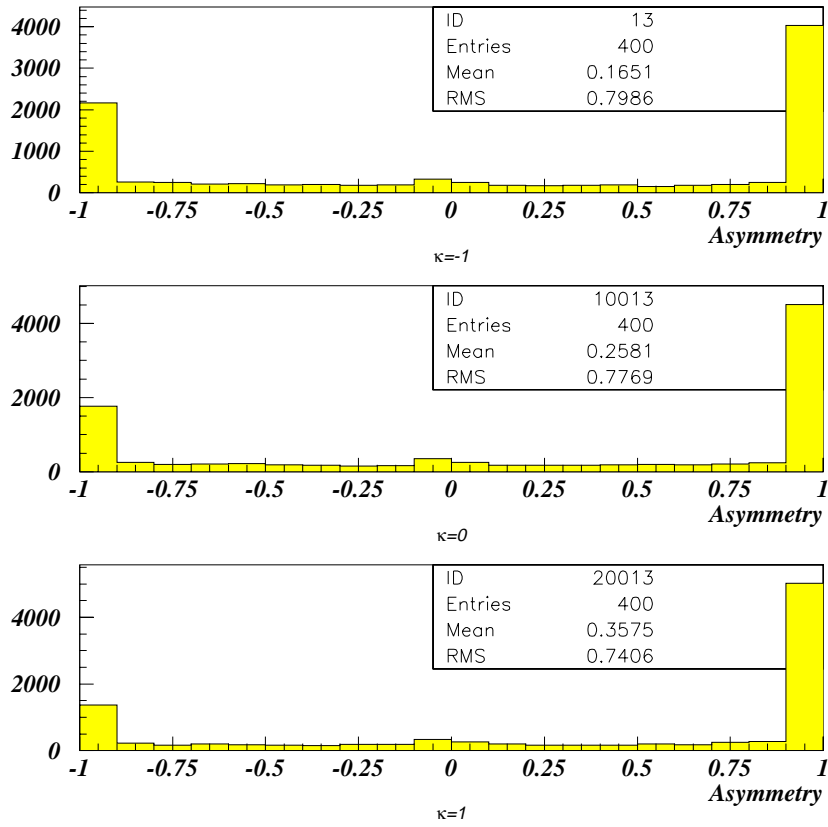
Figure 5.27: Asymmetry distributions when jets are assigned to the wrong leptons.

different assumptions are turned on or off. The table clearly shows that a strong bias is effected when the wrong jet is assigned to a lepton and the fitter tries to solve the system. Figure 5.26 shows the asymmetry distribution when correct assignment of jets and leptons is done. Figure 5.27 shows the asymmetry distribution when the systems are solved with only the incorrect combinations. Neutrino scanning merely dilutes the information and smearing of events actually gains some of the lost sensitivity. The sensitivity is defined as

$$\text{Sensitivity} = \frac{\frac{\mathcal{A}(\kappa=1) - \mathcal{A}(\kappa=0)}{\sigma_{\mathcal{A}}(\kappa=0)}}{0.25}. \tag{5.12}$$

In the ideal case of perfect information, the numerator evaluates to 0.25, and this definition of sensitivity is a figure of merit by which we can gauge the loss of information incurred by the method used in this analysis. Not only the slope of $\mathcal{A}$ as a function of κ, but also the width of the asymmetry distribution is important in the measure of sensitivity. It is interesting to note that the smearing actually regains some of the lost sensitivity and is beneficial to the reconstruction of the dilepton events. The sensitivity of events generated with resolution smearing is 0.72.

Correct Combination	Correct η_ν	Smeared	$\kappa = -1$	$\kappa = 0$	$\kappa = 1$	Sensitivity
Yes	Yes	No	-0.17	0.0	0.19	0.85
Yes	No	No	-0.14	0.0	0.14	0.77
No	No	No	0.02	0.13	0.25	0.75
No	Yes	No	-0.04	0.09	0.23	0.79
No	Yes	Yes	-0.03	0.10	0.24	0.83
Wrong	No	No	0.17	0.26	0.36	0.51

Table 5.4: Mean asymmetry for Monte Carlo events passed through the event fitter with various assumptions. The events were generated without any resolution smearing. The "No" in the first column indicates that both the correct and the wrong combination are both used. The asymmetries when only the wrong combination is used, are shown in the last line.

5.6.1 Result of Asymmetry Method

The result of asymmetry measurement is

$$\mathcal{A} = 0.30 \pm 0.22$$

which translates into

$$\kappa = 2.3 \pm 2.5,$$

if the linear relation between reconstructed $\mathcal{A}$ and κ is assumed to hold

beyond $-1 \leq \kappa \leq 1$.

5.7 Multivariate Analysis

While the method described above, using a single variable of asymmetry $\mathcal{A}$, provides a very simplified analysis of the problem, as Figure 5.23 shows, we have lost sensitivity through this approach. A multivariate analysis might recover some of the lost sensitivity.

The spin-correlation coefficient κ is not a property of any single event, but is determined from the distribution of a sufficient number of events. And we would like to extract as much information about the original $(\cos\theta_+, \cos\theta_-)$ as possible.

We present two approaches to this problem. The first method will be a binned likelihood method in 2 dimensional phase space of $(\cos\theta_+, \cos\theta_-)$. We will add the likelihoods of reconstructed $(\cos\theta_+, \cos\theta_-)$ of 6 events and compare it to Monte Carlo predictions.

The next method we use is based on probability density estimator (PDE) [68]. PDE is a new multivariate event classifier, used to identify signals in the presence of backgrounds. Similar to neural networks, a training cycle is involved, where the classifier is presented with training samples, consisting of both signal and background events. The classifier analyzes events in multi-dimensional space, and when a pattern is presented, it yields a likelihood

that it corresponds to signal(f_s) or background (f_b). Although it functions in a manner similar to that of a conventional neural network, its training is completely deterministic. Reordering events used in the training does not affect the outcome of the PDE classifier.

5.7.1   The Limiting Case of Complete Information

We can find how well κ can be measured in the limiting case of complete information, as follows. We generate two random numbers x and y, each ranging from -1 to 1, following the distribution $1 + \kappa xy$. We divide these "events" in a 3×3 matrix of nine bins of equal size spanning (x, y) space. This is done for eventual comparison with our low-statistics data sample. For ensembles with a fixed number of events, we fit the distribution in the (x, y) space to $f(\kappa; x, y) = 1 + \kappa xy$ with κ as parameter. After generating and fitting such ensembles, the uncertainty in κ can be obtained from the spread of the fitted values. Figures 5.28 and 5.29 show the distributions of fitted κ on ensembles of 6, 60 and 150 events, for $\kappa = 0$ and $\kappa = 1$, respectively. For an ensemble of 6 events generated at $\kappa = 0$, the fit yields $\kappa_{fit} > 1$, 22% of the time, while for an ensemble of 6 events generated at $\kappa = 1$, only 60% of the time does it yield κ greater than unity. Of course, $\kappa > 1$ has no physical

meaning, other than the fact that such ensembles have stronger tendencies to be positively correlated. Ensembles with few events display a structure that arises from the restricted number of ways a small number of events (e.g., 6) can populate our symmetric 3×3 grid. Ensembles for larger numbers of events yield smaller errors, and with 150 events, ideally one should be able to distinguish the presence of spin correlation at almost 4 standard deviations from a fit of the kind described above.

While with 150 dilepton samples, we can expect the statistical uncertainty in the asymmetry variable will drop from 0.20 to events would be 0.04, corresponding to about 2 standard deviations for the difference expected between the prediction for uncorrelated and correlated spins. It is therefore desirable to have a better procedure than just the analysis method based on $\mathcal{A}$, to recover some of the lost sensitivity.

5.7.2   Binned Likelihood Method

In order to take into account of the full information available in the data, a fit in the $(\cos\theta_+, \cos\theta_-)$ space would appear desirable. As before, each event is passed through the event fitter and the returned weights used to fill a 3x3 grid of $(\cos\theta_+, \cos\theta_-)$ values. These are combined after normalizing
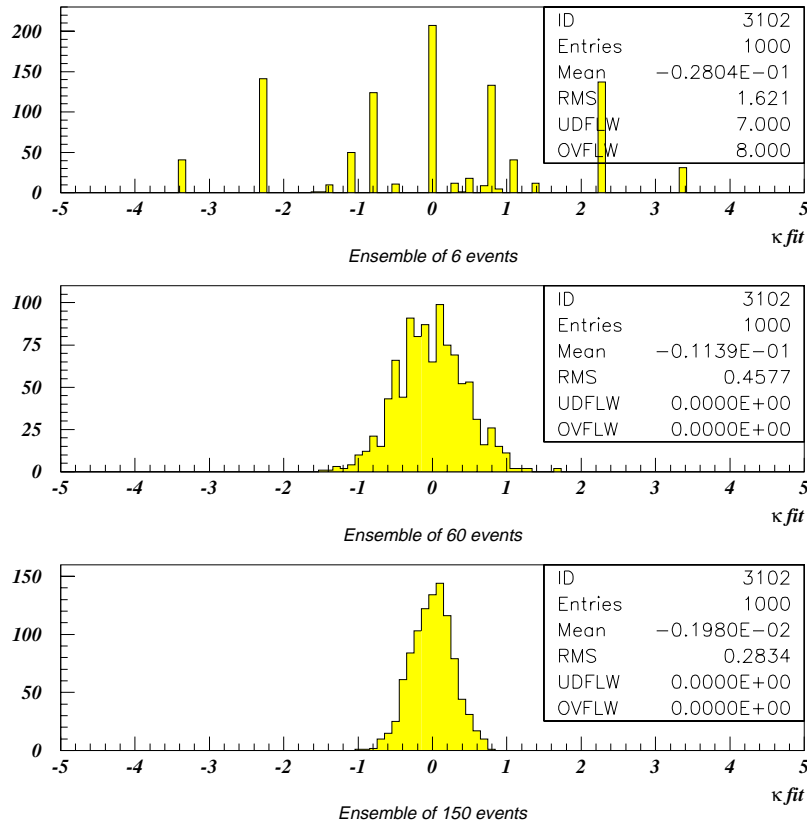
Figure 5.28: Distribution of κ_{fit} for 1,000 ensembles of 6, 60 and 150 events, generated at $\kappa = 0$.
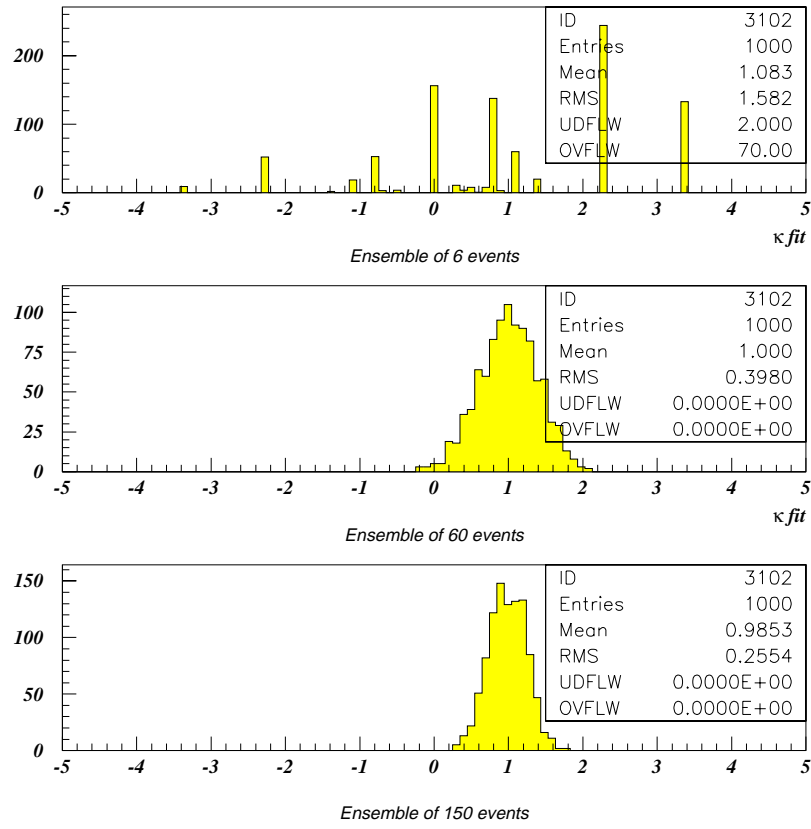
Figure 5.29: Distribution of κ_{fit} for 1,000 ensembles of 6, 60 and 150 events, generated at $\kappa = 1$.

the distribution from each event to 1. Monte Carlo events, generated at $\kappa = -1(10{,}000$ events) and $\kappa = 1(10{,}000$ events) are treated in a similar manner, and used for comparing with data.

The likelihood is defined by the product of Poisson probabilities over the 3x3=9 bins,

$$\mathcal{L} = \prod_{i=1}^{9} \frac{e^{-\mu_i} \mu_i^{N_i}}{N_i!}, \tag{5.13}$$

where μ_i is the expected number of event permutations in each bin i, and is calculated as:

$$\mu_i(\kappa) = \mu_{isignal}(\kappa) + \mu_{ibackground}, \tag{5.14}$$

where the sum of $\mu_{ibackground}$ is made equal to the total number of expected background events. The N_i represent the number of permutations in each bin i. The result for our data is shown in Figure 5.30. Integrating the area beneath the likelihood curve, we obtain $\kappa > -0.2$ at 68% C.L.

There is a question as to whether we are justified in calculating the likelihood in the manner described above. A brute force approach of explicitly generating the likelihood was investigated. Here, a linear combination of 8 weights (since the sum of nine weight equals one) is found so that the new variables are independent of each other. This is easily done by calculating the covariance matrix and diagonalizing it using Monte Carlo signal events and
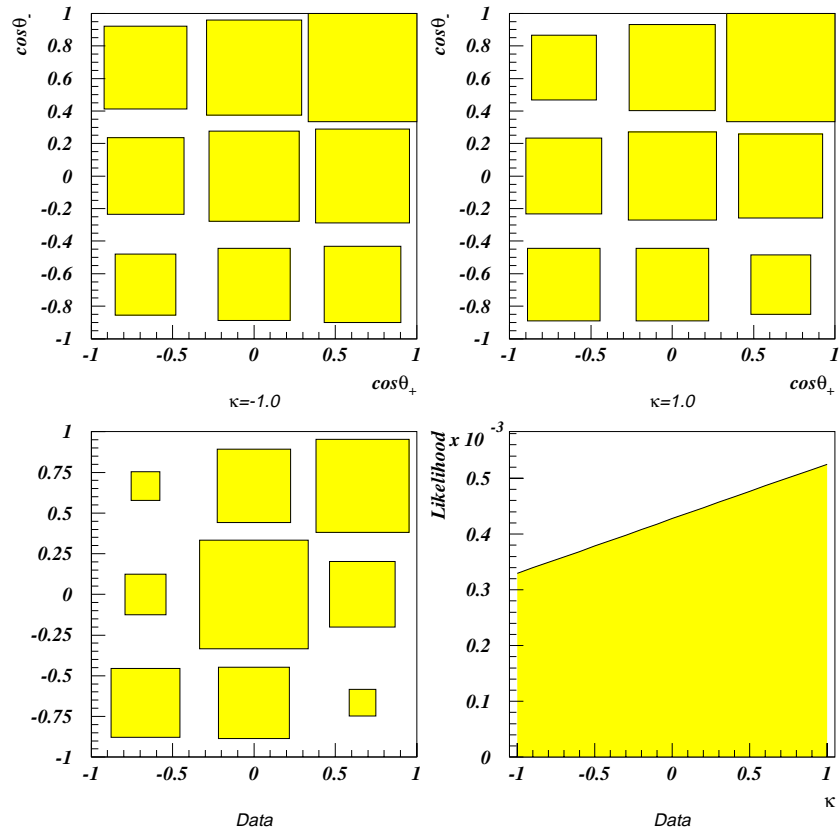
Figure 5.30: Result of a two-dimensional binned likelihood fit to the data, using the Monte Carlo simulations for $\kappa = 1$ and $\kappa = -1$ for signal, and contributions from background.

background events. Then distributions of these 8 new variables are found by filling them with the Monte Carlo and background events (Figure 5.31). To get a likelihood value for the ensemble, we apply the same transformation to the weights from the 3×3 grid. Then from the distribution, we calculate the following likelihood

$$\mathcal{L} = \prod_{i=1}^{8} f_i(w_i'), \tag{5.15}$$

where f_i is the distribution of weights for ith transformed variable and w_i are transformed weights of our data. This method yields $\kappa > -0.25$ at 68% C.L as shown in Figure 5.32.

To see the statistical sensitivity of this method, ensemble tests were done with ensembles of 150 events generated at $\kappa = 0$. The extracted κ in Figure 5.33 corresponds to the most likely value for each ensemble where likelihood has its peak value. From the figure, we see that the statistical significance exceeds only 2.5 standard deviations relative to $\kappa = 1$ for expectations from Run II.

5.7.3 PDE

The PDE classifier can also be regarded as a variant of the covariance matrix approach [68]. In the classical covariance matrix, both signal and background
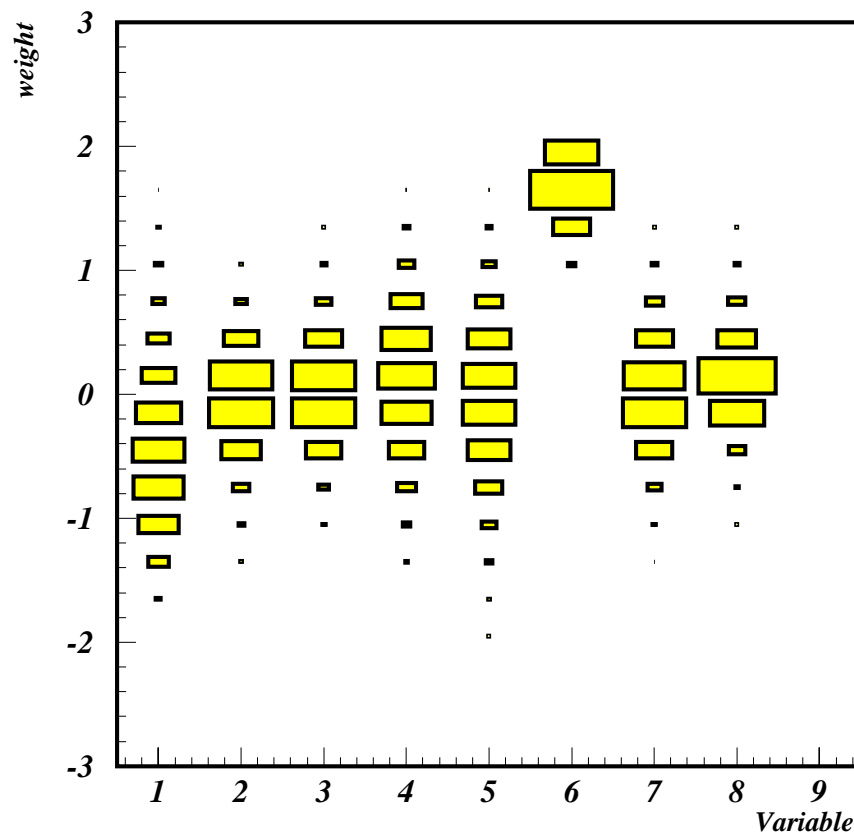
Figure 5.31: Distribution of weights for 8 transformed variables. The new 8 variables are linear combinations of old variables, the y axis shows the distribution of weights
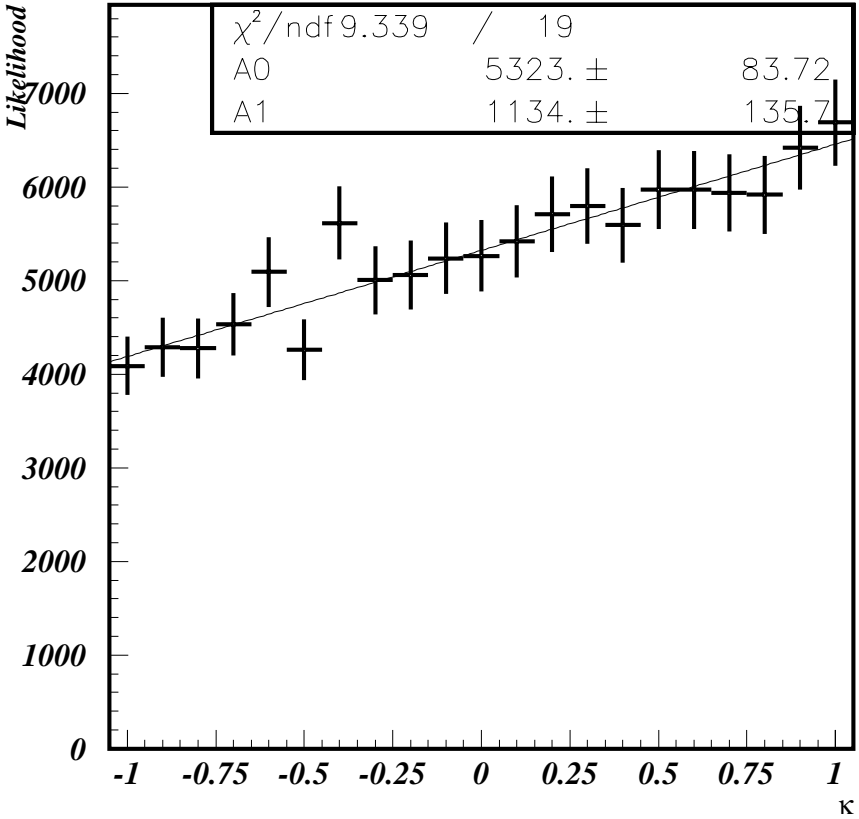
Figure 5.32: Distribution of likelihood as a function of κ with explicit likelihood construction. The errors are point to point correlated.
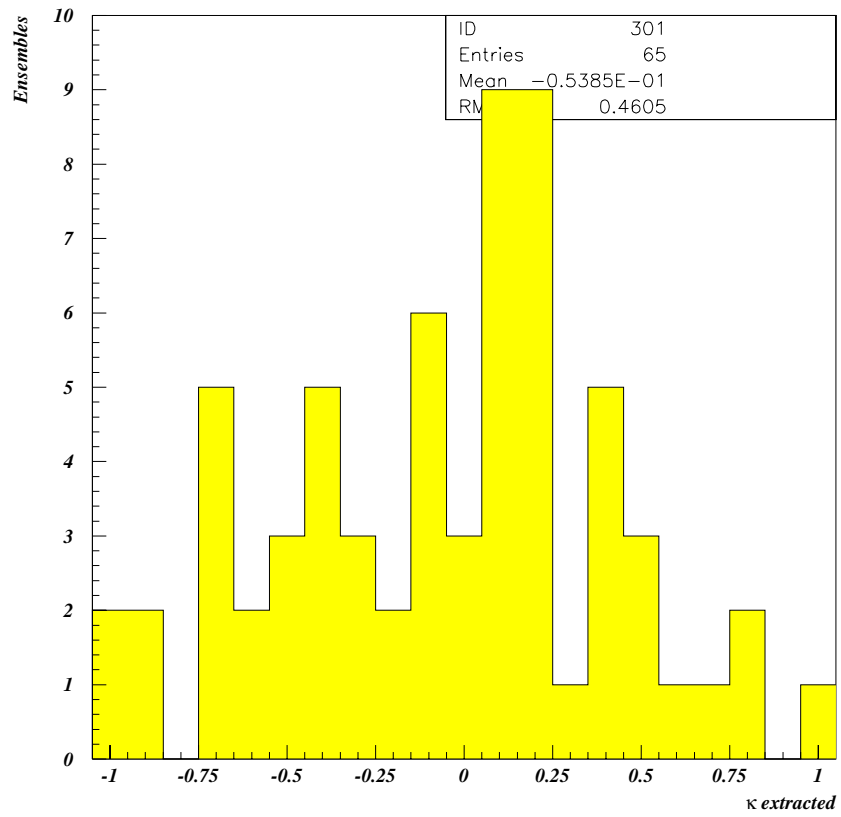
Figure 5.33: Result of two-dimensional binned likelihood fits to 65 ensembles of 150 spin-uncorrelated events. The result of the most likely value of κ are plotted assuming $\kappa = 0$ in the generation of the Monte Carlo ensembles.

probability densities are estimated using the following density functions for signal ($f_s(\vec{x})$) and background ($f_b(\vec{x})$):

$$f_s(\vec{x}) = \frac{1}{\sqrt{(2\pi)^d \det(\Sigma_s)}} \exp(-\frac{1}{2}(\vec{x} - \vec{\mu_s})\Sigma_s^{-1}(\vec{x} - \vec{\mu_s})^T) \qquad (5.16)$$

$$f_b(\vec{x}) = \frac{1}{\sqrt{(2\pi)^d \det(\Sigma_b)}} \exp(-\frac{1}{2}(\vec{x} - \vec{\mu_b})\Sigma_b^{-1}(\vec{x} - \vec{\mu_b})^T), \qquad (5.17)$$

where μ_s, μ_b and Σ_s, Σ_b are the means and the covariance matrices for the signal and the background events. While these classifiers are relatively easy to use, their power to model non-linear boundaries between the signal an background classes is rather limited.

Consider a random variable X with density f, and suppose that $x_1, \ldots, x_n$ is a set of randomly chosen values of X. To estimate f from the chosen set $\{x_n\}$, we consider cumulative distribution function

$$F(x) = P(X \leq x) = \int_{-\infty}^{x} f(u)du. \qquad (5.18)$$

The distribution $F(x)$ can be estimated by counting the number of samples x_i that are smaller than the value x:

$$F(x) \approx \hat{F}(x) \equiv \frac{1}{N} Number\{x_i | x_i \leq x\}. \qquad (5.19)$$

Since the density corresponds to the derivative of $F(x)$, by taking a numerical derivative, we get:

$$
\begin{aligned}
f(x) &\approx \frac{1}{2h}\left(\hat{F}(x+h) - \hat{F}(x-h)\right) \quad (5.20)\\
&= \frac{1}{2Nh}Number\{x_i| -h < x_i - x \leq h\} \equiv \hat{f}(x).
\end{aligned}
$$

if K is the uniform density function on the interval $-1 \leq u < 1$,

$$
K(u) = \quad \tfrac{1}{2}, \quad -1 \leq u < 1, \quad (5.21)
$$

$$
0, \quad \text{otherwise.}
$$

then $\hat{f}(x)$ can also be written as

$$
\hat{f}(x) = \frac{1}{Nh}\sum_{i=1}^{N} K(\frac{x - x_i}{h}). \quad (5.22)
$$

The *smoothing parameter h* could be likened to "bin width" in a histogram. Consequently, what is calculated in Equation 5.22 is the number of samples in a particular bin divided by the total number of samples achieving proper normalization. One could devise different ways of defining the kernel K. A standard Gaussian kernel will be assumed, with $K(x) = \sqrt{1/(2\pi)}\exp(-x^2/2)$.

Extension of this simple one-dimensional example to a multi-dimensional case requires that the covariance of the kernel reflect the covariance of the density f being estimated. An appropriate linear transformation to the data can transform the inputs into uncorrelated variables, making the problem tractable. The transformation to be applied is based on the covariance matrix derived using PDE.

5.7.4   Analysis Using PDE Method

As before, the $(\cos\theta_+, \cos\theta_-)$ space is divided into 3×3 bins. The reconstructed $\cos\theta_+ \cdot \cos\theta_-$ distributions for events generated in each of the 9 separate regions, and passed through the dilepton fitter, are shown in Figure 5.34, and their shapes are clearly different, indicating sensitivity to their origin.

Each one-dimensional distribution of $\cos\theta_+ \cdot \cos\theta_-$ are binned into 6 equal intervals and normalized to unity. The contents of these 6 bins are used as weights$(w_1 \ldots w_6)$ to be presented to the PDE classifier. The problem is 5 dimensional, since there is a normalization condition and therefore only $w_1 \ldots w_5$ are needed to specify the weights. There are significant variations from the "templates" for the nine different input regions, and this enhances
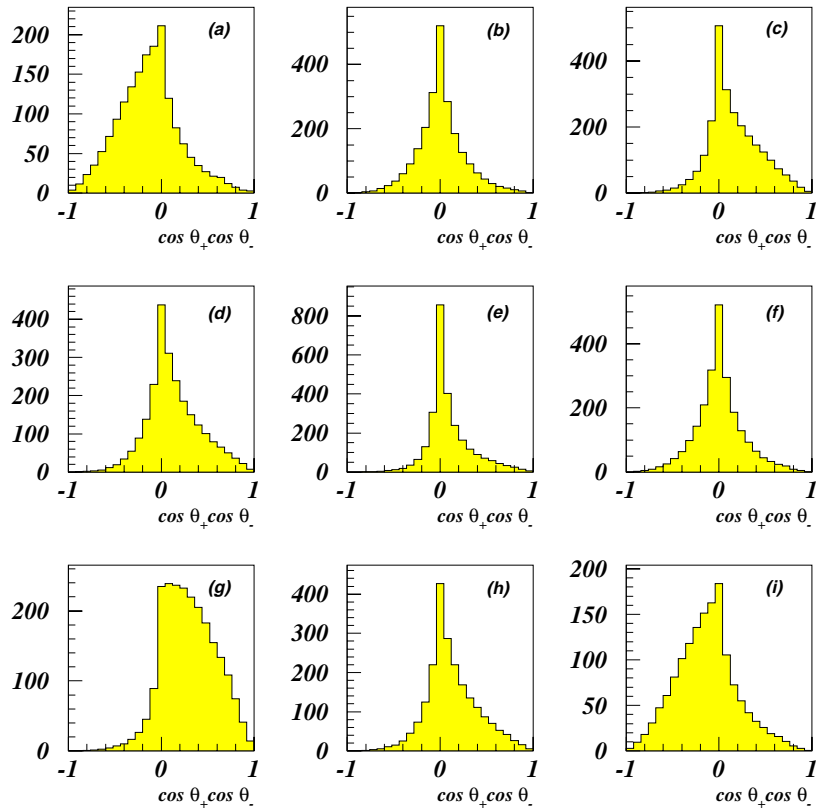
Figure 5.34: Distributions in reconstructed $\cos\theta_+ \cdot \cos\theta_-|$ for events generated in the nine regions of $(\cos\theta_+, \cos\theta_-)$ space designated by (a)-(i). Region (a) corresponds to $\cos\theta_+$ lying between 0.33 and 1.0 and $\cos\theta_-$ between -1.0 and -0.33, (g) to $\cos\theta_+$ and $\cos\theta_-$ between -1.0 and -0.33, etc.

the utility of the PDE classifier. PDE can be trained to recognize such variations and to classify them accordingly.

The PDE is trained separately for each input region on the 3-by-3 grid. For example, we use the sample of $t\bar{t}$ Monte Carlo events for which the input values are $\cos\theta_+ > 1/3$ and $\cos\theta_- > 1/3$, which corresponds to the histogram shown in the upper right hand corner of Figure 5.34. Training is performed using the expected nature of $t\bar{t}$ by presenting the signal Monte Carlo events and background samples. In this way, we generated trained form $PDE_1 \ldots PDE_9$. After the training, any sample of new events can be classified according to the relative likelihood of coming from a particular input point of the 3-by-3 grid, corresponding to each PDE_i would with relative signal(f_{si}) and background (f_{bi}) probability densities for the particular grid point i.

The performance of the PDE depends on the choice of the previously mentioned *smoothing parameter h*. Figure 5.35 shows the inferred input distributions after reconstruction of 2500 event samples were generated in the region corresponding to Figure 5.34(c). The results do not appear to be sensitive to the smoothing parameter h. Probability density theory predicts

that the optimal h for any problem is expected to be [68]:

$$h = \left[\left(\frac{4}{d+2} \right)^{1/(d+4)} N^{-1/(d+4)} \right], \qquad (5.23)$$

where d is the number of inputs dimensionality and N is the number of events in the training samples. For training samples of 2500 events and dimension of $d = 5$, $h \approx 0.4$ corresponds to the optimal choice.

For $t\bar{t}$ data, a likelihood function can be constructed, the number of expected $t\bar{t}$ signal and expected background events as follows:

$$\mathcal{L}_i = \frac{f_{si} n_s + f_{bi} n_b}{n_s + n_b}. \qquad (5.24)$$

The values of f_{si} and f_{bi} for each event are returned by the PDE_i. The likelihood is interpreted as a relative probability density, and the posterior probability for each event being in the ith bin in the 3x3 grid is given by $f_i = \mathcal{L}_i / \sum_{j=1}^{9} \mathcal{L}_j$. The posterior probability for the 6 dilepton channel events as a function of κ is shown in Figure 5.36.

Another way of constructing the likelihood in Equation 5.24 is to simply use $\mathcal{L} = f_s$ and then add the background effects by adding the expected
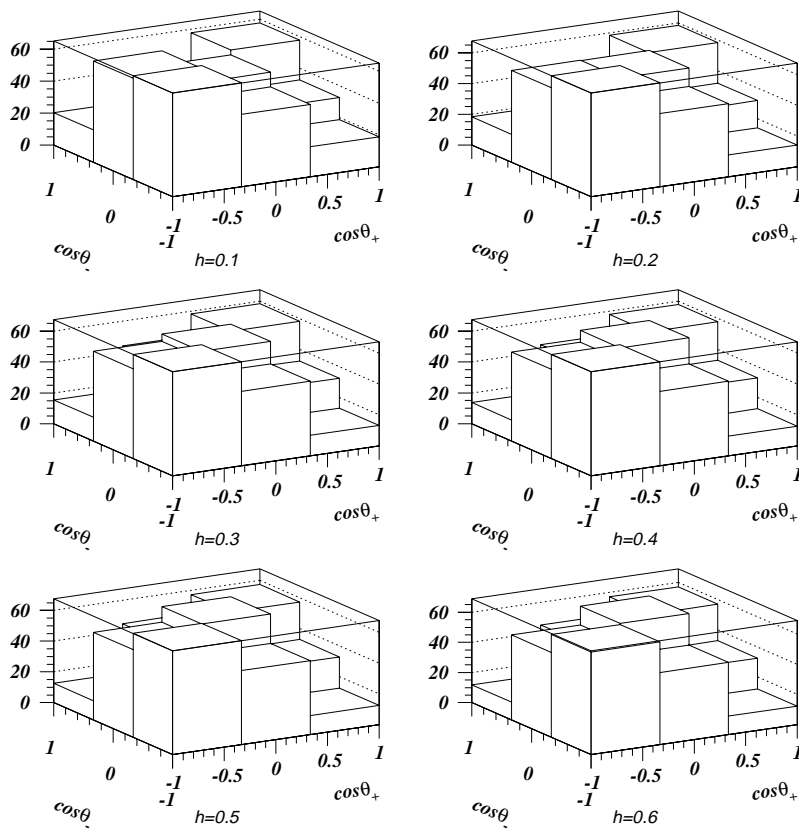
Figure 5.35: Output of PDE for 2500 event samples generated in $1/3 < \cos\theta_+ < 1$ and $1/3 < \cos\theta_- < 1$.
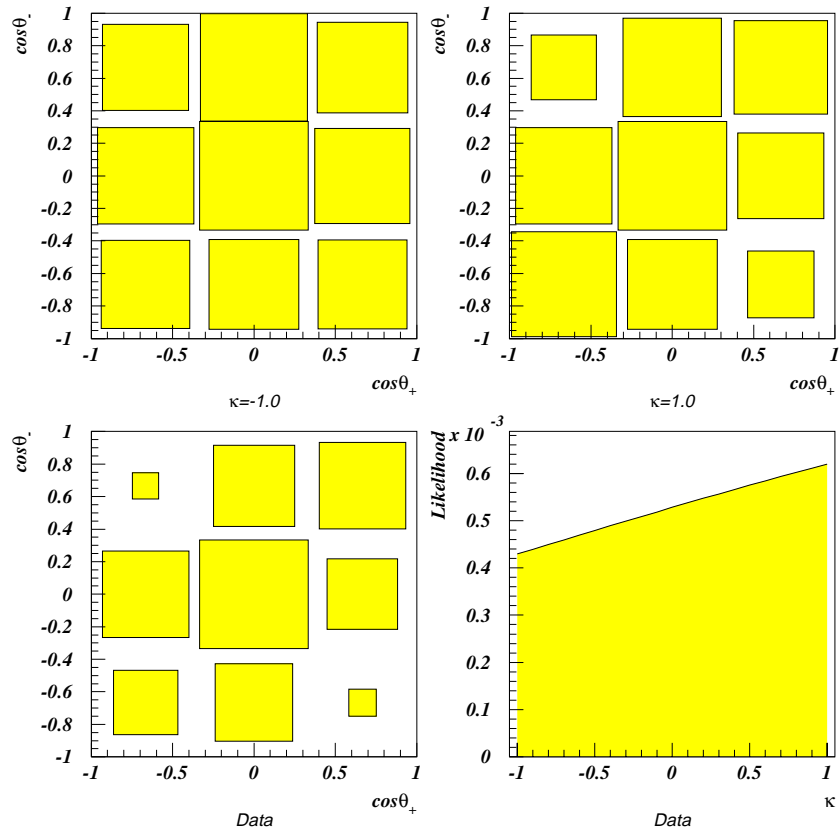
Figure 5.36: Top figures show the expected distribution in the 2 dimensional $\cos\theta_+ vs \cos\theta_-$ space for $\kappa = -1$ and $\kappa = 1$ respectively using the PDE method. The bottom left figure shows the event distributions of the data. The bottom right figure is the posterior Poisson probability for observing our data as a function of κ.

posterior distribution μ_{ib} in the $(\cos\theta_+, \cos\theta_-)$ space to the signal μ_{is}.

$$\mu_i = \mu_{si} + \mu_{bi} \qquad (5.25)$$

The result of using this method is shown in Figure 5.37, $\kappa > -0.25$ at 68% CL.

5.7.5   Ensemble Tests

Ensembles tests were performed to verify the results of the PDE analysis method. Ensembles were generated at a fixed value of κ and passed through the PDE classifier. For each ensemble, the value of κ at which the posterior probability becomes maximum was chosen as the fitted κ. The distributions of κ thus extracted for ensembles of 150 events, generated at $\kappa = 0$ and $\kappa = 1$, are shown in Figures 5.38 and 5.39, respectively.   From these ensemble tests, we see that 2 out of 65 times, we get either $\kappa = 1$ or $\kappa = -1$ for spin-uncorrelated events, thus the significance achievable at Run II will be about 2.5 standard deviations.   And this significance is similar to what we can reach using the simpler asymmetry or the 2-dimensional binned likelihood methods.

For ensembles of 6 events, the results are shown in Figures 5.40 and 5.41.
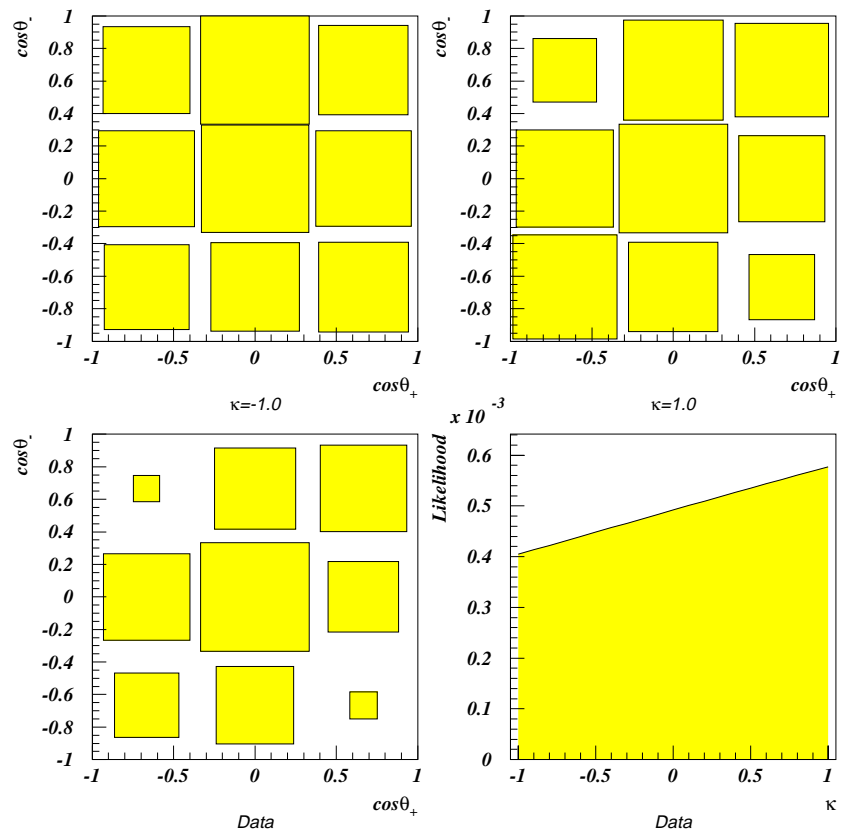
Figure 5.37: Posterior probability for observing our data using the second method of defining likelihood.
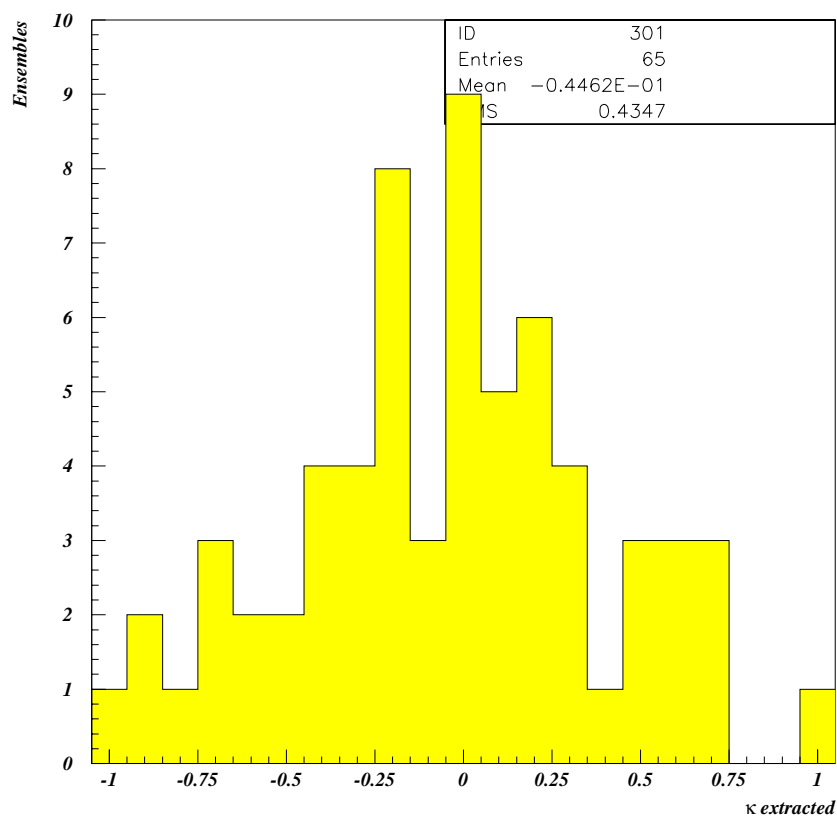
Figure 5.38: Distribution of κ extracted using the PDE method from 65 ensembles of 150 events, which were generated at $\kappa = 0$.
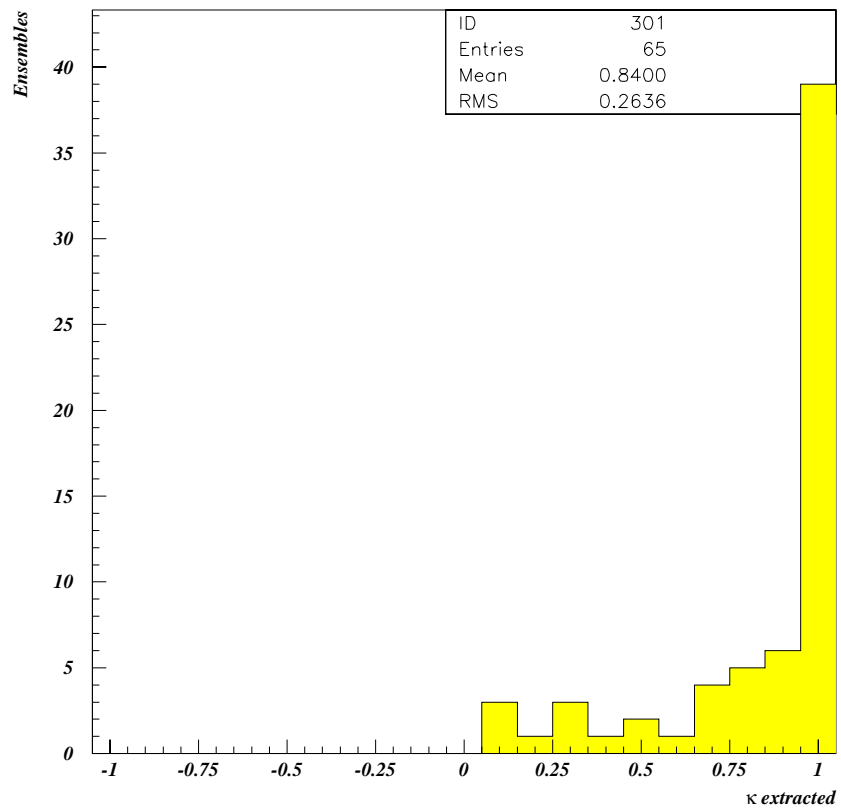
Figure 5.39: Distribution of κ extracted using the PDE method from 65 ensembles of 150 events, which were generated at $\kappa = 1$.

5.8 Systematics

With the 6 events available from Run I data, the statistical error will overwhelm any systematic uncertainties. However for Run II, where we expect more than 150 $t\bar{t}$ events in the dilepton channels, a detailed study of systematics will surely be necessary.

In the generators so far used, the extra radiations were turned off. But it might be important to include them as it might create some added difficulty associated with combinatorics.

5.8.1 Effects of Radiation

The matrix element currently available does not include the effects of extra radiation [63]. However, calculation has been done for $e^+e^- \rightarrow t\bar{t}g$ [69]. And shows that the effects of extra radiation is very small in case of $t\bar{t}$ production through annihilation of e^+e^-. While we await the full calculation of radiation effects in case of top-pair production through $p\bar{p}$, many theorists think the effects will be small [70].

However, the effects of radiation on spin-uncorrelated events can be stud-
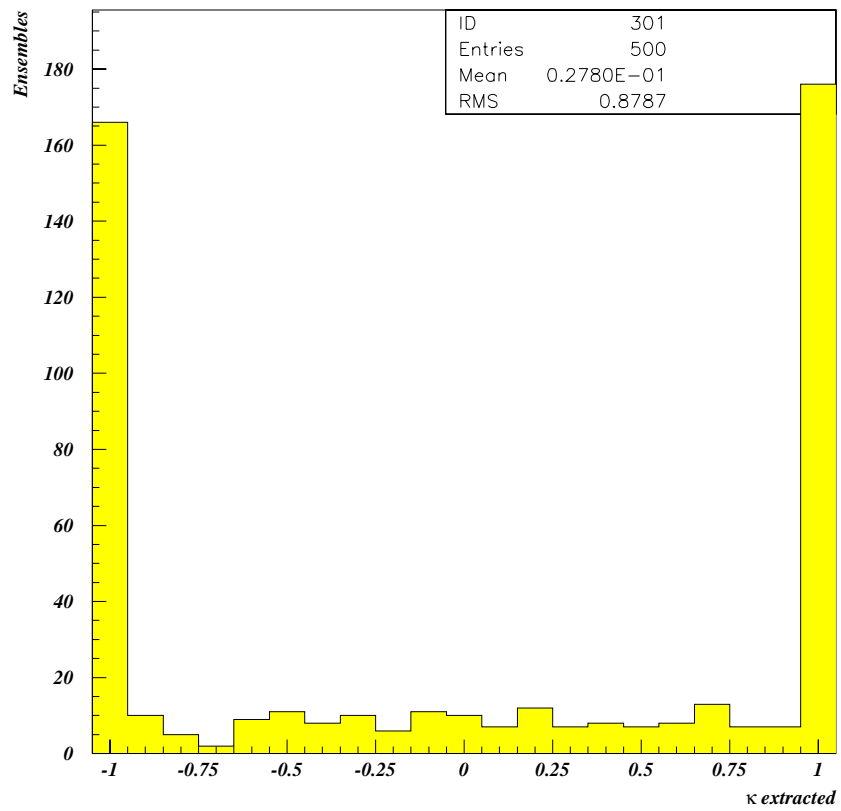
Figure 5.40: Distribution of κ extracted from 500 ensembles of 6 events, which were generated at $\kappa = 0$.
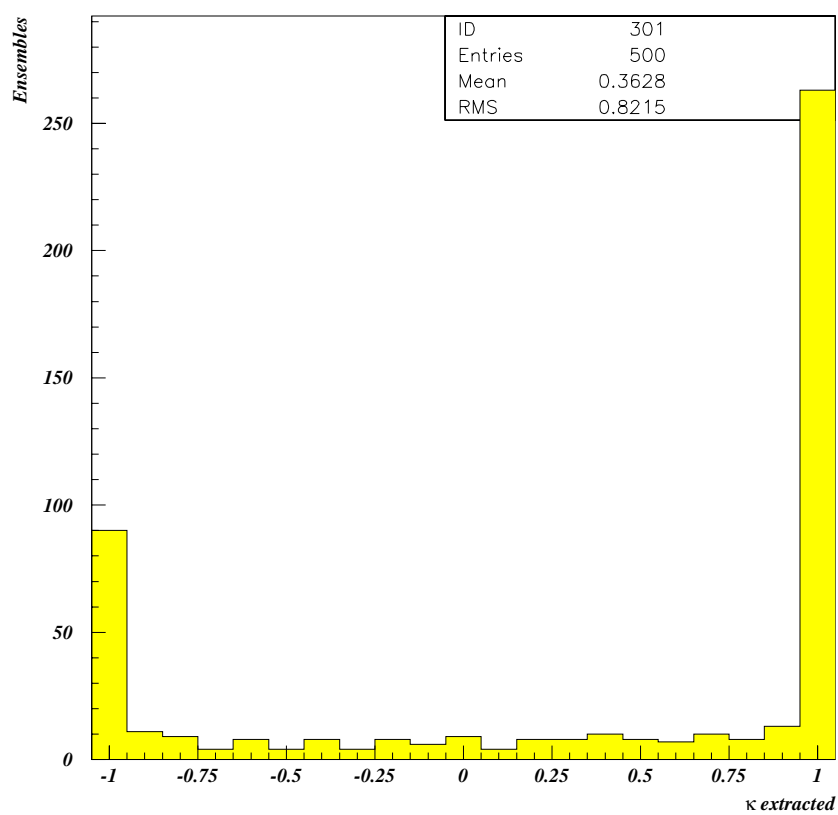
Figure 5.41: Distribution of κ extracted from 500 ensembles of 6 events, which were generated at $\kappa = 1$.

ied easily as event generators such as HERWIG or PYTHIA have initial and final state radiation effects. Ensemble tests on fully detector simulated HER-WIG events, using PYTHIA events without radiation as templates, reveal that extra radiation does not induce any noticeable change in the mean κ extracted (Figure 5.42). The fact that the width does not change means that the sensitivity is not affected either.

The difference in the mean of distributions in Figures 5.38 and 5.42 is 0.13 ± 0.11, where the error is due to Monte Carlo statistics. From the previous section, the resolution on κ due to statistics of 150 events is 0.42. And therefore, the systematic uncertainty due to extra radiation is still small.

5.9   Result and Discussion

The spin correlation factor extracted from 6 dilepton channel is $\kappa > -0.25$ at 68% CL. Analysis using asymmetry variable yields $\kappa = 2.3 \pm 2.5$, but central value of $\kappa > 1$ has no physical meaning. However, it is interesting to note that the low-end of κ measurement from asymmetry method coincides with the 68% confidence limit of likelihood method. The PDE method was used as a cross check, since PDE was used in the dilepton top mass analysis.

In the next run which will start in the year 2000, we expect 10 times more
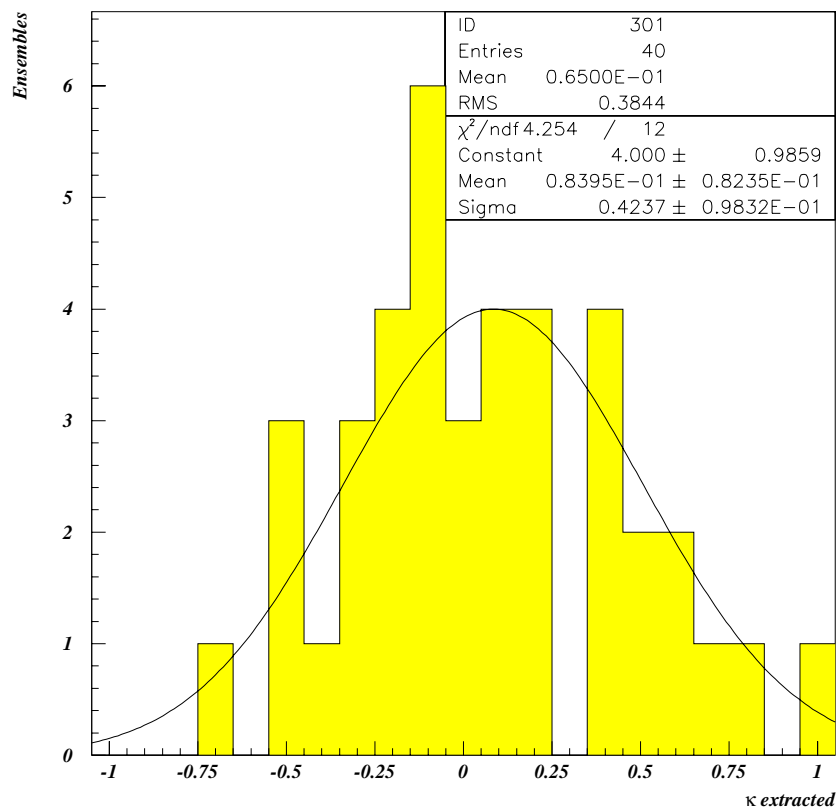
Figure 5.42: Distribution of κ extracted from ensembles of 150 fully detector simulated HERWIG events, which shows that no extra bias is introduced by the radiation.

luminosity, 40% increase in $t\bar{t}$ production cross section due to increased beam energies and greater acceptance due great improvements in tracking and b-tagging abilities. We expect more than 150 signal events in the dilepton channels alone. In addition to increased statistics, b-tagging ability may make it possible to use events in the $l + jets$ channels. Spin correlation can be observed at better than 2.5 standard deviations when systematics can be neglected.

Conclusion

Spin correlation is expected to be seen in the $t\bar{t}$ system produced from $p\bar{p}$ collisions due to the short lifetime of the top quark. The importance of observing the spin correlation lies in the fact that spin correlation is a signature of quarks that are almost free from long-distance QCD effects. It will also give us information about $|V_{tb}|$ without having to assume three generations of quarks and is sensitive to new physics.

In this thesis, a study of spin correlation of top quark pairs have been presented. Events in the dilepton channels are analyzed in an optimized spin quantization basis (off-diagonal basis). The dilepton channels are cleaner and suffer less from combinatorics than $\ell + jets$ channels, and more importantly, particles most sensitive to the polarization of the top quark are identified. Thus, these channels are quite suitable for the study of spin correlation. Dilepton events are reconstructed using the neutrino-weighting method

which was used in the mass analysis in these channels. The angles θ_+ and θ_- between the off-diagonal bases and the flight direction of leptons are calculated from the solutions returned by the event fitter. The two dimensional distributions of $(\cos\theta_+, \cos\theta_-)$ can be parameterized as $1 + \kappa \cos\theta_+ \cos\theta_-$, where κ is the correlation factor. By folding the effects of finite resolutions and acceptances into the theoretical predictions and comparing with the data distribution, information on κ can be extracted. Using the method of binned likelihood we obtain a lower bound of $\kappa > -0.25$ at 68%.

Although this does not rule out the hypothesis that the spins of top quark pairs are not correlated, this analysis is the first of its kind. And in the next run at the Tevatron, one should be able to distinguish spin correlation at better than 2.5 standard deviations.

Appendix A

Useful Numbers and Equations

in High-Energy Experiments

A.1 Energy Loss of Particles

- Ionization energy loss by charged particle of mass M:

$$-\frac{dE}{dx} = Kz^2\frac{Z}{A}\frac{1}{\beta^2}\left[\frac{1}{2}\ln\frac{2m_ec^2\beta^2\gamma^2T_{max}}{I^2} - \beta^2 - \frac{\delta}{2}\right] \qquad (A.1)$$

where,

$$K = 4\pi N_A r_e^2 m_e c^2 = 0.307\,\text{MeV g}^{-1}\,\text{cm}^2 \qquad (A.2)$$

$$T_{max} \quad = \quad \frac{2m_e c^2 \beta^2 \gamma^2}{1 + 2\gamma m_e/M + (m_e/M)^2}. \tag{A.3}$$

$$I \quad : \quad \text{Mean excitation energy} \approx (10 \pm 1\text{eV}) \times Z. \tag{A.4}$$

$$\delta \quad : \quad \text{Density effect correction.} \tag{A.5}$$

If $M >> 2\gamma m_e$ then the equation above can be approximated by:

$$-\frac{dE}{dx} = 0.307 z^2 \frac{Z}{A} \frac{1}{\beta^2} \left[\ln(1 \times 10^5 \beta^2 \gamma^2) - \beta^2 \right] \tag{A.6}$$

- Ionization loss minima:

$$\beta\gamma \approx 3 \tag{A.7}$$

with

$$-dE/dx \approx 1 \sim 2 \text{ MeV/g/cm}^2 \tag{A.8}$$

- Radiation length:

$$X_0 = \frac{716 A}{Z(Z+1)\ln(287/\sqrt{Z})} \text{ g/cm}^2 \tag{A.9}$$

- Critical energy:

$$E_c = \frac{610}{Z + 1.24} \text{ MeV} \tag{A.10}$$

$(M/m_e)^2$ should be multiplied to find the critical energy for an incident particle with mass M.

- Multiple scattering:

$$\theta_{\text{plane}}^{\text{rms}} = \frac{13.6 \text{ MeV}}{\beta cp} z \sqrt{\frac{x}{X_0}} \qquad (A.11)$$

- Moliere radius:

$$R_M = \frac{X_0 \; 21 \text{ MeV}}{E_c} \qquad (A.12)$$

- Photoelectric cross section: $\propto Z^5$

- Mean free path of photon: $\frac{9}{7}X_0$

A.2 Numbers Related to Particle Detectors

- Organic scintillator photon yields: 100 eV/photon

- NaI light output: 25 eV/photon

- Čerenkov light output: $N_{p.e.} \approx 90 \text{ cm}^{-1} \langle \sin \theta_c \rangle$, where $\cos \theta_c = (n\beta)^{-1}$. Assuming detection efficiency of 30% and light collection efficiency of 90%.

Material	Z	$\lambda_I \left(\frac{\text{g}}{\text{cm}^2}\right)$	$\frac{dE}{dx}\big|_{min} \left(\frac{\text{MeV}}{\text{g}\cdot\text{cm}^2}\right)$	$X_0 \left(\frac{\text{MeV}}{\text{g}\cdot\text{cm}^2}\right)$	Density $\left(\frac{\text{g}}{\text{cm}^3}\right)$
Be	4	75.2	1.59	65.19	1.85
C	6	86.3	1.75	42.70	2.27
Al	13	106.4	1.62	24.01	2.70
Ti	22	124.9	1.48	16.17	4.54
Fe	26	131.9	1.45	13.84	7.87
W	74	185	1.15	6.76	19.3
Pb	82	194	1.12	6.37	11.35
U	92	199	1.082	6.00	18.95
H_2O		86.3	1.991	36.08	1.00
SiO_2		97.4	1.70	27.05	2.20
Ethane gas		75.7	2.304	45.47	1.36×10^{-3}
Polystyrene		81.9	1.936	43.72	1.032
BGO		157	1.251	7.97	7.1
CsI		167	1.243	8.39	4.53
G10		90.2	1.87	33.0	1.7

Table A.1: Physical properties of materials frequently used in high-energy physics.

- Semiconductor detectors

  - Physical properties of Silicon:

    $\mu_e = 1350 \text{ cm}^2/\text{Vs}$, $\mu_h = 480 \text{ cm}^2/\text{Vs}$. Mobilities are almost constant for $E < 10^3 \text{ V/cm}$. For E between $10^3 - 10^4 \text{ V/cm}$, μ varies as $E^{-1/2}$ and as E^{-1} for $> 10^4 \text{ V/cm}$. The velocity saturates to about 10^7 cm/s.

  - Average energy for electron-hole creation:

    3.62 eV (Si at 300K), 2.96 eV (Ge at 77K).

- Fano factor: ~ 0.12

- Gaseous detectors

  - Typical ion mobility: $1 \sim 1.5 \times 10^{-4} \mathrm{m}^2 \cdot \mathrm{atm/V} \cdot \mathrm{s}$. Electron mobility is typically 1000 times greater than this.

  - Mean energy for ion-electron creation:

    22 eV (Xe), 26 eV (Ar), $C_4 H_{10}$.

  - Fano factor: $0.2^{+0.01}_{-0.02}$ (Ar 100%)

  - Typical gas amplification in proportional mode: $\sim 10^3$.

- Photomultiplier tubes

  - Typical gain: $\sim 10^6$.

  - Dark current: on the order of nA.

  - Gain variation: $\propto N \delta V_{in}$, where N is the number of stages

- Particle momentum in a uniform magnetic field: $p_T = 0.3 z B R$, where B is the magnetic field strength in Tesla, R in m and p_T in GeV

- Particle momentum resolution in tracker:

– Resolution due to finite position resolution measurement:

$$\left(\frac{\delta p_T}{p_T}\right)_{pos} = \sqrt{\frac{720}{N+4}}\frac{\delta r}{0.3BL^2},\tag{A.13}$$

where N is the number of points sampled and δr is the position resolution.

– Resolution due to multiple scattering:

$$\left(\frac{\delta p_T}{p_T}\right)_{ms} = \frac{13.6\text{ MeV}}{\beta c p_T}z\sqrt{\frac{x}{X_0}}\tag{A.14}$$

• Statistics related numbers and formulae

– FWHM $= 2.35\sigma$

– $P(\mu - \sigma < x < \mu + \sigma) = 0.683$

– $P(\mu - 2\sigma < x < \mu + 2\sigma) = 0.955$

– $P(\mu - 3\sigma < x < \mu + 3\sigma) = 0.9973$

– $P(\mu - 4\sigma < x < \mu + 4\sigma) = 0.999937$

– $P(\mu - 5\sigma < x < \mu + 5\sigma) = 0.999999427$

– Gaussian distribution:

$$f(x; \mu, \sigma^2) = \frac{1}{\sqrt{2\pi}\sigma} \exp(-\frac{(x-\mu)^2}{2\sigma^2}). \qquad \text{(A.15)}$$

– Poisson distribution:

$$f(r; \mu) = \frac{\mu^r e^{-\mu}}{r!}. \qquad \text{(A.16)}$$

– Breit-Wigner:

$$f(m; M_0, \Gamma) = \frac{1}{2\pi} \frac{\Gamma}{(m-M_0)^2 + (\Gamma/2)^2}. \qquad \text{(A.17)}$$

Appendix B

Notations and Conventions

B.1 Natural Units and Conventions

- Natural Units:

$$\hbar \;=\; c \;=\; 1, \;\; (\hbar \;=\; \frac{h}{2\pi}) \;.$$

- Transform rules of Unit:

$$
\begin{aligned}
1 \text{ kg} &= 5.61 \times 10^{26} \text{ GeV} : \left(\frac{\text{GeV}}{\text{c}^2}\right), \\
1 \, m &= 5.07 \times 10^{15} \text{ GeV}^{-1} : \left(\frac{\hbar c}{\text{GeV}}\right), \\
1 \text{ sec} &= 1.52 \times 10^{24} \text{ GeV}^{-1} : \left(\frac{\hbar}{\text{GeV}}\right),
\end{aligned}
$$

$$1 \text{ TeV} \; = \; 10^3 \text{ GeV} \; = \; 10^6 \text{ MeV} \; = \; 10^9 \text{ KeV} \; = \; 10^{12} \text{ eV},$$

$$1 \text{ fermi} \; = \; 1 \text{ fm} \; = \; 10^{-13} \text{ cm} \; = \; 10^{-15} \text{ m} \; = \; 5.07 \text{ GeV}^{-1},$$

$$(1 \text{ fermi})^2 \; = \; 10 \text{ mb} \; = \; 10^4 \; \mu\text{b} \; = \; 10^7 \text{ nb} \; = \; 10^{10} \text{ pb} \; = \; 10^{13} \text{ fb},$$

$$1 \; b \; = \; 10^2 \text{ fm}^2 \; = \; 10^{-24} \text{ cm}^2 \; = \; 10^{-28} \text{ m}^2,$$

$$(1 \text{ GeV})^{-2} \; = \; 0.389 \text{ mb} \; = \; 3.89 \; \times \; 10^8 \text{ pb} \; .$$

B.2 Metric Tensor

Our Metric Tensor $g_{\mu\nu}$ in Minkowski Space $\{x^\mu \; : \; (\; \mu \; = \; 0,1,2,3 \;)\}$,

$$g_{\mu\nu} \; = \; g^{\mu\nu} \; = \; \begin{pmatrix} +1 & 0 & 0 & 0 \\ 0 & -1 & 0 & 0 \\ 0 & 0 & -1 & 0 \\ 0 & 0 & 0 & -1 \end{pmatrix} .$$

B.3 Coordinates and Momenta

The space-time coordinates $(t, x, y, z) \equiv (t, \boldsymbol{x})$ are denoted by the covariant four-vector:

$$x^\mu \; \equiv \; \left(x^0, x^1, x^2, x^3\right)$$

$$\equiv \ (t, x, y, z) \ .$$

The covariant four-vector x^μ is obtained by the sign of the space components:

$$
\begin{aligned}
x_\mu &\equiv \ (x_0, x_1, x_2, x_3) \\
&\equiv \ (t, -x, -y, -z) \\
&= \ g_{\mu\nu} x^\nu \ .
\end{aligned}
$$

The inner product is given by

$$
\begin{aligned}
x \cdot x &\equiv \ x^\mu x_\mu \\
&= \ t^2 - \boldsymbol{x}^2 \ .
\end{aligned}
$$

Momentum vectors are similarly defined by

$$
\begin{aligned}
p^\mu &\equiv \ (p^0, p^1, p^2, p^3) \\
&\equiv \ (E, p_x, p_y, p_z) \\
&= \ g^{\mu\nu} p_\nu \ .
\end{aligned}
$$

The inner product is given by

$$
\begin{aligned}
p_1 \cdot p_2 &\equiv p_1^{\mu} p_{2\mu} \\
&= E_1 E_2 - \boldsymbol{p}_1 \cdot \boldsymbol{p}_2 \ .
\end{aligned}
$$

B.4 Pauli Matrices

- Pauli σ Matrices:

$$
\sigma_1 = \begin{pmatrix} 0 & 1 \\ 1 & 0 \end{pmatrix} \ , \quad
\sigma_2 = \begin{pmatrix} 0 & -i \\ i & 0 \end{pmatrix} \ , \quad
\sigma_3 = \begin{pmatrix} 1 & 0 \\ 0 & -1 \end{pmatrix} \ .
$$

- The Relations of Pauli Matrices:

$$
\begin{aligned}
\{\sigma_i, \sigma_j\} &= 2\delta_{ij}, \\
[\sigma_i, \sigma_j] &= 2i\varepsilon_{ijk}\sigma_k \ .
\end{aligned}
$$

- The Properties of Pauli Matrices:

$$
\sigma_i^{\dagger} = \sigma_i, \ \det(\sigma_i) = -1, \ \mathrm{Tr}[\sigma_i] = 0 \ .
$$

- Useful Relation:

$$(\, \boldsymbol{\sigma} \, \cdot \, \boldsymbol{a} \,)(\, \boldsymbol{\sigma} \, \cdot \, \boldsymbol{b} \,) \; = \; (\, \boldsymbol{a} \, \cdot \, \boldsymbol{b} \,) + i \, \boldsymbol{\sigma} \, \cdot (\, \boldsymbol{a} \, \times \, \boldsymbol{b} \,) \, .$$

B.5 γ Matrices

- Dirac γ Matrices, $\gamma^\mu \; = \; (\gamma^0, \; \boldsymbol{\gamma} \,)$:

$$\{\gamma^\mu, \gamma^\nu\} \;\; = \;\; \gamma^\mu \gamma^\nu \; + \; \gamma^\nu \gamma^\mu \; = \; 2 \; g^{\mu\nu},$$

$$[\gamma^\mu, \gamma^\nu] \;\; = \;\; \gamma^\mu \gamma^\nu \; - \; \gamma^\nu \gamma^\mu \; = \; - \, 2i \; \sigma^{\mu\nu},$$

$$\gamma_\mu \;\; = \;\; g_{\mu\nu} \gamma^\nu \; = \; (\gamma^0, - \; \boldsymbol{\gamma} \,) \, .$$

- γ_5 Matrix:

$$\gamma_5 \equiv \;\; \gamma^5 \; = \; i \gamma^0 \gamma^1 \gamma^2 \gamma^3 \; = \;\; - \frac{i}{4!} \varepsilon_{\mu\nu\lambda\sigma} \gamma^\mu \gamma^\nu \gamma^\lambda \gamma^\sigma \; ,$$

$$\varepsilon^{0123} \;\; = \;\; - \varepsilon_{0123} \; = \;\; + 1 \, .$$

- The Relation of γ_5 Matrix:

$$\gamma_5^2 \;\; = \;\; 1,$$

$$\{\gamma_5, \gamma^\mu\} = 0 \ .$$

- Familiar Presentation of γ:

$$\gamma^0 = \begin{pmatrix} 1 & 0 \\ 0 & -1 \end{pmatrix} , \ \boldsymbol{\gamma} = \begin{pmatrix} 0 & \boldsymbol{\sigma} \\ -\boldsymbol{\sigma} & 0 \end{pmatrix} , \ \gamma_5 = \begin{pmatrix} 0 & 1 \\ 1 & 0 \end{pmatrix} ,$$

where $\boldsymbol{\sigma}$ is given by

$$\boldsymbol{\sigma} = (\sigma_1, \sigma_2, \sigma_3).$$

B.6   Dirac Spinors

Dirac spinors for fermion with momentum p, $u_\lambda(p)$ and for anti-fermion with momentum p $v_\lambda(p)$ satisfy following equations. (p: momentum , λ: spin components , m: fermion mass.)

- Equations of Motion:

$$(\not{p} - m)u_\lambda(p) = 0,$$

$$(\not{p} + m)v_\lambda(p) = 0 \ .$$

- Normalization:

$$\bar{u}_\lambda(p)u_{\lambda'}(p) = 2m\,\delta_{\lambda\lambda'},$$

$$\bar{v}_\lambda(p)v_{\lambda'}(p) = -2m\,\delta_{\lambda\lambda'}\ .$$

- Projection Operators (In the case of Spin Sum):

$$\sum_\lambda u_\lambda(p)\bar{u}_\lambda(p) = \not{p} + m,$$

$$\sum_\lambda v_\lambda(p)\bar{v}_\lambda(p) = \not{p} - m\ .$$

B.7   Spin Vector

spin vector s^μ for fermions is taken to be,

$$s^\mu \equiv \left(\frac{\vec{p}\cdot\vec{s}}{m},\ \vec{s}+\frac{\vec{p}(\vec{p}\cdot\vec{s})}{m(p^0+m)}\right)\ .$$

where

$$(\vec{s})^2 = 1,\ \ s^2 = s^\mu s_\mu = -1,\ s^\mu\,p_\mu = s\cdot p = 0\ .$$

- The Relations between Spin Vector and Spinor:

$$\bar{u}(p,s)\gamma^{\mu}\gamma_5 u(p,s) \ = \ 2m \ s^{\mu} \ .$$

- Projection Operators:

$$u(p,s)\bar{u}(p,s) \ = \ (\slashed{p} \ + \ m)\frac{1+\gamma_5\slashed{s}}{2},$$

$$v(p,s)\bar{v}(p,s) \ = \ (\slashed{p} \ - \ m)\frac{1+\gamma_5\slashed{s}}{2} \ .$$

Appendix C

Useful Formulae

C.1 Dirac γ Matrices

- $\gamma^\dagger$ and $\overline{\gamma}$:

$$\gamma^{\mu\dagger} = \gamma^0 \gamma^\mu \gamma^0 ,$$

$$\gamma^{0\dagger} = \gamma^0 , \; \gamma^{k\dagger} = -\gamma^k \; (\text{where} \; k = 1, \, 2, \, 3) ,$$

$$\gamma^{5\dagger} = \gamma^5 , \; \sigma_{\mu\nu}^\dagger = \sigma_{\mu\nu} ,$$

$$\overline{\Gamma} \equiv \gamma^0 \Gamma^\dagger \gamma^0 ,$$

$$\overline{\gamma}^\mu = \gamma^0 \gamma^{\mu\dagger} \gamma^0 = \gamma^\mu , \; \overline{\gamma^\mu \gamma^5} = \gamma^\mu \gamma^5 ,$$

$$\overline{\sigma}^{\mu\nu} = \gamma^0 \sigma^{\mu\nu\dagger} \gamma^0 = \sigma^{\mu\nu} ,$$

$$\overline{i\gamma_5} \;=\; \gamma^0 \left(i\gamma_5\right) \gamma^0 \;=\; i\gamma_5 \;,$$

$$\overline{\rlap{/}a\,\rlap{/}b\,\rlap{/}c\,\rlap{/}d\cdots\rlap{/}p} \;=\; \rlap{/}p\cdots\rlap{/}c\,\rlap{/}b\,\rlap{/}a \;.$$

- Matrix Element:

$$\left[\bar{u}(p',s')\,\Gamma\,u(p,s)\right]^{\dagger} \;=\; \bar{u}(p,s)\,\overline{\Gamma}\,u(p',s') \;,$$

- Trace Theorems:

$$\mathrm{Tr}\left[\gamma^{\mu_1}\gamma^{\mu_2}\cdots\gamma^{\mu_n}\right] \;=\; 0 \;\;(\text{ for } n = \text{odd }) \;,$$

$$\mathrm{Tr}\,1 \;=\; 4 \;,$$

$$\mathrm{Tr}\left[\gamma^\mu\gamma^\nu\right] \;=\; 4g^{\mu\nu} \;,$$

$$\mathrm{Tr}\left[\gamma^\mu\gamma^\nu\gamma^\lambda\gamma^\sigma\right] \;=\; 4\left(g^{\mu\nu}g^{\lambda\sigma} \;-\; g^{\mu\lambda}g^{\nu\sigma} \;+\; g^{\mu\sigma}g^{\nu\lambda}\right) \;,$$

$$\begin{aligned}
\mathrm{Tr}\left[\gamma^\lambda\gamma^\mu\gamma^\nu\gamma^\rho\gamma^\sigma\gamma^\tau\right] \;=\;& g^{\lambda\mu}\mathrm{Tr}\left[\gamma^\nu\gamma^\rho\gamma^\sigma\gamma^\tau\right] - g^{\lambda\nu}\mathrm{Tr}\left[\gamma^\mu\gamma^\rho\gamma^\sigma\gamma^\tau\right] \\[4pt]
&+ g^{\lambda\rho}\mathrm{Tr}\left[\gamma^\mu\gamma^\nu\gamma^\sigma\gamma^\tau\right] - g^{\lambda\sigma}\mathrm{Tr}\left[\gamma^\mu\gamma^\nu\gamma^\rho\gamma^\tau\right] \\[4pt]
&+ g^{\lambda\tau}\mathrm{Tr}\left[\gamma^\mu\gamma^\nu\gamma^\rho\gamma^\sigma\right] \;,
\end{aligned}$$

$$\begin{aligned}
\mathrm{Tr}\left[\gamma^{\mu_1}\gamma^{\mu_2}\cdots\gamma^{\mu_n}\right] \;=\;& g^{\mu_1\mu_2}\mathrm{Tr}\left[\gamma^{\mu_3}\gamma^{\mu_4}\cdots\gamma^{\mu_n}\right] \\[4pt]
&- g^{\mu_1\mu_3}\mathrm{Tr}\left[\gamma^{\mu_2}\gamma^{\mu_4}\cdots\gamma^{\mu_n}\right] \\[4pt]
&+ \cdots + g^{\mu_1\mu_n}\mathrm{Tr}\left[\gamma^{\mu_1}\gamma^{\mu_2}\cdots\gamma^{\mu_{n-1}}\right] \;\;(\text{ for } n = \text{even }) \;,
\end{aligned}$$

$$\text{Tr}\left[\gamma_5\gamma^{\mu_1}\gamma^{\mu_2}\cdots\gamma^{\mu_n}\right] = 0 \quad (\text{ for } n \leq 3)$$

$$\text{Tr}\left[\gamma_5\gamma^\mu\gamma^\nu\gamma^\lambda\gamma^\sigma\right] = -4i\varepsilon^{\mu\nu\lambda\sigma} \ ,$$

$$\text{Tr}\left[\gamma_5\gamma^\lambda\gamma^\mu\gamma^\nu\gamma^\rho\gamma^\sigma\gamma^\tau\right] = -4i(\varepsilon^{\lambda\mu\nu\rho}g^{\sigma\tau} - \varepsilon^{\lambda\mu\nu\sigma}g^{\rho\tau} + \varepsilon^{\lambda\mu\nu\tau}g^{\rho\sigma}$$
$$- \varepsilon^{\nu\tau\sigma\rho}g^{\lambda\mu} + \varepsilon^{\mu\tau\sigma\rho}g^{\lambda\nu} - \varepsilon^{\lambda\tau\sigma\rho}g^{\mu\nu}) \ .$$

- γ Identities:

$$\gamma_\mu\gamma^\mu = 4 \ ,$$

$$\gamma_\mu\gamma^\nu\gamma^\mu = -2\gamma^\nu \ ,$$

$$\gamma_\mu\gamma^\lambda\gamma^\nu\gamma^\mu = 4g_{\lambda\nu} \ ,$$

$$\gamma_\mu\gamma^\lambda\gamma^\nu\gamma^\sigma\gamma^\mu = -2\gamma^\sigma\gamma^\nu\gamma^\lambda \ ,$$

$$\gamma_\mu\gamma^\lambda\gamma^\nu\gamma^\sigma\gamma^\rho\gamma^\mu = 2(\gamma^\rho\gamma^\lambda\gamma^\nu\gamma^\sigma + \gamma^\sigma\gamma^\nu\gamma^\lambda\gamma^\rho) \ ,$$

- Version:

$$\gamma_\mu \not{a}\gamma^\mu = -2 \not{a} \ ,$$

$$\gamma_\mu \not{a} \not{b}\gamma^\mu = 4a \cdot b \ ,$$

$$\gamma_\mu \not{a} \not{b} \not{c}\gamma^\mu = -2 \not{c} \not{b} \not{a} \ ,$$

$$\gamma_\mu \not{a} \not{b} \not{c} \not{d}\gamma^\mu = 2 (\not{d} \not{a} \not{b} \not{c} + \not{c} \not{b} \not{a} \not{d})$$

- Other Relations:

$$g^{\mu\nu}\varepsilon^{\lambda\sigma\tau\rho} - g^{\mu\lambda}\varepsilon^{\nu\sigma\tau\rho} + g^{\mu\sigma}\varepsilon^{\nu\lambda\tau\rho} - g^{\mu\tau}\varepsilon^{\nu\lambda\sigma\rho} + g^{\mu\rho}\varepsilon^{\nu\lambda\sigma\tau} \; = \; 0 \; ,$$

$$(g^{\mu\nu}\varepsilon^{\lambda\sigma\tau\rho} \; = \; g^{\mu\lambda}\varepsilon^{\nu\sigma\tau\rho} + g^{\mu\sigma}\varepsilon^{\lambda\nu\tau\rho} + g^{\mu\tau}\varepsilon^{\lambda\sigma\nu\rho} + g^{\mu\rho}\varepsilon^{\lambda\sigma\tau\nu}) \; .$$

C.2 Conventions for Dimensional Regularization

- γ Identities (D-dimension):

$$\gamma_\mu\gamma^\mu \; = \; D \; ,$$

$$\gamma_\mu\gamma^\nu\gamma^\mu \; = \; (2-D)\gamma^\nu \; ,$$

$$\gamma_\mu\gamma^\lambda\gamma^\nu\gamma^\mu \; = \; 4g_{\lambda\nu} + (D-4)\gamma^\lambda\gamma^\nu \; ,$$

$$\gamma_\mu\gamma^\lambda\gamma^\nu\gamma^\sigma\gamma^\mu \; = \; -2\gamma^\sigma\gamma^\nu\gamma^\lambda - (D-4)\gamma^\lambda\gamma^\nu\gamma^\sigma \; ,$$

$$\gamma_\mu\gamma^\lambda\gamma^\nu\gamma^\sigma\gamma^\rho\gamma^\mu \; = \; 2(\gamma^\rho\gamma^\lambda\gamma^\nu\gamma^\sigma + \gamma^\sigma\gamma^\nu\gamma^\lambda\gamma^\rho) + (D-4)\gamma^\lambda\gamma^\nu\gamma^\sigma\gamma^\rho \; ,$$

- Version:

$$\gamma_\mu \; \rlap{/}{a}\gamma^\mu \; = \; (2-D) \; \rlap{/}{a} \; ,$$

$$\gamma_\mu \, \slashed{a} \, \slashed{b} \gamma^\mu \;\; = \;\; 4a \cdot b \; + \; (D-4) \, \slashed{a} \, \slashed{b} \; ,$$

$$\gamma_\mu \, \slashed{a} \, \slashed{b} \, \slashed{c} \gamma^\mu \;\; = \;\; -2 \, \slashed{c} \, \slashed{b} \, \slashed{a} - (D-4) \, \slashed{a} \, \slashed{b} \, \slashed{c} \; ,$$

$$\gamma_\mu \, \slashed{a} \, \slashed{b} \, \slashed{c} \, \slashed{d} \gamma^\mu \;\; = \;\; 2 \, (\slashed{d} \, \slashed{a} \, \slashed{b} \, \slashed{c} + \slashed{c} \, \slashed{b} \, \slashed{a} \, \slashed{d}) + (D-4) \, \slashed{a} \, \slashed{b} \, \slashed{c} \, \slashed{d} \; .$$

- Expansion in ε:

$$a^\varepsilon \;\; = \;\; e^{\varepsilon \ln a} \;\; = \;\; 1 + \varepsilon \ln a + \frac{\varepsilon^2}{2!} (\ln a)^2 + \frac{\varepsilon^3}{3!} (\ln a)^3 + \mathcal{O}(\varepsilon^4) \; ,$$

$$\Gamma(\varepsilon) \;\; = \;\; \frac{1}{\varepsilon} - \gamma_E + \frac{\varepsilon}{2} (\gamma_E^2 + \frac{\pi^2}{6}) + \mathcal{O}(\varepsilon^2) \; ,$$

$$\Gamma(\varepsilon - 1) \;\; = \;\; -\frac{1}{\varepsilon} - (\gamma_E - 1) - \frac{\varepsilon}{2} (\gamma_E^2 - 2\gamma_E + \frac{\pi^2}{6}) + \mathcal{O}(\varepsilon^2) \; ,$$

$$\Gamma(\varepsilon - n) \;\; = \;\; \frac{(-1)^n}{n!} \left[\frac{1}{\varepsilon} + (\sum_{k=1}^n \frac{1}{k}) - \gamma_E \right] + \mathcal{O}(\varepsilon) \; .$$

- Γ - Function:

$$z\Gamma(z) \;\; = \;\; \Gamma(z+1) \; ,$$

$$\Gamma(z)\Gamma(1-z) \;\; = \;\; \frac{\pi}{\sin \pi z} \; ,$$

$$\Gamma\left(z + \frac{1}{2}\right) \Gamma\left(-z + \frac{1}{2}\right) \;\; = \;\; \frac{\pi}{\cos \pi z} \; ,$$

$$\Gamma(2z) \;\; = \;\; \frac{2^{2z-1}}{\sqrt{\pi}} \Gamma(z) \Gamma\left(z + \frac{1}{2}\right) \; ,$$

$$\Gamma(1) \;\; = \;\; \Gamma(2) \;\; = \;\; 1, \Gamma(3) \;\; = \;\; 2, \; \Gamma(n+1) \;\; = \;\; n!,$$

$$\Gamma\left(\frac{1}{2}\right) \;\; = \;\; \sqrt{\pi} \; , \Gamma\left(\frac{3}{2}\right) \;\; = \;\; \frac{\sqrt{\pi}}{2} \; , \Gamma\left(\frac{5}{2}\right) \;\; = \;\; \frac{3\sqrt{\pi}}{4} \; ,$$

$$\Gamma\left(n + \frac{1}{2}\right) = \frac{(2n-1)!!}{2^n}\sqrt{\pi} = \frac{(2n)!}{4^n n!}\sqrt{\pi},$$

$$\Gamma\left(-n + \frac{1}{2}\right) = \frac{(-)^n 2^n}{(2n-1)!!}\sqrt{\pi} = \frac{(^4)^n n!}{(2n)!}\sqrt{\pi}.$$

- ψ - Function:

$$\psi(1) = -\gamma , \; \psi(2) = 1 - \gamma , \psi(n) = \sum_{i=1}^{n-1}\frac{1}{i} - \gamma ,$$

$$\psi\left(\frac{1}{2}\right) = -\ln 4 - \gamma , \psi\left(\pm n + \frac{1}{2}\right) = 2\sum_{i=1}^{n}\frac{1}{2i-1} - \ln 4 - \gamma .$$

- β - function:

$$B(x,y) \equiv \int_0^1 \xi^{x-1}(1-\xi)^{y-1} \qquad (x, y > 0) ,$$

$$B(x,y) = B(y,x) ,$$

$$B(x,y) = 2\int_0^{\pi/2} d\theta \cos^{2x-1}\theta \; \sin^{2y-1}\theta ,$$

$$B(x,x) = 2^{1-2x}B(x, \frac{1}{2}) ,$$

$$B(x,y) = \frac{\Gamma(x)\Gamma(y)}{\Gamma(x+y)} .$$

- Feynman Parametrization:

$$\frac{1}{a_1 a_2 \cdots a_n} = (n-1)!\int d\alpha_1 d\alpha_2 \cdots d\alpha_n \frac{\delta(1 - \alpha_1 - \alpha_2 - \cdots - \alpha_n)}{(\alpha_1 a_1 + \alpha_2 a_2 + \cdots + \alpha_n a_n)^n} ,$$

$$\frac{1}{AB} = \int_0^1 dx \frac{1}{[xA + (1-x)B]^2} \ ,$$

$$\frac{1}{A^\alpha B^\beta} = \frac{\Gamma(\alpha+\beta)}{\Gamma(\alpha)\Gamma(\beta)} \int_0^1 dx \frac{x^{\alpha-1}(1-x)^{\beta-1}}{[xA + (1-x)B]^{\alpha+\beta}} \ ,$$

$$\frac{1}{ABC} = \int_0^1 dx \int_0^{1-x} dy \frac{2}{[xA + yB + (1-x-y)C]^3} \ .$$

- D-Dimension Integral:

$$\int \frac{d^D k}{(2\pi)^D} \frac{1}{[k^2 - L]^n} = \frac{i}{(4\pi)^{\frac{D}{2}}} (-)^n \frac{\Gamma\left(n - \frac{D}{2}\right)}{\Gamma(n)} L^{\frac{D}{2}-n} \ ,$$

$$\int \frac{d^D k}{(2\pi)^D} \frac{k^2}{[k^2 - L]^n} = \frac{i}{(4\pi)^{\frac{D}{2}}} (-)^{n+1} \frac{\Gamma\left(n - 1 - \frac{D}{2}\right)}{\Gamma(n)} \frac{D}{2} L^{\frac{D}{2}+1-n} \ ,$$

$$\int \frac{d^D k}{(2\pi)^D} \frac{k^\mu k^\nu}{[k^2 - L]^n} = \frac{i}{(4\pi)^{\frac{D}{2}}} (-)^{n+1} \frac{\Gamma\left(n - 1 - \frac{D}{2}\right)}{\Gamma(n)} \frac{g^{\mu\nu}}{2} L^{\frac{D}{2}+1-n} \ ,$$

$$\int \frac{d^D k}{(2\pi)^D} \frac{k^\mu k^\nu k^\lambda k^\rho}{[k^2 - L]^n} = \frac{i}{(4\pi)^{\frac{D}{2}}} (-)^n \frac{\Gamma\left(n - 2 - \frac{D}{2}\right)}{\Gamma(n)}$$
$$\times \frac{1}{4} \left(g^{\mu\nu} g^{\lambda\rho} + g^{\mu\lambda} g^{\nu\rho} + g^{\mu\rho} g^{\nu\lambda} \right) L^{\frac{D}{2}+2-n} \ ,$$

$$\int \frac{d^D k}{(2\pi)^D} k^\mu k^\nu f\left(k^2\right) = \frac{g^{\mu\nu}}{D} \int \frac{d^D k}{(2\pi)^D} k^2 f\left(k^2\right) \ .$$

C.3   SU(N) Generators

The SU(N) Generators $T^a(a = 1, 2, \ldots, N^2 - 1)$ are hermitian and traceless matrices, which generate the closed SU(N) algebra.

$$\left[T^a, T^b \right] = i f^{abc} T^c .$$

The fundamental representation is N-dimensional where T^a satisfy an additional relation

$$\left\{ T^a, T^b \right\} = \frac{1}{N} \delta_{ab} + d^{abc} T^c ,$$

which is consistent with the normalization

$$\mathrm{Tr} \left(T^a T^b \right) = \frac{1}{2} \delta_{ab} .$$

Here d^{abc} is totally symmetric in a, b and c.

It's given by

$$d^{abc} = 2 \mathrm{Tr} \left[\{ T^a, T^b \} T^c \right] .$$

According to above equations we get following relation.

$$T^a T^b = \frac{1}{2N}\delta_{ab} + \frac{1}{2}d^{abc}T^c + \frac{1}{2}i f^{abc}T^c \ .$$

The SU(N) structure constants satisfy following relation.

$$f^{ade}f^{bef}f^{cfd} = \frac{N}{2}f^{abc} \ .$$

and Jacobi Identities

$$f^{abe}f^{cde} + f^{cbe}f^{dae} + f^{dbe}f^{ace} = 0 \ ,$$

$$f^{abe}d^{cde} + f^{cbe}d^{dae} + f^{dbe}d^{ace} = 0 \ .$$

For The SU(3) Generators and structure constants are explicitly written down as follows.

$$\lambda_1 = \begin{pmatrix} 0 & 1 & 0 \\ 1 & 0 & 0 \\ 0 & 0 & 0 \end{pmatrix}, \lambda_2 = \begin{pmatrix} 0 & -i & 0 \\ i & 0 & 0 \\ 0 & 0 & 0 \end{pmatrix},$$

$$\lambda_3 = \begin{pmatrix} 1 & 0 & 0 \\ 0 & -1 & 0 \\ 0 & 0 & 0 \end{pmatrix}, \lambda_4 = \begin{pmatrix} 0 & 0 & 1 \\ 0 & 0 & 0 \\ 1 & 0 & 0 \end{pmatrix},$$

$$\lambda_5 = \begin{pmatrix} 0 & 0 & -i \\ 0 & 0 & 0 \\ i & 0 & 0 \end{pmatrix}, \lambda_6 = \begin{pmatrix} 0 & 0 & 0 \\ 0 & 0 & 1 \\ 0 & 1 & 0 \end{pmatrix},$$

$$\lambda_7 = \begin{pmatrix} 0 & 0 & 0 \\ 0 & 0 & -i \\ 0 & i & 0 \end{pmatrix}, \lambda_8 = \frac{1}{\sqrt{3}} \begin{pmatrix} 1 & 0 & 0 \\ 0 & 1 & 0 \\ 0 & 0 & -2 \end{pmatrix},$$

where $\quad T^a = \dfrac{\lambda^a}{2}.$

Non-zero components of structure constants are

$$f^{123} = 1,$$

$$f^{147} = -f^{156} = f^{246} = f^{257} = f^{345} = -f^{367} = \frac{1}{2},$$

$$f^{458} = f^{678} = \frac{\sqrt{3}}{2}.$$

Now we can get some formulae, of course these formulae are independent of

the explicit representation of SU(N) Generators and structure constants.

$$(T^c T^c)_{ij} = C_2(R)\delta_{ij} \; ,$$

$$T^c T^a T^c = \left[-\frac{1}{2} C_2(G) + C_2(R) \right] T^a \; ,$$

$$\mathrm{Tr}\left[T^a T^b \right] = \frac{1}{2}\delta^{ab} \; ,$$

$$\mathrm{Tr}\left[T^a T^b T^c \right] = \frac{1}{4}(d^{abc} + i f^{abc}) \; ,$$

$$\mathrm{Tr}\left[T^a T^b T^c T^d \right] = \frac{1}{4N}\delta^{ab}\delta^{cd} + \frac{1}{8}(d^{abe} + i f^{abe})(d^{cde} + i f^{cde}) \; ,$$

$$f^{abc} T^b T^c = \frac{i}{2} f^{abc} f^{bcd} T^d$$

$$= \frac{i}{2} C_2(G) T^a \; .$$

$$C_2(R) = \frac{N^2 - 1}{2N}$$

$$f^{acd} f^{bcd} = C_2(G)\delta^{ab} = N\delta^{ab} \; .$$

Appendix D

Feynman Rules

D.1   QED Lagrangian

$$\mathcal{L}_{\mathrm{QED}} \;=\; \mathcal{L}_{class} \;+\; \mathcal{L}_{gauge} \;.$$

$$\mathcal{L}_{class} \;=\; \bar{\psi}\,(i\,\not{D}\;-\;m)\,\psi \;-\; \frac{1}{4}F_{\mu\nu}F^{\mu\nu}\;,$$

$$\mathcal{L}_{gauge} \;=\; -\frac{1}{2\alpha}\,(\partial^{\mu}A_{\mu})^{2}\;\;.$$

- Covariant Derivative and Field Strength Tensor:

$$D_\mu \equiv \partial_\mu - ieA_\mu \ ,$$

$$F_{\mu\nu} \equiv \partial_\mu A_\nu - \partial_\nu A_\mu \ ,$$

We split up the above Lagrangian into the free part $\mathcal{L}_0$ and the interaction part $\mathcal{L}_I$.
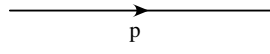
$$\mathcal{L}_{\mathrm{QED}} \equiv \mathcal{L}_0 + \mathcal{L}_I \ ,$$

$$\mathcal{L}_0 = \bar{\psi}(i\partial\!\!\!/ - m)\psi - \frac{1}{4}(\partial_\mu A_\nu - \partial_\nu A_\mu)(\partial^\mu A^\nu - \partial^\nu A^\mu)$$

$$- \frac{1}{2\alpha}(\partial^\mu A_\mu)^2 \ ,$$

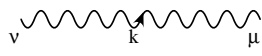$$\mathcal{L}_I = e\,\bar{\psi}\gamma^\mu\psi A_\mu.$$
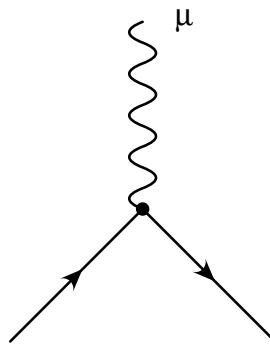
D.2   QED Feynman Rules

- Fermion Propagator:

$$\frac{i}{\not{p} - m + i\varepsilon}$$

- Photon Propagator:

$$\frac{-i}{k^2 + i\varepsilon}\left[g_{\mu\nu} - (1 - \alpha)\frac{k_\mu k_\nu}{k^2 + i\varepsilon}\right]$$

- Photon - Fermion Vertex:

$$ie\gamma_\mu$$

D.3   QCD Lagrangian

$$\mathcal{L}_{\text{QCD}} \;=\; \mathcal{L}_{class} \;+\; \mathcal{L}_{gauge} \;+\; \mathcal{L}_{ghost} \;,$$

$$
\begin{aligned}
\mathcal{L}_{class} &= \bar{\psi}\left(i\slashed{D} - m\right)\psi \;-\; \frac{1}{4}F^a_{\mu\nu}F^{\mu\nu,a} \;, \\
\mathcal{L}_{gauge} &= -\frac{1}{2\alpha}\left(G^\mu A^a_\mu\right)^2 \;, \\
\mathcal{L}_{ghost} &= \left(\partial^\mu \chi^{*a}\right)D^{ab}_\mu \chi^b \;.
\end{aligned}
$$

- χ, χ^* represent ghost and anti-ghost field.

- G^μ is given following,

  1. Coulomb Gauge: $\cdots$ $G^\mu = (0, \nabla)$

  2. Covariant Gauge: $\cdots$ $G^\mu = \partial^\mu$

     (a) Feynman Gauge: $\cdots \alpha = 1$

     (b) Landau Gauge: $\cdots \alpha = 0$

  3. Axial Gauge: $\cdots$ $G^\mu = n^\mu$ (Light-cone Vector)

  4. Temporal Gauge: $\cdots$ $G^\mu = (1, \; \mathbf{0} \;)$

- Covariant Derivative and Field Strength Tensor:

$$D_\mu \equiv \partial_\mu - ig_s A_\mu^a T^a \;,$$

$$F_{\mu\nu} \equiv \partial_\mu A_\nu - \partial_\nu A_\mu - ig_s \left[A_\mu, A_\nu\right]$$

$$= \left(\partial_\mu A_\nu^a - \partial_\nu A_\mu^a + g_s f^{abc} A_\mu^b A_\nu^c\right) T^a \;.$$

We split up the above Lagrangian into the free part $\mathcal{L}_0$ and the interaction part $\mathcal{L}_I$.

$$\mathcal{L}_{\text{QCD}} \equiv \mathcal{L}_0 + \mathcal{L}_I \;,$$

$$\mathcal{L}_0 = \bar{\psi}(i\slashed{\partial} - m)\psi - \frac{1}{4}(\partial_\mu A_\nu^a - \partial_\nu A_\mu^a)(\partial^\mu A^{a\nu} - \partial^\nu A^{a\mu})$$

$$- \frac{1}{2\alpha}(\partial^\mu A_\mu^a)^2 + (\partial_\mu \chi^{*a})(\partial^\mu \chi^a) \;,$$

$$\mathcal{L}_I = g_s \bar{\psi}\gamma^\mu T^a \psi A_\mu^a - \frac{g_s}{2} f^{abc}(\partial_\mu A_\nu^a - \partial_\nu A_\mu^a) A^{\mu b} A^{\nu c}$$

$$- \frac{g_s^2}{4} f^{abc} f^{ade} A_\mu^b A_\nu^c A^{\mu d} A^{\nu e} - g_s f^{abc}(\partial^\mu \chi^{*a})\chi^b A^{\mu c} \;.$$

D.4   Notation and Conventions

- Covariant Derivative:

$$D_{\mu,ij}[A] \equiv \partial_\mu \delta_{ij} - ig_s A_\mu^a [T^a]_{ij} \;,$$

$$D_\mu^{ab}[A] \;\equiv\; \partial_\mu \delta^{ab} \;-\; g_s f^{abc} A_\mu^c \;.$$

- Field Strength:

$$[D_\mu, D_\nu]_{ij} \;\equiv\; -ig_s F_{\mu\nu}^a [T^a]_{ij} \;,$$

$$[D_\mu, D_\nu]^{ab} \;\equiv\; -ig_s F_{\mu\nu}^c [T^c]^{ab}$$

$$=\; -g_s f^{abc} F_{\mu\nu}^c \;,$$

$$F_{\mu\nu}^a \;=\; \partial_\mu A_\nu^a \;-\; \partial_\nu A_\mu^a \;+\; g_s f^{abc} A_\mu^b A_\nu^c \;.$$

- Dual Tensor:

$$\tilde{F}^{\mu\nu} \;\equiv\; \frac{1}{2} \varepsilon^{\mu\nu\rho\sigma} F_{\rho\sigma} \;,$$

$$\tilde{F}^{\mu\nu a} \;=\; \frac{1}{2} \varepsilon^{\mu\nu\rho\sigma} \left(\partial_\rho A_\sigma^a \;-\; \partial_\sigma A_\rho^a \;+\; g_s f^{abc} A_\rho^b A_\sigma^c \right) \;.$$
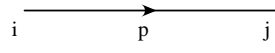
- Bianchi Identity:

$$[D_\mu, [D_\nu, D_\rho]] \;+\; [D_\nu, [D_\rho, D_\mu]] \;+\; [D_\rho, [D_\mu, D_\nu]] \;=\; 0 \;.$$

Thus we get follow identity.

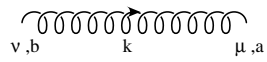$$\varepsilon^{\mu\nu\rho\sigma} \left[D_\mu, \left[D_\nu, D_\rho \right] \right] \;=\; 0 \; .$$
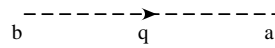
D.5   QCD Feynman Rules

- Fermion Propagator:

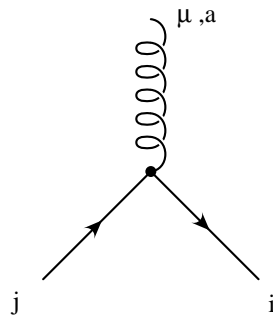$$\frac{i\delta^{ij}}{\not{p} - m + i\varepsilon}$$

- Gluon Propagator:

$$\frac{-i\delta_{ab}}{k^2 + i\varepsilon}\left[g_{\mu\nu} - (1 - \alpha)\frac{k_\mu k_\nu}{k^2 + i\varepsilon}\right]$$
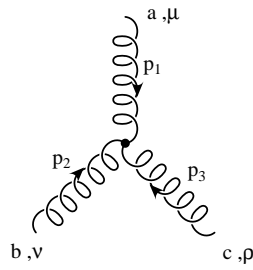
- Ghost Propagator:

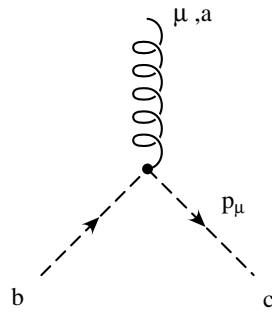$$\frac{-i\delta_{ab}}{q^2 + i\varepsilon}$$

- Gluon - Fermion Vertex:
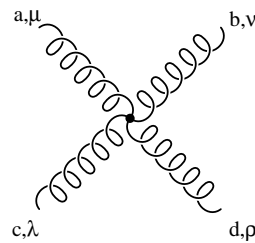

$$ig_s\gamma_\mu T^a_{ij}$$

- Gluon 3-point Vertex:

$$g_s f^{abc}\left[g_{\mu\nu}(p_1 - p_2)_\rho + g_{\nu\rho}(p_2 - p_3)_\mu + g_{\rho\mu}(p_3 - p_1)_\nu\right]$$

- Gluon - Ghost Vertex:

$$-g_s f^{abc} p_\mu$$

- Gluon 4-point Vertex:

$$- \quad ig_s^2 f^{abe} f^{cde} \left(g_{\mu\lambda} g_{\nu\rho} - g_{\mu\rho} g_{\nu\lambda} \right)$$

$$- \quad ig_s^2 f^{ace} f^{bde} \left(g_{\mu\nu} g_{\lambda\rho} - g_{\mu\rho} g_{\nu\lambda} \right)$$

$$- \quad ig_s^2 f^{ade} f^{cbe} \left(g_{\mu\lambda} g_{\nu\rho} - g_{\mu\nu} g_{\rho\lambda} \right)$$
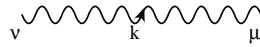
D.6 Electro-Weak Feynman Rule

- Z^0 Boson Propagator:
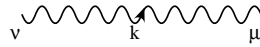
$$\frac{-i}{k^2 - M_Z^2 + i\varepsilon}\left[g_{\mu\nu} - (1 - \alpha_Z)\frac{k_\mu k_\nu}{k^2 - \alpha_Z M_Z + i\varepsilon}\right]$$

- W Boson Propagator:

$$\frac{-i}{k^2 - M_W^2 + i\varepsilon}\left[g_{\mu\nu} - (1 - \alpha_W)\frac{k_\mu k_\nu}{k^2 - \alpha_W M_W + i\varepsilon}\right]$$

- Photon - Fermion Vertex:

$$ieQ_\gamma(f)\gamma^\mu$$
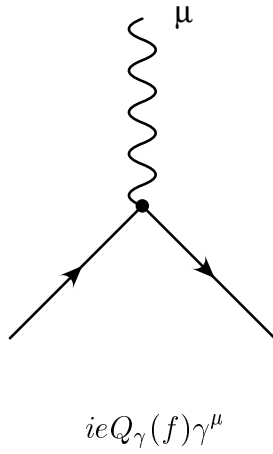
- Z^0 Boson - Fermion Vertex:

$$ie\left[Q_Z^R(f)\gamma_R^\mu + Q_Z^L(f)\gamma_L^\mu\right]$$
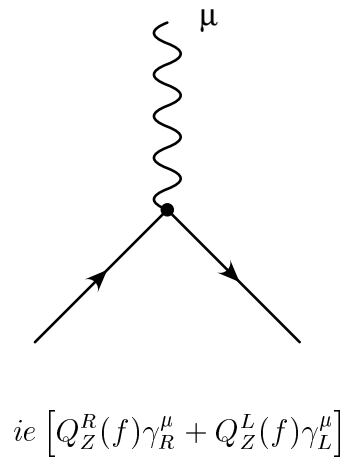
- Coefficients $Q_\gamma(f), Q_Z^{R,L}(f)$:

When "f" stands for lepton $(e^-, \mu^-$ and $\tau^-)$, then coefficients $Q_\gamma(f)$, $Q_Z^R(f)$
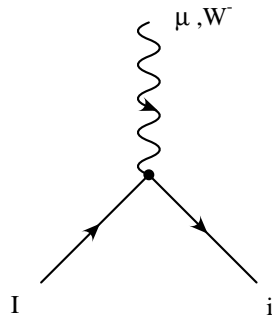
and $Q_Z^L(f)$ are

$$Q_\gamma(f) \;=\; -1 \;, \; Q_Z^R(f) \;=\; \frac{\sin\theta_w}{\cos\theta_w}, \; Q_Z^L(f) \;=\; \frac{2\sin^2\theta_w - 1}{2\sin\theta_w\cos\theta_w} \;.$$

While "f" stands for Quark, we get

$$Q_\gamma(\mathrm{U}) \;=\; \frac{2}{3}, \; Q_Z^R(\mathrm{U}) \;=\; \frac{-2\sin\theta_w}{3\cos\theta_w}, \; Q_Z^L(\mathrm{U}) \;=\; \frac{3 - 4\sin^2\theta_w}{6\sin\theta_w\cos\theta_w},$$

$$Q_\gamma(\mathrm{D}) \;=\; -\frac{1}{3}, \; Q_Z^R(\mathrm{D}) \;=\; \frac{\sin\theta_w}{3\cos\theta_w}, \; Q_Z^L(\mathrm{D}) \;=\; \frac{-3 + 2\sin^2\theta_w}{6\sin\theta_w\cos\theta_w} \;,$$

where the suffices U, D mean up-type (u, c, t) and down-type (d, s, b)

quarks.

- W Boson - Fermion Vertex:

$$-i\frac{e}{\sqrt{2}\sin\theta_W}C_{iI}\gamma_L^\mu.$$

Coefficients C_{iI}:

When "i, I" stand for leptons (e^-, μ^-, τ^- and (ν_e, ν_μ, ν_τ), then coefficients $C_{iI} = 1$. While "i, I" stand for Quark, we get $C_{iI} = V_{iI}$, where V_{iI} is Cabbibo-Kobayashi-Maskawa mixing parameter.

Bibliography

[1] S. Weinberg, *Phys. Rev. Lett.* **19**, 1264 (1967). A. Salam, in *Elementary Particle Physics*, ed. N. Svartholm (Almqvist and Wiksells, Stockholm, 1968): p. 367.

[2] Particle Data Group, Review of Particle Properties, *Eur. Phys. Jour.* C **3**, 1 (1998).

[3] LEP Electroweak Working Group and the SLD Heavy Flavor and Electroweak Groups, *A Combination of Preliminary Electroweak Measurements and Constraints on the Standard Model*, CERN-EP/99-015 (1999).

[4] F. Parodi *et. al.*, Constraints on the parameters of the V_{CKM} matrix at the end of 1997, hep-ph/9802289.

[5] Kerson Huang, *Quarks, Leptons & Gauge Fields*, World Scientific Publishing (1982).

[6] H. Arason *et al.*, *Phys. Rev.* D **46**, 3945 (1992).

[7] M. Sher, *Phys. Lett.* B **317**, 159 (1993).

[8] F. Butler *et al.*, *Nucl. Phys.* B **430**, 179 (1994), M. Alford *et al.*, *Nucl. Phys.* B (Proc. Suppl.) **47**, 370 (1996).

[9] H. L. Lai *et al.*, *Global QCD Analysis of Parton Structure of the Nucleon: CTEQ5 Parton Distributions*, hep-ph/9903282.

[10] S. Adler, *Phys. Rev.* **177**, 2426 (1969).

[11] J. S. Bell and R. Jackiw, *Nuovo Cimento* **60A**, 47 (1969).

[12] S. L. Glashow, J. Iliopoulos and L. Maiani, *Phys. Rev.* D **2**, 1285 (1970).

[13] L. B. Okun, *Leptons and Quarks*, North-Holland Publishing Company (1982).

[14] G. L. Kane, "Top Quark Topics" in *Gauge Bosons and Heavy Quarks* (Proceedings of the Eighteenth SLAC Summer Institute on Particle Physics, Stanford, 1990) ed. J. Hawthorne, p. 126. (unpublished)

[15] S. Abachi *et al.*(DØ Collaboration), *Phys. Rev. Lett.* **74**, 2632 (1995).

[16] F. Abe *et al.*(CDF Collaboration), *Phys. Rev. Lett.* **74**, 2626 (1995).

[17] B. Abbott *et al.* (DØ Collaboration), hep-ex/9808029, submitted to *Phys. Rev.* D, B. Abbott *et al.* (DØ Collaboration), *Phys. Rev. Lett.* **80**, 2063 (1998). F. Abe *et al.* (CDF Collaboration), *Phys. Rev. Lett.* **82**, 271 (1999). F. Abe *et al.* (CDF Collaboration), *Phys. Rev. Lett.* **80**, 2767 (1998). B. Abbott *et al.* (DØ Collaboration), *Phys. Rev.* D **58**, 052001 (1998). F. Abe *et al.* (CDF Collaboration), *Phys. Rev. Lett.* **79**, 1992 (1997). F. Abe *et al.* (CDF Collaboration), *Phys. Rev. Lett.* **80**, 2773 (1998). S. Abachi *et al.* (DØ Collaboration), *Phys. Rev. Lett.* **79**, 1203 (1997). B. Abbott *et al.* (DØ Collaboration), FERMILAB-PUB-98-130-E, submitted to *Phys. Rev.* D.

[18] M. Gluck, J. F. Owens and E. Reya, *Phys. Rev.* D **17**, 2324 (1978); B. L. Combridge, *Nucl. Phys.* B **151**, 429 (1979); J. Babcock, D. Sivers and S. Wolfram, *Phys. Rev.* D **18**, 162 (1978); K. Hagiwara and T. Yoshino, *Phys. Lett.* B **80**, 282 (1979); L. M. Jones and H. Wyld, *Phys. Rev.* D **17**, 782 (1978); H. Georgi *et al.*, *Ann. of Phys.* **114**, 273 (1978).

[19] P. Nason, S. Dawson and R. K. Ellis, *Nucl. Phys.* B **303**, 607 (1988);

P. Nason, S. Dawson and R. K. Ellis, *Nucl. Phys.* B **327**, 49 (1989); Erratum: *Nucl. Phys.* B **335**, 260 (1990).

[20] W. Beenakker, H. Kuijf, W. L. van Neerven and J. Smith, *Phys. Rev.* D **40**, 54 (1989); W. Beenakker, R. Meng, G. A. Schuler and J. Smith, *Nucl. Phys.* B **351**, 507 (1991).

[21] E. Laenen *et al.*, *Phys. Lett.* B **321**, 254 (1994).

[22] E. L. Berger and H. Contopanagos, *Phys. Lett.* B **361**, 115 (1995).

[23] S. Catani *et al.*, *Phys. Lett.* B **378**, 329 (1996).

[24] John F. Donoghue, Eugene Golowich and Barry R. Holstein, *Dynamics of the Standard Model*, Cambridge University Press (1992).

[25] G. Mahlon and S. Parke, *Phys. Lett.* B **411**, 173 (1997).

[26] T. Stelzer and S. WillenBrock, *Phys. Lett.* B **374**, 169 (1996).

[27] Adam F. Falk and Michael E. Peskin, *Phys. Rev.* D **49**, 3320 (1994).

[28] E. Eichten and K. Lane, *Phys. Lett.* B **327**, 129 (1994).

[29] C. Hill and S. Parke, *Phys. Rev.* D **49**, 4454 (1994).

[30] G. Mahlon and S. Parke, *Phys. Rev.* D **53**, 4886 (1996).

[31] Kang Young Lee *et al.*, Large Extra Dimension Effects on the Spin Configuration of the Top Quark Pair at e^+e^- Colliders, hep-ph/9905227.

[32] M. Jeżabek, *Nucl. Phys.* B **37B**, 197 (1994).

[33] F. Halzen and A. Martin *Quarks and Leptons*, John Wiley & Sons (1984).

[34] H. Wiedemann, *Particle Accelerator Physics*, Springer-Verlag (1993).

[35] J.D. Cockroft, E.T.S. Walton, Proc. of the Royal Soc. of London **A136**, 619 (1932).

[36] S. Abachi *et al.*, *Nucl. Instrum. Methods* A **338**, 185 (1994).

[37] C. Gerber *et al.*, DØ internal note No. 2140, October 1994 (unpublished).

[38] J. Yu, Ph.D thesis, SUNY at Stony Brook, *Determination of the Strong Coupling Constant (α_s) and a Test of Perturbative QCD Using W+Jets Processes in the DØ Detector*, August 1993, p.31 (unpublished).

[39] J. Bantly *et al.*, DØ internal note No. 2544, December 1995 (unpublished).

[40] J. Bantly *et al.*, FERMILAB-TM-1995, February 1997 (unpublished).

[41] J. Drinkard, Proc. 8th Meeting of the American Physical Society, Division of Particles and Fields, Albaquerque, NM (1994).

[42] J. Butler, DØ internal note No. 1682, February 1993 (unpublished).

[43] S. Abachi *et al.*, *Phys. Rev.* D **52**, 4877 (1995).

[44] Ties Behnke, Ph.D. Thesis, State University of New York at Stony Brook, August 1989.

[45] Gene Álvarez, Ph.D. Thesis, Indiana University, June 1996.

[46] Myungyun Pang, Ph.D. Thesis, Iowa State University, 1994.

[47] M. Narain for the DØ Collaboration, *Electron Identification in the DØ Detector*, Fermilab-Conf-93/054-E, 1993 (unpublished).

[48] R. Engelmann *et al.*, *Nucl. Instrum. Methods* **216**, 45 (1993).

[49] U. Heintz and M. Narain, DØ internal note No. 2355, November 1994 (unpublished).

[50] U. Heintz and M. Narain, DØ internal note No. 2386, November 1994 (unpublished).

[51] Q. Zhu, Ph.D. Thesis, New York University, April 1994.

[52] E. Gallas, DØ internal note No. 2066, April 1994 (unpublished).

[53] R. Astur, Ph.D. Thesis, Michigan State University, 1992.

[54] R. Kehoe and R. Astur, DØ internal note No. 2908, May 1996 (unpublished).

[55] F. Hsieh, DØ internal note No. 3130, November 1996 (unpublished).

[56] R. Kehoe, Ph.D. Thesis, University of Notre Dame, January 1997.

[57] S. Abachi *et al.*(DØ Collaboration), *Phys. Rev. Lett.* **75**, 1034 (1995).

[58] R. Hall *et al.*, DØ internal note No. 2591, October 1996 (unpublished).

[59] "Measurement of the Top Quark Mass in the Dilepton Channel.", B. Abbott *et al.*, Submitted to Phys. Rev. D, FERMILAB-PUB-98/261-E, hep-ex/980829.

[60] Erich Varnes, Ph.D. Thesis, UC Berkeley, Spring 1997.

[61] G. Marchesini *et al.*, *Comp. Phys. Comm.* **67**, 465 (1992).

[62] T. Sjöstrand, *Comp. Phys. Comm.* **82**, 74 (1994).

[63] R. Kleiss and W.J. Stirling, *Z. Phys.* C **40**, 419 (1988).

[64] R. Kleiss and W.J. Stirling, *Comp. Phys. Comm.* **40**, 359 (1986).

[65] W. T. Giele, E. W. N. Glover, David A. Kosower, *Nucl. Phys.* B **403**, 633 (1993).

[66] R. Raja, Fermilab-Conf-96-232, 1996.

[67] Stephen Parke and Yael Shadmi, *Phys. Lett.* B **387**, 199 (1996).

[68] Lasse Holström, *et al.*, *Comp. Phys. Comm.* **88**, 195 (1995).

[69] J. Kodaira, T. Nasuno, S. Parke, *Phys. Rev.* D **59**, 014023 (1999).

[70] Private communications with Stephen Parke and Lynn Orr.